Doctoral Dissertation

Study of Neutrino-Water Interactions using Nuclear Emulsion Detectors with Improved Event Reconstructions

Takahiro Odagawa

High Energy Physics Group
Division of Physics and Astronomy
Graduate School of Science
Kyoto University

February, 2023

Abstract

This thesis reports studies of neutrino-nucleus interactions using nuclear emulsion detectors with improved measurements of the charged particle kinematics.

To explain the matter-antimatter asymmetry in the universe, the CP violation is required. The discovery of the CP violation in the lepton sector is one of the main goals in the current and future neutrino oscillation experiments. The T2K experiment is a long-baseline neutrino oscillation experiment, and it has indicated the CP violation. One of the largest sources of systematic error in the T2K experiment is the uncertainty of the neutrino-nucleus interactions. This uncertainty stems from the nuclear models which describe hadrons inside the nucleus. To better understand such a "nuclear-effect," it is important to measure the hadrons with a wide coverage of the phase space. In particular, in the low-momentum region, the experimental data are lacking, and the models have not been tested in detail so far.

To understand the neutrino interactions on water, the measurement using nuclear emulsion detectors, called the NINJA experiment, has been started recently. The nuclear emulsion has an excellent spatial resolution which lowers the proton detection threshold down to $200\,\mathrm{MeV}/c$. This low momentum threshold will give new data of low-momentum protons which cannot be detected by the other experiments.

Two improvements in the NINJA experiment are reported. First, a larger detector is built to achieve higher statistics. In the NINJA experiment, scintillator detectors are used to get the beam timing information and identify muon tracks. A new scintillation tracker is developed which consists of plastic scintillator bars specially arranged with deliberate gaps between each other. By recognizing the hit pattern, a positional resolution of a few mm is achieved while keeping the number of readout channels as small as 248. The structure enables the detector to cover an area of $1\,\mathrm{m} \times 1\,\mathrm{m}$ without increasing the number of channels.

Second, the momentum reconstruction analysis is also improved. A new method using multiple Coulomb scatterings is developed. The method is based on the maximum likelihood to newly consider the energy deposit inside the detector volume. In addition, the treatment of the angle calculation in the method is also updated. The method highly reduces the bias observed in the low-momentum region from 25% to 1%. The resolution of the method is evaluated to be 10% for a $500\,\mathrm{MeV}/c$ muon passing through 69 iron plates. The particle identification is also developed in this study, and the 99% proton identification efficiency with 99% purity is achieved.

Using the developed methods, the data collected with a 75-kg water target are analyzed, and the results with a partial target mass of 8 kg are presented. The results show that the hadron multiplicity is a powerful tool to discriminate the interaction modes with a wide coverage for the charged particle kinematics. The results also indicate that the improvements play important roles in the measurements. Charged-current neutrino-water interactions with two protons and no pions are detected with the $200\,\mathrm{MeV}/c$ proton momentum threshold for the first time. The sample will be an important input to study the neutrino interaction models. The methods developed in this study will contribute to further studies of neutrino interactions in the NINJA experiment. Future NINJA results will help to reduce the systematic error in the long-baseline neutrino oscillation experiments and thus to discover the CP violation in the lepton sector.

Acknowledgment

In these five years of my research life in the graduate school, I have got a lot of supports from many people. I would like to express my gratitude to every one of them.

First of all, I would like to appreciate my supervisor, Prof. Tsuyoshi Nakaya. He always gave me new opportunities of challenges, and they were always encouraging. I felt delighted when he proposed that we write a paper about a momentum reconstruction method with multiple Coulomb scatterings since it is worth publishing. I led a wonderful research life in the Kyoto High Energy Physics group owing to him. I would also like to show my gratitude to Dr. Tatsuya Kikawa, who is my another supervisor. He was always welcoming to discuss and gave me a lot of advice. He also gave me many comments on my theses, papers, documents, and slides.

I would like to express my gratitude to the NINJA collaboration. Dr. Tsutomu Fukuda, the spokesperson of the NINJA experiment, always gave me a lot of interesting comments. I learned how the "emulsionist" analyzes the data from his comments and works. Dr. Yosuke Suzuki is one of the most respectable researcher I have ever met. His attitude to the data, statistics, and analyses is always careful and enlightening. Even after he left from the graduate school, he gave me essential data and comments to my study. Without him, the work in this thesis could not be finalized at all. Hiroaki Kawahara is also one of the best colleagues in the NINJA experiment. The emulsion shifter was the most complicated detector in the NINJA physics run, and he dealt with the data so carefully. He provided the essential inputs in the muon track matching. I cannot think of the NINJA experiment without both of them. I would also like to show my appreciation to Dr. Ayami Hiramoto, ex-collaborator of the NINJA experiment. My research life started from a talk with her when I entered the graduate school. I asked her a lot of questions about the scintillation tracker and neutrino interaction analyses, and she always answered to me clearly and easily. I would like to thank Prof. Masahiro Komatsu, Prof. Akihiro Minamino, Prof. Osamu Sato, and Prof. Hiroshi Shibuya for their advice in the paper review meetings. I am also grateful to the other NINJA colleagues, Dr. Ali Ajmi, Ayaka Kasumi, Dr. Tomokazu Matsuo, Kosaku Mizuno, Mayuko Naiki, Dr. Hitoshi Oshima, Tomoki Takao, and all the past and current members for their effort in carrying out the NINJA experiment.

I would also like to show my appreciation to the WAGASCI/Baby MIND group in the T2K experiment. Kenji Yasutome gave me crucial information about the WAGASCI detectors and neutrino beam flux. Both of my papers cannot be written without the information from him. I also asked a lot of questions and requirements about the WAGASCI software, and he always kindly and quickly responded to me. Giorgio Pintaudi developed well-structured WAGASCI

software, where the NINJA Monte Carlo simulation is based. Without the software, our research could not have gone further anymore. In particular, he ran WAGASCI re-weight software for us, which was essential in our evaluation of the systematic uncertainties. I would also like to express my gratitude to all the past and current members in the WAGASCI/Baby MIND group who developed and validated the analysis.

In the operation and analyses of the NINJA experiment, we had many helps from the T2K collaboration. Prof. Yoshinari Hayato gave us many essential comments on the physics and sensitivities of the NINJA experiment. He also kindly helped me to develop and rewrite the code of NEUT for the simulation study of the heavy water interaction, which is unfortunately not described in this thesis. I would also like to appreciate the members of the T2K neutrino beam group for their help during the detector operation and analysis, giving me the information of the neutrino beam. In addition, I enjoyed staying at Tokai with the past and current T2K staff and students.

I am also grateful to the past and current members in the Kyoto High Energy Physics group. I owe a lot of things to my colleagues in the Kyoto group: Tomofumi Abe, Takuji Ikemitsu, Soichiro Kuribayashi, Masanori Tajima, Masayuki Hatano, and Yuya Mino. I would also like to thank Prof. Atsuko Ichikawa, Prof. Osamu Tajima, Prof. Roger Wendell, Dr. Toshi Sumida, Dr. Junya Suzuki, and Dr. Shunsuke Adachi. I had many help from the secretaries: Tanizawa-san, Sekiguchi-san, and Sasaki-san.

Finally, I would like to thank my parents and sister; Naoto Odagawa, Noriko Odagawa, and Mami Odagawa. Thanks to their support to this day, I have been able to believe in myself for all time in my life.

Contents

Chapter 1

Introduction

In the standard model (SM), a neutrino is an elementary particle without mass nor electric charge and only interacts via the weak interactions. Currently, neutrinos are expected to be one of the keys to exploring physics beyond the SM. For the current and future neutrino oscillation experiments to reach new physics in the lepton sector, understanding the neutrino interaction in the sub-GeV energy region is essential. In this region, a neutrino interacts with a nucleus inside the nuclear medium, and the interactions are described by complicated nuclear models. Since the cross section is dependent on such models, understanding the neutrino interaction is not easy. To better understand the models, it is important to measure the kinematics of the emitted hadrons from the neutrino interactions. In this thesis, we developed new techniques to measure the kinematics of charged particles emitted from the neutrino interactions using nuclear emulsion detectors. As an introduction, we briefly review the theory and experiments of neutrino physics in this chapter.

1.1 Neutrino

Neutrino was first postulated by W. Pauli in 1930 [1]. F. Reines and C. L. Cowan first observed electron anti-neutrinos from a reactor in 1952 [2]. After the first detection, L. M. Lederman, M. Schwartz, and J. Steinberger detected muon neutrinos from pion decays in 1962 [3], and the existence of different species (today called "flavor") of neutrinos was discovered. The third species of neutrinos, tau neutrino, was directly discovered by the DONUT (Direct Observation of the NU Tau) experiment in 2000 [4]. The number of neutrino flavors lighter than the half mass of Z^0 boson is measured to be 2.9840 ± 0.0082 by the LEP (Large Electron–Positron collider) and SLC (SLAC Linear Collider) colliders [5, 6].

1.2 Neutrino oscillation

In the SM, neutrinos do not have masses. However, the observation of the neutrino oscillation shows that they actually have tiny masses. In this section, an overview of the neutrino oscillation is described.

1.2.1 Theory of neutrino oscillation

When neutrinos have masses and their eigenstates are different between the flavor and the mass, they can change the flavors during the flight since the time propagation is carried out under the mass eigenstates. This phenomenon is called "neutrino oscillation." The flavor eigenstates of neutrinos $|\nu_\alpha\rangle\,(\alpha = e, \mu, \tau)$ are expressed as a mixture of three mass eigenstates $|\nu_i\rangle\,(i = 1, 2, 3)$ as

$$|\nu_\alpha\rangle = \sum_i U_{\alpha i}\,|\nu_i\rangle\,. \tag{1.1}$$

Here, U is a 3×3 unitary matrix known as the Pontecorvo–Maki–Nakagawa–Sakata (PMNS) matrix [7, 8]:

$$\begin{aligned} U &= \begin{pmatrix} U_{e1} & U_{e2} & U_{e3} \\ U_{\mu 1} & U_{\mu 2} & U_{\mu 3} \\ U_{\tau 1} & U_{\tau 2} & U_{\tau 3} \end{pmatrix} \\ &= \begin{pmatrix} 1 & 0 & 0 \\ 0 & c_{23} & s_{23} \\ 0 & -s_{23} & c_{23} \end{pmatrix} \begin{pmatrix} c_{13} & 0 & s_{13}e^{-i\delta_{\mathrm{CP}}} \\ 0 & 1 & 0 \\ -s_{13}e^{i\delta_{\mathrm{CP}}} & 0 & c_{13} \end{pmatrix} \begin{pmatrix} c_{12} & s_{12} & 0 \\ -s_{12} & c_{12} & 0 \\ 0 & 0 & 1 \end{pmatrix} \begin{pmatrix} e^{i\alpha_1/2} & 0 & 0 \\ 0 & e^{i\alpha_2/2} & 0 \\ 0 & 0 & 1 \end{pmatrix}, \end{aligned} \tag{1.2}$$

where $c_{ij} = \cos\theta_{ij}$ and $s_{ij} = \sin\theta_{ij}$, and θ_{ij} is the mixing angle between two mass eigenstates, $|\nu_i\rangle$ and $|\nu_j\rangle$. The parameter δ_{CP} is known as the Dirac CP-violating phase, and the CP symmetry in the lepton sector is violated in the case of $\delta_{\mathrm{CP}} \neq 0,\ \pi$. When $\delta_{\mathrm{CP}} \neq 0,\ \pi$, the elements of the PMNS matrix are complex, and thus the difference between the particle and anti-particle emerges. In the neutrino oscillation, $\nu_\alpha \to \nu_\beta$ and $\bar{\nu}_\alpha \to \bar{\nu}_\beta$ $(\alpha \neq \beta)$ have different oscillation probabilities when $\delta_{\mathrm{CP}} \neq 0,\ \pi$. The parameters α_1 and α_2 are known as the Majorana CP-violating phases. When neutrino is the Dirac fermion, $\alpha_1 = 0$ and $\alpha_2 = 0$, while when neutrino is the Majorana fermion [9], they can be non-zero. The Majorana phases also represent the CP violation in the lepton sector, but they do not appear in the neutrino oscillation.

The time propagation of the neutrinos in a vacuum is expressed by the Schrödinger equation[1]:

$$i\frac{\mathrm{d}}{\mathrm{d}t}\,|\nu_i(t)\rangle = \mathcal{H}_0\,|\nu_i(t)\rangle = E_i\,|\nu_i(t)\rangle\,, \tag{1.3}$$

where $\mathcal{H}_0$ is the Hamiltonian in a vacuum, and E_i is the energy eigenvalue of the mass eigenstate, $|\nu_i\rangle$. The time dependence of the mass eigenstate can be thus expressed as

$$|\nu_i(t)\rangle = e^{-iE_it}\,|\nu_i\rangle\,. \tag{1.4}$$

Using Eqs. (1.1) and (1.4), the time propagation of the neutrino flavor eigenstate can be written as

$$|\nu_\alpha(t)\rangle = \sum_i U_{\alpha i}e^{-iE_it}\,|\nu_i\rangle\,. \tag{1.5}$$

[1] Hereafter, we use the natural unit $\hbar = c = 1$ in this section.

Neutrinos are light and can be regarded as relativistic particles. Thus, Eq. (1.5) can be written as

$$\begin{aligned} |\nu_\alpha(t)\rangle &= \sum_i U_{\alpha i} e^{-ip_i t} \exp\left(-\frac{im_i^2 t}{2E_i}\right) |\nu_i\rangle \\ &= \sum_{i,\beta} U_{\alpha i} e^{-ip_i t} \exp\left(-\frac{im_i^2 t}{2E_i}\right) U^\dagger_{\beta i} |\nu_\beta\rangle \,. \end{aligned} \tag{1.6}$$

Here, E_i is approximated as

$$E_i = \sqrt{p_i^2 + m_i^2} \simeq p_i + \frac{m_i^2}{2p_i} \simeq p_i + \frac{m_i^2}{2E_i} \tag{1.7}$$

since $p_i \gg m_i$.

The probability of the neutrino oscillation from ν_α to ν_β is then calculated as

$$\begin{aligned} P(\nu_\alpha \to \nu_\beta) &= |\langle \nu_\beta | \nu_\alpha(t) \rangle|^2 \\ &= \left| \sum_{i,\beta} U_{\alpha i} e^{-ip_i t} \exp\left(-\frac{im_i^2 t}{2E_i}\right) U^\dagger_{\beta i} \right|^2 \\ &= \sum_{i,j} U^\dagger_{\alpha i} U_{\beta i} U_{\alpha j} U^\dagger_{\beta j} \exp\left(-\frac{i(m_i^2 - m_j^2)t}{2E}\right) \\ &= \sum_{i,j} U^\dagger_{\alpha i} U_{\beta i} U_{\alpha j} U^\dagger_{\beta j} \exp\left(-\frac{i\Delta m_{ij}^2 t}{2E}\right) \\ &= \delta_{\alpha\beta} - 4 \sum_{i>j} \mathrm{Re}\{U^*_{\alpha i} U_{\beta i} U_{\alpha j} U^*_{\beta j}\} \sin^2\left(\frac{\Delta m_{ij}^2 L}{4E}\right) \\ &\quad + 2 \sum_{i>j} \mathrm{Im}\{U^*_{\alpha i} U_{\beta i} U_{\alpha j} U^*_{\beta j}\} \sin\left(\frac{\Delta m_{ij}^2 L}{2E}\right), \end{aligned} \tag{1.8}$$

where

$$\delta_{\alpha\beta} = \begin{cases} 1 & (\alpha = \beta) \\ 0 & (\alpha \neq \beta), \end{cases} \tag{1.9}$$

$\Delta m_{ij}^2 = m_i^2 - m_j^2$ is a mass-squared difference, and $L = t$ is a traveling distance of the neutrino. In this calculation, since m_i is small compared to p_i, the momentum and energy of the neutrino are considered to be the same between different mass eigenstates; $E_i = E_j = E$, $p_i = p_j$ $(i \neq j)$. For example, in current accelerator-based long-baseline neutrino oscillation experiments, the

muon neutrino disappearance probability in the muon neutrino beam,

$$P(\nu_\mu \to \nu_\mu) \simeq 1 - 4c_{13}^2 s_{23}^2 (c_{12}^2 c_{23}^2 + s_{12}^2 s_{13}^2 s_{23}^2) \sin^2 \Phi_{32}, \tag{1.10}$$

is used, where $\Phi_{ij} = \Delta m_{ij}^2 L/4E$, and $\Delta m_{21}^2 \ll |\Delta m_{32}^2|$ is assumed.

1.2.2 Matter effect

In the previous section, the theory of the neutrino oscillation in a vacuum is discussed. When neutrinos pass through dense matter, they are affected by the coherent scatterings with electrons in the matter. All three flavors of neutrinos can be affected via Z^0 boson, while only electron neutrinos can be scattered via $W^\pm$ boson. Thus, only electron neutrinos feel an additional potential from the matter, and such an effect is called "matter effect" or Mikheyev–Smirnov–Wolfenstein (MSW) effect [10, 11]. The Schrödinger equation and the potential considering the matter effect can be written as

$$i\frac{\mathrm{d}}{\mathrm{d}t} |\nu_\alpha(t)\rangle = (\mathcal{H}_0 + \mathcal{V}) |\nu_\alpha(t)\rangle , \tag{1.11}$$

$$\mathcal{V} = \begin{pmatrix} \sqrt{2} G_\mathrm{F} n_e & 0 & 0 \\ 0 & 0 & 0 \\ 0 & 0 & 0 \end{pmatrix}. \tag{1.12}$$

Here, G_F is the Fermi constant, and n_e is the electron density in the matter. The sign of the potential $\mathcal{V}$ is inverted for anti-neutrinos. In current accelerator-based neutrino oscillation experiments, the matter effect by the earth has to be considered. The first-order approximated solution of Eq. (1.11) gives the electron neutrino appearance probability from the muon neutrino beam:

$$\begin{aligned} P(\nu_\mu \to \nu_e) \simeq\ & 4c_{13}^2 s_{13}^2 s_{23}^2 \sin^2 \Phi_{31} \\ & + 8c_{13}^2 s_{12} s_{13} s_{23} (c_{12} c_{23} \cos\delta_\mathrm{CP} - s_{12} s_{13} s_{23}) \cos\Phi_{32} \sin\Phi_{31} \sin\Phi_{21} \\ & - 8c_{13}^2 c_{12} c_{23} s_{12} s_{13} s_{23} \sin\delta_\mathrm{CP} \sin^2\Phi_{32} \sin^2\Phi_{31} \sin^2\Phi_{21} \\ & - 2c_{13}^2 s_{12}^2 s_{23}^2 \frac{aL}{E} (1 - 2s_{13}^2) \cos\Phi_{32} \sin\Phi_{31} \\ & + 8c_{13}^2 s_{13}^2 s_{23}^2 \frac{a}{\Delta m_{31}^2} (1 - 2s_{13}^2) \sin\Phi_{31}, \end{aligned} \tag{1.13}$$

where $a = 2\sqrt{2} G_\mathrm{F} n_e E$. The first three terms of Eq. (1.13) are derived from the neutrino oscillation in a vacuum, while the forth and fifth terms represent the matter effect. In Eq. (1.13), $\delta_\mathrm{CP} \to -\delta_\mathrm{CP}$ and $a \to -a$ give the oscillation probability of anti-neutrinos, $P(\bar{\nu}_\mu \to \bar{\nu}_e)$.

1.2.3 Discovery of neutrino oscillation

The experimental study of the neutrino oscillation started from the so-called "solar neutrino problem." In 1968, the Homestake experiment first observed electron neutrinos produced from the nuclear fusion in the sun, so-called solar neutrinos [12]. Although solar neutrinos were detected, the number was around 1/3 less than expected. Since then, similar observations were reported by the Kamiokande [13], GALLEX (GALLium EXperiment) [14], GNO (Gallium Neutrino Observatory) [15], and SAGE (Soviet–American Gallium Experiment) [16] experiments, and this deficit of the neutrino flux was called the solar neutrino problem.

The observation of the neutrino oscillation brought the idea of the solar neutrino oscillation as a solution of the solar neutrino problem. The measurement of atmospheric neutrino flux by the Kamiokande experiment showed a deficit of atmospheric muon neutrinos and discussed the neutrino oscillation to explain the deficit [17]. In 1998, the successor of the Kamiokande detector, Super-Kamiokande, reported the evidence of the atmospheric neutrino oscillation with higher statistics [18]. Atmospheric neutrinos are generated as the decay products of the hadrons from the cosmic ray collisions on nuclei in the atmosphere. The main process in the atmospheric neutrino generation is the pion decay ($\pi^+ \to \mu^+ + \nu_\mu$) and the subsequent muon Michel decay ($\mu^+ \to e^+ + \bar{\nu}_\mu + \nu_e$). Thus, the ratio of the number of atmospheric muon neutrinos ($\nu_\mu + \bar{\nu}_\mu$) to that of electron neutrinos ($\nu_e + \bar{\nu}_e$) is expected to be two. However, the result shows a deficit of the number of muon neutrinos and its zenith angle dependence as shown in Fig. 1.1.

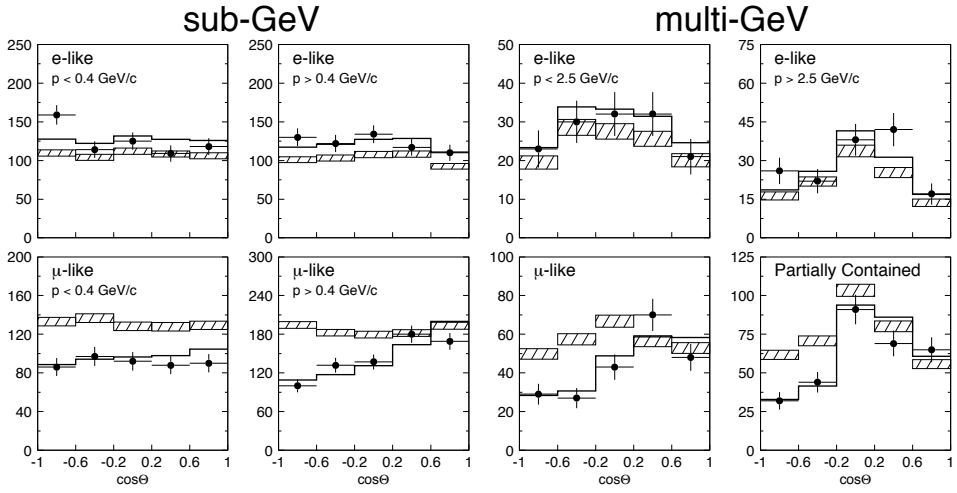

Figure 1.1: Zenith angle distributions of charged leptons from the atmospheric neutrino interactions in the Super-Kamiokande detector. Upward-going particles have $\cos\Theta < 0$, and downward-going particles have $\cos\Theta > 0$. The hatched region shows the expectation for no oscillations, and the bold line is the best fit expectation for $\nu_\mu \leftrightarrow \nu_\tau$ oscillations [18].

The evidence of the neutrino oscillation leads to the solar neutrino oscillation as the solution for the solar neutrino problem. The direct solution to the solar neutrino problem was reported by the SNO (Sudbury Neutrino Observatory) experiment in 2001 [19]. SNO is a 1 kt heavy water

(D_2O) Cherenkov detector. Three different reactions can be used to measure solar neutrinos; Electron Scattering (ES: $\nu_x + e^- \to \nu_x + e^-$), Charged Current (CC: $\nu_e + d \to e^- + p + p$), and Neutral Current (NC: $\nu_x + d \to \nu_x + p + n$). The ES reaction has different cross sections between electron neutrinos and the other flavors, while the CC reaction is only sensitive to electron neutrinos. The NC reaction has the same cross sections for all the flavors. Thus, the comparison of the reactions can provide a fraction of the flavor change due to the neutrino oscillation. Combining the SNO and Super-Kamiokande results [20], the evidence of the solar neutrino oscillation was established. Finally, combined with the result of the KamLAND (Kamioka Liquid scintillator Anti-Neutrino Detector) experiment [21], it is shown that the solution to the solar neutrino problem is the neutrino oscillation with the MSW effect in the solar matter.

1.2.4 Measurement of neutrino oscillation parameters

Nowadays, experiments using not only the naturally-produced neutrinos (solar or atmospheric neutrinos) but also the artificially-produced neutrinos (reactor or accelerator neutrinos) have been carried out. The oscillation parameters in the PMNS matrix have been measured with various neutrino energy scales and traveling distances.

The parameters θ_{12} and Δm^2_{21} have been measured by solar and long-baseline reactor neutrino experiments. The electron neutrino disappearance probability of solar neutrinos has been measured by the Homestake [12], Super-Kamiokande [22], SNO [23], and Borexino [24] experiments. The solar neutrino oscillation probability in the energy region higher than a few MeV is approximated as $\sin^2\theta_{12}$, and the most precise measurement of θ_{12} can be achieved. Besides, the electron anti-neutrino survival probability of reactor neutrinos has been measured by the KamLAND experiment [25]. The oscillation probability for the KamLAND experiment is approximated as

$$P \simeq 1 - 2c^2_{12}s^2_{12}\sin^2 2\Phi_{21}. \tag{1.14}$$

The distortion of the reactor anti-neutrino spectra gives the most precise measurement of Δm^2_{21}.

The parameter θ_{13} has been measured by short-baseline reactor and long-baseline accelerator neutrino experiments. The first constraint on θ_{13} was given by the Chooz experiment [26] in 1999. In 2011, the T2K (Tokai to Kamioka) experiment reported that θ_{13} has a non-zero value by measuring the electron neutrino appearance [27]. In the short-baseline ($L \sim 1\,\mathrm{km}$) reactor experiments, the survival probability of electron anti-neutrino is approximated as

$$P \simeq 1 - 4c^2_{13}s^2_{13}\sin^2\left(c^2_{12}\Phi_{31} + s^2_{12}\Phi_{32}\right). \tag{1.15}$$

In Eq. (1.15), the value of $c^2_{12}\Phi_{31} + s^2_{12}\Phi_{32}$ can be precisely measured by the other experiments. Thus, the determination of θ_{13} can be achieved using reactor neutrinos. These days, the parameter is precisely measured by the Daya Bay [28], Double Chooz [29], and RENO (Reactor Experiment for Neutrino Oscillation) [30] experiments.

The parameters θ_{23} and $|\Delta m^2_{32}|$ are measured by long-baseline accelerator and atmospheric neutrino experiments. The K2K (KEK to Kamioka) [31], MINOS/MINOS+ (Main Injector

Table 1.1: Summary of the best-fit values of the neutrino oscillation parameters [39, 40]. NO and IO represent the mass ordering explained in Sect. 1.2.5.

Parameter	Ordering	Best-fit $\pm 1\sigma$	3σ range
$\sin^2\theta_{12}$	NO	$0.304^{+0.012}_{-0.012}$	0.269–0.343
	IO	$0.304^{+0.013}_{-0.012}$	0.269–0.343
$\sin^2\theta_{23}$	NO	$0.573^{+0.018}_{-0.023}$	0.405–0.620
	IO	$0.578^{+0.017}_{-0.021}$	0.410–0.623
$\sin^2\theta_{13}$	NO	$0.02220^{+0.00068}_{-0.00062}$	0.02034–0.02430
	IO	$0.02238^{+0.00064}_{-0.00062}$	0.02053–0.02434
$\Delta m^2_{21}\,[10^{-5}\,\mathrm{eV}^2/c^4]$	NO, IO	$7.42^{+0.21}_{-0.20}$	6.82–8.04
$\Delta m^2_{31}\,[10^{-3}\,\mathrm{eV}^2/c^4]$	NO	$2.515^{+0.028}_{-0.028}$	2.4315–2.599
$\Delta m^2_{32}\,[10^{-3}\,\mathrm{eV}^2/c^4]$	IO	$-2.498^{+0.028}_{-0.029}$	-2.584–-2.413
$\delta_{\mathrm{CP}}\,[^\circ]$	NO	194^{+52}_{-25}	105–405
	IO	287^{+27}_{-32}	192–361

Neutrino Oscillation Search) [32], T2K [33], and NOνA (NuMI Off-axis ν_e Appearance) [34] experiments measured the parameters by the muon neutrino disappearance measurement using accelerator neutrinos. The OPERA (Oscillation Project with Emulsion-tRacking Apparatus) experiment also measured the parameters using the tau neutrino appearance in the accelerator neutrino beam [35]. In addition, the Super-Kamiokande [36] and IceCube/DeepCore [37] experiments measured the parameters using the atmospheric neutrino oscillation.

Finally, all the mixing angles and mass-square differences are measured with 5% precision, while the value of δ_{CP} is not yet known. This value can be measured by the electron neutrino and anti-neutrino appearances in long-baseline accelerator neutrino experiments. The current constraint on the value is given by the T2K [33] and NOνA [34] experiments, and the CP conservation is excluded with a 90% confidence level by the T2K experiment [38]. The current best-fit values of the neutrino oscillation parameters are summarized in Table 1.1.

1.2.5 Unsolved questions

Today, all the mixing angles and mass-square differences are precisely measured. However, there are still unsolved questions in neutrino physics, and some of them can be solved by the more precise measurement of the neutrino oscillation. According to the parameters in Table 1.1, the PMNS matrix has larger mixing angles than the Cabibbo–Kobayashi–Maskawa (CKM) matrix [41, 42], i.e. leptons are largely mixed than quarks. One of the most interesting topics in the neutrino mixing is the mixing of ν_2 and ν_3. The mixing angle θ_{23} has the largest uncertainty among the parameters, and it is close to $\pi/4$, which corresponds to the maximal mixing. The existence of the maximal mixing in the lepton sector may be a hint of new symmetry. Thus, more precise measurements of θ_{23} are necessary to clarify whether the unknown symmetry in the lepton sector exists or not.

The determination of the mass ordering is also crucial to understand the neutrino physics.

The parameter Δm^2_{21} measured by the solar neutrino experiments and KamLAND experiment is conventionally defined as positive, i.e. $m_2 > m_1$. The value of Δm^2_{32} is measured by the long-baseline accelerator and atmospheric neutrino experiments, and the result shows $\Delta m^2_{21} \ll |\Delta m^2_{32}|$. However, the probability of the neutrino oscillation in a vacuum is independent of the sign of Δm^2_{32}. Therefore, there are two possibilities of the order of the neutrino masses: the Normal Ordering (NO), $m_1 < m_2 < m_3$ and the Inverted Ordering (IO), $m_3 < m_1 < m_2$. The difference of the mass ordering changes the matter effect in the oscillation probability, thus it can be determined by atmospheric or accelerator-based neutrino experiments since the neutrinos feel a large matter effect from the earth. The result from Super-Kamiokande favors NO [36], but it is not yet determined.

In the current and future long-baseline accelerator neutrino experiments, the discovery of the CP violation in the neutrino oscillation is the primary goal. The matter-antimatter asymmetry in the universe requires the CP violation according to Sakharov's condition [43]. However, the currently-known CP violation in the quark sector [44–46] cannot explain the matter-antimatter asymmetry in the universe. There are many attempts to discover new CP violations, and the measurement of δ_{CP} in the neutrino oscillation is one of the most promising ones among them. In the $\nu_\mu \to \nu_e$ oscillation probability in Eq. (1.13), δ_{CP} emerges in the second-leading term. Since all mixing angles were found to have non-zero values, the measurement of δ_{CP} is possible through the measurement of the $\nu_\mu \to \nu_e$ and $\bar{\nu}_\mu \to \bar{\nu}_e$ oscillation probabilities. Currently, δ_{CP} is constrained by the T2K and NOνA experiments as described in Sect. 1.2.4. By the T2K experiment, the CP conservation in the lepton sector is excluded by a 90% confidence level, but it is still unknown. The current sensitivities are statistically limited, thus the next-generation experiments with larger detectors, Hyper-Kamiokande [47] and DUNE (Deep Underground Neutrino Experiment) [48] experiments, are under construction. In these next-generation experiments, the sensitivities will be limited by systematic uncertainties. One of the largest systematic sources is the uncertainty of the neutrino-nucleus interaction models. Even for the T2K experiment, the uncertainty of the neutrino interaction models should be studied further. To measure the neutrino oscillation parameters, the comparison of the neutrino energy spectra before and after the oscillation is necessary. This comparison is dependent on the neutrino-nucleus interaction models, and a reliable set of the models is a critical input to the analysis. The uncertainty of the neutrino interaction models changes the expected rate of the neutrino interactions and bias the reconstructed value of the neutrino energy as described in Sect. 3.3.1. In addition, the current understanding of the uncertainty of the neutrino interaction models is based on the results from various measurements, but the data is still lacking. There are lots of unknown items in the neutrino interaction and its models. In particular, a large phase space of emitted hadrons is not in detail measured yet. The current status of the measurement of the hadrons from neutrino interactions is described in Sect. 3.3.2. To reduce and understand such an uncertainty, a better understanding of the neutrino-nucleus interactions is crucial.

1.3 Neutrino interaction

In this section, neutrino interactions are briefly described. Details of the neutrino interaction models used in the sub- and multi-GeV neutrino energy region will be explained in Chap. 3. Neutrino interacts only via the weak force (except gravitational force). When the neutrino energy is not enough to create real weak bosons, i.e. below the unification energy, $\mathcal{O}(100\,\mathrm{GeV})$, the weak interaction is always mediated by virtual weak bosons. The propagator of this process is proportional to $1/M^2$, where M is the mass of the weak bosons, thus the interaction cross section is much smaller than the electromagnetic force. The interaction mediated by $W^{\pm}$ boson is called a charged-current (CC) interaction, while that mediated by Z^0 boson is called a neutral-current (NC) interaction. The charged- and neutral-currents are respectively written as

$$j^{\mu\pm} = \bar{u}\frac{-ig_W}{2\sqrt{2}}\gamma^{\mu}(1-\gamma^5)u, \tag{1.16}$$

$$j^{\mu 0} = \bar{u}\frac{-ig_Z}{2\sqrt{2}}\gamma^{\mu}(g_V - g_A\gamma^5)u, \tag{1.17}$$

where u and $\bar{u}$ are Dirac spinors, g_W and g_Z are the coupling strengths, γ^{μ} and $\gamma^5 = i\gamma^0\gamma^1\gamma^2\gamma^3$ are the Dirac matrices, and g_V and g_A are the vector and axial-vector coupling constants, respectively. The Feynman diagrams of the charged- and neutral-current interactions are shown in Fig. 1.2.

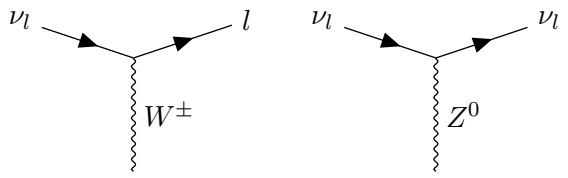

Figure 1.2: Diagrams of charged-current (left) and neutral-current (right) interactions.

The NC interactions are identical to all flavors of neutrinos. In the neutrino oscillation experiments, it is important to identify the incoming neutrino flavors, therefore the CC interactions are commonly used. In the current and future long-baseline neutrino oscillation experiments, the neutrino energy is around sub- or multi-GeV. In this energy region, neutrinos interact with nucleons bounded in nuclei of target materials. The effective Lagrangian of the neutrino-nucleon interaction is written as

$$\mathcal{L}_{\mathrm{eff}} = \frac{G_{\mathrm{F}}}{\sqrt{2}}(j_{\mu}^{\dagger}(k,k')J^{\mu}(p,p')) + \mathrm{h.c.}, \tag{1.18}$$

where $j_{\mu}^{\dagger}(k,k')$ is a leptonic current, $J^{\mu}(p,p')$ is a hadronic current, k and k' are the initial and final four-momenta of leptons, respectively, and p and p' are the initial and final four-momenta of nucleons, respectively. Figure 1.3 shows the interaction described by Eq. (1.18). The differential

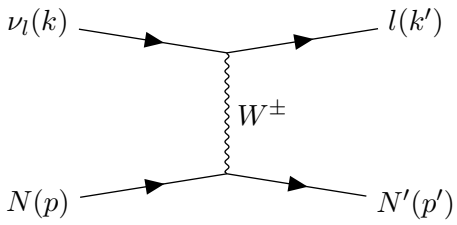

Figure 1.3: Diagram of the neutrino-nucleon interaction.

cross section of the CC neutrino-nucleon interaction can be obtained as

$$\frac{\mathrm{d}\sigma}{\mathrm{d}q^2} = \frac{1}{32\pi}\frac{G_{\mathrm{F}}^2\cos^2\theta_{\mathrm{C}}}{M^2E_\nu^2}L_{\alpha\beta}H^{\alpha\beta}, \tag{1.19}$$

where q^2 is the square of the four-momentum transfer, M is the nucleon mass, θ_{C} is the Cabibbo angle, and $L_{\alpha\beta}$ and $H^{\alpha\beta}$ are the leptonic and hadronic tensors, respectively. The leptonic tensor is simply calculated as

$$L_{\alpha\beta} = k_\alpha k'_\beta + k'_\alpha k_\beta - g_{\alpha\beta}(k\cdot k') - i\epsilon_{\alpha\beta\gamma\delta}k'^{\gamma}k^{\delta}, \tag{1.20}$$

where $g_{\alpha\beta}$ is the Lorentz metric tensor and $\epsilon_{\alpha\beta\gamma\delta}$ is the Levi-Civita symbol. On the other hand, the hadronic tensor is complicated because it includes QCD (Quantum ChromoDynamics) physics and the many-body effect. Thus, the tensor normally depends on the models, and the cross section is different in each model. To better understand the neutrino interaction models in this energy region, a measurement of hadrons from the interactions is important.

Many experiments are ongoing to measure and understand the neutrino interactions in this energy region [49, 50]. Because the detectors in these experiments do not have sufficient efficiencies for hadrons in some phase space, especially in a low-momentum region, they have focused on the measurement of the charged lepton from the interactions. In addition, for the T2K and Hyper-Kamiokande experiments, measurement of neutrino-water interactions is essential since they use water Cherenkov detectors as their far detector. Thus, a new detector to measure the neutrino-water interactions with a wide coverage for the hadrons is significant. NINJA (Neutrino Interaction research with Nuclear emulsion and J-PARC Accelerator) is an experiment aiming to precisely measure neutrino-water interactions using high-intensity neutrino beam from J-PARC (Japan Proton Accelerator Research Complex) and nuclear emulsions. The nuclear emulsion detector has a very precise three-dimensional spatial resolution, and it allows us to detect very short tracks of low-momentum hadrons. Details of the NINJA experiment are described in Chap. 4. In the previous measurement of the NINJA experiment, the target mass was limited by the number of readout channels in some detector. The momentum reconstruction of the charged particles using a nuclear emulsion detector was also developed in the previous measurements, but it resulted large bias of the reconstructed value and systematic uncertainties. In order to increase the statistics and improve the measurements, they needed to

be resolved. In this thesis, the development and improvement of several analysis techniques in the muon track matching and momentum reconstruction are reported, which is used to measure the neutrino-water interactions using nuclear emulsion detectors. Using the developed methods, the study of the neutrino-water interactions is performed.

1.4 Outline of this thesis

The remainder of this thesis is organized as follows. In Chap. 2, an overview of the T2K experiment is described. Chapter 3 introduces neutrino interaction models in the sub- and multi-GeV neutrino energy region. Chapter 4 describes the overview of the NINJA experiment and its first physics run, and Chap. 5 describes the Monte Carlo (MC) simulation for this measurement. The analysis strategy of the NINJA experiment is briefly summarized in Chap. 6. Chapter 7 describes the data taking and event reconstruction in the NINJA detectors, and the event selection is shown in Chap. 8. Chapter 9 shows the momentum reconstruction and particle identification (PID). In Chap. 10, the result of the measurement in the physics run is shown. Chapter 11 discusses the possible improvements and future prospects in the NINJA experiment. Finally, Chap. 12 concludes this thesis.

Chapter 2

T2K Experiment

T2K is a long-baseline neutrino oscillation experiment in Japan. This chapter first introduces beamlines and detectors in the T2K experiment. After that, the latest results and future prospects of the T2K experiment are also described.

2.1 Overview of the T2K experiment

The T2K experiment is an ongoing long-baseline neutrino oscillation experiment [51] started in 2009. In 2011, the T2K experiment indicated that θ_{13} has a non-zero value by observing the ν_e appearance. So far, the T2K experiment measured θ_{23} and Δm^2_{32} with one of the best precisions in the world and excluded the CP conservation with a 90% confidence level [33]. Figure 2.1 shows a cross-sectional view of the T2K experiment. A high-intensity neutrino beam mainly consisting of ν_μ or $\bar{\nu}_\mu$ is directed to the far detector: Super-Kamiokande. The beam is firstly detected by the near detectors in J-PARC, and the neutrino flux and cross-section parameters are constrained. The neutrino spectra at Super-Kamiokande are fitted by the constrained parameters and neutrino oscillation probabilities, and the oscillation parameters are obtained.

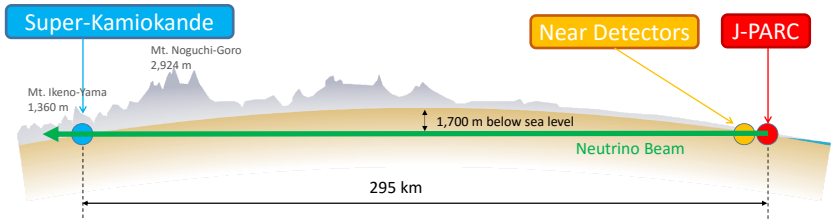

Figure 2.1: Cross-sectional view of the T2K experiment.

2.2 J-PARC accelerators

The J-PARC accelerator consists of three parts; LINear ACcelerator (LINAC), Rapid Cycling Synchrotron (RCS), and Main Ring (MR) as shown in Fig. 2.2. H^- ions are first accelerated

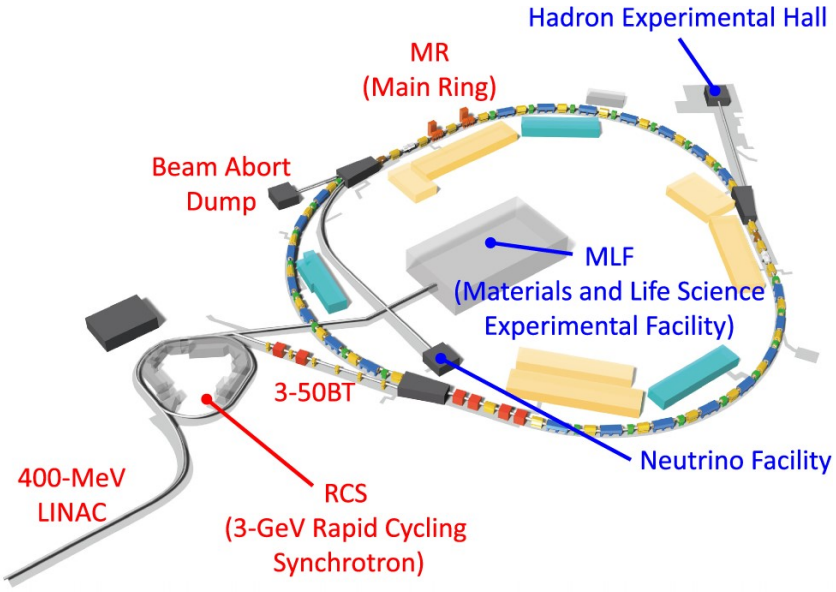

Figure 2.2: J-PARC accelerators and experimental facilities [52].

Table 2.1: Summary of parameters of the proton beam from MR.

Parameter	Value as of 2021
Beam power	522.6 kW
Beam energy	30 GeV
Number of protons	2.6×10^{14}/spill
Spill cycle	2.48 s
Number of bunches	8
Width of a bunch	58 ns

up to 400 MeV in LINAC, and they are converted to protons at injection to RCS. The protons are accelerated to 3 MeV in RCS, and then they are finally injected into MR and accelerated to 30 GeV. The beam spill has an eight-bunch structure, and each bunch has a 58-ns width. The bunches are separated by around 580 ns. Parameters of the proton beam from MR in 2021 are summarized in Table 2.1. After the MR upgrade in 2022, the spill cycle will be shortened to 1.32 s. In longer term prospects, the spill cycle will be eventually 1.16 s, and the number of protons will be increased to 3.3×10^{14}/spill. In 2023, the beam power will be 750 kW at highest and continue to increase up to 1.3 MW.

2.3 J-PARC neutrino beamline

The proton beam from J-PARC MR is extracted to the neutrino beamline directing to the far detector, Super-Kamiokande. The beamline is separated into the primary and secondary beamlines. At the downstream of the secondary beamline, the beam dump and MUon MONitor

(MUMON) [53, 54] are located.

2.3.1 Primary beamline

The proton beam from J-PARC MR is bent to the direction toward Super-Kamiokande by super conducting magnets. In the primary beamline, the intensity and profile of the proton beam are monitored. Five current transformers, 50 beam loss monitors, 21 electrostatic monitors, and 19 segmented secondary emission monitors are used to measure the proton beam. In addition, a wire secondary emission monitor and beam induced fluorescence monitor are now under research and development.

2.3.2 Secondary beamline

Protons from the primary beamline impinging the graphite target produce hadrons, mainly pions. The proton beam at the target is monitored by the optical transition radiation monitor [55]. The charged pions are focused by three magnetic horns [56] and decay into neutrinos in a decay volume, which is a 94 m tunnel located at downstream of the target.

$$\pi^+ \to \mu^+ + \nu_\mu, \tag{2.1}$$

$$\pi^- \to \mu^- + \bar{\nu}_\mu. \tag{2.2}$$

By changing the polarity of the horn current, the sign of the focused pion charge can be switched. Thus, neutrino and anti-neutrino enhanced beams can be selected. In the Forward Horn Current (FHC) mode, the beam is enriched by neutrinos, while in the Reverse Horn Current (RHC) mode, the beam is enriched by anti-neutrinos.

2.3.3 Off-axis method

The neutrinos produced by the decay of the hadrons have a broad energy spectrum. Given a certain length of the baseline, the neutrino energy maximizing (minimizing) the oscillation probability is determined, and thus the neutrino energy spectrum should be as narrow as possible around the expected value. To produce a narrow-band neutrino beam, the T2K experiment employs an off-axis method. Super-Kamiokande is located 2.5° away from the central beam axis. When a pion decays into a muon and a muon neutrino, the neutrino energy E_ν is written as

$$E_\nu = \frac{m_\pi^2 - m_\mu^2}{2(E_\pi - p_\pi \cos\theta_\nu)}, \tag{2.3}$$

where m_π and m_μ are the pion and muon masses, respectively, E_π and p_π are the energy and momentum of the parent pion, respectively, and θ_ν is the angle between the parent pion and the outgoing neutrino directions. When θ_ν has a non-zero value, E_ν does not exceed a certain value even when p_π increases. Figure 2.3 shows neutrino oscillation probabilities and neutrino flux at Super-Kamiokande with different off-axis angles. The 2.5° off-axis provides a narrow-band neutrino beam with a peak around $E_\nu = 0.6\,\mathrm{GeV}$, which is well suited to see the maximum

or minimum neutrino oscillation probability at Super-Kamiokande. Although this method is a good tool to see the neutrino oscillation effect, the spectrum changes largely by the change of the off-axis angle. In the T2K experiment, the off-axis angle is required to be stable within 1 mrad. To monitor the neutrino beam direction, MUMON and the on-axis near detector, Interactive Neutrino GRID (INGRID) [57], are operated.

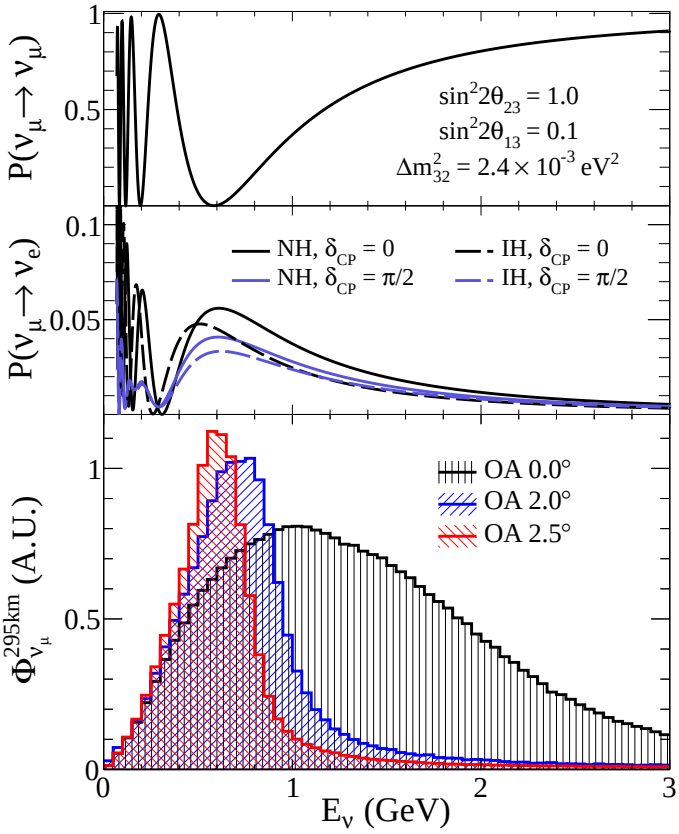

Figure 2.3: Neutrino oscillation probabilities and neutrino flux at Super-Kamiokande. The top and middle figures show $P(\nu_\mu \to \nu_\mu)$ and $P(\nu_\mu \to \nu_e)$, respectively, and the bottom one shows neutrino flux with different off-axis angles (OA). In this figure, NO and IO are shown as NH (Normal Hierarchy) and IH (Inverted Hierarchy), respectively.

2.3.4 MUMON

MUMON measures the intensity and profile of the muon flux from the decay of hadrons downstream of the beam dump, which is behind the decay volume. The measurement of the muon beam gives the indirect measurement of the neutrino beam profile since the muon and neutrino are co-generated from the hadron decay as shown in Eqs. (2.1) and (2.2). To directly measure the neutrino beam profile, it is necessary to accumulate event statistics for many beam spills. Thus, MUMON is the only detector which can measure the bunch-by-bunch beam profile and essential for the operation of the T2K experiment. For the robustness, MUMON is composed

of two independent detectors, silicon PIN photodiodes and ionization chambers. Both detectors are placed in a 7×7 array on the surface perpendicular to the beam and cover a $1.5\,\mathrm{m} \times 1.5\,\mathrm{m}$ area. After the MR upgrade in 2022, the current silicon PIN photodiodes will suffer more radiation damage, and frequent replacement will be necessary. On the other hand, the ionization chambers will show non-linearity of the signals due to the space charge effects by the higher intensity beam. Thus, a new detector as MUMON is necessary in the future operation of the T2K experiment. An Electron Multiplier Tube (EMT) is now considered to be the successor of MUMON [58].

2.4 Near detectors

The neutrino beam is detected by the near detectors located at 280 m downstream of the graphite target. There are three kinds of near detectors in the T2K near detector hall. The on-axis detector, INGRID, is placed to monitor the neutrino beam. The main off-axis detector, ND280, is located at the same off-axis angle as Super-Kamiokande, 2.5°. It constrains parameters of flux and neutrino interactions at Super-Kamiokande and measures cross sections of the neutrino interactions on a few target materials such as water or hydrocarbon. A new off-axis detector complex, WAGASCI (WAter Grid And SCIntillator) complex, has been operated since 2019 at a different off-axis angle from ND280, 1.5°. It measures neutrino interactions especially on water with a unique detector structure.

2.4.1 INGRID

Figure 2.4 shows the T2K on-axis detector, INGRID, which consists of 14 identical modules. Seven and the other seven modules are aligned horizontally and vertically, respectively. The dimension of one module is $1.5\,\mathrm{m} \times 1.5\,\mathrm{m}$, thus it covers 10-m horizontal and vertical lengths. INGRID directly measures the event rate and profile of the neutrino beam. At the location of INGRID, the 1σ width of the neutrino beam is around 5 m, which can be sufficiently covered by the modules. The number of protons impinging the graphite target is called protons on target (POT), which is measured by the proton beam monitor in the primary beamline. The event rate is defined as the number of neutrino events observed in each module per POT. The center and width of the neutrino beam are obtained from the Gaussian fitting to the number of events in horizontal and vertical modules. The beam center is obtained from the mean of the Gaussian, and the width of the beam is from the Gaussian 1σ value. Figure 2.5 shows an example of a neutrino beam profile measured by INGRID. MUMON can measure the bunch-by-bunch beam profile, but it only measures high-momentum muons, thus only the partial information of the parent pion kinematics can be obtained. On the other hand, INGRID can directly measure the profile, but it is only possible on day-by-day basis.

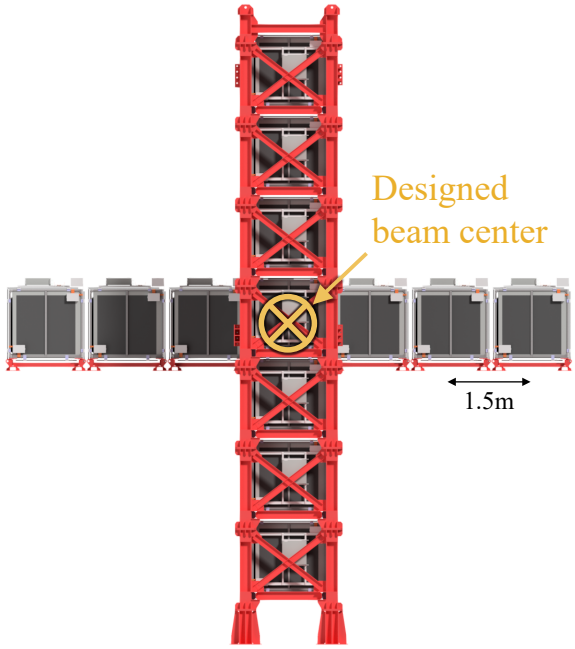

Figure 2.4: On-axis near detector: INGRID.

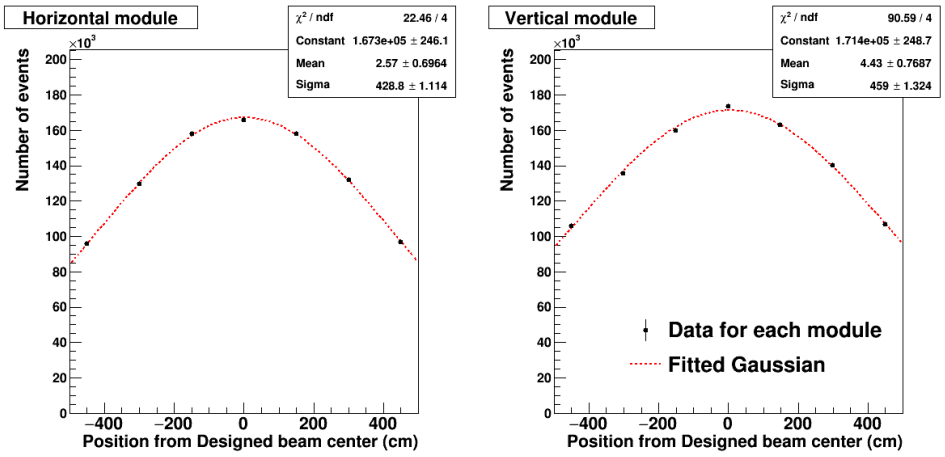

Figure 2.5: Example of a neutrino beam profile measured by INGRID.

Figure 2.6 shows an exploded view of one INGRID module. It has a sandwich structure of 9 iron plates and 11 plastic scintillator tracking planes. Each iron plate has a 6.5-cm thickness, and it is used as a neutrino interaction target. Each scintillator tracking plane consists of 24 vertical and 24 horizontal scintillator bars. The dimension of each bar is 120 cm × 5 cm × 1 cm. The scintillation light from each bar is collected by a wavelength shifting (WLS) fiber inserted in a hole along the bar. The light is detected by a Multi-Pixel Photon Counter (MPPC) attached to one edge of the WLS fiber [59]. The MPPC and WLS fiber are also used in the scintillation tracker in the NINJA experiment, and the details are described in Chap. 4.

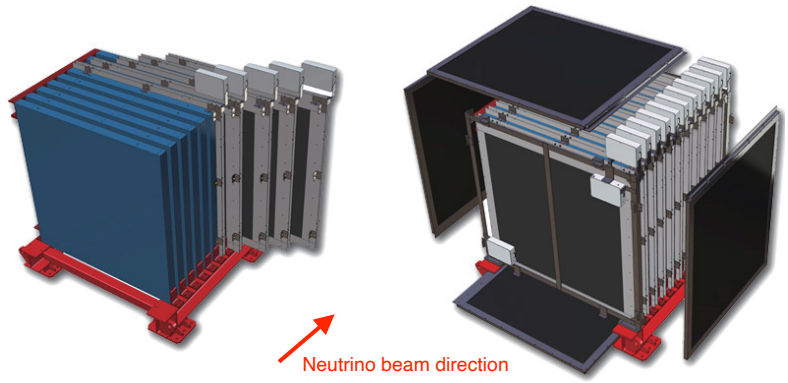

Figure 2.6: Exploded view of one INGRID module. The neutrino beam direction is perpendicular to the tracking planes and iron plates.

Figure 2.7 shows event rates and beam profiles measured by MUMON and INGRID for all the T2K runs. The measured event rates and beam profiles in Fig. 2.7 are stable enough and satisfy the requirement for the operation of the T2K experiment.

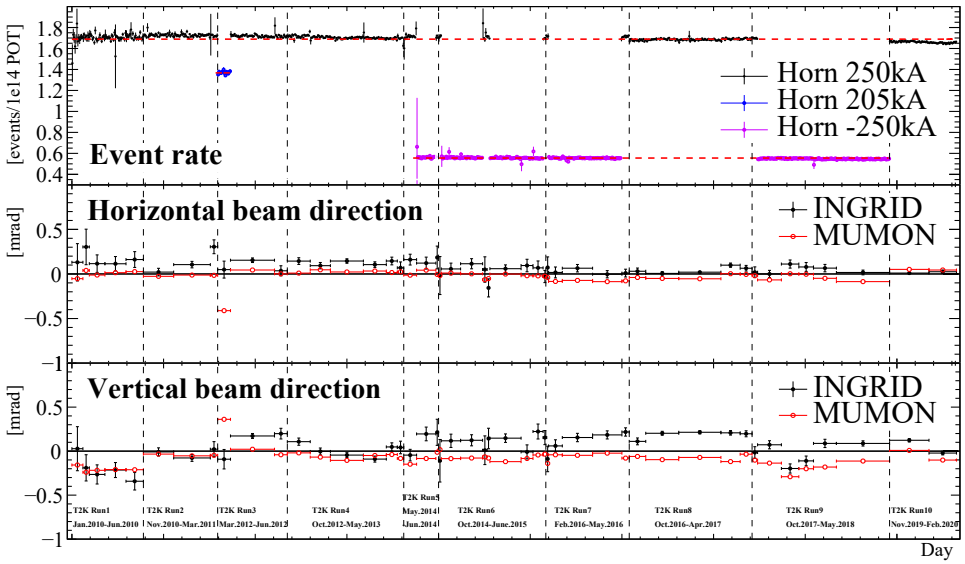

Figure 2.7: Event rates and beam profiles measured by MUMON and INGRID.

2.4.2 ND280

The left side of Fig. 2.8 shows an exploded view of ND280. ND280 is a detector suite to measure neutrino interactions on a few materials with tracking and calorimetric detectors. The detectors

are placed inside a 0.2 T dipole magnet, which was originally used in the UA1 (Underground Area 1) [60] experiment. The sub-detectors in ND280 are as follows:

- Pi-zero Detector (P0D) [61]
  P0D is a detector specialized in the measurement of neutral pions from neutrino interactions. The neutral pions are a background in the ν_e CC interaction measurement in Super-Kamiokande. P0D was installed the most upstream of ND280 and will be replaced by the upgraded detectors described below. It has a sandwich structure of tracking layers of plastic scintillator bars, target water layers, and radiator layers made of lead or brass. Here, the water layer is selected since it is the same target material as Super-Kamiokande.

- Fine Grained Detector (FGD) [62]
  Two FGD modules are installed downstream of P0D. They play a role of the neutrino interaction target and the tracker. The upstream FGD is a fully-active tracking detector composed of only plastic scintillator bars. On the other hand, to measure the neutrino interaction on water at 2.5° off-axis, which is the same target and off-axis as Super-Kamiokande, the downstream FGD has a sandwich structure of inactive water layers and active scintillator tracking planes. The plastic scintillator bars have the size of $1\,\mathrm{cm} \times 1\,\mathrm{cm} \times 186\,\mathrm{cm}$.

- Time Projection Chamber (TPC) [63]
  Three TPCs are installed upstream and downstream of FGDs. They precisely measure the momentum and charge sign of a charged particle from the neutrino interaction in FGDs by the curvature of its trajectory in the magnetic field. They also measure the energy deposit along the track. The particle identification of the charged particle is performed with the measured momentum and energy deposit information. TPCs are filled with an argon-based gas, and the signal is read out by MicroMEGAS (Micro-MEsh GAsious Structure) [64] planes.

- Electromagnetic CALorimeter (ECAL) [65]
  The sub-detectors mentioned above are surrounded by ECAL, which consists of plastic scintillator layers and lead layers. Electromagnetic showers produced in the lead layers by electrons or photons are measured by this detector.

- Side Muon Range Detector (SMRD) [66]
  SMRD consists of plastic scintillators and iron layers. The scintillator planes are inserted between iron layers of the UA1 magnet yoke. SMRD detects the muon tracks from the neutrino interactions with a large angle. In addition, it is also used as the trigger detector for the cosmic-muon tracks.

As described above, P0D was uninstalled from ND280 in 2022, and new sub-detectors will be installed as shown in the right side of Fig. 2.8 [67]. The new sub-detectors in the ND280 upgrade are as follows:

- Super Fine Grained Detector (SFGD)
  SFGD is a new fully-active tracker in ND280. It consists of plastic scintillator cubes, whose size is 1 cm × 1 cm × 1 cm. The cubes are piled up with 192 × 182 × 56, and each cube is read out three-dimensionally with WLS fibers and MPPCs. The structure has a high granularity, a better spatial resolution than FGDs, and 4π acceptance.

- High Angle TPC (HA-TPC)
  Two HA-TPCs are installed above and below SFGD. The concept of particle detection and measurement is the same as the conventional TPCs, but readout MicroMEGAS is updated [68]. It measures the tracks from the neutrino interactions in SFGD with a large angle.

- Time Of Flight counter (TOF) [69]
  SFGD and HA-TPCs are surrounded by six TOF counters. They consist of plastic scintillators and provide precise information on the crossing time of a charged particle track. Combining the information with the timing measurement in SFGD, they measure the direction of the track and separate neutrino interactions in SFGD from external backgrounds.

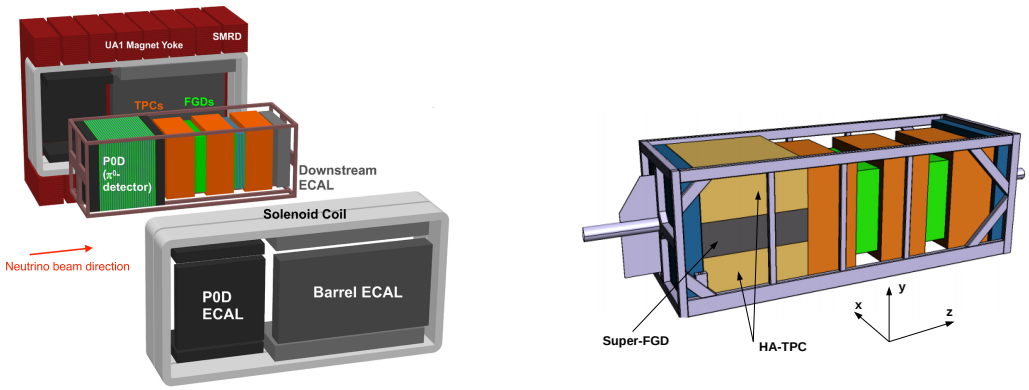

Figure 2.8: Exploded view of ND280 before (left) and after (right) upgrade [67]. P0D will be replaced to SFGD and HA-TPC, which are surrounded by six TOF counters. The TOF counters are not shown in this figure.

Obtained kinematical distributions of muons are fitted, and parameters of the neutrino flux and neutrino interaction models are constrained. With the constrained parameters, the prediction of observed neutrino events at Super-Kamiokande gets more precise. In addition, ND280 has measured various cross sections of neutrino interactions [70–82].

2.4.3 WAGASCI complex

WAGASCI complex is a newly installed near detector complex on the lowest floor of the near detector hall (B2 floor). It aims to measure neutrino-nucleus interactions on water and hydrocarbon with a slightly different neutrino beam spectrum from ND280. Figure 2.9 shows the

detector setup of the WAGASCI complex on the B2 floor. The detectors in the WAGASCI complex are as follows:

- Proton Module [83, 84]
  Proton Module is a fully-active target detector composed of plastic scintillators. It used to be located in front of the INGRID horizontal modules and was moved to the B2 floor. The module consists of 36 tracking planes, arranged by 18 horizontal and 18 vertical layers alternately, and 4 veto planes surrounding the detector. Each tracking plane consists of two types of plastic scintillator bars: INGRID type (1200 mm × 50 mm × 10 mm) and SciBar type (1200 mm × 25 mm × 13 mm). The former is the same type as used in INGRID, and the latter is the same type as used in the SciBar detector [85] in the K2K and SciBooNE (SciBar Booster Neutrino Experiment) [86] experiments.

- WAter Grid And SCIntillator (WAGASCI) module [87, 88]
  WAGASCI modules are water target detectors consisting of plastic scintillator bars. The size of one bar is 1020 mm × 24 mm × 3 mm. A grid structure of the plastic scintillator bars is implemented inside a tank filled with 0.6 t water. The structure allows us to measure tracks from the neutrino interactions with 4π acceptance. In addition, a large fraction of water inside the module, around 80%, enables the measurement of the neutrino-water interactions with low internal background events in the scintillator bars. Two modules are placed in front of Proton Module and Baby MIND, respectively, and the setup implements a large solid angle for muons covered by WMRDs and Baby MIND described below.

- Wall Muon Range Detector (WMRD)
  WMRD consists of 11 iron layers and 10 plastic scintillator layers. One scintillator layer consists of 8 scintillator bars, and the size of each scintillator bar is 1800 mm × 800 mm × 7 mm. Two WMRDs are placed on both sides of the Proton Module and WAGASCI modules. They detect muon tracks from neutrino interactions in the modules with a large angle.

- Prototype Magnetized Iron Neutrino Detector (Baby MIND)
  Baby MIND is a magnetized muon range detector (MRD). It is composed of 18 detector modules and 33 magnet modules. One detector module consists of horizontal and vertical layers, and they are made of plastic scintillator bars. The size of the horizontal and vertical scintillator bars are 3000 mm × 31 mm × 7.5 mm and 210 mm × 195 mm × 7.5 mm, respectively. One magnet module is a 3-cm thickness magnetized iron plate, and a 1.5 T magnetic field is applied inside it. Baby MIND has sufficient material to stop $\sim 1.5\,\mathrm{GeV}/c$ muon inside the detector, and the momentum and charge of muon can be measured by the range and curvature of the trajectory.

2.5 Far detector: Super-Kamiokande

Super-Kamiokande is a 50 kt water Cherenkov detector [89]. The T2K experiment uses Super-Kamiokande as its far detector. Super-Kamiokande is a cylindrical tank filled with water. The

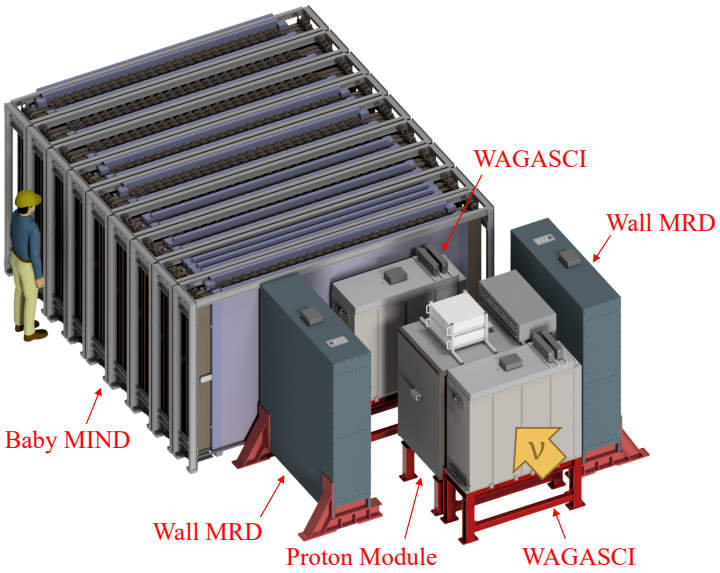

Figure 2.9: WAGASCI complex and the detector setup.

water was pure before it is replaced with Gadolinium-loaded water (SK-Gd) in 2020 [90]. The SK-Gd has better neutron detection efficiency owing to Gadolinium's large neutron capture cross section. Thus, it has improved sensitivity to the diffuse supernova neutrino flux. The size of the tank is 39 m in diameter and 40 m in height. The tank is optically separated into an inner detector (ID) and an outer detector (OD). On the wall of the ID, the ring pattern of the Cherenkov light of the charged particles from the neutrino interactions is detected with 11 129 photomultiplier tubes (PMTs). While in the OD, the external backgrounds such as cosmic muons are identified with 1 885 PMTs. The water Cherenkov detector has the capability of muon and electron identification. The Cherenkov light from a muon has a clear ring shape, while that from an electron has a fuzzy shape due to electromagnetic showers. The identification of the lepton flavor from the neutrino interaction is especially important for the T2K experiment since the measurement of the neutrino oscillation probabilities uses CC interactions, i.e. the flavor of neutrino is identified by the flavor of the charged lepton in the final state of the interaction. SK has a 99% accuracy of the μ/e separation, and it is essential in the T2K experiment. The particle identification, vertex, energy, and direction reconstructions are done by fitting the hit pattern of the ring.

2.6 Latest results from the T2K experiment

The T2K experiment has collected data since 2010. The accumulated POT so far are 2.17×10^{21} for the FHC mode and 1.65×10^{21} for the RHC mode by 2022. Figure 2.11 shows a history of the MR beam power and the accumulated POT. Using the data collected by 2021, the T2K experiment has measured and constrained the neutrino oscillation parameters with one of the best precisions in the world [38].

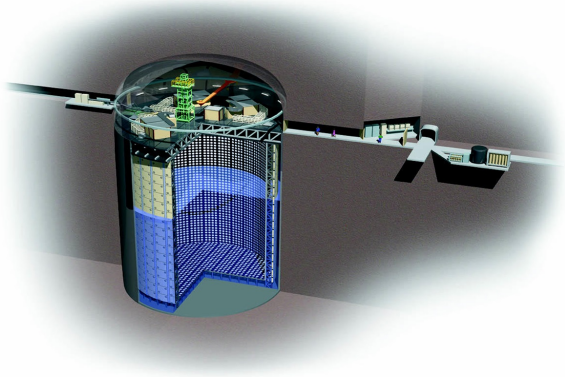

Figure 2.10: Schematic view of the Super-Kamiokande detector. Taken from `https://www.ipmu.jp/en/node/1655`.

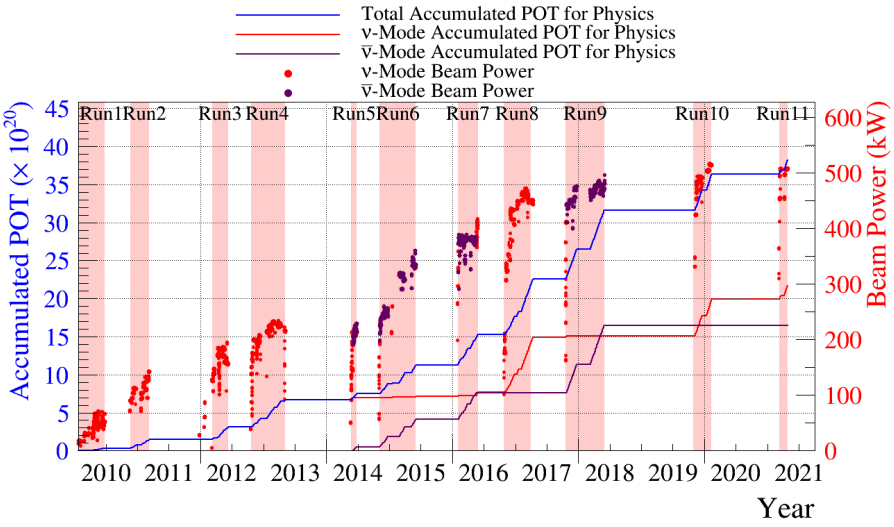

Figure 2.11: History of the beam power and accumulated POT.

As for the ν_μ and $\bar{\nu}_\mu$ disappearance modes, three samples of the observed events at SK are used in the analysis:

- ν_μ1R : one muon-like ring in the FHC mode
- $\bar{\nu}_\mu$1R : one muon-like ring in the RHC mode
- ν_μCC1π^+ : one or two muon (pion)-like ring(s) with one or two decay electron(s) in the FHC mode

Figure 2.12 shows the reconstructed spectra of ν_μ and $\bar{\nu}_\mu$ events observed at Super-Kamiokande. The dip around 600 MeV in the ν_μ1R and $\bar{\nu}_\mu$1R samples corresponds to the maximum oscillation probability. According to Eq. (1.10), $\sin^2\theta_{23}$ and $|\Delta m^2_{32}|$ can be obtained from the depth and position of the dip. The observed 90% confidence region of $\sin^2\theta_{23}$ and Δm^2_{32} with the reactor

constraint for $\sin^2\theta_{13}$ is shown in Fig. 2.13 with results from other experiments. In particular, the T2K experiment gives the most precise result of $\sin^2\theta_{23}$.

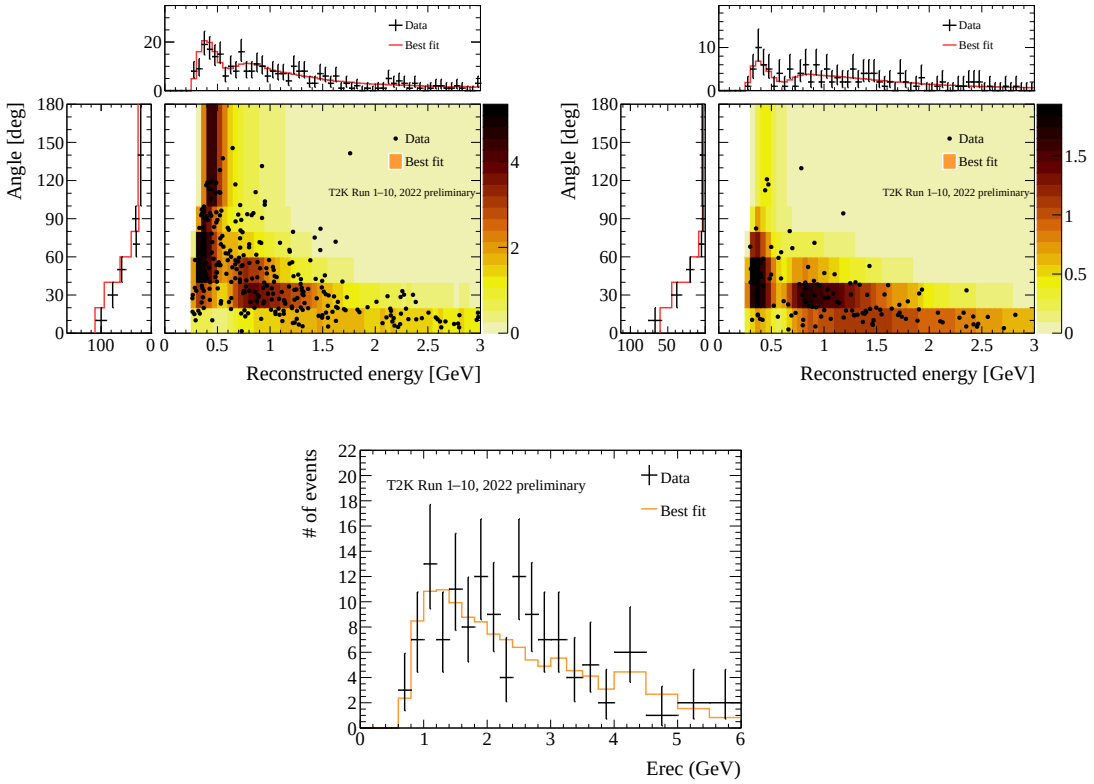

Figure 2.12: Reconstructed spectra of the ν_μ and $\bar{\nu}_\mu$ events observed at Super-Kamiokande. The spectra of the ν_μ1R (top left) and $\bar{\nu}_\mu$1R (top right) samples are shown as the two-dimensional distributions of the reconstructed neutrino energy and muon angle, while the ν_μCC1π^+ sample (bottom) is shown as the reconstructed energy spectrum. The best-fit distributions are shown in colored histograms with the observed data points.

The ν_e and $\bar{\nu}_e$ events are also categorized into three samples:

- ν_e1R : one electron-like ring in the FHC mode
- $\bar{\nu}_e$1R : one electron-like ring in the RHC mode
- ν_e1R + 1 d.e. : one electron-like ring with one decay electron in the FHC mode

Figure 2.14 shows the reconstructed spectra of ν_e and $\bar{\nu}_e$ events observed at Super-Kamiokande. The correlation of the total numbers of ν_e and $\bar{\nu}_e$ events gives the constraint on δ_{CP}. Figure 2.15 shows the total numbers of events and their prediction with various oscillation parameters. The current data and best-fit values are consistent with $\delta_{\mathrm{CP}} = -\pi/2$, where this tendency can be interpreted as the CP violation in the lepton sector, but it is still unknown. The observed $\Delta\chi^2$ function of δ_{CP} is shown in Fig. 2.16. As already mentioned in Sect. 2.1, the CP conservation is

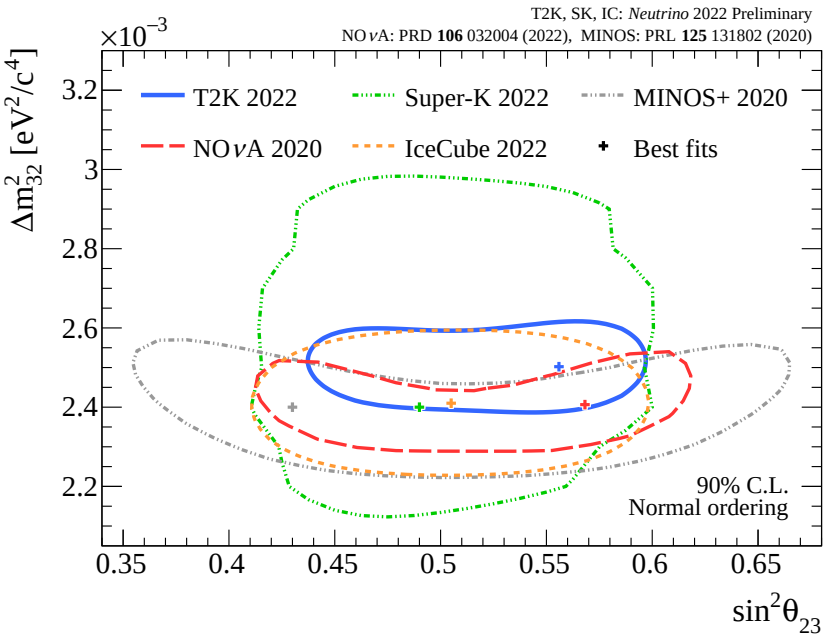

Figure 2.13: Observed 90% confidence region of $\sin^2\theta_{23}$ and Δm^2_{32}. The $\sin^2\theta_{13}$ value is constrained by the reactor experiments, and NO is assumed. NOνA [34], Super-Kamiokande [91], IceCube [92], and MINOS+ [32] results are also shown.

excluded by a 90% confidence level. Table 2.2 summarizes the best-fit values of the oscillation parameters measured by the T2K experiment.

Currently, the results are limited by statistical uncertainty. To achieve more precise results, it is essential to increase statistics. J-PARC MR is now being upgraded for a higher beam power by raising the spill frequency, and 1.3 MW is expected to be realized by 2028 [52]. The current intensity of the electromagnetic horns has been also increased from 250 kA to 320 kA [93]. The charged hadrons are more concentrated by this current, and neutrino flux is expected to be 10% larger than ever before. Moreover, Hyper-Kamiokande, which has around a 8.4 times larger fiducial volume than that of Super-Kamiokande is now under construction. These upgrades are essential to achieve a 5σ observation of the CP violation in the lepton sector by the measurement of neutrino oscillation. After these upgrades, the measurement will be limited by systematic uncertainty. Table 2.3 summarizes the systematic uncertainty on the number of events measured at Super-Kamiokande. The uncertainties of the flux and cross-section models are the dominant sources of systematic uncertainty. Although they are significantly reduced by the ND280 constraint, it should be improved shortly. The T2K experiment is trying to further improve the understanding of the neutrino interaction models by the ND280 upgrade and WAGASCI complex, and several external experiments are also ongoing. In addition, there are several uncertainties that cannot be constrained by ND280. Such parameters should be also well understood by other experiments. In the next chapter, an introduction of the neutrino-nucleus interactions and current problems of the neutrino interaction models are discussed.

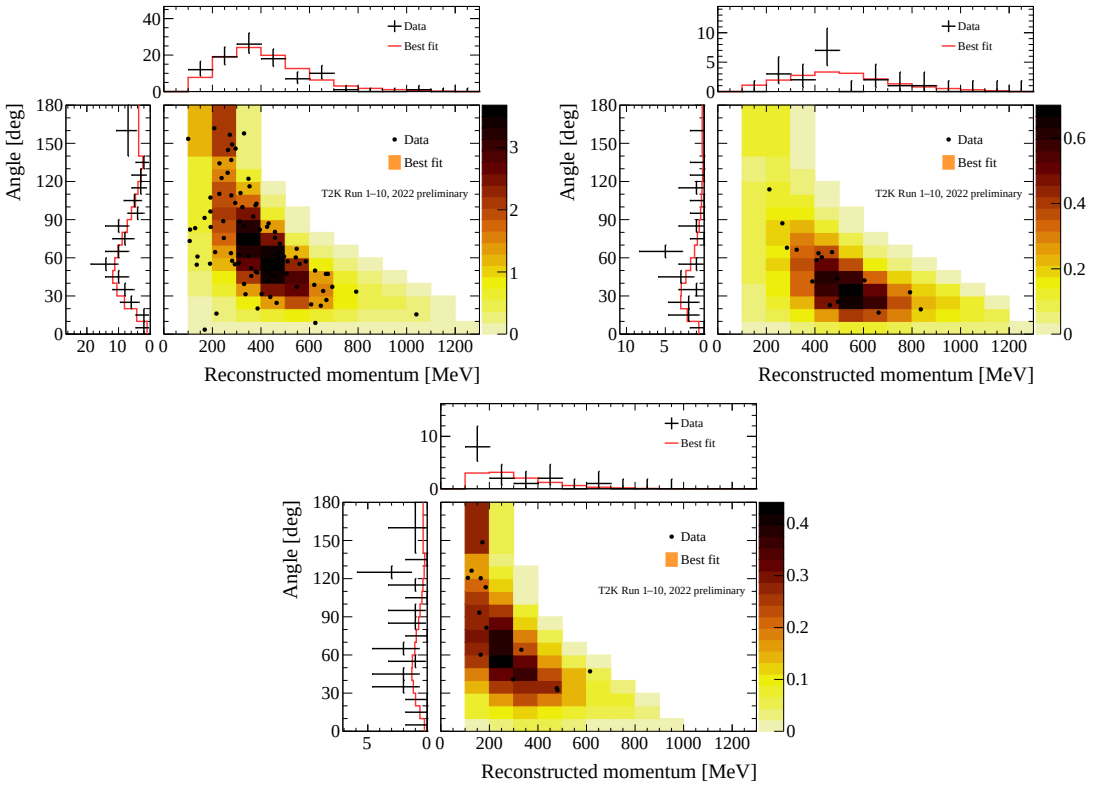

Figure 2.14: Reconstructed spectra of the ν_e and $\bar{\nu}_e$ events observed at Super-Kamiokande. The spectra of the ν_e1R (top left), $\bar{\nu}_e$ (top right), and ν_e1R + 1 d.e. (bottom) samples are shown, respectively. The best-fit distributions are shown in colored histograms with the observed data points.

Table 2.2: Current best-fit values of the neutrino oscillation parameters measured by the T2K experiment. Only the parameters of interest in the current T2K experiment are shown.

Parameter	Ordering	Best-fit $\pm 1\sigma$
$\sin^2\theta_{23}$	NO	$0.559^{+0.018}_{-0.078}$
	IO	$0.560^{+0.019}_{-0.041}$
$\Delta m^2_{32}[10^{-3}\,\mathrm{eV}^2/c^4]$	NO	$2.506^{+0.047}_{-0.059}$
$\lvert\Delta m^2_{13}\rvert[10^{-3}\,\mathrm{eV}^2/c^4]$	IO	$2.473^{+0.051}_{-0.054}$
δ_{CP}	NO	$-2.18^{+1.22}_{-0.47}$
	IO	$-1.37^{+0.52}_{-0.68}$

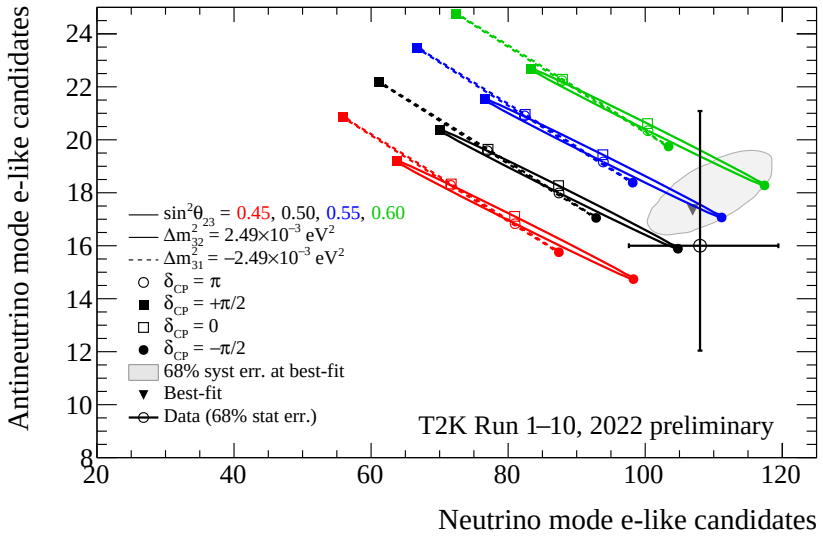

Figure 2.15: The numbers of the ν_e and $\bar{\nu}_e$ events observed at Super-Kamiokande and their prediction with various oscillation parameters. The error bars represent the 1σ confidence interval for the mean of a poisson distribution given the observed data point. The underlaid contour represents the 1σ region of the predicted numbers of the events with the best-fit oscillation parameters.

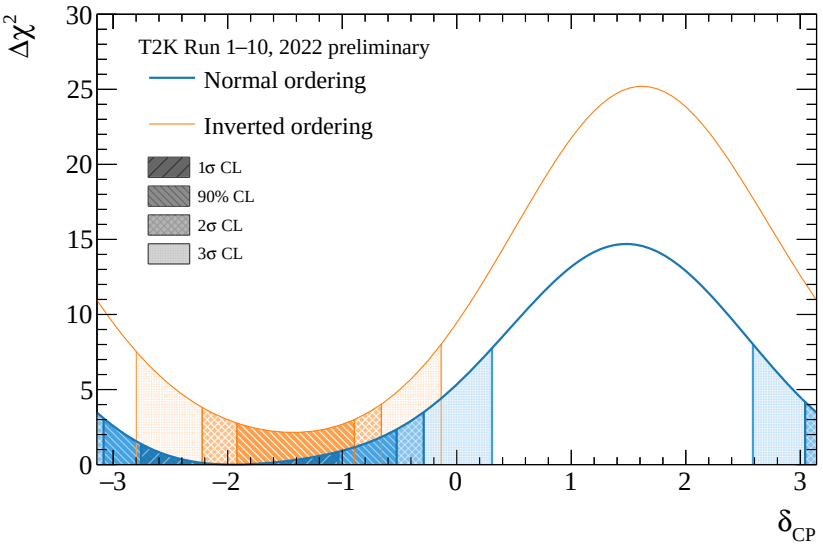

Figure 2.16: Observed $\Delta\chi^2$ function of δ_{CP} and the confidence level regions. $\Delta\chi^2$ is calculated with respect to the best-fit value over the both mass orderings.

Table 2.3: Systematic uncertainty (%) on the number of events measured at the far detector in the T2K experiment [38]. Flux + Xsec (w/ ND280 constr.) denotes the combined effect from the ND280 constrained flux and interaction parameters, while Xsec (ND280 unconstr.) represents the interaction parameters which cannot be constrained by ND280. SK detector includes the detector systematics of Super-Kamiokande as well as the secondary interactions and photo-nuclear effects inside it. Each column corresponds to each event category at Super-Kamiokande, and the last column is the error on the ratio of ν_e and $\bar{\nu}_e$ one ring events.

Error source	ν_μ1R	$\bar{\nu}_\mu$1R	ν_μ CC $1\pi^+$	ν_e1R	$\bar{\nu}_e$1R	ν_e1R + 1 d.e.	$\nu_e/\bar{\nu}_e$
Flux + Xsec (w/ ND280 constr.)	2.7	2.6	2.2	2.8	2.7	3.4	2.3
Xsec (ND280 unconstr.)	0.7	2.4	1.4	2.9	3.3	2.8	3.7
SK detector	2.0	1.7	4.1	3.1	3.8	13.6	1.2
All	3.4	3.9	4.9	5.2	5.8	14.3	4.5

Chapter 3

Neutrino Interaction

As described in the previous chapters, it is important to understand neutrino-nucleus interactions for the more precise measurement of the neutrino oscillation parameters. In particular, it is essential to understand the neutrino interaction on the target nucleus used in the recent experiments, e.g. carbon, oxygen, or argon. Such interactions are complicated because they are affected by QCD physics and the many-body effect. In this chapter, a brief picture of neutrino-nucleus interaction models and the so-called nuclear effect is first described. There are several neutrino interaction simulators, such as NEUT [94], GENIE (Generates Events for Neutrino Interaction Experiments) [95], NuWro [96], NUANCE [97], and GiBUU (Giessen Boltzmann–Uehling–Uhlenbeck) [98]. In the T2K and NINJA experiments, NEUT is used as the nominal simulator, thus the models used in NEUT are explained in the following sections. The status of current experiments to measure the neutrino-nucleus interactions then follows.

3.1 Neutrino interactions with a nucleus

3.1.1 Charged current quasi-elastic scattering

Charged-current quasi-elastic (CCQE) interaction is a dominant interaction in the T2K energy region, and it is used as the main signal channel. Figure 3.1 shows diagrams of the CCQE interactions. The CCQE interaction is a two-body scattering between a lepton and a nucleon: $\nu_l + n \to l^- + p$. In the T2K experiment, the incoming neutrino direction is known. Assuming the two-body interaction between two free particles, the incoming neutrino energy can be reconstructed only from the outgoing lepton kinematics as

$$E_\nu = \frac{m_n E_l - m_l^2/2 + (m_p^2 - m_n^2)/2}{m_n - E_l + p_l \cos\theta_l}, \tag{3.1}$$

where E_ν is the incoming neutrino energy, m_p, m_n, and m_l are the proton, neutron, and lepton masses, respectively, and E_l, p_l, and θ_l are the outgoing lepton energy, momentum, and angle with respect to the incoming neutrino direction, respectively.

The cross section of the CCQE interaction is formalized by Llewellyn Smith [99]. The

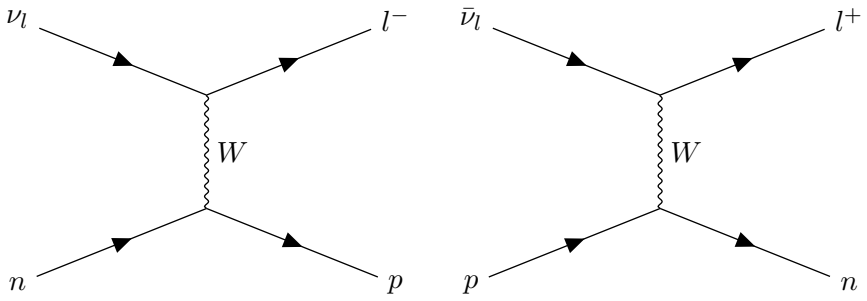

Figure 3.1: Diagrams of neutrino (left) and anti-neutrino (right) CCQE interactions.

differential cross section is given as a function of the square of the four-momentum transfer (Q^2):

$$\frac{\mathrm{d}\sigma}{\mathrm{d}Q^2} = \frac{G_{\mathrm{F}}^2 M^2 \cos^2\theta_C}{8\pi E_\nu^2}\left[A(Q^2) \pm B(Q^2)\frac{s-u}{M^2} + C(Q^2)\frac{(s-u)^2}{M^4}\right]. \tag{3.2}$$

Here, the parameters s and u are the Mandelstam kinematic variables, and the sign before $B(Q^2)$ is for neutrinos (+) and anti-neutrinos (−), respectively. The functions $A(Q^2)$, $B(Q^2)$, and $C(Q^2)$ are expressed as

$$\begin{aligned} A(Q^2) = \frac{m_l^2 + Q^2}{M^2}\Big[&(1+\tau)F_A^2 - (1-\tau)(F_V^1)^2 + \tau(1-\tau)(\xi F_V^2)^2 + 4\tau(\xi F_V^1 F_V^2) \\ &-\frac{m_l^2}{4M^2}\big((F_V^1 + \xi F_V^2)^2 + (F_A + 2F_P)^2 - 4(1+\tau)F_P^2\big)\Big], \end{aligned} \tag{3.3}$$

$$B(Q^2) = 4\tau F_A(F_V^1 + \xi F_V^2), \tag{3.4}$$

$$C(Q^2) = \frac{1}{4}(F_A^2 + (F_V^1)^2 + \tau(\xi F_V^2)^2). \tag{3.5}$$

Here, $\tau = Q^2/4M^2$, and $\xi = (\mu_p/\mu_N - \mu_n/\mu_N) - 1$, where μ_p and μ_n are the neutrino and proton magnetic moments, respectively, and μ_N is the nuclear magneton. The functions F_V^1 and F_V^2 are the vector form factors, F_A is the axial-vector form factor, and F_P is the pseudoscalar form factor, respectively.

The form factors express a spatial distribution of weak charge in the nucleon. The vector form factors are represented as

$$F_V^1(Q^2) = \left(1 + \frac{Q^2}{4M^2}\right)^{-1}\left[G_E^V(Q^2) + \frac{Q^2}{4M^2}G_M^V(Q^2)\right], \tag{3.6}$$

$$\xi F_V^2(Q^2) = \left(1 + \frac{Q^2}{4M^2}\right)^{-1}\left[G_M^V(Q^2) - G_E^V(Q^2)\right], \tag{3.7}$$

where G_E^V and G_M^V are the electric and magnetic Sachs form factors [100], respectively. When

we assume an exponential function as electric and magnetic moment spatial distributions,

$$\rho(r) = \rho(0)\exp(-Mr), \tag{3.8}$$

a dipole form factor can be obtained by a Fourier transform. The Sachs form factors can be expressed in dipole functions as

$$G_E^V(Q^2) = \frac{1}{(1+Q^2/M_V^2)^2}, \tag{3.9}$$

$$G_M^V(Q^2) = \frac{1+\xi}{(1+Q^2/M_V^2)^2}, \tag{3.10}$$

where M_V is the vector mass. M_V can be accurately determined by electron scattering experiments as $M_V = 0.84\,\mathrm{GeV}/c^2$ [101]. The dipole form factors in Eqs. (3.9) and (3.10) well describe the observations for $Q^2 < 2\,\mathrm{GeV}^2/c^2$ region, while they need to be tuned in $Q^2 > 2\,\mathrm{GeV}^2/c^2$ region. Thus, BBBA05 form factors [102], which is phenomenologically tuned to the electron scattering experiments, are currently used in NEUT.

Analogously to the vector form factor, the axial-vector form factor is also represented by the dipole function,

$$F_A(Q^2) = \frac{g_A}{\left(1+Q^2/\left(M_A^{\mathrm{QE}}\right)^2\right)^2}, \tag{3.11}$$

where $g_A = -1.276$ is accurately determined by the β decay experiments [103, 104]. The axial-vector mass $M_A^{\mathrm{QE}} = 1.026 \pm 0.021\,\mathrm{GeV}/c^2$ is given by measurements of the neutrino interactions using the bubble chambers [105]. However, there is a discrepancy between the results from the bubble chamber experiments and other experiments using heavier nuclei. The discrepancy will be discussed in Sect. 3.2. When the Partially Conserved Axial Current (PCAC) is assumed [106], the pseudoscalar form factor can be expressed as

$$F_P(Q^2) = \frac{2M^2}{Q^2+M_\pi^2}F_A(Q^2), \tag{3.12}$$

where M_π is the pion mass. According to Eq. (3.3), the pseudoscalar form factor only appears in the last term of $A(Q^2)$, which is the order of m_l^2/M^2. Thus, it is negligible for electron or muon neutrino experiments.

3.1.2 Resonant pion production

The second most probable interaction in the T2K energy region is the resonant single pion production via baryon resonances. The following CC interactions are examples of pion productions

via the Δ resonance.

$$\begin{aligned}
\nu_l + p &\to l^- + \Delta^{++} \to l^- + p + \pi^+ \\
\nu_l + n &\to l^- + \Delta^{+} \to l^- + p + \pi^0 \\
\nu_l + n &\to l^- + \Delta^{+} \to l^- + n + \pi^+ \\
\bar{\nu}_l + p &\to l^+ + \Delta^{0} \to l^+ + p + \pi^- \\
\bar{\nu}_l + p &\to l^+ + \Delta^{0} \to l^+ + n + \pi^0 \\
\bar{\nu}_l + n &\to l^+ + \Delta^{-} \to l^+ + n + \pi^-
\end{aligned}$$

Here, Δ can be other heavier resonances when the incident neutrino energy allows the process. For example, the interaction via the Δ resonance can occur when the incident neutrino energy exceeds around 400 MeV. Figure 3.2 shows diagrams of CC resonant pion productions (CCRES) via the Δ resonance. These interactions can be backgrounds for the CCQE interactions when the produced pions are not reconstructed due to their low momentum or re-interaction inside the nucleus. In the T2K experiment, the neutrino energy is reconstructed by Eq. (3.1), thus this background not only mimics the CCQE interactions but also biases the reconstructed neutrino energy distribution. Moreover, this mode is being added to the signal mode of the T2K experiment. Thus, the understanding of CCRES is important.

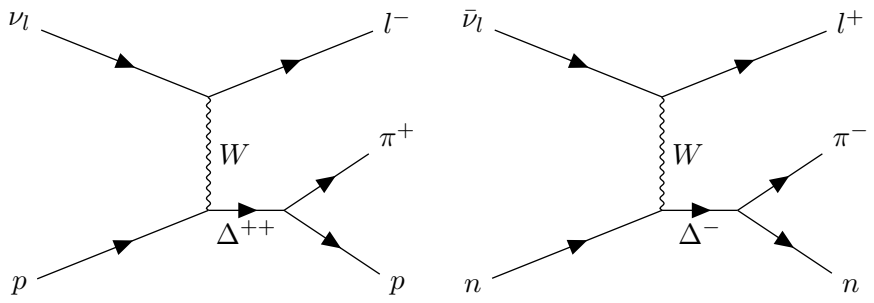

Figure 3.2: Example diagrams of neutrino (left) and anti-neutrino (right) CCRES interactions.

The Rein–Sehgal model [107] has been commonly used as the model of the resonant pion production. In the Rein–Sehgal model, 18 resonances that have the invariant mass $W < 2\,\mathrm{GeV}/c^2$ are considered. Besides, isospin $I = 1/2$ non-resonant background is also taken into account. Because the lepton mass is not considered in the Rein–Sehgal model, the corrections in Refs. [108, 109] are applied. Recently, a new model which simultaneously treats resonant and non-resonant interactions, and their interference in the helicity basis [110] is also being added to NEUT. The vector form factor of CCRES is precisely determined by the measurement of pion productions by electron scatterings [111], while the axial-vector form factor has uncertainty. The axial-vector form factor of the resonant pion production is also assumed to be a dipole function:

$$C_5^A(Q^2) = \frac{C_5^A}{\left(1 + Q^2/\left(M_A^{\mathrm{RES}}\right)^2\right)^2}, \tag{3.13}$$

where the axial-vector mass $M_A^{\mathrm{RES}} = 0.95 \pm 0.15\,\mathrm{GeV}/c^2$ and $C_5^A = 1.01 \pm 0.12$, which correspond to M_A^{QE} and g_A in the CCQE interactions, respectively.

3.1.3 Coherent pion production

In a coherent pion production, a neutrino scatters on a whole nucleus. This process occurs when the momentum transfer is low enough, and thus the particles in the final state go in the incident neutrino direction. The possible modes are

$$\nu_l + A \to l^- + A + \pi^+$$
$$\nu_l + A \to \nu_l + A + \pi^0,$$

where A is a nucleus. The Rein–Sehgal model [112, 113] is implemented in NEUT to simulate the coherent pion production. The measured results of the coherent pion production above 7 GeV agree with the Rein–Sehgal model based on the PCAC assumption, but it is not the case in the lower energy region [71, 114, 115]. To get better consistency with the current measurements [116], the model in NEUT is tuned to the Berger–Sehgal model [117] which predicts smaller cross section in the low energy region.

3.1.4 Deep inelastic scattering

When the energy of neutrino exceeds a few GeV, the neutrino interacts with quarks in the nucleus. This process is called deep inelastic scattering (DIS). Figure 3.3 shows examples of diagrams of the DIS interactions.

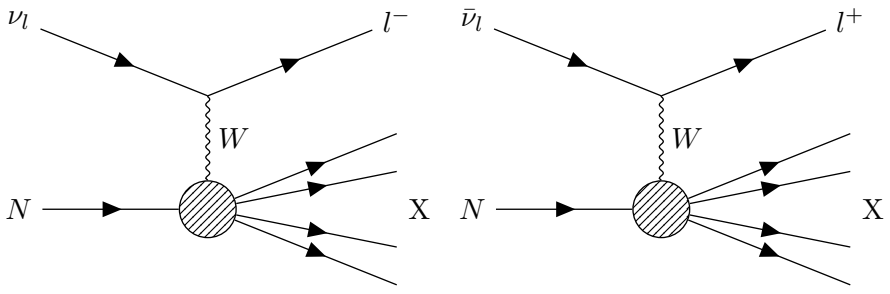

Figure 3.3: Example diagrams of neutrino (left) and anti-neutrino (right) DIS interactions.

The parton distribution functions by Glück *et al.* [118] (GRV98) is used to calculate DIS in NEUT, and the cross section includes the modification by Bodek and Yang [119] for a small Q^2 region. The multi-hadron final state is simulated by PYTHIA/JETSET [120] for events in

$W > 2\,\mathrm{GeV}/c^2$ region, while that in $W < 2\,\mathrm{GeV}/c^2$ is simulated by the parton distribution function and modification by Bodek and Yang.

3.1.5 Neutral current interactions

In an NC interaction, there are no charged lepton in its final state, thus it is hard to measure the NC interaction. The NC single π^0 productions are one background source for the ν_e CC interaction measurement since photons from $\pi^0 \to 2\gamma$ produce an electromagnetic shower and mimic the electron-like signal. In the T2K energy region, (quasi-)elastic interaction is the dominant mode of the NC interactions.

3.2 Nuclear effects

Measurements of neutrino interactions started in the 1970s by bubble chambers, which measured neutrino interaction on hydrogen or deuterium. The models described in Sect. 3.1 are constructed to explain the results of the bubble chamber experiments. However, it is not the case for the recent neutrino experiments. This is because the bubble chamber experiments used light nuclei as their target, while the recent experiments use heavier targets such as carbon, oxygen, or argon. In the heavier nucleus, the nucleon is more affected by the so-called "nuclear-effect," which distorts the final state particles. It has to be considered for the current and future neutrino oscillation experiments to reduce their systematic uncertainties. To construct more reliable neutrino-nucleus interaction models, it is essential to measure various kinematics of particles in the final state. Many experiments including NINJA are ongoing to precisely measure neutrino-nucleus interactions on various target materials. In this section, three nuclear effects: nuclear modeling, nucleon-nucleon correlation, and final state interactions are discussed.

3.2.1 Nuclear modeling

Thus far in this chapter, the nucleons are treated as at rest. However, the nucleons are bounded by and moving inside the nucleus in reality. When the nucleons have initial kinematics, the kinematics of the final state particles are changed by the event-by-event boost in the lab frame. The motion of nucleons prior to the interaction is called the Fermi motion. Three models to describe such motions and partial nucleon-nucleon correlation are introduced below: relativistic Fermi gas (RFG) [121], local Fermi gas (LFG) [122–125], and spectral function (SF) [126, 127] models.

The RFG model is the simplest nuclear model among the three models. In this model, the nucleons are assumed to be an ideal Fermi gas uniformly distributed in a nucleus, where the nucleons are not interacting between each other. The momentum states are filled from the lowest (ground) to the highest. The momentum of the highest state is called the Fermi momentum. Thus, the momentum-energy distribution can be expressed as

$$P(\mathbf{p}, E) = \theta(p_\mathrm{F} - |\mathbf{p}|)\delta(E + \sqrt{M^2 + |\mathbf{p}|^2} - E_\mathrm{B}), \tag{3.14}$$

where $\theta(x)$ is a step function, $\delta(x)$ is a delta function, p_{F} is the Fermi momentum, and E_{B} is the binding energy. According to Eq. (3.14), the nucleons inside the nucleus are moving with the momentum lower than p_{F}. All momentum states lower than p_{F} are filled with the nucleons. Since nucleons are fermions, they follow the Pauli exclusion principle. Thus, only the interactions with the scattered nucleons with a larger momentum than p_{F} are allowed. The Fermi momentum is measured by electron scattering experiments as around 200–250 MeV/c for ^{12}C or ^{16}O [128, 129].

The LFG model is the extended version of the RFG model where the local density of the nucleons are considered. The local density function $\rho(r)$ is assumed to follow Woods–Saxon distribution [130], and p_{F} is dependent on the radial position of the nucleus such that $p_{\mathrm{F}} \propto \rho(r)^{1/3}$. In the LFG model, the distribution of the initial momentum of the nucleon is broader, and the cut-off seen in the RFG model is removed.

The SF model by Benhar *et al.* is more sophisticated nuclear model which treats the momentum and energy two-dimensionally. In the LFG model, nucleons are still treated as the non-interacting fermions except the local density. However, in reality, the nucleon-nucleon correlations in the nuclear medium change the Fermi motion. In the SF model, E_{B} is called not binding energy but removal energy because the nucleons are not bound by one single value of the energy. The probability distribution function of the momentum-energy is obtained from electron scattering experiments and the shell model. The consideration of the nucleon-nucleon correlations allows the nucleons to get higher momentum than p_{F}, and the distribution of the momentum gets broader than the LFG model. In this thesis, the SF model is used as the nominal model since the latest NEUT uses it. Figure 3.4 compares three nuclear models in the space of the energy and momentum of the nucleon.

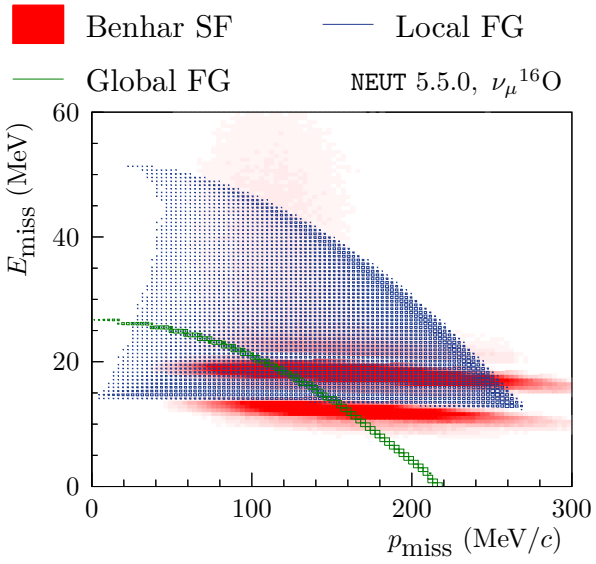

Figure 3.4: Comparison of three nuclear models [94]. The RFG model is shown as "Global FG" in this figure.

3.2.2 Nucleon-nucleon correlation

The M_A^{QE} value was fitted by the bubble chamber experiments and obtained as $M_A^{\mathrm{QE}} = 1.026 \pm 0.021\,\mathrm{GeV}/c^2$. However, in 2006, the K2K experiment reported that $M_A^{\mathrm{QE}} = 1.20 \pm 0.1\,\mathrm{GeV}/c^2$ was obtained from the measurement of neutrino interactions on oxygen [131]. In 2010, the MiniBooNE experiment also measured the ν_μ CCQE interactions on carbon, and the best-fit value was $M_A^{\mathrm{QE}} = 1.35 \pm 0.17\,\mathrm{GeV}/c^2$ [132]. The discrepancy between the bubble chamber experiments and the heavier target experiments had become known as "MiniBooNE M_A puzzle." Figure 3.5 shows the results from the MiniBooNE experiment and the LSND (Liquid Scintillator Neutrino Detector) [133] and NOMAD (Neutrino Oscillation MAgnetic Detector) [134] experiments in the different energy range. A simple RFG model cannot explain the results from different experiments.

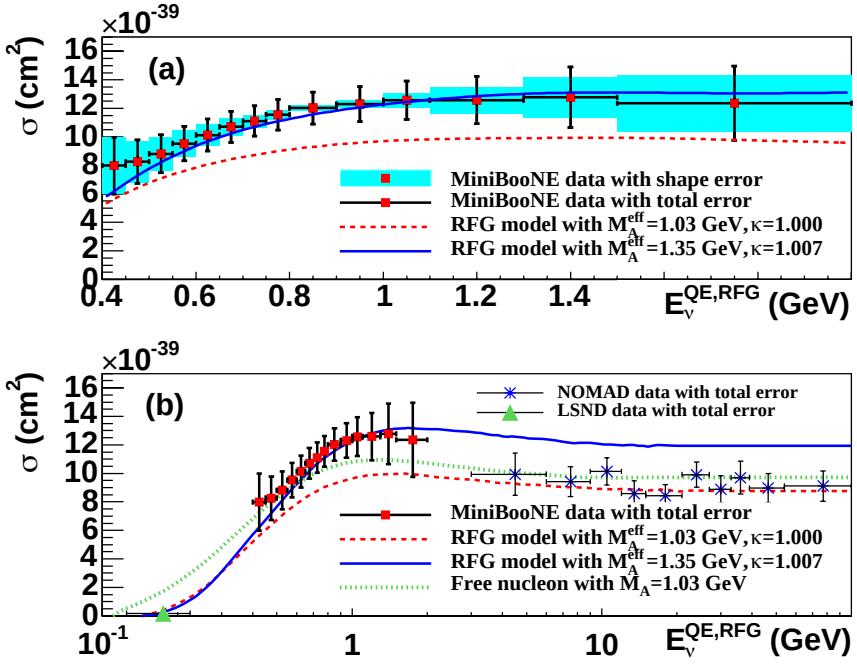

Figure 3.5: Measurement of ν_μ CCQE interactions by the MiniBooNE experiment [132]. (a) Assuming the RFG model, $M_A^{\mathrm{QE}} = 1.35 \pm 0.17\,\mathrm{GeV}/c^2$ is obtained from the results, and this is inconsistent to the best-fit value to the bubble chamber experiments, $M_A^{\mathrm{QE}} = 1.03\,\mathrm{GeV}/c^2$. (b) A comparison to the LSND [133] and NOMAD [134] experiments.

The MiniBooNE M_A puzzle is nowadays considered to be explained by the nucleon-nucleon correlation inside the nucleus. In the heavy nucleus, the nucleons inside the nucleus are correlated with each other. The correlation mediated by the real pion is called the long-range correlation, while that by the heavier mesons is called the short-range correlation. Such correlations are observed in electron scattering experiments [135–137], and the vector component of the cross section is known to be affected by them [138]. However, it is yet unknown that such correlations also exist in the axial-vector part. The long-range correlation in the RFG model is estimated by

the random phase approximation (RPA) [123]. The RPA accounts for the effect on the meson propagator inside the nuclear medium, and the Q^2 distribution of the cross section is affected. Among the short-range correlations, on the other hand, so-called two-particle-two-hole (2p2h) interactions are of interest. Several models of the 2p2h interactions are proposed by Nieves *et al.* [123], Martini *et al.* [139], and Megias *et al.* [140]. The model proposed by Nieves *et al.* is also called the Valencia model, and that by Megias *et al.* is SuSAv2 (Super Scaling Approach). In this formalism, the CCQE interaction is treated as a one-particle-one-hole (1p1h) interaction. When a neutrino interacts with a correlated pair of proton and neutron, two protons and one charged lepton are emitted. The MiniBooNE experiment uses the Cherenkov detector, and such protons are rarely detected in the Cherenkov detector. Thus, the event selection in the MiniBooNE experiment only required a single muon-like ring, and such 2p2h interactions can mimic the CCQE interaction.

Figure 3.6 shows diagrams of the 2p2h interactions. The main component of the 2p2h interactions is the meson exchange current (MEC), nucleon-nucleon correlation (NN), contact, and pion in flight terms. In any cases, the correlations are mediated by pions while the charged-current vertices are different. As shown in Fig. 3.7, while the simple RFG model can explain the result from the MiniBooNE experiment with $M_A^{\mathrm{QE}} = 1.32\,\mathrm{GeV}/c^2$, it can be also predicted by the RFG model with the RPA correction and 2p2h interactions, and $M_A^{\mathrm{QE}} = 1.049\,\mathrm{GeV}/c^2$, which is comparable to the bubble chamber results.

It should be noted that no 2p2h interaction models can predict outgoing hadron kinematics. In addition, the uncertainties of the models are significantly large, and there are only indirect evidences of the existence of the 2p2h interactions in the axial-vector part. One of the specific features of the 2p2h interactions is two nucleons in its final state. Thus, to evaluate and constrain the 2p2h models, it is important to observe nucleons with a large phase space. However, detection of low-momentum protons are difficult in the conventional detectors such as the Cherenkov detector or the scintillator tracking detector. In the Cherenkov detector, such protons do not exceed the Cherenkov threshold, and in the scintillator tracking detector, to keep the large detector volume with the realistic number of readout channels, the positional resolution is not sufficient to track such protons. The NINJA experiment uses nuclear emulsion films which allow us to detect short-range tracks of charged hadrons with a wide angular acceptance. Measurement of low-momentum protons down to $200\,\mathrm{MeV}/c$ can be achieved by the nuclear emulsion detectors, which will give essential information to improve our understandings of the 2p2h interaction models.

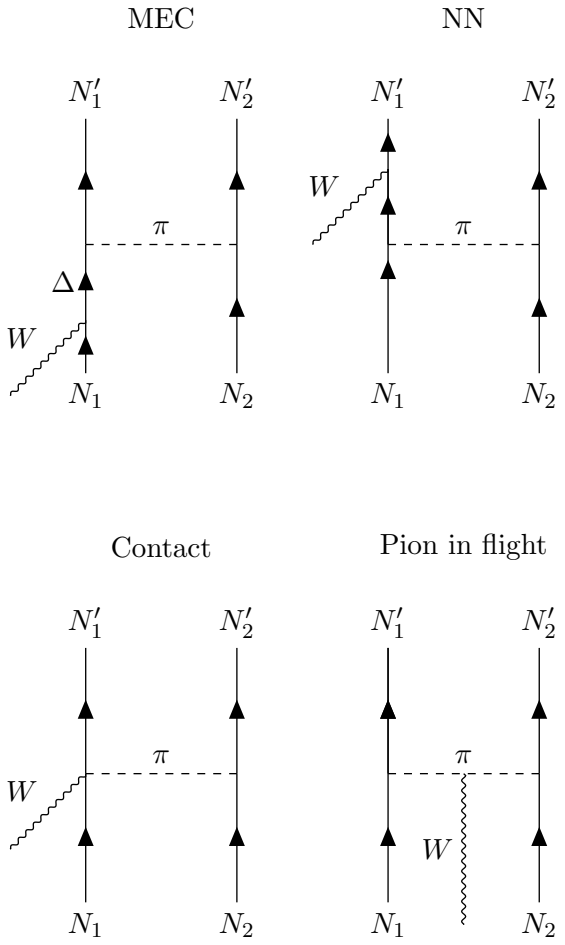

Figure 3.6: Diagrams of the 2p2h interactions.

3.2.3 Final state interaction

In the actual observation, we cannot detect the particles just after the primary process of the neutrino-nucleon scattering. The hadrons after the primary process are likely to re-interact inside the nucleus, and only those after the re-interactions are detected. Such re-interactions of hadrons are called final state interactions (FSI), and it is difficult to model or constrain with experimental data. The main components of FSI in the T2K energy region are pion elastic scattering, absorption, charge exchange, and production. Figure 3.8 shows a schematic image of FSI.

In NEUT, the intranuclear cascade model is used to simulate FSI. Each hadron from the neutrino interaction vertex is propagated by a step whose size is based on the mean free path. After each step, the hadronic re-interaction is calculated with the probability of each process and the local nucleon density, and the simulation is iterated until the hadron is emitted from the nucleus or absorbed. For pions, in the $p_\pi < 500\,\mathrm{MeV}/c$ region, the simulation of FSI is based on the model by Salcedo *et al.* [143]. On the other hand for the higher momentum region,

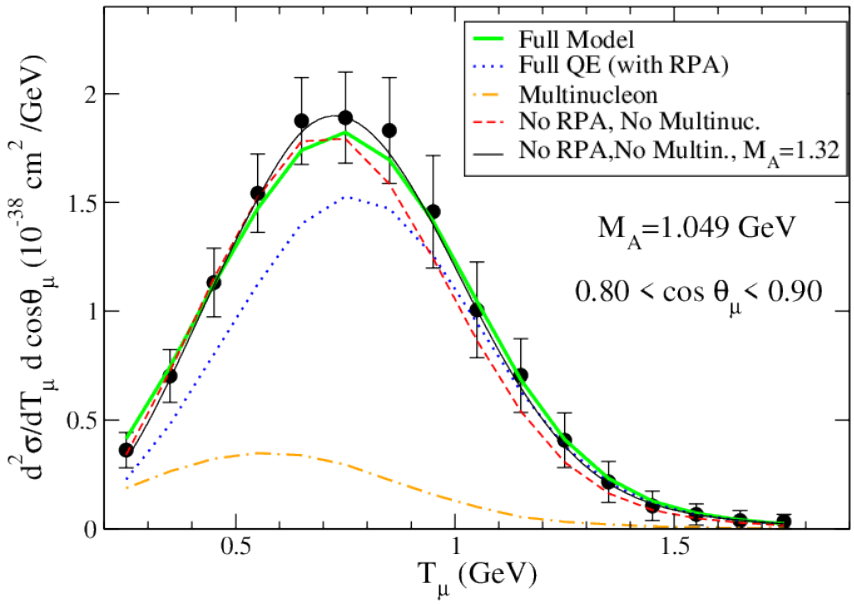

Figure 3.7: CCQE double differential cross section in muon angle and energy with several models. The data points are the results from the MiniBooNE experiment [132]. The data can be explained by the RFG model without nucleon-nucleon correlations ($M_A^{\mathrm{QE}} = 1.32\,\mathrm{GeV}/c^2$). While it can be well fitted with the RFG model with RPA and 2p2h interactions ($M_A^{\mathrm{QE}} = 1.049\,\mathrm{GeV}/c^2$) [141].

production of multi hadrons is also considered. The cross sections of each process are tuned by the pion-nucleus scattering data up to $2\,\mathrm{GeV}/c$, and the kinematics after FSI is calculated by the phase shift analysis with medium corrections [144, 145]. Kaons, etas, and omegas are similarly treated as high momentum pions. FSI of the nucleons are based on the model by Bertini *et al.* [146]. Re-interactions of not only hadrons but also leptons are considered recently. Such contribution is treated using the optical potential and Coulomb effects [147]. The effect from the optical potential is considered to affect differently for neutrino and anti-neutrino interactions, thus the understanding of it is important in the search for the CP violation in the neutrino oscillation experiments.

In addition to FSI, particles sometimes also interact with materials before detected. Such interactions are called secondary interactions (SI). The nuclear emulsion detector used in this study has a high sampling structure of 2.3-mm thick target water layers and nuclear emulsion films. The charged particles from the water layer are seldom scattered before being detected. Thus, the measurement almost free from SI can be achieved in the NINJA experiment.

3.3 Neutrino interaction measurement experiments

As mentioned in Sect. 3.2, measurements of neutrino interactions started in the 1970s by bubble chambers. The Gargamelle experiment was the first experiment using a bubble chamber and observed NC interactions [148]. A series of bubble chamber experiments in the US then measured

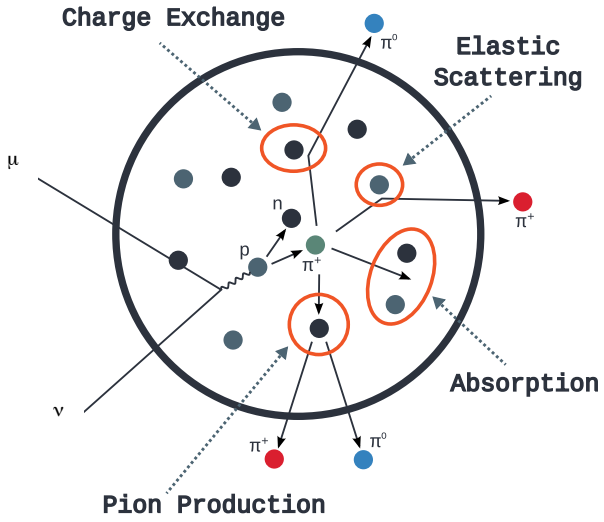

Figure 3.8: Schematic image of FSI [142].

the neutrino interactions on free nucleons [149–151]. Owing to these results, the understanding of the neutrino interactions on free nucleon significantly proceeded. Currently, many neutrino oscillation experiments use heavier nuclei as the target, and more comprehensive models to describe the whole picture of the neutrino interactions are anticipated.

3.3.1 Measurement of CC0π cross sections

As mentioned in Sect. 2.6, a better understanding of the neutrino-nucleus interactions is essential in the T2K and other neutrino experiments. In the energy region of the T2K experiment, CCQE is the dominant interaction mode, and the T2K experiment uses its topology as the signal. With an assumption of the two-body scattering, the incoming neutrino energy can be reconstructed only from the outgoing charged lepton kinematics as shown in Eq. (3.1). This is an important feature since Super-Kamiokande is almost insensitive to nucleons from the neutrino interactions. However, as introduced in Sect. 3.2, there are many possible sources for the non-CCQE interaction to mimic the signal. For example, when pions are absorbed inside the nucleus due to FSI, or not detected due to SI or its low momentum, it is selected as the CCQE-like signal in detectors. In addition, the 2p2h interaction will be also selected as the signal since nucleons are not detected in Super-Kamiokande. When we use Eq. (3.1) to predict the distribution of the reconstructed neutrino energy, it is significantly biased for the non-CCQE interactions. Besides, the reconstruction of the CCQE interaction still has a broad width due to the Fermi motion. In the oscillation analysis, it is essential to reconstruct the incoming neutrino energy and predict the number of neutrinos since the oscillation probabilities are determined from them. For the more precise measurement, the measurement of the cross sections of each neutrino interaction mode and an understanding of their models are necessary. Figure 3.9 shows results of the ν_μ and $\bar{\nu}_\mu$ CC inclusive cross sections from various measurements [152]. Above 10 GeV, the cross sections are well explained by the proportionality to the neutrino energy, while

below 10 GeV, where the CCQE interaction is more dominant, there is a large discrepancy. For the T2K experiment, the understanding of the CCQE-like interactions is especially anticipated. Instead of the CCQE measurement, the CC0π measurements are favored for this motivation. To interpret the measurement results as that of the CCQE interactions, we should rely on the neutrino interaction models, which are poorly understood. On the other hand, the measurement based on the final state topology is not strongly model-dependent.

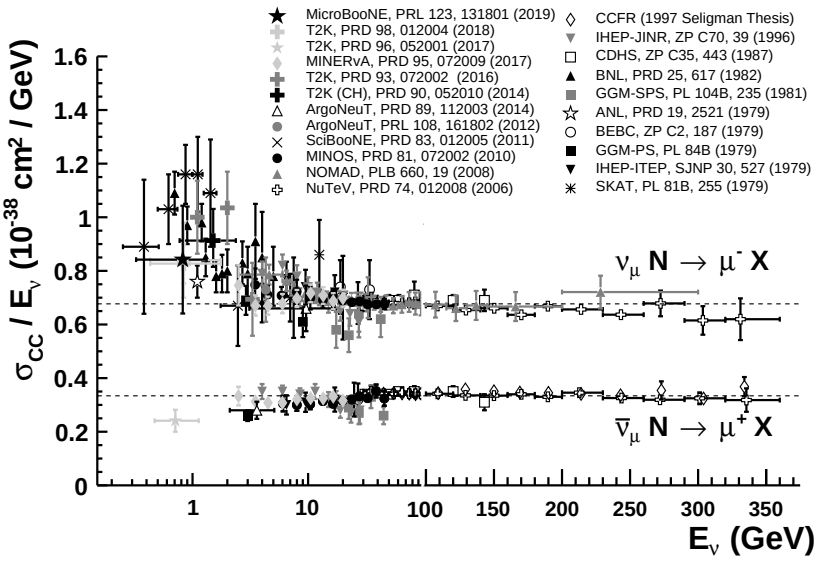

Figure 3.9: Results of the ν_μ and $\bar{\nu}_\mu$ CC inclusive cross sections from various experiments [152].

3.3.2 Measurement of hadron kinematics from neutrino interactions

To better understand the CCQE interactions, it is important to measure the CC interactions without pions with N protons (CC0πNp) with a low momentum threshold for hadrons. The measurement of low-momentum protons provides essential information about the nuclear effects. To achieve a low momentum threshold, detectors should have the capability of detecting short tracks. The bubble chamber used in the 1970s is one example of such detectors, and another technique is a liquid argon time projection chamber (LArTPC) [153]. The LArTPCs have been operated in several neutrino experiments such as the ICARUS (Imaging Cosmic And Rare Underground Signals) [154], ArgoNeuT (Argon Neutrino Teststand) [155], and MicroBooNE [50] experiments. In the US, the LArTPCs are developed for the next-generation neutrino experiments such as the SBN (Short Baseline Neutrino) program [156] and DUNE [48]. The LArTPC consists of a large mass of purified liquid argon in an electric field. The excited electrons are drifted by the electric field, and collected and amplified by wire cells. They have a positional resolution of a few millimeters with a large target mass and are therefore suited to understand the hadron kinematics.

The first measurement of low-momentum protons from the neutrino interactions with a

LArTPC was conducted by the ArgoNeuT experiment with a 240 kg target mass [157]. They reported "back-to-back" proton pairs in the CC0π interactions. Two protons from the 2p2h interaction are expected to be emitted back-to-back in the center-of-mass frame of the nucleon pair. Therefore, when the pair is emitted to the transverse direction to the beam, the protons are observed as back-to-back. On the other hand, if one proton is additionally produced by FSI in the CCQE interaction, such protons are not always observed as back-to-back. The left plot in Fig. 3.10 shows the correlation between the lower momentum of and the opening angles between two protons in CC0π events. The statistics were not sufficient to conclude some physics, but they measured back-to-back proton pairs with $\cos\gamma < -0.95$ as shown in the right figure of Fig. 3.10, where γ is the opening angle between two protons.

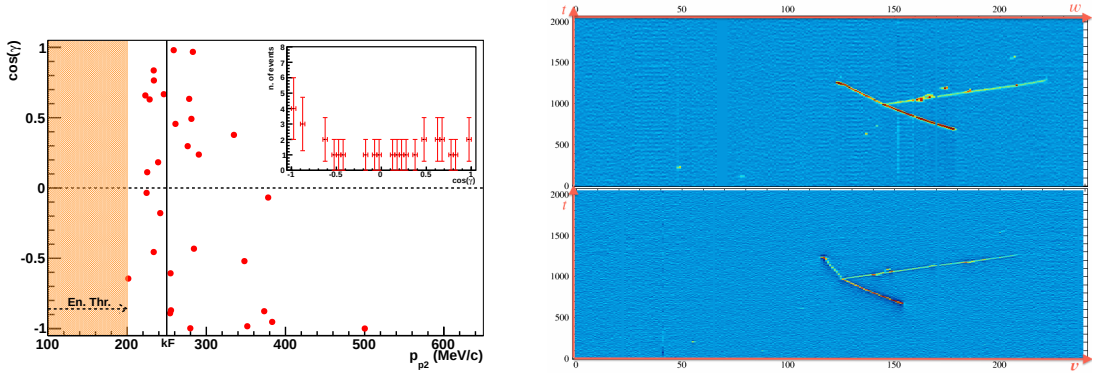

Figure 3.10: Relation between the lower momentum of and the opening angles between two protons in CC0π events (left) and an example of the event display (right) by the ArgoNeuT experiment [157].

To get more statistics, the MicroBooNE experiment started with a 170 t target mass in 2015. A similar analysis has been conducted with the 300 MeV/c proton momentum threshold. The result shown in Fig. 3.11 is not consistent with the proposed excess by the ArgoNeuT experiment. To have a better understanding of the 2p2h interactions, the measurement of the two protons with larger statistics is still necessary.

Another approach is recently proposed by the T2K or MINERνA (Main Injector Neutrino ExpeRiment to study ν-A interactions) [49] experiment. Since ND280 in the T2K experiment and the MINERνA detector are scintillator tracking detectors, it is difficult to achieve a momentum threshold as low as the bubble chambers or LArTPCs while keeping the target mass. In the CCQE interaction without the nuclear effects, the outgoing lepton and proton should be balanced with respect to the incoming neutrino direction. In other words, the imbalance of the particles indicates the nuclear effects [159, 160]. Transverse Kinematic Imbalance (TKI) is one example of variables representing such an imbalance. The Single Transverse Variables (STVs)

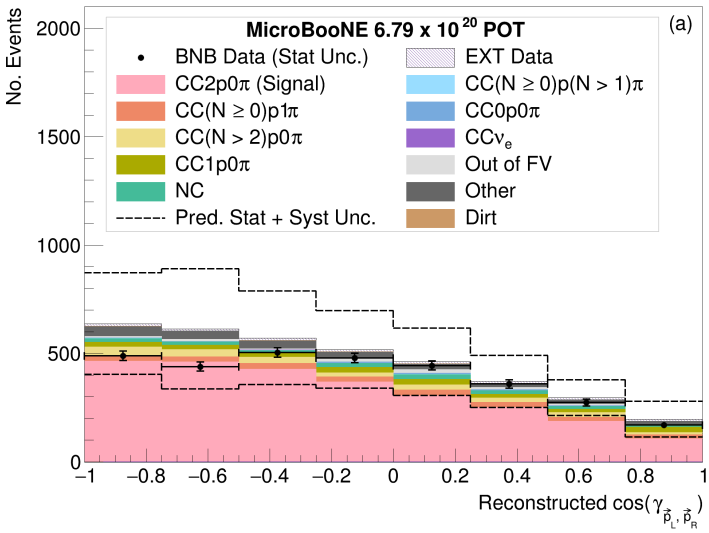

Figure 3.11: Opening angle distribution of two protons in CC0π2p events in the lab frame measured by the MicroBooNE experiment [158].

for CC0π1p are defined as follows;

$$\delta p_T = |\vec{\mathbf{p}}_T^{\,l'} + \vec{\mathbf{p}}_T^{\,N'}|, \tag{3.15}$$

$$\delta\alpha_T = \arccos \frac{-\vec{\mathbf{p}}_T^{\,l'} \cdot \delta p_T}{p_T^{l'} \delta p_T}, \tag{3.16}$$

$$\delta\phi_T = \arccos \frac{-\vec{\mathbf{p}}_T^{\,l'} \cdot \vec{\mathbf{p}}_T^{\,N'}}{p_T^{l'} p_T^{N'}}. \tag{3.17}$$

Here, l' and N' represent the lepton and nucleon (proton) momentum vectors, respectively, and T represents that the vector is projected on the transverse plane with respect to the incoming neutrino direction. As shown in Fig. 3.12, STVs are defined on the transverse plane to the incoming neutrino direction, where $\vec{\mathbf{p}}_\nu$ is the incoming neutrino momentum. The first variable δp_T represents a momentum imbalance, and the second one $\delta\alpha_T$ does the acceleration of the final state hadron. The third variable $\delta\phi_T$ represents an imbalance of the directions which can be measured only with angular information.

The measurements of the STVs by ND280 [76] show that any of the current neutrino interaction models cannot explain the events, and the most preferred model is the SF with 2p2h interactions. Figure 3.13 shows the result of the $\delta\alpha_T$ differential cross section measurement by ND280 with the 500 MeV/c proton momentum threshold. ND280 also measured TKI for CC1π^+Np where $N \geq 1$ [82]. The measurement is also sensitive to the free nucleon (the proton in hydrogens of CH or H_2O) and not easy to compare to the results from the CC0π STV measurements. So far there is no conclusion about the choice of the neutrino interaction models by the TKI measurements in the T2K experiment, and further studies are ongoing.

The MINERνA experiment also reported the measurements of the TKI with the 450 MeV/c

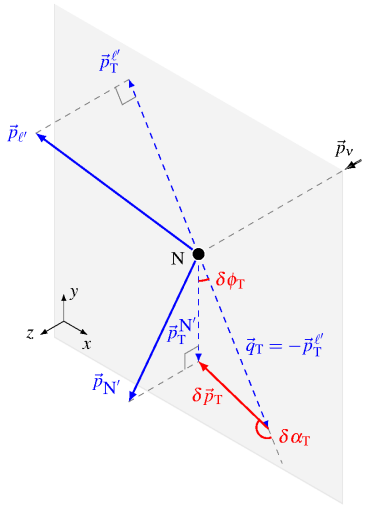

Figure 3.12: Definitions of the STVs [159].

proton momentum threshold [161–163]. Figure 3.14 shows the result of the $\delta\alpha_T$ differential cross section measurement by the MINERνA experiment [161]. The distribution is not well explained by the default neutrino interaction models implemented in GENIE. In the MINERνA experiment, as well as ND280, there are other results of the TKI measurements. The comparison of the results to that of the CC0π STV measurements is not so easy, and further studies are needed.

The LArTPCs are excellent detectors, but they can only measure the neutrino interactions on argon. Although the new variables of imbalance measured by the T2K or MINERνA experiment show another way to measure the nuclear effects, they are not still well understood. To better constrain the neutrino interaction models including the one of 2p2h, a lower momentum threshold is required. In particular, for the T2K and Hyper-Kamiokande experiments, understanding the neutrino interactions on water is essential. Figure 3.15 shows expected distributions of the proton momentum from the 2p2h interactions detected as CC0π2p events on a water target. To cover the most region of the proton momentum, the $\sim 200\,\mathrm{MeV}/c$ proton momentum threshold is needed. The NINJA detectors have a low momentum threshold and large angular acceptance for protons from the neutrino interactions on a water target. In the following section, the features of the detectors in the NINJA experiment and its physics goals are presented.

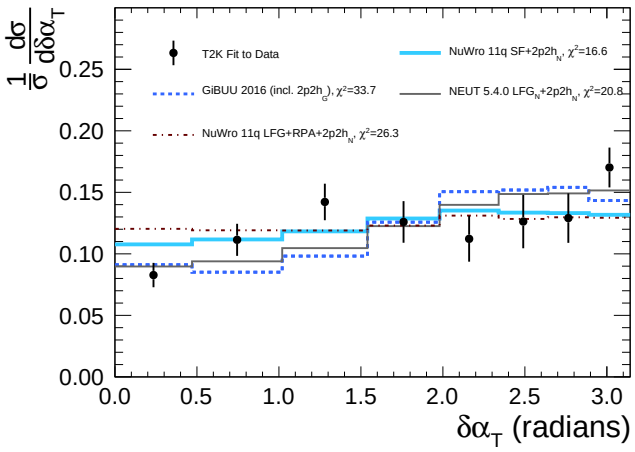

Figure 3.13: Differential cross section as a function of $\delta\alpha_T$ by ND280 [76].

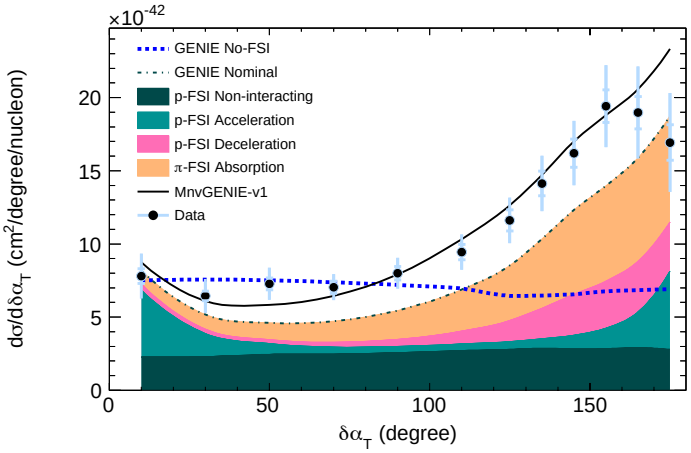

Figure 3.14: Differential cross section as a function of $\delta\alpha_T$ by the MINERνA experiment [161].

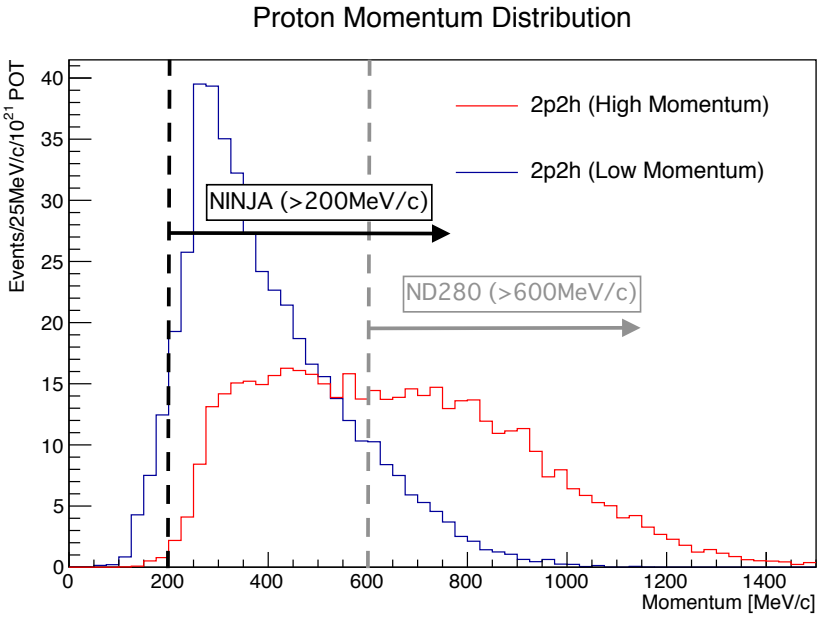

Figure 3.15: Momentum distribution of protons from the neutrino 2p2h interactions on a water target. The distributions of the higher and lower momentum of the protons are shown. The current proton momentum threshold by ND280 measurement (before upgrade) is shown by a gray line, while that of the NINJA is shown by a black one.

Chapter 4

NINJA Experiment

The NINJA experiment is a precise measurement of neutrino-nucleus interactions with nuclear emulsion films in the T2K near detector hall. As described in the previous chapters, measurement of low momentum protons with wide angular acceptance on water target is important for the precise measurement of the neutrino oscillation parameters. The NINJA experiment uses water-target nuclear emulsion detectors which have a very good spatial resolution and wide angular acceptance. First, an overview of the NINJA experiment, especially its first physics run (J-PARC E71a), is introduced in this chapter. Then, the detectors and data taking configurations in the physics run are described.

4.1 Overview of the NINJA experiment

The main purpose of the NINJA experiment is to precisely measure neutrino-nucleus interactions on variety of materials with a capability of a detection of short-range hadrons and to better understand neutrino-nucleus interaction models. To achieve a low momentum threshold to detect short-range hadrons, the NINJA experiment uses a detector with an alternate structure of nuclear emulsion films and target material layers. Nuclear emulsion is a three-dimensional tracking device which has a high granularity and 4π acceptance. The alternate structure of the nuclear emulsion films and target layers allows us to detect tracks of the short-range hadrons emitted from various materials between the films.

4.1.1 Nuclear emulsion

The nuclear emulsion is one of the most conventionally used devices in particle physics. It has played important roles in the discoveries of pions [164] and the charm particles [165] in cosmic rays, the direct observation of tau neutrinos in the DONUT experiment [4], and the discovery of the tau neutrino appearance by the OPERA experiment [166]. The nuclear emulsion is made by silver bromide (AgBr) crystals dispersed in gelatin. It is sensitive to charged particles, and their trajectories get visible as a latent image after a development process. Since each silver grain functions as a detector element, it has a very high granularity and can record short tracks three-dimensionally.

The mechanism of detection of charged particles in nuclear emulsion films is shown in Fig. 4.1. An emulsion film is a plastic base film coated with emulsion gel on both sides. The thicknesses of a plastic base and an emulsion gel used in the physics run are 210 µm and 70 µm, respectively. When a charged particle passes through the emulsion, electrons are generated and captured in the lattice defects of the surface of the crystals. The negatively charged crystals make silver atoms by deoxidizing silver ions around them. More than three silver atoms are gathered to make a latent image, and all silver ions are deoxidized to make a silver grain in the development process. The size of these grains is typically a few hundred nanometers, and the trajectory is detected as a series of the grains by a microscope. Since there are dozens of silver grains in a 100 µm track, the position and angle of the track can be precisely reconstructed.

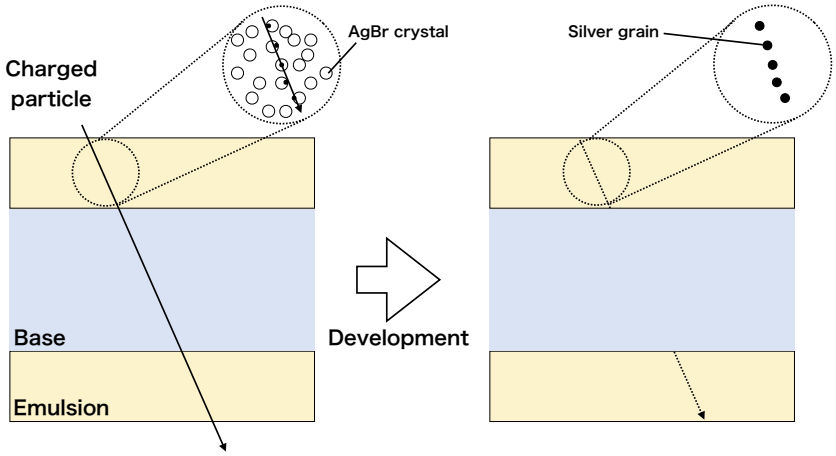

Figure 4.1: Mechanism of detection of charged particles in nuclear emulsion films.

4.1.2 Concept of the detector setup

To achieve the measurement of ν_μ CC interactions, the NINJA experiment uses several kinds of detectors. The basic principle of the detector setup is shown in Fig. 4.2. The main target detector, Emulsion Cloud Chambers (ECCs) are installed the most upstream of the neutrino beam direction. The ECC is composed of alternating layers of emulsion films and target materials. The nuclear emulsion films in the ECC record all tracks of charged particles from the neutrino interactions in the target. The ECCs are installed upstream of an MRD which has a sandwich structure of scintillator and iron planes. The MRD detects muons from neutrino interactions in the ECCs. The nuclear emulsion films have very good positional and angular resolutions while they do not have timing information. Thus, not only the tracks from the neutrino interactions but all tracks of charged particles after the production and before the development process are recorded in the films. The dominant component of such tracks is the cosmic-muon tracks. On the other hand, the MRD has beam-timing information, while the positional and angular resolutions are around $\mathcal{O}$(cm) and $\mathcal{O}$(0.1 rad), respectively. The resolutions of the MRD are insufficient to select a correct track to be connected from all the tracks accumulated in the nuclear emulsion films. Thus, other devices providing both good positional, angular, and timing

information are installed between the ECC and MRD. Such detectors are called "timestamp detectors." In the NINJA experiment, two types of the timestamp detectors were used so far: an emulsion shifter [167–169] and a scintillating fiber tracker [170].

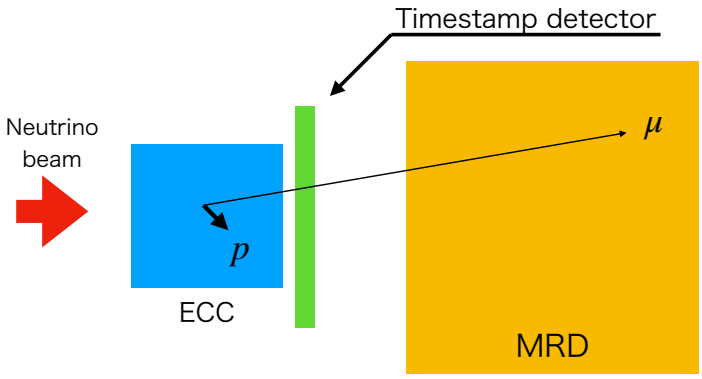

Figure 4.2: Conceptual detector setup in the NINJA experiment.

The surfaces of the emulsion films in the ECC and the emulsion shifter, and the scintillator planes in the other detectors are almost orthogonal to the beam direction. The direction orthogonal to the emulsion films or the scintillator planes is defined as the z direction, and the x direction is the horizontal and the y direction is the vertical, i.e. the z direction is almost the same as the beam direction. In this study, analyses such as the event selection, evaluation of the detector performances, and momentum reconstruction and particle identification are based on the x-y-z coordinate, while the measured angles in the final results of the neutrino interaction measurements are defined as those with respect to the beam direction.

4.1.3 History of the NINJA experiment

The NINJA experiment has conducted a series of detector runs and pilot runs since 2014. Table 4.1 summarizes the history of the NINJA experiment. In the first few years, the NINJA experiment performed feasibility studies of the ECCs in the T2K near detector hall, and the first neutrino events were detected in the beam exposure in 2015 [171]. In 2015, the first water target ECC was installed in the T2K near detector hall. The physics results with 60 kg iron target [168, 169] and 4 kg water target [170] have been reported so far. In this thesis, we use the data collected in the first physics run of the NINJA experiment, which was conducted from November 2019 to February 2020.

4.2 Latest results from the NINJA experiment

So far, the NINJA experiment has measured neutrino interaction on iron and water. These results are important information for the construction of better models of the neutrino-nucleus interactions. In addition, the results have shown the necessity of several improvements in the analysis, whose details are shown in Sect. 4.2.3.

Table 4.1: History of the NINJA experiment

J-PARC experiment	NINJA run	Period	Beam	Target and mass
T60	Runs 1–3	Nov. 2014 – Dec. 2014	$\bar{\nu}$	Fe (2.0 kg)
	Run 4	Feb. 2015 – Apr. 2015	$\bar{\nu}$	Fe (2.0 kg)
	Run 5	May 2015 – Jun. 2015	$\bar{\nu}$	H_2O (1.0 kg)
	Run 6	Feb. 2016 – May 2016	$\nu/\bar{\nu}$	Fe (60 kg)
T66	Run 7	Jan. 2017 – Apr. 2017	ν	H_2O (1.3 kg)
T68	Run 8a	Oct. 2017 – Dec. 2017	$\bar{\nu}$	H_2O (4.0 kg)
	Run 8b	Mar. 2018 – May 2018	$\bar{\nu}$	H_2O (4.0 kg)
E71a	Physics Run a	Nov. 2019 – Feb. 2020	ν	H_2O (75 kg)/Fe (130 kg)
T81	Run 9	Mar. 2021 – Apr. 2021	ν	D_2O (9.1 kg)
E71b	Physics Run b	planned	ν	under discussion

4.2.1 Iron target results

The measurement of ν_μ CC interactions on a 60 kg iron target has been performed using the data collected from February to May 2016. The detectors were exposed to the on-axis FHC neutrino beam in J-PARC whose averaged energy was 1.49 GeV and the data corresponded to 4.0×10^{19} POT. So far, the measurements of the flux-averaged total cross section [168] and kinematics of the charged particles [169] were reported. The measured value of the total cross section is consistent to the prediction of the MC simulation and other experiments [83, 172, 173] as shown in Fig. 4.3. The kinematics of the hadrons from the neutrino interaction is one of the main targets of the NINJA experiment. Figure 4.4 shows the measured kinematics distributions of the protons and charged pions. Although the statistics are limited, those distributions show

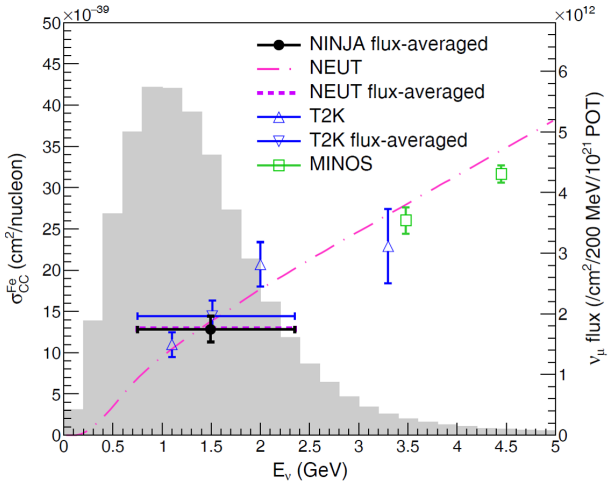

Figure 4.3: Flux-averaged total cross section of the ν_μ CC interaction on iron [168]. The gray histogram is the neutrino flux. The black plot is the results with 68% region of the neutrino flux as the horizontal and the total error as the vertical errors.

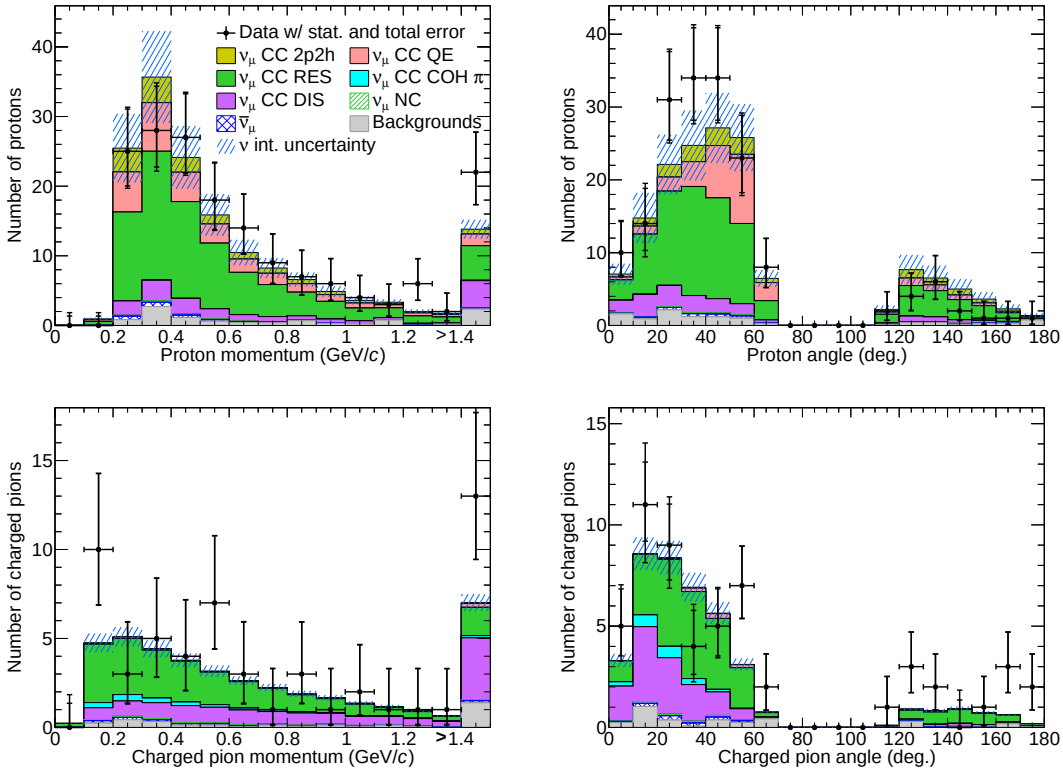

Figure 4.4: Distributions of the hadron kinematics in the measurement of ν_μ CC interactions on iron target. The proton momenta (top left) and angles (top right), and the pion momenta (bottom left) and angles (bottom right) are shown [169].

discrepancy between the data and the MC prediction, e.g. the MC prediction underestimates the back-scattered protons, overestimates the low-momentum pions, and so on.

The analysis of the data taken in the RHC mode in this period is currently ongoing. The preliminary results show a significant discrepancy in the low-momentum back-scattering pions as shown in Fig. 4.5.

4.2.2 Water target results

The measurement of $\bar{\nu}_\mu + \nu_\mu$ CC interactions on a 4 kg water target has been performed using the data collected from October 2017 to May 2018. The detectors were placed on the T2K beam axis as with the measurements in Sect. 4.2.1. The data corresponded to 7.1×10^{20} POT, and 86 events in total were found. Figure 4.6 shows the distributions of protons and charged pions [170]. The statistics are also limited in this measurement, but the result shows the tendency of overestimating the pions in the MC prediction, while the number of protons is consistent between the data and the MC prediction.

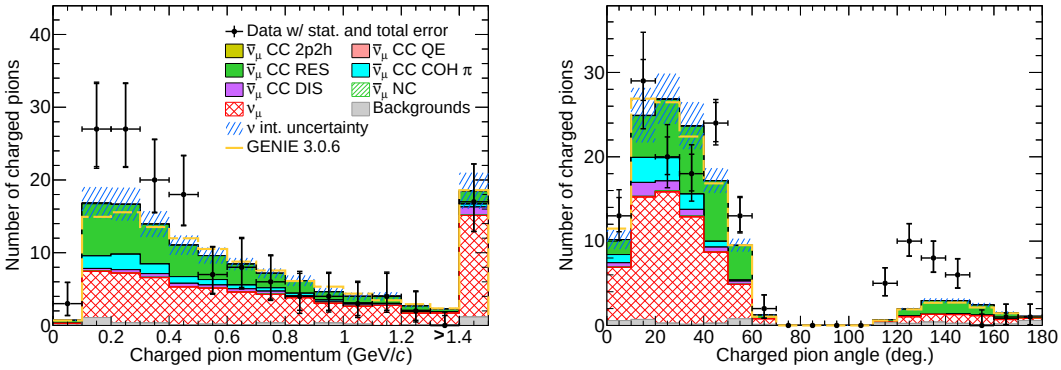

Figure 4.5: Distributions of the pion kinematics in the measurement of $\bar{\nu}_\mu$ CC interactions on an iron target with the RHC neutrino beam mode. The distributions of momenta (left) and angles (right) are shown.

4.2.3 Required improvements

The previous measurements from the NINJA experiment show the high capability of the nuclear emulsion detectors in study of the neutrino interactions. To obtain a more precise measurement of the hadron kinematics, it is essential to increase the statistics. To achieve higher statistics, the size of the detectors should be increased. Thus, the NINJA experiment conducted the physics run with a 75 kg water target, which is about 20 times larger than the measurements in Sect. 4.2.2. The physics run has been conducted in 2019–2020. The collected data are used in this thesis, and the detailed information will be described in the following sections. The cross section of the detectors to the neutrino beam is extended to 1 m $\times$ 1 m, while it was around 30 cm $\times$ 30 cm in the previous measurement. This extension requires the larger timestamp detector to cover the nuclear emulsion detectors and connect the muon tracks to the downstream muon range detector. However, it is not easy to simply extend the size of the existing detector since the number of readout channels will be too large. In addition to the detector size, the efficiency of matching muon tracks between the ECC and MRD highly deteriorates in the large angular region as shown in Fig. 4.7. The extension is required to be performed without increasing the number of readout channels, with the detection efficiency kept or even improved.

The angular acceptance is also required to be improved. In the previous results, the angular acceptance was limited to $|\tan\theta| < 1.3$ due to the limit of the film scanning system. However, to get the information of the hadron kinematics as much as possible, the acceptance needs to be extended.

As shown in the previous sections, the NINJA experiment has not measured the ν_μ CC interactions on water thus far. Although the results of the previous measurements showed important information to consider the new neutrino interaction models, the measurement of ν_μ CC interactions on the water target is more important for the T2K experiment since it is the most dominant interaction in Super-Kamiokande. In addition to the neutrino species and the target material, the neutrino energy was higher than that at ND280 and Super-Kamiokande. The main neutrino interaction mode differs by the neutrino energy, and CCQE is dominant in

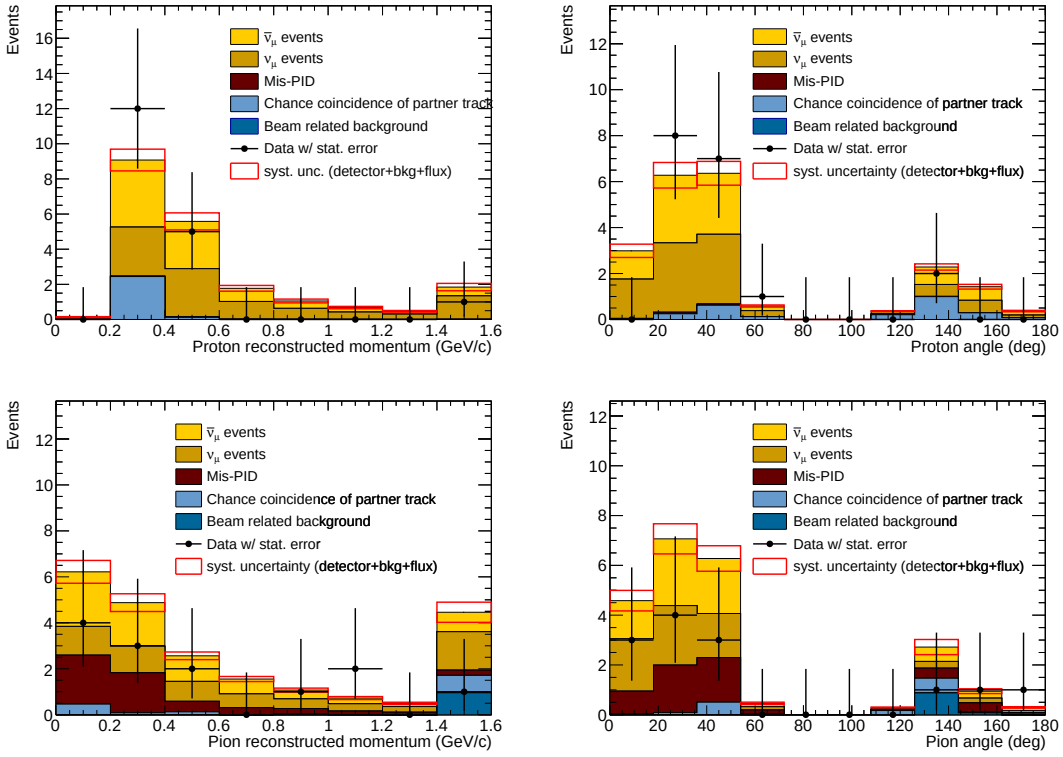

Figure 4.6: Distributions of the hadron kinematics in the measurement of ν_μ CC interactions on a water target. The proton momenta (top left) and angles (top right), and the pion momenta (bottom left) and angles (bottom right) are shown [170].

the sub-GeV neutrino energy region. The NINJA physics run is the first measurement of the ν_μ CC interactions on a water target with the sub-GeV mean neutrino energy using the nuclear emulsion detectors.

After the increase of the statistics, the systematic uncertainties should be also improved. One of the dominant uncertainties in the measurement of protons and pions in the previous measurement is the PID performance. Figure 4.8 shows the breakdown of the systematic errors from the uncertainties of the detector response in the previous measurement [174]. The error from the PID performance is twice larger than the other sources. This large uncertainty is attributed to two things. One is that the response of the nuclear emulsion to the energy deposit is not understood well, and the other is that the previous method of the momentum reconstruction is not suitable for particles with a low momentum or a large emitted angle.

The energy deposit of the charged particles can be obtained from the blackness of the track in the nuclear emulsion, but it is dependent on various factors, e.g. temperature, humidity, duration from the production, angle, and so on. Thus, the data-driven calibration is required in each experiment, but it was not conducted in the previous measurement because the number of tracks was not sufficient. In the physics run, the method of the PID and the evaluation of its systematic uncertainty are required to be highly improved.

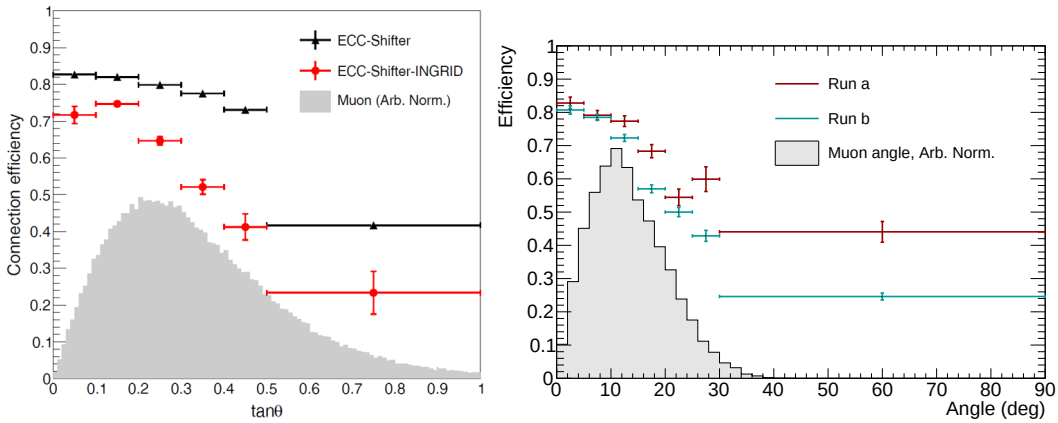

Figure 4.7: Muon matching efficiencies in the previous measurements. The measurement of neutrino-iron interactions used the emulsion shifter [168] (left) and that of the neutrino-water interactions used the scintillating fiber tracker [170] (right).

As for the momentum reconstruction, the dominant momentum and angular regions are different between the previous and next runs. In the previous measurements, the energy loss in the nuclear emulsion detector is not considered in the momentum reconstruction using multiple Coulomb scatterings (MCS), which will be described in Chap. 9. This method was used in the momentum reconstruction of high-momentum particles which exit from the nuclear emulsion detector. Thus, the energy deposit was not considered to have significant effect on the performance. However, in the physics run, the neutrino energy is lower than the previous runs, and it will have a larger impact. Besides, in the larger angular region, MCS was not properly treated. When the angle is not so large, $\tan\theta \simeq \theta$ is satisfied. Because $\tan\theta$ can be more directly calculated from the data, $\tan\theta$ was used in the previous measurement. However, when the angle is not so small, this approximation is not satisfied anymore. Therefore, the more proper treatment of the angles in the method is required.

In this thesis, we focus on two improvements. One is the development of a new scintillation tracker as a new timestamp detector, and its analysis. This study highly improves the statistics of the NINJA physics run. The other is the development and improvement of the momentum reconstruction method using MCS in the ECC. We improved the method to consider the energy deposit inside the detector volume using the maximum likelihood method with a modified treatment of the angles of the particles. This improvement is important not only for the momentum reconstruction itself but also for the PID because the PID uses the reconstructed momentum using MCS.

4.3 Overview of the NINJA physics run

One of the main goals of the NINJA physics run is to measure the ν_μ CC interactions on a water target with a low momentum threshold and wide angular acceptance for hadrons. The total target mass is 250 kg and the main target is 75 kg of water. The nuclear emulsion detectors

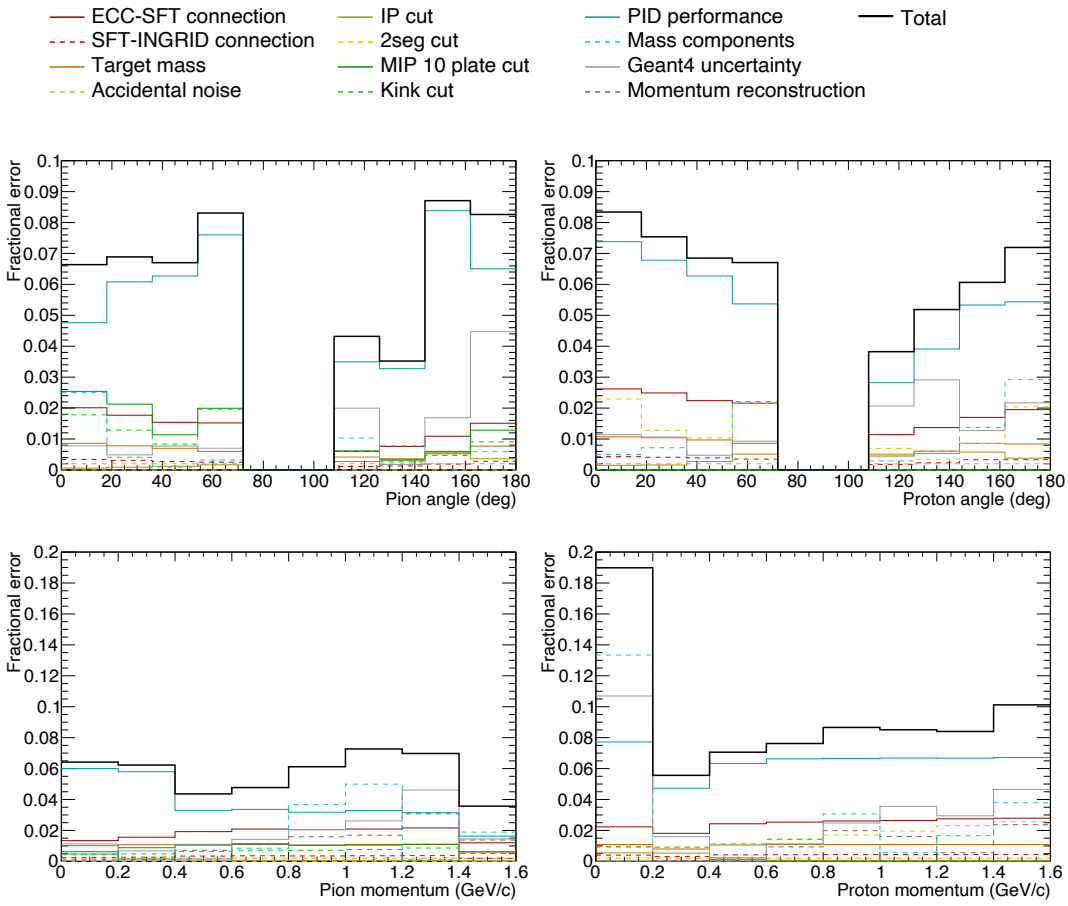

Figure 4.8: Systematic errors from the uncertainties of the detector response in the measurement of the neutrino-water interactions in the NINJA experiment [174].

were operated between the detectors of the WAGASCI complex on the B2 floor of the T2K near detector hall, which corresponds to the off-axis 1.5°, as shown in Fig. 4.9 and exposed to the T2K neutrino beam operated in the FHC mode from November 2019 to February 2020. The results will be provided with a 19 times larger target mass than the previous measurement of the neutrino-water interactions in the NINJA experiment. Moreover, this is the first measurement of the neutrino-water interactions with the FHC mode neutrino beam in the NINJA experiment. In the following sections, the detectors and data taking of the NINJA physics run are described.

4.4 NINJA detectors

In the NINJA physics run, we installed the water target ECCs in the most upstream of the detector setup. In the most downstream, Baby MIND is used as the MRD. As the timestamp detectors, we newly developed two kinds of detectors: an emulsion shifter and a scintillation

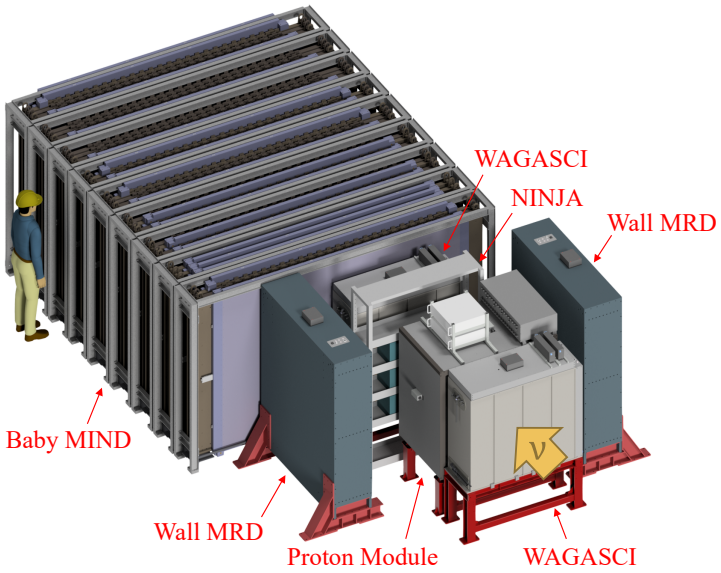

Figure 4.9: WAGASCI complex and NINJA, and their setup.

Table 4.2: Summary of the NINJA detectors.

Detectors	Position & angle	Time	PID
ECC	$\mathcal{O}$(µm) & $\mathcal{O}$(mrad)	N/A	p/π (μ)
Emulsion shifter	$\mathcal{O}$(µm) & $\mathcal{O}$(mrad)	4 hour	N/A
Scintillation tracker	2–3 mm	$\mathcal{O}$(ns)	N/A
Baby MIND	$\mathcal{O}$(cm) & $\mathcal{O}$(10 mrad)	$\mathcal{O}$(ns)	μ/hadron

tracker. The detectors and their brief performances are summarized in Table 4.2.

4.4.1 ECC

The ECC is the main detector in the NINJA experiment. It is composed of alternating layers of emulsion films and target materials. The structure of the water ECC used in the NINJA physics run is shown in Fig. 4.10. The ECC consists of 58 of 2.3-mm thick water layers and 59 tracking units in 1-cm thick acrylic desiccator. In the tracking unit, two 25 cm × 25 cm emulsion films are attached on both sides of a 500-µm thick iron (SUS316L) plate, and all of them are vacuum-packed together. The iron plates are used as supporting structures for the emulsion films as well as to measure the momentum of charged particles. They are placed perpendicularly to the z direction. The high sampling rate of the ECC in the z direction allows us to detect short tracks of charged particles from the water layers in the neighboring nuclear emulsion films. We require charged particles to penetrate at least one tracking unit, which results in the 200 MeV/c momentum threshold for protons.

In the downstream of the water ECC part, an iron ECC is employed to secure the number of iron plates used in the momentum reconstruction using multiple Coulomb scatterings. One iron ECC consists of 12 emulsion films and 11 iron plates, followed by the inside special sheet

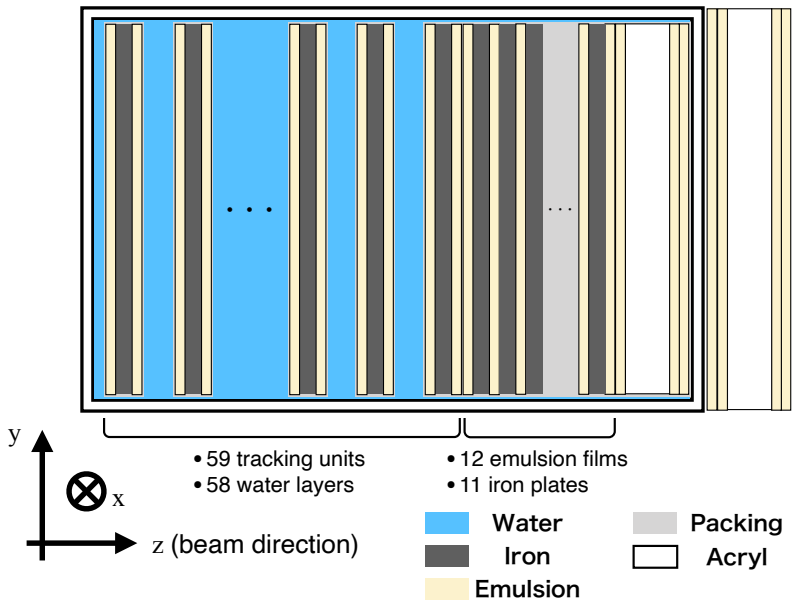

Figure 4.10: Structure of an ECC in the NINJA experiment [175].

(ISS) consisting of a 2-mm thick acrylic plate and four emulsion films. They are vacuum-packed together as shown in Fig. 4.10. In addition, an outside special sheet (OSS) is placed outside of the desiccator. The ISS and OSS are used to connect muon tracks between the ECC and the emulsion shifter.

The total target mass of one water ECC is 8.2 kg and we use 9 ECCs. Thus, the total water target mass in the NINJA physics run is around 75 kg.

4.4.2 Baby MIND

The ECC has an excellent performance for the measurement of the hadron tracks. However, it has only 2–3 radiation length units in the z direction. Thus, the muon tracks rarely stop in the ECC volume in our neutrino energy region although the identification and momentum reconstruction of muon tracks are necessary to study the ν_μ CC interactions. To distinguish muons from the other particles, especially charged pions, an MRD, which has sufficient materials to stop muon tracks, is necessary. In the previous measurements, INGRID was used for this purpose, while the physics run uses Baby MIND, which has wider angular acceptance, a larger material thickness, and a magnetic field inside the detector.

4.4.3 Timestamp detectors

To reconstruct the ν_μ CC events that occurred in the ECC, the three-dimensional tracks reconstructed in Baby MIND are required to coincide with the same particle's tracks in the ECC. Thus, the tracks in Baby MIND are extrapolated to the location of the ECC. However, all tracks during the whole beam exposure are accumulated in the nuclear emulsion films with the density

of $\mathcal{O}(10^4)/\mathrm{cm}^2$. The positional and angular resolutions of Baby MIND are not sufficient to select a correct candidate to be matched in the ECC. Timestamp detectors are used to match muon tracks between the ECC and Baby MIND. The timestamp detector has better positional and angular resolutions than those of Baby MIND, which are sufficient to select a correct candidate in the ECC. In addition, it can provide timing information so that the track matching between the ECC and Baby MIND without the cosmic-muon tracks is realized.

So far, an emulsion shifter [167, 168] or a scintillating fiber tracker [170] was used as the timestamp detectors in the NINJA experiment. The emulsion shifter provides precise information of position and angle of the nuclear emulsion films, while the timing resolution was 5–50 s. The principle of the emulsion shifter is described in the next section. The scintillating fiber tracker consisted of 1024 scintillating fibers with a cross section of 1 mm-square. It has a 1-ns timing information and a positional resolution of a few hundred micrometers, but the number of readout channels is more than 500 and the enlargement is not easy, e.g. to cover an area of $1\,\mathrm{m} \times 1\,\mathrm{m}$, the number of fibers will be more than 3000.

In the NINJA physics run, the timestamp detectors are required to cover an area of the 3×3 ECC array, i.e. approximately $1\,\mathrm{m} \times 1\,\mathrm{m}$, which is ten times larger than the previous runs. To realize both the larger coverage area and the good positional and angular resolutions without significantly increasing the number of readout channels of the scintillator detector, an emulsion shifter and a scintillation tracker are both used as the timestamp detectors.

4.4.3.1 Emulsion shifter

An emulsion shifter has been originally developed for cosmic-electron balloon experiments [176] and recently used in the GRAINE (Gamma-Ray Astro-Imager with Nuclear Emulsion) experiment [177–183].

Figure 4.11 shows a cross-sectional view of the emulsion shifter in the NINJA physics run. The emulsion shifter consists of two moving walls, one fixed wall, and one tracker special sheet (TSS). The size of one emulsion film used in the emulsion shifter is $102\,\mathrm{cm} \times 34\,\mathrm{cm}$ to cover large acceptance for muons with small insensitive areas. One emulsion film area corresponds to three horizontal ECCs. The fixed wall is a middle wall of the emulsion shifter made of glass fiber reinforced plastic (GFRP). Vacuum-packed two emulsion films attached on each side of acrylic plate are set on the upstream of the GFRP plate. Two moving walls are placed the upstream and downstream of the fixed wall. They horizontally moves 2 mm every four hours and four days, respectively. The former is called "fast-moving wall," and the latter is called "slow-moving wall." Figure 4.12 shows the history of the operation of the moving walls during the beam exposure. The movement is controlled by stepping motors and microcomputers. The moving wall is made of aluminum honeycomb to reduce their mass without losing rigidness. Three emulsion films on one side of an acrylic plate are vacuum-packed together and attached on the inner side of the wall. The TSS is vacuum-packed two emulsion films attached on each side of an acrylic plate. The TSS is directly attached on the surface of the scintillation tracker.

After the film development and scanning, the tracks are reconstructed in each wall. Using the positional and angular information, the tracks are connected between each wall in consideration

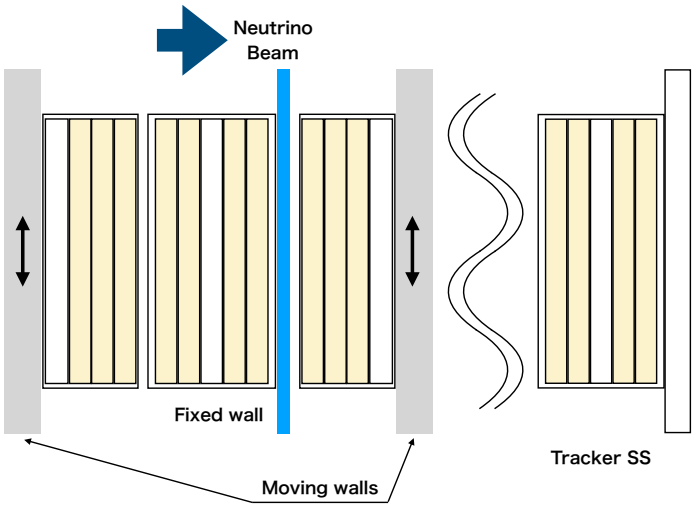

Figure 4.11: Schematic cross-sectional view of the emulsion shifter in the NINJA physics run.

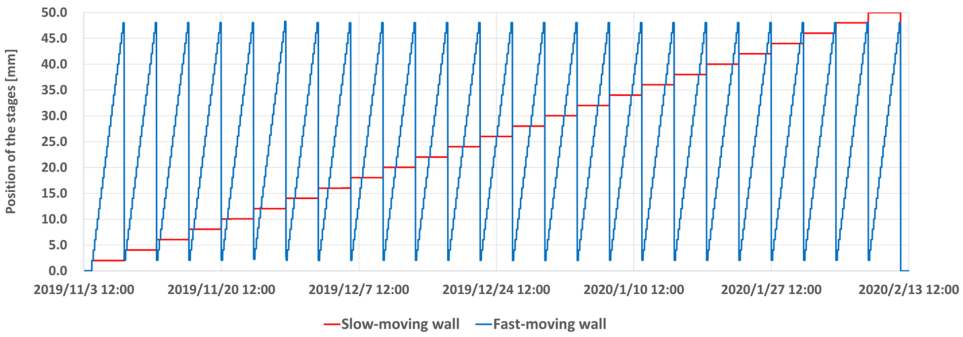

Figure 4.12: Operation of each moving wall in the emulsion shifter. The fast-moving wall moves 2 mm every four hours, while the slow-moving wall does every four days.

of horizontal positional displacement due to the movement of the walls. Since the pattern of the displacement between each wall differs every four hours, the horizontal positional difference of the same particle between each wall has four-hour timing information. Figure 4.13 shows the horizontal positional displacement between the moving walls and the fixed wall. Each peak in the distributions is called "a spot," and each pair of the spots corresponds to four-hour timing. Before and after the beam exposure, the moving walls were also kept in the different positions to make reference spots.

4.4.3.2 Scintillation tracker

The other timestamp detector in the NINJA physics run is a scintillation tracker [184]. The emulsion shifter provides four-hour timing information to each track with excellent positional and angular resolutions. However, it is still not easy to select one candidate in the ECC to

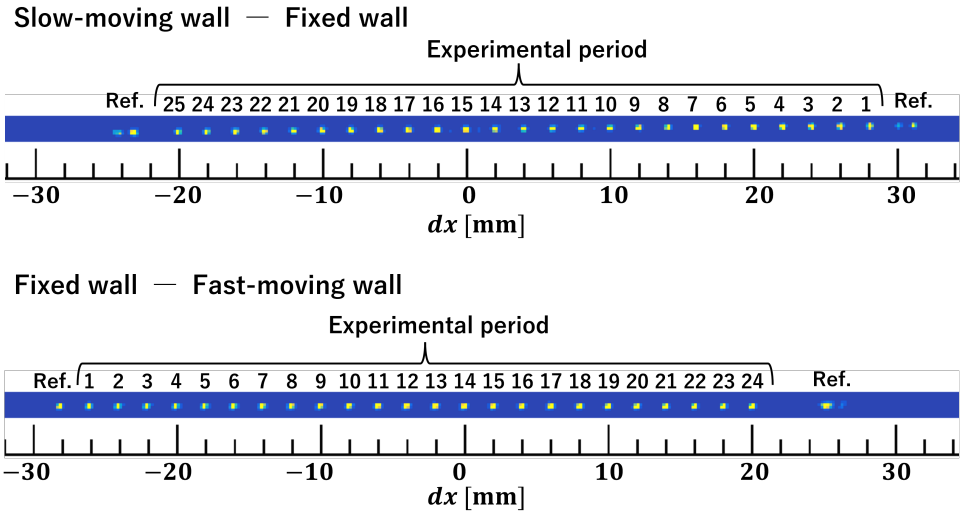

Figure 4.13: Spots observed during the beam exposure. The horizontal positional displacements between the slow-moving wall and the fixed wall (up) and the fast-moving wall and the fixed-wall (bottom).

be matched with a track reconstructed in Baby MIND due to the accumulated cosmic-muon tracks. The data acquisition (DAQ) system of the scintillation tracker is synchronized to the neutrino beam timing, and the time resolution is $\mathcal{O}$(ns). Thus, the track matching between the scintillation tracker and Baby MIND are almost free from the cosmic background. The reconstructed position and angle of the matched track between the scintillation tracker and Baby MIND are more precise than those of the tracks reconstructed with only the information from Baby MIND. Using these precise position and angle, the tracks are connected between the emulsion shifter and the scintillation tracker.

The scintillation tracker has to cover a 1 m × 1 m area perpendicular to the z direction in the NINJA physics run. To realize such a large coverage with a reasonable number of read-out channels and a sufficient positional resolution, the scintillation tracker consists of plastic scintillator bars specially arranged with deliberate gaps between each other. The muons from neutrino interactions in the ECC make hits in the scintillator bars, and the scintillation light is propagated with the WLS fibers and read by MPPCs.

The scintillation tracker consists of two identical modules, each made of four layers. One module is used to reconstruct the horizontal position of the particle, where the scintillator bars are vertically set, and the other module is to reconstruct the vertical position, where the bars are horizontally set. Figure 4.14 shows the conceptual design of a module of the scintillation tracker. One layer is made of scintillator bars aligned with a gap equal to 1/3 of the scintillator width. The second layer is shifted by 2/3 of the scintillator width relative to the first layer, and the third and fourth layers are shifted by 1/6 of the scintillator width relative to the first and second layers, respectively. A black sheet is inserted between the second and third layers to avoid the optical cross-talk between the layers.

The arrangement of the scintillator bars makes a virtual segmentation of 1/6 of the width of

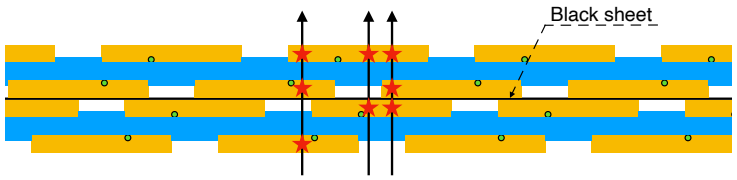

Figure 4.14: Conceptual design of the scintillation tracker. The orange areas show the plastic scintillator bars while the blue ones represent support structures. The green circle in each scintillator bar represents the WLS fiber [184].

the scintillator bar by getting the hit pattern. Thus, the positional resolution of the scintillation tracker is better than the case expected from the width of the scintillator bar. The number of readout channels also profits in this design. For instance, when we require the segmentation of w by arranging the scintillator bars without gaps, l/w channels are necessary, where l is the length of the edge of the coverage area. In this design, the number of readout channels is $4 \times l/8w = l/2w$, which is half of the case without gaps. In addition to the good positional resolution and less readout channels, the design generally does not have insensitive areas due to the edges of the scintillator bars. Viewed from the z direction, the edges are covered by scintillator bars in the neighboring layer. Thus, the entire area of the scintillation tracker is sensitive, and it achieves detection efficiency of nearly 100%. The reconstruction of the position and angle, and the performance of the scintillation tracker are described in Chap. 7.

In the scintillation tracker, the same plastic scintillator bars as in the WAGASCI module are used. The length of the bar is around 1 m, while the thickness and width are 3 mm and 24 mm, respectively. For minimum ionizing particles (MIPs) penetrating the bar in the z direction, the mean light yield of the scintillator bar is measured to be more than 10 p.e. (photoelectron equivalent). To cover a 1 m $\times$ 1 m area, 248 scintillator bars are used in total. It is primarily composed of polystyrene and infused with 1% of PPO ($C_{15}H_{11}NO$) and 0.03% of POPOP ($C_{24}H_{16}N_2O_2$). The bar is coated with TiO_2-based white reflective paint in order to increase the light yield and optically separate each scintillator bar. When a charged particle passes through the scintillator, the scintillation light with mean wavelength of 420 nm is emitted.

The scintillation light is collected and transported through a WLS fiber, Kuraray Y11(200), whose diameter is 1 mm. The mean wavelength is shifted from 420 nm to around 470 nm, which is close to MPPC's most sensitive wavelength. The scintillator bar has a 1.2-mm depth groove on one side to put the fiber, and optical cement is applied not to lose the light yield. The attenuation length of the fiber is longer than 3.5 m, and it is long enough for the 1 m transportation. The transportation of the light consists of multiple total reflections between the core and double clad as shown in Fig. 4.15. The specifications of the Kuraray Y11(200) are summarized in Table 4.3.

The MPPC is a photon-counting silicon sensor that uses avalanche photo-diodes (APDs) operated in parallel in the Geiger mode. The schematic circuit of one MPPC is shown in Fig. 4.16. When a photoelectron enters one APD pixel operated in the Geiger mode, electron-

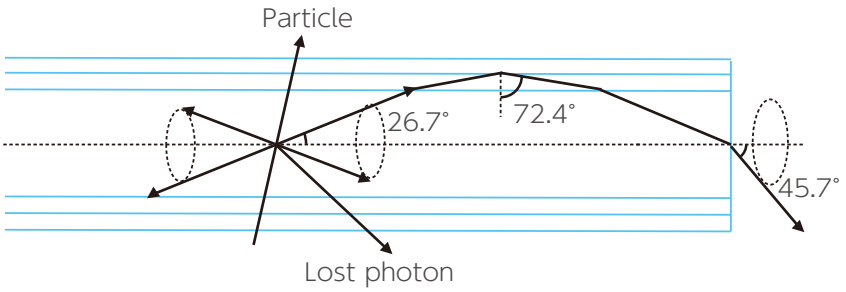

Figure 4.15: Schematic view of the transportation of the light in the WLS fiber [185].

Table 4.3: Specifications of Kuraray Y11(200) [185].

Specification	Value
Diameter	1 mm
Core	Polystyrene ($n = 1.59$)
Inner clad	Polymethyl methacrylate ($n = 1.49$)
Outer clad	Fluorinated polymer ($n = 1.42$)
Absorption peak	430 nm
Emission peak	476 nm
Attenuation length	> 3.5 m

hole pairs are generated in the depletion layer. This induces the avalanche amplification in the pixel, and the gain of 10^5–10^6 is obtained. The avalanche is quenched by a resistor, and the charge of single pixel is expressed as

$$Q = C(V - V_{\mathrm{bd}}), \tag{4.1}$$

where Q is the charge, C is the capacitance of the pixel, V_{bd} is the breakdown voltage, and V is the applied voltage, which is a few or several volts above V_{bd}. Combining the charges from all the pixels, the total charge from an MPPC can be written as NQ, where N is the number of pixels where the photoelectrons pass. When the number of photoelectrons is relatively small, N can be considered as the number of photoelectrons. Thus, the MPPC has a photon-counting capability. On the other hand. when the number of photoelectrons is comparable to or even larger than the number of pixels, multiple photoelectrons enter the same pixel, which leads to the saturation.

The MPPC signal is not only induced by the photoelectrons but by thermal carriers. This random noise is called the dark noise and mimics the signal by the photoelectrons. The rate of the dark noise increases with higher temperature. In this measurement, the MPPCs are placed in the cooling shelter with the scintillation tracker and emulsion detectors as described in Sect. 4.5. Moreover, the DAQ of the detectors is synchronized to the beam timing, and it reduces the dark noise contamination.

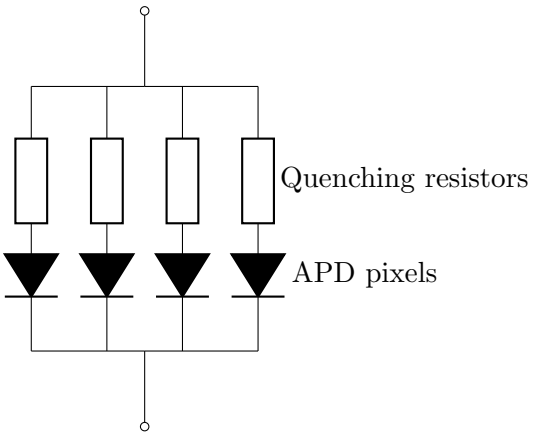

Figure 4.16: Schematic circuit of one MPPC.

Table 4.4: Specifications of MPPC S13081-050CS(X1) [186].

Specification	Value
Size of a sensitive area	1.3 mm × 1.3 mm
Number of pixels	667
Size of one pixel	50 µm × 50 µm
Operation voltage	∼ 54 V
Noise rate (> 0.5 p.e., 25 °C)	< 100 kHz
Cross-talk rate	∼ 1%
Photon detection efficiency	∼ 35%
Sensitive wavelength	320–900 nm
Most sensitive wavelength	460 nm

One edge of the WLS fiber on each scintillator bar is connected to one MPPC. In the scintillation tracker, Hamamatsu MPPC S13081-050CS(X1) is used. The specifications of the MPPC are summarized in Table 4.4.

NIM EASIROC (Extended Analogue Si-pm Integrated ReadOut Chip) modules [187] are used to read out signals from the MPPCs. Each EASIROC module can operate 64 MPPCs at once, thus four modules are operated for the scintillation tracker. Figure 4.17 shows a diagram of the trigger timing for the DAQ of the scintillation tracker. A beam window is generated by the beam trigger signal provided by the J-PARC neutrino beamline which comes 31 µs before the neutrino arrival. The trigger threshold for each channel is set to 2.5 p.e., and channels exceeding the threshold are treated as hits. When there are hits in both the horizontal and vertical modules, the hold signal is generated. The hold signal is used to hold the pulse height of the signal in each channel. In each channel, the earliest coincidence of the horizontal and vertical hits in each spill are recorded by the ADC (Analogue to Digital Converter) and multi-hit TDC (Time to Digital Converter), while the latter ones are recorded by only the multi-hit TDC. Due to the dynamic range of the multi-hit TDC, the tracks within seven bunches from the hold signal timing are recorded. If there are no hits in a spill, a dummy trigger is created by delaying

Table 4.5: Summary of accumulated POT in the NINJA physics run. "Recorded POT" means the POT recorded by the scintillation tracker [184].

Period	Delivered POT (10^{20})	Recorded POT (10^{20})
Nov. 7, 2019 – Dec. 19, 2019	2.64957	2.64841
Jan. 14, 2020 – Feb. 12, 2020	2.11645	2.11531
Total	4.76602	4.76372

the beam trigger signal, which ensures the scintillation tracker to acquire data once in each spill.

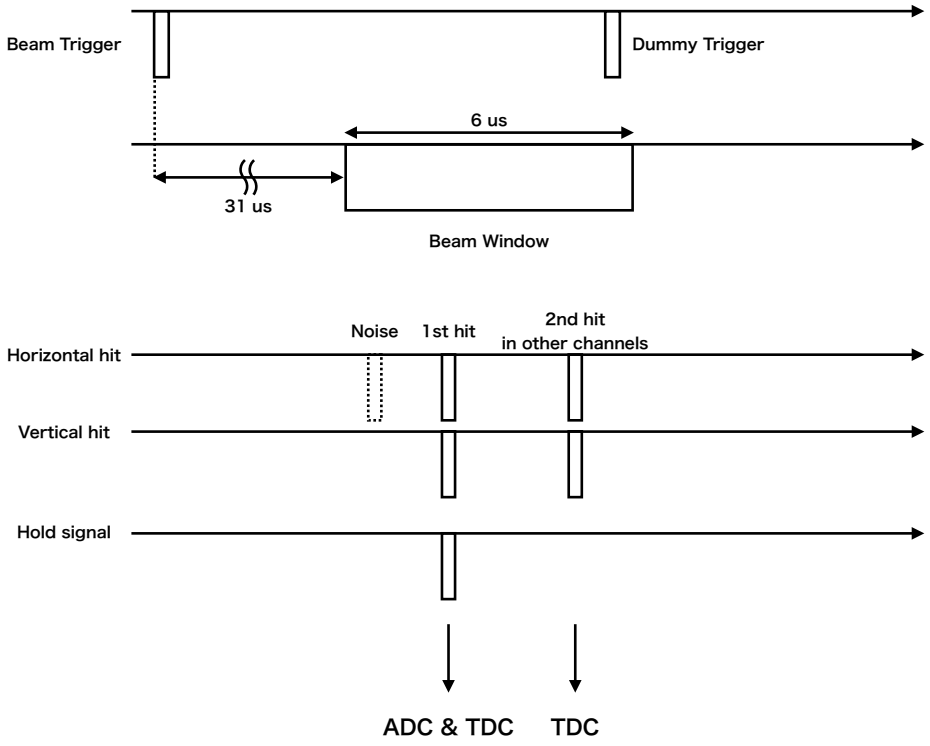

Figure 4.17: Diagram of the trigger timing for the data acquisition of the scintillation tracker.

4.5 Data taking

In the NINJA physics run, there are two periods of the neutrino beam exposure. The first period is from November to December 2019, and the second is from January to February 2020. Table 4.5 summarizes POT delivered from the J-PARC accelerator and recorded by the scintillation tracker. The data acquisition efficiency of the scintillation tracker is more than 99.9%. The inefficiency is due to the run change of the DAQ system.

The stability of the data taking of the scintillation tracker is also checked with the event rate. Figure 4.18 shows the sand muon event rate detected by the scintillation tracker. The sand muon is a muon from neutrino interactions in the upstream wall of the near detector hall. The plot shows the number of events with more than three hits in the scintillation tracker normalized by POT. The number of neutrino events should be proportional to the number of neutrinos, which expected to be proportional to POT. The averaged event rate is different between 2019 and 2020, but it is stable during each period. The difference can be attributed to the change of the beam configuration because there was a beam shut down between two periods.

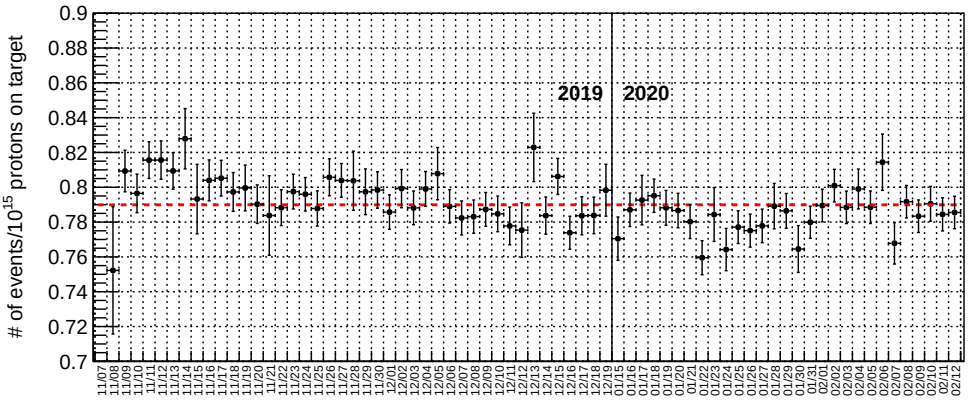

Figure 4.18: Sand muon event rate of the scintillation tracker [184].

The quality of the emulsion films is dependent on the temperature and humidity, and the operation of MPPCs are also dependent on the temperature. During the beam exposure, the ECCs, the emulsion shifter, and the scintillation tracker were operated inside a cooling shelter. Thus, stability of the temperature and humidity is essential. Figure 4.19 shows the temperature and humidity inside the cooling shelter during 2019[1]. On Nov. 28, 2019, the temperature slightly decreased because the temperature outside significantly decreased around that day. Except this drop, they were stable for the whole period.

[1] We failed to record 2020 data, but they were checked during the beam exposure and no problem was found.

Figure 4.19: Temperature and humidity inside a cooling shelter during 2019.

Chapter 5

Neutrino Event Simulation

The Monte Carlo (MC) simulation was developed for the estimation of the signals and backgrounds. The simulation is separated into three parts. JNUBEAM [188] developed by the T2K experiment is used to simulate the neutrino flux at the location of the detectors. Using the simulated neutrino flux as an input, NEUT [94] simulates the neutrino interactions on materials in the detectors. Then, the interaction of the secondary particles are simulated in the Geant4 (Geometry and tracking) [189–191]-based detector simulation. In this analysis, ν_μ and $\bar{\nu}_\mu$ interactions on water, iron, and hydrocarbon in the FHC mode beam are generated. Figure 5.1 shows an overview of the MC simulation.

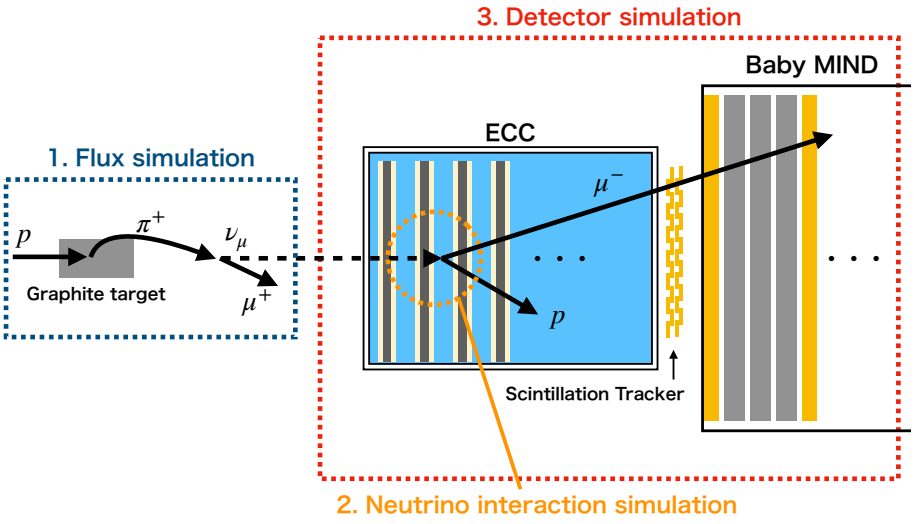

Figure 5.1: Overview of the Monte Carlo simulation.

5.1 Neutrino flux

The neutrino flux at the detector location is simulated by JNUBEAM. JNUBEAM is a custom-made Geant3 [192]-based software developed by the T2K neutrino beam group. First, the

interaction of 30 GeV protons in the graphite target is simulated by FLUKA 2011.2 (FLUktuierende KAskade) [193, 194]. The particles from the hadron interaction are then transferred into JNUBEAM, where the geometry of the beamline is constructed. In JNUBEAM, the secondary hadrons are propagated, and they interact or decay. The neutrinos are generated from the decay of the hadrons, especially charged pions. The interactions of the pions and other hadrons exiting from the target is tuned by the T2K replica target data taken by NA61/SHINE (SPS Heavy Ion and Neutrino Experiment) [195–198] and other experiments. Figure 5.2 shows the predicted neutrino flux at the location of the NINJA detectors. The mean energy of the ν_μ component is 0.89 GeV, and that of the $\bar{\nu}_\mu$ component is 1.1 GeV.

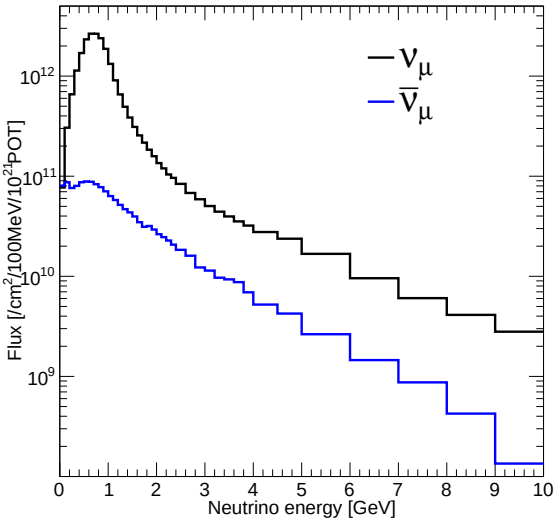

Figure 5.2: Predicted ν_μ and $\bar{\nu}_\mu$ fluxes in the FHC neutrino mode beam at the location of the NINJA detectors.

5.2 Neutrino-nucleus interaction

The neutrino flux simulated by JNUBEAM is then used to generate the neutrino-nucleus interactions inside materials. The interactions are simulated by NEUT 5.4.0.1. The ν_μ and $\bar{\nu}_\mu$ interactions on water, iron, and hydrocarbon are generated. Table 5.1 summarizes the nominal interaction models used in this analysis. The details of the models are described in Chap. 3. The SF model by Benhar *et al.* [126] is used as the nuclear model inside the nucleus for the CCQE interactions, and the axial-vector mass M_A^{QE} is set to $1.03\,\mathrm{GeV}/c^2$. For the 2p2h interactions, the model by Nieves *et al.* [123] is used. The Rein–Sehgal model [107, 108] is used for the resonant single pion production with Graczyk–Sobczyk form factor [109]. The axial-vector mass for the resonant pion production, M_A^{RES}, is set to $0.95\,\mathrm{GeV}/c^2$. The coherent pion production is simulated using the Berger–Sehgal model [117]. The DIS interaction is described by the parton distribution functions GRV98 [118] and the Bodek–Yang modification [119]. Finally, a

Table 5.1: Neutrino interaction models used in the nominal MC simulation.

Mode	Model
CCQE	Spectral Function [126] ($M_A^{\mathrm{QE}} = 1.03\,\mathrm{GeV}/c^2$)
2p2h	LFG + Nieves *et al.* [123]
Other Modes	RFG
Single Pion Production	Rein–Sehgal [107, 108] with Graczyk–Sobczyk form factor [109] ($M_A^{\mathrm{RES}} = 0.95\,\mathrm{GeV}/c^2$)
Coherent Pion Production	Barger–Sehgal [117]
DIS	GRV98 PDF [118] modified by Bodek and Yang [119]

semiclassical intranuclear cascade model is used to simulate FSI.

5.3 Detector response

After the neutrino interactions are generated by NEUT, the secondary particles are simulated by Geant4-based detector simulation. The framework is based on Geant4 version 10.6.2. Particles from the neutrino interactions are transported, and their secondary particles are also simulated. In this simulation, the cross-sectional shape of the scintillator bars is modeled as an octagon to reproduce the insensitive area due to the reflector coatings. Figure 5.3 shows the cross-sectional dimension of the scintillator bar used in the WAGASCI modules and the scintillation tracker.

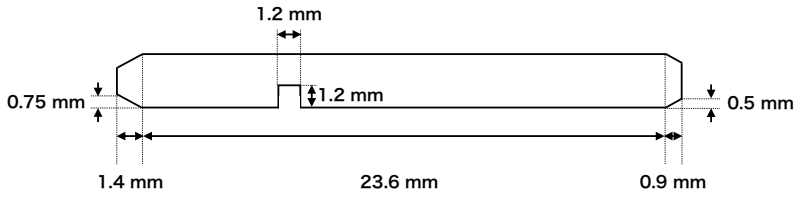

Figure 5.3: Cross-sectional dimension of the scintillator bar in the MC simulation.

The response of Baby MIND and the other detectors in the WAGASCI complex are implemented by the T2K experiment. The response of the scintillation tracker is newly added. The energy deposit by charged particles inside each scintillator bar is converted to the number of photons. First, the quenching effect of the scintillator follows the empirical formula known as Birks' law [199]. The parameter in Birks' law is measured for the scintillators used in INGRID, and the same value is used in this simulation. Then, the attenuation inside the scintillator and the WLS fiber is also simulated. The non-linearity of the EASIROC ADC is negligible in our region of interest, but that from the saturation by the number of the MPPC pixels is taken into account. Finally, the photo detection efficiency and the gain of the MPPC are considered. The two parameters are set so that the light yield distribution of the muons from the neutrino interaction in the upstream wall is consistent between the data and MC simulation as shown in Fig. 5.4. After the light yield calculation, the true position of the charged particle (x, y, z) and light yield in each scintillator are recorded. In addition to the response of the scintillators, the

dark noise of the MPPCs are added with a probability based on the measurements before the experiment.

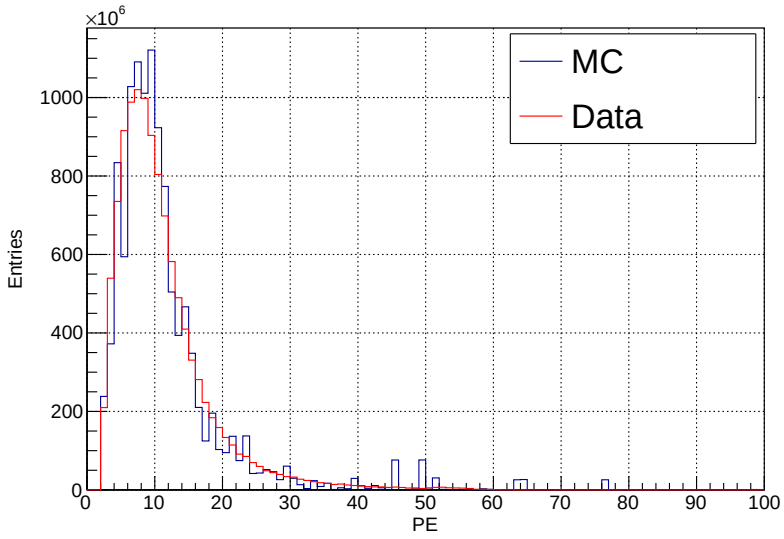

Figure 5.4: Light yield distribution for muons from the neutrino interaction in the upstream wall.

Figure 5.5 shows the schematic view of the simulation of the response of one emulsion film. In each film, two emulsion layers are sensitive to the charged particles. For simplicity, the emulsions are sensitive only to muons, protons, and charged pions in this study. When a charged particle crosses the border of the emulsion and base layers, the true position of it is obtained. Using the two positions on both sides of the base, the position and angle in one emulsion film are calculated in addition to the sum of the energy deposit inside both of the emulsion layers. The position of the particle between the upstream emulsion and base layers is treated as the true position of the particle. The angle of the particle is calculated as $\tan\theta_x = (x_2 - x_1)/70\,\mu\text{m}$, where x_1 and x_2 are the horizontal positions of the particle on the upstream and downstream sides of the base, respectively, and 70 µm is the thickness of the base. $\tan\theta_y$ is similarly calculated using the vertical positional information. Position (x, y, z), angle ($\tan\theta_x$, $\tan\theta_y$), momentum, and energy deposit in each film are recorded. Here, momentum is recorded just for reference. Although not only the emulsion films in the ECCs but also the emulsion shifter are implemented, we only use the simulated emulsion film data in the ECCs. The track detection of the emulsion shifter, or the track matching between the emulsion shifter and the scintillation tracker are mainly evaluated by the data, and the simulation is not used in those evaluations.

The detector simulation uses QGSP BERT (Quark Gluon String Precompound and the Bertini cascade model) as the default physics list. A change of the physics list leads to a slight difference of secondary interactions of the particles and thus the systematic uncertainty in the measurement of hadron kinematics. Such an uncertainty is also studied using the different physics lists. The neutrino interactions in the water layers in the ECCs are simulated as our

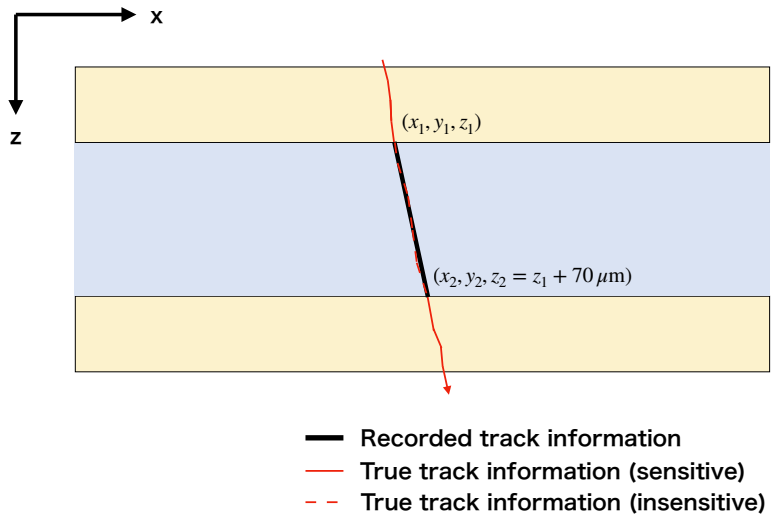

Figure 5.5: Simulation of the response of a nuclear emulsion film.

signal, and those in the iron layers in the ECCs, detectors of the WAGASCI complex, and the upstream wall of the hall are also simulated for the background study.

Chapter 6

Analysis Strategy

6.1 Analysis strategy of the NINJA experiment

The goal of the NINJA physics run is to measure the flux-averaged single-differential cross sections of the neutrino-water interactions as a function of the charged particle kinematics. To introduce methods to extract the differential cross sections, the measurement of the flux-averaged inclusive cross section is first described. This method is used in the measurement of ν_μ CC interactions on iron [168]. The flux-averaged inclusive cross section, σ, is expressed as

$$\sigma = \frac{N - N_{\mathrm{bkg}}}{\phi T \epsilon}, \tag{6.1}$$

where N is the total number of selected events in the data. N_{bkg} is the number of expected backgrounds, ϕ is the integrated ν_μ flux, and ϵ is the selection efficiency predicted by the MC simulation, and T is the total number of target nucleons. As described in Sect. 3.3, it is already known that only the inclusive cross section cannot give sufficient data to understand the neutrino interactions on nucleus. Thus, it is important to measure the differential cross sections.

There are several approaches to measure the differential cross sections. The analysis of the WAGASCI complex in Ref. [88] adopted the method using the unfolding matrix. The unfolding matrix U_{ij} represents a probability that an event in the i-th true bin is found in the j-th reconstructed bin. The matrix represents the response of the detector such as the accuracy or resolution of the momentum reconstruction. Using the unfolding matrix, the cross section is expressed as

$$\frac{d\sigma}{dx_i} = \sum_{j \in \text{reco. bins}} U_{ij} \frac{N_j - N_{\mathrm{bkg},j}}{\phi T \epsilon_j \Delta x_j}, \tag{6.2}$$

where x_i is the kinematic variables. N_j is the number of selected events in the j-th reconstructed bin, and $N_{\mathrm{bkg},j}$ and ϵ_j are the number of background events and efficiency evaluated by the MC simulation, respectively. The value is also divided by the width of the j-th reconstructed bin, Δx_j. In the analysis in Ref. [88], the unfolding matrix is calculated by the D'Agostini unfolding [200], where the matrix is iteratively calculated using the Bayesian inversion formula.

In a more sophisticated way, the latest measurements of differential cross sections in the T2K experiment are performed with an unregularized binned likelihood fitting method [82]. The NINJA experiment is also planning to use a similar method to extract the cross sections. To obtain the number of signal events in the i-th true bin, the minimization of the χ^2 function:

$$\chi^2 = -2\log(L) = -2\log(L_{\text{stat.}}) - 2\log(L_{\text{syst.}}) \tag{6.3}$$

is performed. Here, the statistical component is defined as

$$\begin{aligned}\chi^2_{\text{stat.}} &= -2\log(L_{\text{stat.}}) \\ &= \sum_{j\in\text{reco. bins}} 2\left(\beta_j N_j^{\text{MC}} - N_j + N_j \log\frac{N_j}{\beta_j N_j^{\text{MC}}} + \frac{(\beta_j-1)^2}{2\sigma_j^2}\right),\end{aligned} \tag{6.4}$$

and the systematic component is defined as

$$\begin{aligned}\chi^2_{\text{syst.}} &= -2\log(L_{\text{syst.}}) \\ &= (\vec{\mathbf{a}}_{\text{syst.}} - \vec{\mathbf{a}}^{\text{prior}}_{\text{syst.}})^T (V^{\text{cov.}}_{\text{syst.}})^{-1} (\vec{\mathbf{a}}_{\text{syst.}} - \vec{\mathbf{a}}^{\text{prior}}_{\text{syst.}}).\end{aligned} \tag{6.5}$$

The statistical component is the modified Poisson likelihood. This likelihood includes the effect from the limited statistics of the MC predicted events using the Barlow–Beeston method [201]. The numbers of selected events in the j-th reconstructed bin in the data and MC prediction are expressed as N_j and N_j^{MC}, respectively. The number of selected events in the MC prediction is expressed as the sum of the signal and background events as

$$N_j^{\text{MC}} = \sum_{i\ \in\text{true bins}} \left(c_i w_{ij}^{\text{sig.}} N_{ij}^{\text{sig.}} + w_{ij}^{\text{bkg.}} N_{ij}^{\text{bkg.}}\right), \tag{6.6}$$

where c_i is a scaling parameter for the i-th true bin, $w_{ij}^{\text{sig.}}$ and $w_{ij}^{\text{bkg.}}$ are weights accounting for the detection of the signal and background events from the i-th true bin in the j-th reconstructed bin, respectively, and $N_{ij}^{\text{sig.}}$ and $N_{ij}^{\text{bkg.}}$ are the numbers of signal and background events in the i-th true bin, contributing to the j-th reconstructed bin, in the MC prediction, respectively. The statistical uncertainty of the MC prediction is considered by including the scaling parameter;

$$\beta_j = \frac{1}{2}\left(-(N_j^{\text{MC}}\sigma_j^2 - 1) + \sqrt{(N_j^{\text{MC}}\sigma_j^2 - 1)^2 + 4N_j\sigma_j^2}\right), \tag{6.7}$$

where σ_j is the relative variance of N_j^{MC}. In the systematic component, vectors of the systematic uncertainties before and after the fitting are represented as $\vec{\mathbf{a}}^{\text{prior}}_{\text{syst.}}$ and $\vec{\mathbf{a}}_{\text{syst.}}$, respectively, and the covariance matrix is written as $V^{\text{cov.}}_{\text{syst.}}$. The number of signal events in the i-th true bin in the data is obtained by minimizing the likelihood in Eq. (6.3). Using the values, the differential

cross section is extracted as follows:

$$\frac{d\sigma}{dx_i} = \frac{N_i^{\text{sig.}}}{\phi T \epsilon_i \Delta x_i}, \tag{6.8}$$

where $N_j^{\text{sig.}} = \sum_{i \in \text{true bins}} c_i w_{ij}^{\text{sig.}} N_{ij}^{\text{sig.}}$.

In the case of the NINJA experiment, x_i is not only the muon momentum and angle, p_μ and $\cos\theta_\mu$, but also that of the protons or charged pions, p_p, $\cos\theta_p$, p_π, $\cos\theta_\pi$, and so on. Owing to the high detection efficiency for the charged hadrons, it will be also intriguing to measure the differential cross section as a function of the transverse kinematic imbalances with a new phase space which has not been covered by the other detectors. In addition to the differential cross section as a function of the kinematics, the measurement of the cross sections separated by the final state topology is also important to understand the neutrino interactions, i.e. x_i represents the number of charged particles. The measurements based on the final state topology are less model-dependent than that based on the interaction modes such as CCQE or CCRES. Since the ECC has a high detection efficiency for a large phase space of the charged hadrons, especially in the low-momentum region, the measurement of CC0π1p events will be more strongly related to that of CCQE, and that of CC1π1p will give a new information about CCRES.

6.2 Analysis in this thesis

According to the description above, we need to evaluate items below to obtain the differential cross section.

- The number of events in each reconstructed bin
- The detection efficiency for the charged particles
- The detector performance such as the momentum resolution
- The estimation of the background events
- The systematic uncertainties and its correlations

Although the goal of the NINJA experiment is the measurement of the differential cross sections, statistics are still not sufficient as described in Chap. 8. Moreover, we would like to get the detailed information on the detector performance and the systematic uncertainties. Thus, in this thesis, we focus on the comparison of the distributions of the reconstructed kinematics between the data and MC prediction. In the MC prediction, the detection efficiency and reconstruction flow are the same as used in the analysis of the data. The comparison gives more direct information of the detector performance, and the interpretation of differences between the data and MC prediction would be simpler.

In the following chapters, the analysis methods and the preliminary result of the measurement of the ν_μ CC interactions on water in the NINJA physics run are reported. In the physics run,

we introduce a new set of the detectors as described in Chap. 4. In addition to the detectors, the analysis methods are highly improved from the previous ones used in the NINJA experiment. The analysis procedure is as follows. Figure 6.1 shows the schematic diagram of the analysis flow.

(1) Tracks of charged particles are reconstructed in each detector. (Chap. 7)

(2) The reconstructed tracks in Baby MIND are identified as muon candidates and connected to the upstream detectors using the emulsion shifter and the scintillation tracker. (Chap. 7)

(3) The muon candidates starting from the inside of the ECC are selected, and the starting points are considered as the neutrino interaction vertices. (Chap. 8)

(4) The hadron tracks from the interaction vertex are collected. The hadron tracks are also called "partner tracks." (Chap. 8)

(5) The momentum reconstruction is applied to each track from the neutrino interaction. After that, the PID are applied to the hadron tracks. (Chap. 9)

(6) Distributions of the reconstructed kinematics are compared to those of the MC prediction with the estimation of the background and the evaluation of the systematic uncertainties. (Chap. 10)

In the track matching in step (3), the scintillation tracker is newly introduced as one of the timestamp detectors. The development of the track matching between the scintillation tracker and Baby MIND, and the performance of it are described in Sect. 7.3. The scintillation tracker has a special arrangement of the plastic scintillator bars, and the reconstruction algorithm takes it into account to improve the positional resolution.

The other main topic of this thesis is the momentum reconstruction method in step (5). The momentum reconstruction using multiple Coulomb scatterings in the ECC has been used in the NINJA experiment, and the method is improved in this study. The new method is based on the maximum likelihood to consider the energy deposit of a charged particle inside the detector volume, and the treatment of the angular information used in the method is modified. The detailed information of the method is described in Sect. 9.2.2

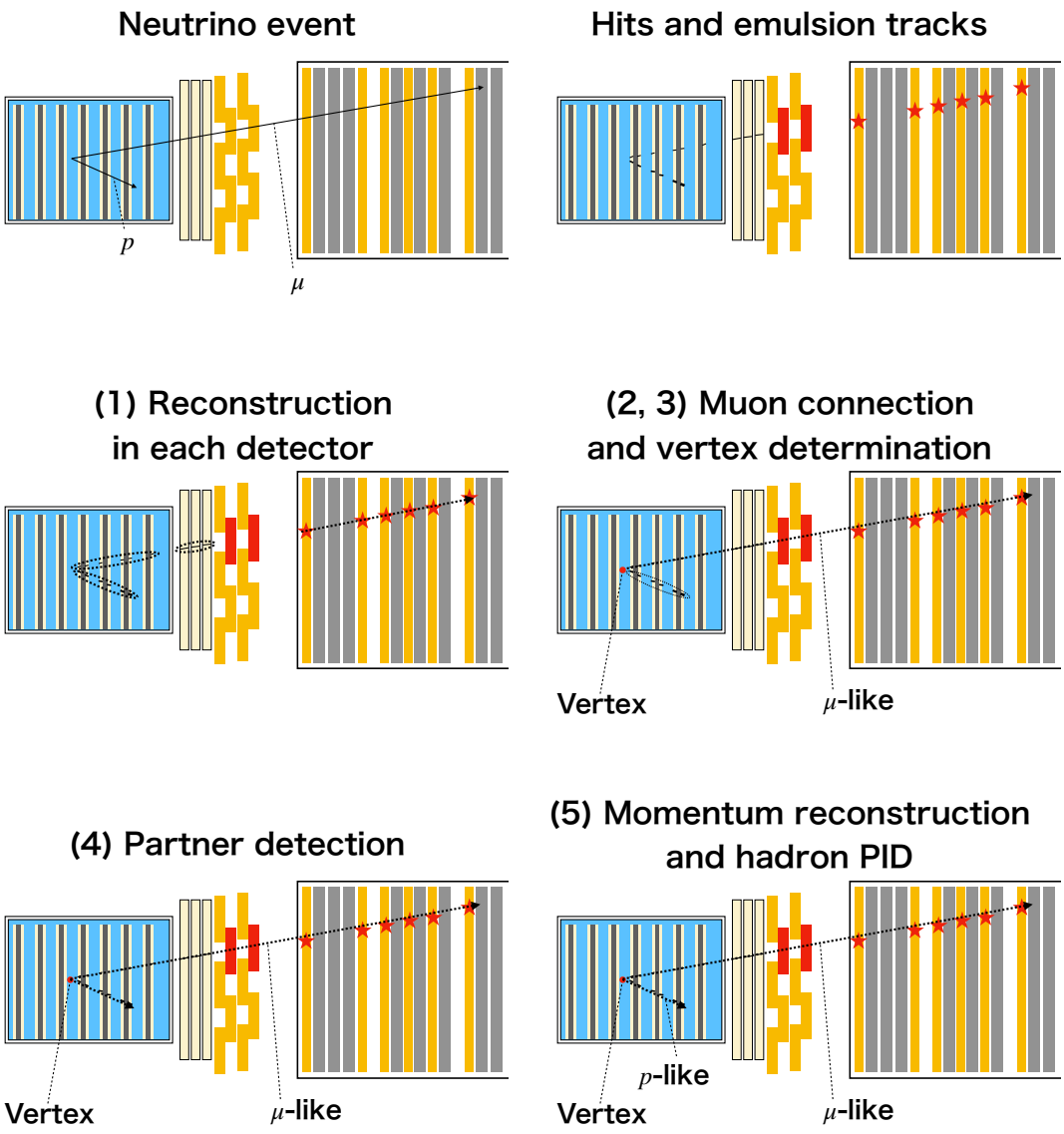

Figure 6.1: Schematic diagram of the analysis flow for a CC0π1p event. Charged particles (upper left) induce hits in the scintillator detectors and tracks in the emulsion films (upper right). The tracks of the particle are reconstructed in each detector (middle left), and the muon candidate is extrapolated to the upstream detectors (middle right). The most upstream point of the muon candidate is regarded as the interaction vertex. Then, the hadron tracks attached to the vertex are searched for (bottom left). Finally, the PID for each hadron is performed as well as the momentum reconstruction (bottom right).

Chapter 7

Track Reconstruction

To reconstruct the neutrino interaction event inside the ECC, track reconstructions inside the ECC and Baby MIND are performed. To match tracks between the detectors, the track matching is then carried out using the emulsion shifter and the scintillation tracker. This chapter describes the method of the track reconstruction, as well as the track matching between the detectors.

7.1 Track reconstruction in the ECC

After the beam exposure, the emulsion films underwent the following processes and then were scanned.

(1) **Development**
After the beam exposure, the emulsion films were developed. First, the films were soaked into a developing solution, and silver ions in the AgBr crystals were deoxidized. Such silver ions were absorbed by silver latent images to make visible silver grains. When the silver grains grew large enough to be observed by microscopes, then the films were soaked into an acid solution to stop the deoxidization. Without this stopping procedure, noise grains by random chemical reactions would be also grown up, and track recognition would be difficult. Then, the rest of the AgBr crystals were eluted in the fixing process, and finally the films were put into running water to remove all remaining chemicals.

(2) **Silver removal**
After the development process, extra silver grains were deposited on the surface of the emulsion films. To scan the emulsion films with a microscope, such silver grains have to be removed; otherwise tracks are hard to be detected. The both surfaces of the emulsion films were wiped out by tissues with ethanol.

(3) **Swelling**
After the development and silver removal processes, the thickness of the emulsion films became about half of that during the beam exposure. This is because almost all AgBr crystals, which are the main component of the nuclear emulsion, were removed during the fixing process. The difference of the thickness distorts the angle of the tracks recorded during

the beam exposure. Moreover, as described in Sect. 7.1.1, to keep sufficient speed and high detection efficiency, the scanning system requires a certain thickness of the emulsion films. Thus, the thickness was restored by the swelling process. The emulsion films were soaked into water, and then the water was replaced by a glycerin solution. The focal depth of the track scanning system, Hyper Track Selector (HTS) [202], is around 4 µm, and the track reconstruction uses 16 tomographic images. Thus, the expected thickness is around $4\,\mu\text{m} \times 16 = 64\,\mu\text{m}$.

7.1.1 Scanning of the emulsion films

The emulsion films were scanned with HTS at Nagoya University. To extend the angular acceptance from $|\tan\theta| < 1.3$ to $|\tan\theta| < 4.0$, where θ is a track angle with respect to the z direction, a new method has been developed for the NINJA physics run [203]. As defined in Sect. 4.1.2, the z direction is perpendicular to the film surface. In the conventional method, the track recognition and reconstruction had been done simultaneously by HTS. However, in the new method, HTS only recognizes the tracks, and the raw data are recorded in the storage servers. After the data are recorded in the servers, the track reconstruction is applied separately. This reduces the duration of scanning one film. Because the operation time of HTS is limited, it is crucial to maintain the process speed. In addition, the track reconstruction in the new method is independent from the manual operation of HTS, and thus the longer time can be used for the track reconstruction. Therefore, a more sophisticated method is applied in the track reconstruction, and high angular accuracy and good S/N are achieved.

For each emulsion gel layer, HTS takes 32 tomographic images with a 2-µm pitch for a 62-µm thickness. Each image is composed of $0.45\,\mu\text{m} \times 0.45\,\mu\text{m}$ image pixels. After the binarization and marginalization of the pixels, when the brightness of a pixel exceeds a threshold value, the pixel is defined as a hit pixel. The track is detected by shifting the tomographic images by a certain shift d so that the hit pixels are aligned in the z direction. In such a case, the angle of the track in the x-z or y-z plane is determined as $\tan\theta = d/L$, where L is the thickness of the emulsion gel layer. Therefore, the angular acceptance of HTS can be expressed as $|\tan\theta| < D/L$, where D is the maximum value of shift. To extend the angular acceptance, a larger D or a smaller L is required. However, the number of calculations is proportional to D^2, while a smaller L results in lower track recognition efficiency since there are a smaller number of silver grains detected. In the new method, to reconstruct a track in one emulsion gel layer, 16 appropriate tomographic images are selected out of 32. This method maintains wide angular acceptance and high recognition efficiency.

A track in the emulsion gel layer is called a "microtrack." Out of 32 tomographic images, 16 even-(odd-)numbered or inner (outer) binarized images are selected as shown in Fig. 7.1. Small-angle microtracks ($|\tan\theta| < 2.25$) are recognized using 16 even-(odd-)numbered images which correspond to $L = 60\,\mu\text{m}$ and $D = 135\,\mu\text{m}$, while large-angle microtracks ($|\tan\theta| < 5.4$) are recognized using 16 inner (outer) images which correspond to $L = 30\,\mu\text{m}$ and $D = 162\,\mu\text{m}$. Using two different patterns of 16 tomographic images, the angular acceptance can be extended. However, the two patterns show different angular accuracy since they use different configurations.

As described in Sect. 7.1.2, performance of our analysis is dependent on the accuracy of the microtracks. It is important to have similar and better accuracy for the both patterns of the microtrack. Thus, the track fitting is applied after the track recognition.

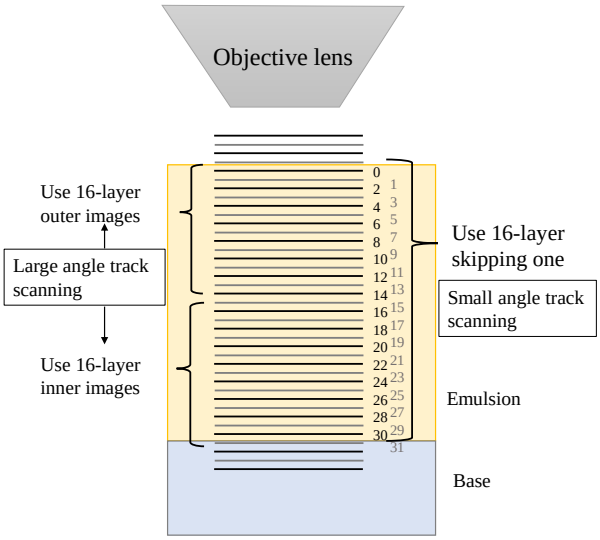

Figure 7.1: Schematic view of 32 tomographic images for a use in the new scanning method [203].

When a microtrack is recognized, it has a positional information of the pixels and the angular information obtained as $\tan\theta = d/L$. The hit pixels along the microtrack are searched for using the positional and angular information from the 16 even-numbered tomographic images. While the track recognition uses different patterns of the tomographic images, the track reconstruction uses only 16 even-numbered tomographic images. Thus, the accuracy of the microtracks can be described by one model for all the patterns. The hit pixels are fitted by a linear function several times using the previous fit results as inputs. After the five-time iterations, the results are almost converged, and the position and angle of the microtracks are determined with sufficient angular accuracy. The angular accuracy of the microtracks after the iterations is shown in Fig. 7.2. After the five-time iterations, the angular accuracy almost converges, and it is sufficient for the track reconstruction in emulsion films described in Sect. 7.1.2. Figure 7.3 shows an example of a recognized microtrack and selected pixels for the fitting.

7.1.2 Track reconstruction in an emulsion film

After the microtracks are recognized and reconstructed, a "basetrack" is reconstructed from a pair of microtracks in the two emulsion gel layers in an emulsion film. The analysis of the nuclear emulsion films is done using the basetracks since the angle of microtracks is not the same as during the beam exposure. This is because the emulsion gel layers distort or shrink by the temperature or humidity fluctuation and the pressure during the beam exposure, and the development and swelling processes. On the other hand, the angle of basetracks, calculated by connecting the edges of two microtracks on the base, preserves its value during the beam

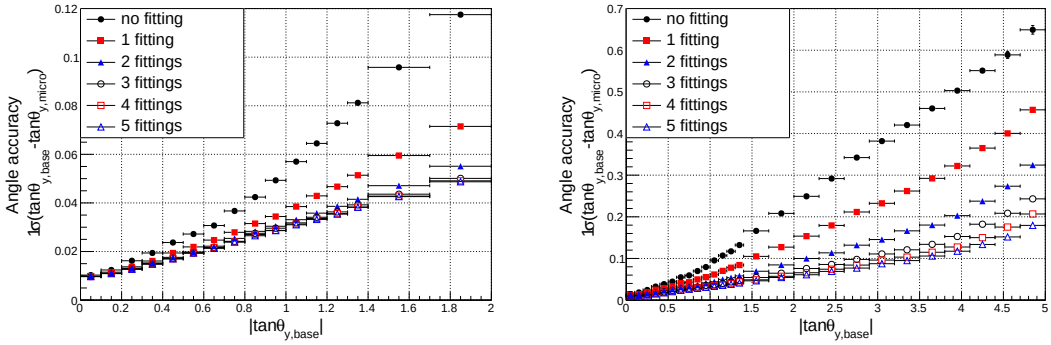

Figure 7.2: Angular accuracy of the microtracks after fitting iterations. The microtrack recognized using 16 even-(odd-)numbered binarized images (left) and that recognized using 16 inner (outer) images (right) both converge after five-time iterations [203].

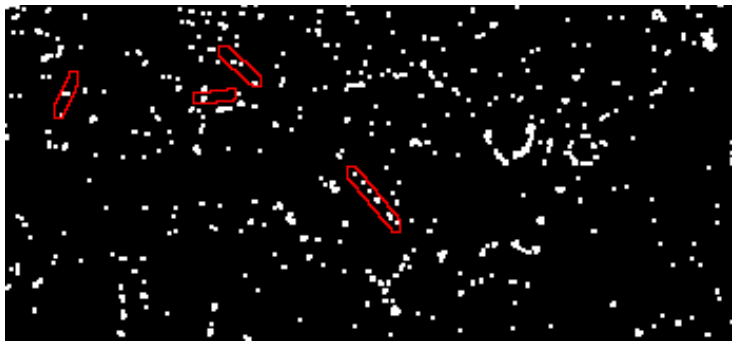

Figure 7.3: Binarized image in an emulsion film of a 155 µm × 72 µm area. The central red circle represents selected pixels in the linear fitting of a microtrack caused by a minimum ionizing particle. The other circles represent noise contributions [203].

exposure, and development and swelling processes because the thickness of the polystyrene base does not change as much as that of the emulsion gel. In addition, the base is thicker than the emulsion gel, and it also leads to the better angular accuracy. The coincidence of two microtracks also reduces the noise tracks and improves S/N. Figure 7.4 shows the relation between a pair of microtracks and a basetrack.

After the correction of the distortion and shrink of the microtracks due to the reasons mentioned above and the difference of diffraction indices between the air and the optical system of HTS, pairs of microtracks are created. The angles of microtracks and a basetrack in the x-z or y-z plane are represented as $\theta_{\mathrm{micro1(2)}}$ and θ_{base}, respectively, as shown in Fig. 7.4. When the all angular differences of microtracks and basetrack is less than $0.05 + 0.15 \times \tan\theta_{\mathrm{base}}$, they are connected to reconstruct a basetrack. This criterion is determined from the accuracy of the microtracks so that more than 5σ of the angular differences are allowed.

In order to reduce noise basetracks, the angular difference in the lateral direction is also checked. The track direction projected onto the x-y plane is called the radial direction, and the

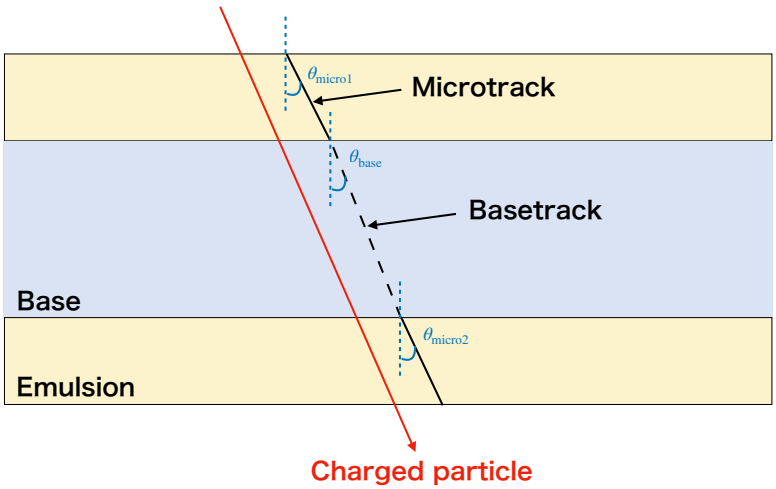

Figure 7.4: Pair of microtracks and a basetrack in an emulsion film.

lateral direction is perpendicular to the radial direction and z direction. In the lateral view, the angle of the tracks is always zero, and the angular accuracy is independent of $\tan\theta_{\text{base}}$. Thus, a cut with better S/N can be applied in this view. When the difference of $\tan\theta$ between microtracks and a basetrack in the lateral direction is larger than 0.05, such a basetrack is rejected. The lateral and radial directions are defined as shown in Fig. 7.5.

Finally, to further reduce noise basetracks attributed to the coincidence of the noise microtracks, a "ranking cut" is applied to each track. The ranking cut uses Volume Pulse Height (VPH) and the linearity of the track. VPH is a value strongly correlated to the number of hit pixels in two microtracks in the basetrack. Since it is almost proportional to the number of silver grains in the emulsion gel layers, VPH indicates dE/dx of the charged particle. The linearity of the track is defined from the angular differences between the microtracks and basetrack in the lateral and radial directions. When VPH is small and the linearity is large, such a basetrack is likely to be attributed to the chance coincidence of low-energy electron tracks from environmental radioactivity or random noise. Therefore, such tracks are rejected. After the ranking cut, the basetrack recognition efficiency is maintained to be more than 98% while the number of noise tracks is reduced by a factor of four.

Due to the limitation of HTS, only around a 10.0 cm × 12.5 cm area can be scanned at once. Since the size of one emulsion film is 25 cm × 25 cm, one film has to be scanned six times to cover the whole area. To treat one film simultaneously, six areas are merged by comparing the basetracks in overlapped regions. Track pairs in the neighboring areas with the positional difference less than 10 µm and the difference of $\tan\theta$ less than 0.03 are regarded as of the same particle. By shifting and rotating the relative position of each area, we get the affine parameters with the maximum number of coincided track pairs. After all tracks are set in the same coordinate, a fine tuning of position is also applied to further minimize the difference of the positions. Then, the tracks in overlapped areas are checked, and multiple tracks are merged into one track.

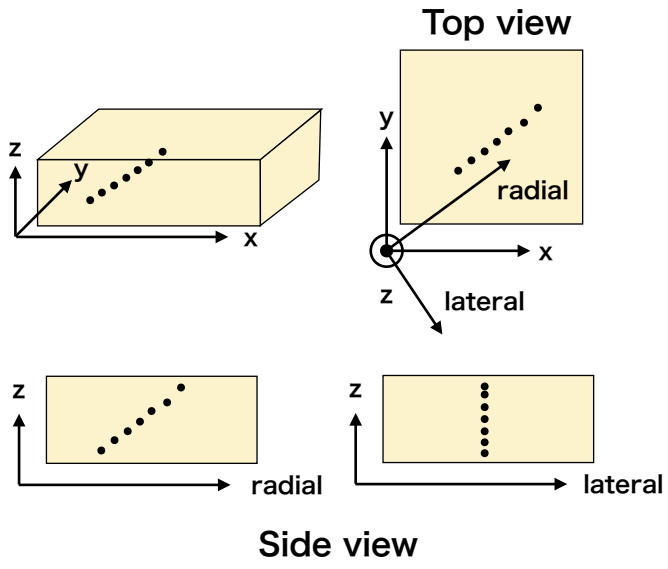

Figure 7.5: Lateral and radial directions. The dots indicate silver grains of a track.

7.1.3 Track connection between the emulsion films

7.1.3.1 Alignment

After the basetrack reconstruction in each emulsion film, a connection process between the films is applied. First, the relative positions and angles between each pair of films during the beam exposure are obtained. This process is called "alignment." It is not easy to get the final alignment parameters at once. Thus, the parameters are approximated one by one and eventually have sufficient precisions. The basic concept of the alignment and the track connection is the same as NETSCAN [204].

Firstly, the two films are assumed to be parallel to each other, and the transformation of positions and angles in the upstream film into the coordinate of the downstream film is calculated. This transformation can be decomposed to the two-dimensional (x, y) linear transformation and the z shift as shown in Eqs. (7.1) and (7.2):

$$\begin{pmatrix} x' \\ y' \\ z' \end{pmatrix} = A \begin{pmatrix} \cos\alpha & -\sin\alpha & 0 \\ \sin\alpha & \cos\alpha & 0 \\ 0 & 0 & 1 \end{pmatrix} \begin{pmatrix} x \\ y \\ z \end{pmatrix} + \begin{pmatrix} dx \\ dy \\ dz \end{pmatrix}, \tag{7.1}$$

$$\begin{pmatrix} \tan\theta_{x'} \\ \tan\theta_{y'} \\ 1 \end{pmatrix} = \begin{pmatrix} \cos\alpha & -\sin\alpha & 0 \\ \sin\alpha & \cos\alpha & 0 \\ 0 & 0 & 1 \end{pmatrix} \begin{pmatrix} \tan\theta_x \\ \tan\theta_y \\ 1 \end{pmatrix} + \begin{pmatrix} d\tan\theta_x \\ d\tan\theta_y \\ 0 \end{pmatrix}. \tag{7.2}$$

Here, A represents a film scaling in the x and y directions, and α is a relative rotation angle.

dx, dy, and dz are the shifts in each direction of position, and $d\tan\theta_x$ and $d\tan\theta_y$ are the shifts in each direction of angle.

Next, the process above is applied to local areas. The positional shift of the emulsion films or scaling cannot be expressed by a linear transformation in a 25 cm × 25 cm area since the shrink and distortion are not uniform in such a large area. In the NINJA physics run, the alignment parameters are calculated in each 2 mm × 2 mm local area of the films. In addition, the angular shrink is not fully corrected in the aforementioned alignment since the thicknesses of the bases can differ between the scanning processes of each film. In order to consider such an effect, the scaling of the thickness of the base is added to Eq. (7.2):

$$\begin{pmatrix} \tan\theta_{x'} \\ \tan\theta_{y'} \\ 1 \end{pmatrix} = B \begin{pmatrix} \cos\alpha & -\sin\alpha & 0 \\ \sin\alpha & \cos\alpha & 0 \\ 0 & 0 & 1 \end{pmatrix} \begin{pmatrix} \tan\theta_x \\ \tan\theta_y \\ 1 \end{pmatrix} + \begin{pmatrix} d\tan\theta_x \\ d\tan\theta_y \\ 0 \end{pmatrix}. \tag{7.3}$$

Here, B represents the angular shrink, or the scaling of the thickness of the base.

So far, the two films are assumed to be parallel in the alignment process, but they are actually tilted to each other. Finally, alignment in the three-dimensional space is applied. This alignment can be expressed as

$$\begin{pmatrix} x' \\ y' \\ z' \end{pmatrix} = Q \begin{pmatrix} S_x & 0 & 0 \\ 0 & S_y & 0 \\ 0 & 0 & S_z \end{pmatrix} \begin{pmatrix} 1 & H_{yx} & H_{zx} \\ 0 & 1 & H_{yz} \\ 0 & 0 & 1 \end{pmatrix} \begin{pmatrix} x \\ y \\ z \end{pmatrix} + \begin{pmatrix} dx \\ dy \\ dz \end{pmatrix}, \tag{7.4}$$

where Q is an orthogonal matrix representing rotations around three axes, S_x, S_y, and S_z represent scalings in each direction, and H_{yx}, H_{zx}, and H_{yz} represent shears between each pair of axes. S_z, H_{zx}, and H_{yz} are already adjusted in the alignment described above, thus they are set to $S_z = 1$, $H_{zx} = 0$, and $H_{yz} = 0$, respectively. More detailed information of the alignment can be found in Ref. [205].

7.1.3.2 Track connection

Basetracks of one charged particle are recorded in each emulsion film. Since the nuclear emulsion does not provide timing information and there exists the inactive water region in the ECC, basetracks induced by the same particle are not clustered as they are. The basetracks in each film need to be connected using positional and angular information of each track. After the alignment process, tracks in two emulsion films are in the same coordinate, thus the positional and angular differences are available. In the NINJA physics run, tracks not only in adjacent films but also skipping one or two films are connected. The criteria of connection of two basetracks are based on the positional and angular differences in the x and y directions and also the lateral and radial directions. The allowances are set in consideration of the positional and angular accuracies, and the scattering of MIPs. The connected pair of basetracks is called a "linklet."

The linklets in one ECC are clustered from the downstream to upstream if they have base-

tracks in common. This collection of the basetracks is called a "chain," and a set of basetracks in all linklets sharing basetracks is called a "group." The group sometimes has a large number of chains attributed to different particles. Such groups are deconvoluted into chains using a graph theory. One linklet is treated as an undirected graph with two nodes of the basetracks and one edge of the connection. After the deconvolution, each chain is regarded as a track of one charged particle in our analysis. The detailed information of the deconvolution is described in Ref. [205]. Figure 7.6 shows the linklet, chain, and group.

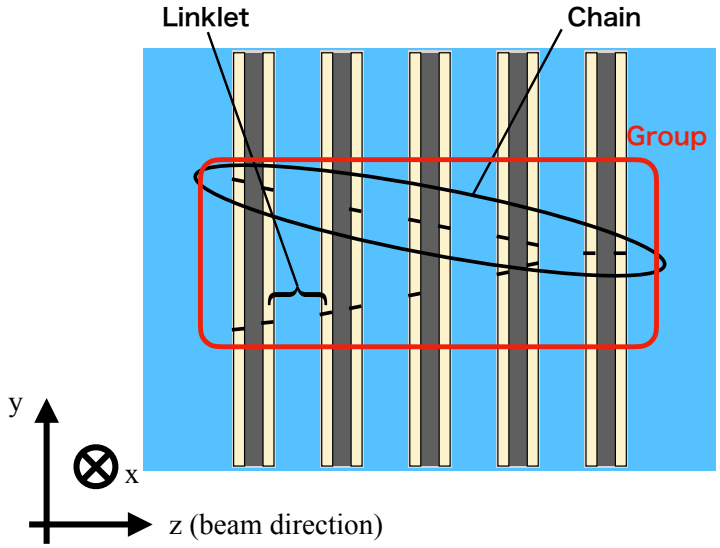

Figure 7.6: Linklet, chain and group.

After the chains are produced and deconvoluted, the most upstream and downstream basetracks of all chains are selected, and they are connected again. Before this process, noise tracks are already reduced since the basetracks are required to be connected with the alignment during the beam exposure, and the connection can be applied with high S/N. Thus, to acquire high chain reconstruction efficiency, the reconnection of chains is applied with looser connection allowances. In addition, the tracks are connected skipping at most not only two but five films.

7.1.3.3 Penetrate check

Although we apply several processes to reduce noise and achieve high chain reconstruction efficiency, some basetracks induced by the same particle are still not connected only with these processes. In particular, basetracks of particles largely scattered during their flight inside the ECC or low-momentum particles sometimes fail to be connected. In our analysis, when a muon from the neutrino interaction is largely scattered inside the ECC, the interaction cannot be correctly identified. In addition, when a muon from the external neutrino interaction largely scattered inside the ECC, it is mis-identified as the neutrino interaction with a back-scattered particle. Thus, upstream of the most upstream basetrack of chains identified as a muon candidate is checked in an event display. If there is another chain with the most downstream basetrack

satisfying the opening angle less than 0.3 rad and the minimum distance less than 200 µm, such a chain is additionally connected to the chain identified as a muon candidate.

When the chains are identified as a proton and seem penetrating near the neutrino interaction vertex candidate, such chains are also checked in detail. Using the reconstructed momentum, VPH, and topological information, they are classified into background or signal tracks.

7.1.4 Efficiency of the emulsion films

The efficiency of each emulsion film is estimated using the reconstructed chains. The basetrack reconstruction efficiency is affected by damaged areas in a film, failure of scanning, distortion of emulsion, and contamination of materials. To evaluate the efficiency in one film, chains satisfying the conditions below are selected.

- Chain penetrating the upstream two and downstream two emulsion films.
- Chain penetrating more than four iron plates.
- Chain with the standard deviation of angular differences in the lateral direction less than 2 mrad.

The last condition is to select high-momentum MIPs. Using these chains, the basetrack in one downstream emulsion film is extrapolated to the evaluated film as a prediction track. Then, the ratio of the number of basetracks with the same position and angle with the prediction track to that of all prediction tracks are defined as the basetrack reconstruction efficiency. Figure 7.7 shows the basetrack reconstruction efficiency as a function of angle. It is higher than 96% for all angular region, and the averaged value is 98%.

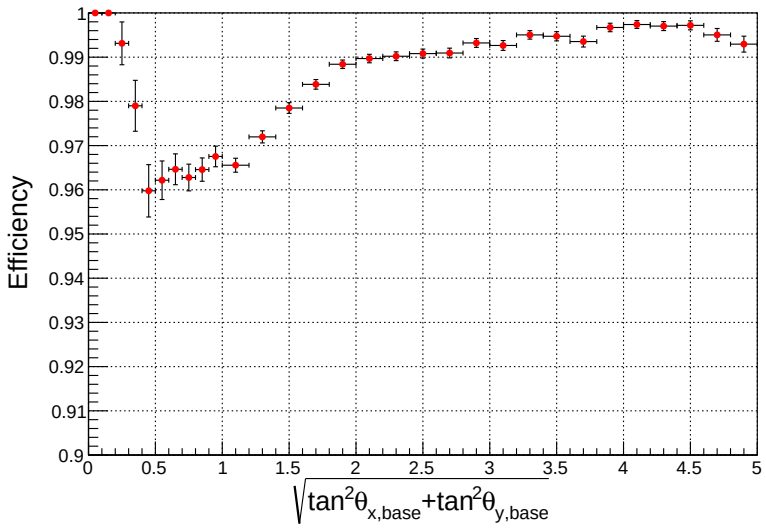

Figure 7.7: Angular dependence of the basetrack reconstruction efficiency.

It is also necessary to consider the chain reconstruction efficiency. By connecting tracks between not only adjacent films but also skipping several emulsion films, the chain reconstruction efficiency is maintained to be high. Moreover, thanks to the chain reconnection and penetrate check processes, the chain reconstruction efficiency is almost 100%, and the inefficiency is negligible.

7.2 Track reconstruction in Baby MIND

To select the ν_μ CC interactions in the ECC, the tracks in Baby MIND are used. The track reconstruction method in Baby MIND is the same as the neutrino interaction analysis in the T2K experiment using the WAGASCI complex. Each hit in Baby MIND has both ADC and TDC information. The ADC information corresponds to the light yield and thus energy deposit in each scintillator bar, while the TDC information is a hit timing in each spill. The hits are clustered and a muon track is reconstructed as follows.

(1) **Time clustering**
All hits in a spill are organized in the order of TDC value, and each hit is put into a time cluster following the order. When the difference of the TDC value between two neighboring hits is larger than 100 ns, the hits are separated into different time clusters. This process reduces the contamination of noise hits.

(2) **Hit clustering**
In Baby MIND, the neighboring scintillator bars in the same plane have an overlapped region. Besides, an optical cross-talk between the neighboring scintillators sometimes produces an additional hit. Thus, hits in neighboring scintillators are put into the same hit cluster.

(3) **Two-dimensional track reconstruction**
The two-dimensional track reconstruction based on the cellular automaton tracking algorithm [206, 207] is applied to the hit clusters. The tracks in the x-z and y-z views are separately reconstructed in this step.

(4) **Three-dimensional track reconstruction**
A pair of the two-dimensional reconstructed tracks in the x-z and y-z views is converted into a three-dimensional track. If the difference of the upstream z-positions of the two-dimensional tracks is smaller than 150 mm and that of the downstream z-positions is smaller than 350 mm, they are combined into a three-dimensional track.

(5) **Upstream plane cut**
Our target is the ν_μ CC interactions in the ECC, thus the muon comes from the upstream of Baby MIND. To reduce the muon tracks from the neutrino interactions in Baby MIND, we finally require the three-dimensional tracks to have hits in either of the first two planes.

7.3 Track matching between the NINJA detectors

In order to analyze the ν_μ CC interactions in the NINJA experiment, the muon tracks in the ECC and Baby MIND need to be connected. The track matching gives the muon identification and beam-timing information. The track matching between the ECC and Baby MIND is applied using the timestamp detectors.

7.3.1 Track reconstruction in the emulsion shifter

The emulsion shifter provides excellent positional and angular information of nuclear emulsion films as well as the four-hour timing information. The emulsion shifter has a fixed wall, two moving walls, Tracker Special Sheet (TSS), and Outside Special Sheet (OSS) to connect tracks from the downstream scintillator detectors to the upstream ECC.

7.3.1.1 Reconstruction in each wall and special sheets

The tracks in each wall and TSS are reconstructed as follows. The size of an emulsion film used in the emulsion shifter is 102 cm × 34 cm, which is one of the largest in recent years. We separate each film into three parts, a 49 cm × 34 cm area in the middle and two 28 cm × 34 cm areas in the edges, and each area corresponds to each ECC. The former area is separated into 16 scanning areas, and the latter ones into 12 scanning areas. The scanning and basetrack reconstruction in the emulsion shifter are the same as in the ECC, but the angular acceptance is limited to $|\tan\theta| < 2.0$ since it focuses only on forward-going muon tracks. After the basetrack reconstruction, the scanning areas are merged into each ECC area using the similar method to the ECC. In addition, the OSSs are also scanned with the emulsion shifter. The size of a film used for the OSS is 33 cm × 28 cm, and it is separated into nine scanning areas.

Three films are vacuum-packed in the moving walls, and four films in the fixed wall, TSS, and OSS. In each wall or Special Sheet (SS), the alignment parameters are calculated as described in Sect. 7.1.3.1. In the emulsion shifter, the scaling of the thickness of the base and tilt between two emulsion films are not necessarily considered since the goal of the emulsion shifter is not to precisely measure the basetrack position and angle but to connect muon tracks among the detectors. After the alignment process, linklets are formed using the positional and angular differences in the lateral and radial directions.

The detection efficiency of each film is at least 90%. In order to improve the detection efficiency and to reduce noise tracks, tracks in the different films in the same wall are combined. As for the moving walls, tracks are selected if two or more films have tracks. The overall track detection efficiency in the moving wall is expressed as

$$E = e^3 + 3e^2(1 - e), \tag{7.5}$$

where e is the detection efficiency of each film, and E is the overall efficiency. When $e = 0.9$, Eq. (7.5) results $E = 0.972$. When there is a basetrack in the most upstream film, the position and angle of the basetrack are regarded as those in the moving wall, while if there is not a

basetrack, the second upstream basetrack is extrapolated to the most upstream film location. On the other hand, in the fixed wall and SSs, tracks are selected if two or more films have tracks except the case that only the downstream two films have tracks. The overall track detection efficiency in this case is expressed as

$$E = e^4 + 4e^3(1-e) + 5e^2(1-e)^2. \tag{7.6}$$

When $e = 0.9$, Eq. (7.6) results $E = 0.988$. In addition, this selection requires a coincidence of two or more films, thus the noise tracks are reduced by this treatment.

Each wall or SS has three or four films. Since the multiple films are combined and each wall or SS has one track information for one particle, the track reconstruction between them is much simpler.

7.3.1.2 Wall connection and timestamp analysis

The alignment of the fixed wall and the moving walls gives the timing information as the shift of the positional differences. The concept of the positional relationship among the films in the emulsion shifter is shown in Fig. 7.8. During the beam exposure, the particles penetrate along a straight line and leave tracks in the walls. After the scanning of the films, they are observed to have a certain shift of the horizontal positional differences between the fixed wall and the moving walls.

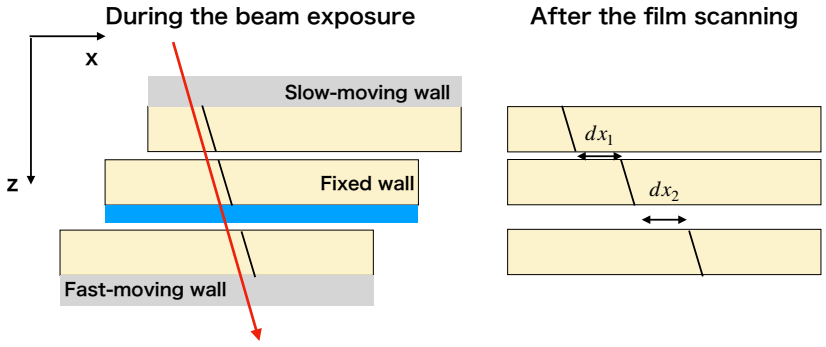

Figure 7.8: Concept of the positional relationship among the films in the emulsion shifter. The left figure shows the films during the beam exposure, and the right shows what we obtain after the film scanning.

Figure 4.13 shows the positional differences between the fixed wall and the moving walls. Since the moving walls move by 2 mm in every four hours and four days, they have a spot structure. The slow-moving wall moves 25 steps, and each spot corresponds to the tracks accumulated during four days. The fast-moving wall is reciprocating during the beam exposure and moves 24 steps in one stroke. Each spot in the fast-moving wall corresponds to the tracks accumulated during 100 hours (4 hours $\times$ 25 repetitions).

To calculate the alignment between the walls, tracks are assorted spot by spot. Tracks in

each spot are cut by a circle with a radius of 600 µm in the two-dimensional positional difference space. Using the tracks inside the circle, the alignment parameter for each spot is calculated. In addition, the gap between the fixed wall and the fast-moving wall changes during the beam exposure, thus additional correction of the gap distance is applied for the fast-moving wall. After the alignment, linklets are made from the tracks in each wall. It should be noted that these linklets are not the connection of the basetracks but that of the reconstructed tracks in each wall. Up to this point, the tracks in the fixed wall are connected to those in the two moving walls and have four-hour timing information expressed as a pair of spots.

Then, the alignment between the fixed wall and TSS, and that between the fixed wall and OSS are calculated. In this calculation, the films are not moving, thus the alignment can be simply obtained. Using the alignment parameters, the tracks in the fixed wall and TSS or OSS are connected. The tracks in TSS are used in the connection with the scintillator detectors since TSS is attached on the upstream surface of the scintillation tracker and the distance is short. On the other hand, the tracks in OSS are used in the connection with the ECC. The tracks in OSS are firstly connected to the tracks in Inside Special Sheet (ISS) and then to the downstream films in the ECC.

7.3.2 Reconstruction and track matching between the scintillation tracker and Baby MIND

The three-dimensional reconstructed track in Baby MIND is first matched with the hit information of the scintillation tracker. Since the DAQ systems of both detectors are triggered with the beam trigger signal, the matching is almost free from cosmic background. This track matching gives more precise information of position and angle than that obtained from only Baby MIND.

7.3.2.1 Hit clustering in the scintillation tracker

As described in Sect. 4.4.3.2, the scintillation tracker reconstructs position by the pattern of hit scintillator bars. The hit threshold of each scintillator bar is set at 2.5 p.e., and at least one hit is required in each module. The hits in the scintillation tracker are clustered in the horizontal and vertical modules separately. One cluster is matched to one three-dimensional track in Baby MIND horizontally or vertically. As shown in Fig. 7.9, when hit scintillator bars are overlapped viewed from the z direction, they are classified into the same cluster; otherwise they are separated into different clusters. Assuming the particle penetrating the module perpendicularly, the position of each cluster is tentatively reconstructed as the averaged value of the straight line which satisfies the hit pattern of the cluster as shown in Fig. 7.10. When the perpendicular line cannot satisfy the hit pattern of the cluster, e.g. the right side of Fig. 7.10, the average of all hit scintillator positions is used as the position.

Two effects are checked to evaluate the hit reconstruction efficiency. One is the accidental noise hit induced by the MPPC dark noise. After the DAQ setup, the total rate of the dark noise exceeding the 2.5 p.e. threshold was measured to be ~ 300 Hz without the neutrino beam exposure. The accidental noise hit leads to $300\,\mathrm{Hz} \times 5\,\mu\mathrm{s} = 0.15\%$ of the DAQ inefficiency, and it is negligible. The other is a bunch pileup. Although the DAQ of the scintillation tracker

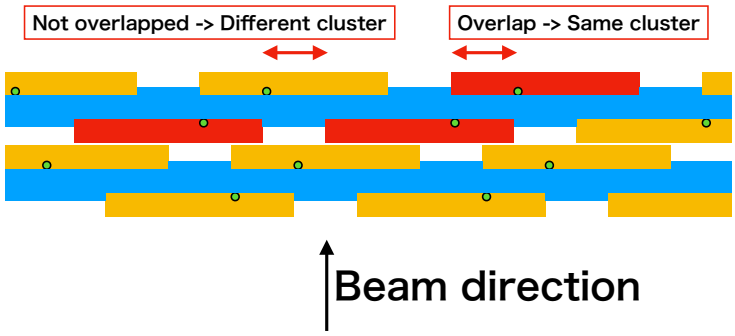

Figure 7.9: Hit clustering in the scintillation tracker. Red areas represent hit scintillator bars. When they are overlapped, they are classified into the same cluster; otherwise they are separated into different clusters [184].

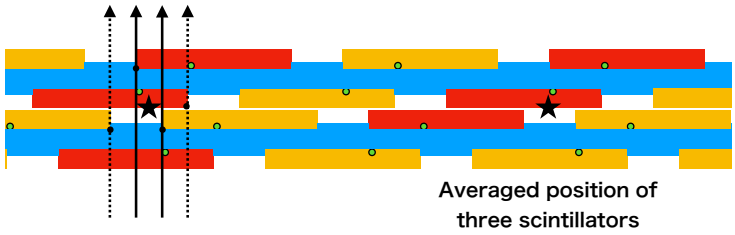

Figure 7.10: Tentative reconstruction of positions in the scintillation tracker. The red areas represent the hit scintillator bars. Each star represents the tentative reconstructed positions of the left and right clusters [184].

records hits in multiple bunches using the multi-hit TDC, its dynamic range cannot cover the whole spill. When there are hits in the first bunch of a spill, hits in the eighth bunch cannot be recorded. The DAQ inefficiency due to this effect is calculated to be around 0.3%, and it is also negligible. The total track matching efficiency between the scintillation tracker and Baby MIND is described in Sect. 7.3.4.

7.3.2.2 Hit–track matching between the scintillation tracker and Baby MIND

The position and angle of the three-dimensional track in Baby MIND are computed by the linear fitting to the hits in the horizontal and vertical views. Using the computed values, the track is extrapolated to the location of the scintillation tracker. It is checked whether or not they fall within the sensitive area of the scintillation tracker. Figure 7.11 shows the differences between the tentative positions reconstructed in Sect. 7.3.2.1 and that extrapolated from Baby MIND in data. Since the width of the horizontal scintillator bar is wider than that of the vertical one, the positional and angular resolutions of the three-dimensional track in Baby MIND are worse in the horizontal view. On the other hand, the tentative reconstruction of positions is identical in the scintillation tracker. Thus, the horizontal distribution is wider than the vertical one.

When the difference of the tentative position and the Baby MIND extrapolated position

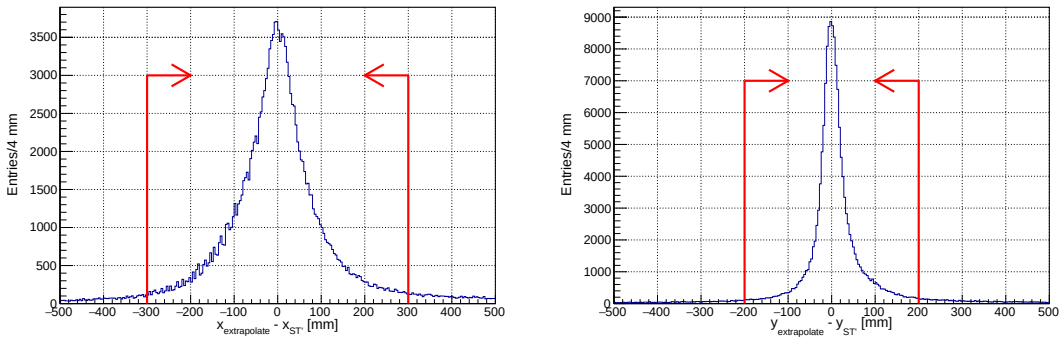

Figure 7.11: Difference of the tentative reconstructed position in the scintillation tracker and the extrapolated position from Baby MIND in data. The horizontal (left) and vertical (right) distributions are shown. The red lines represent selection criteria [184].

is less than 300(200) mm in the horizontal (vertical) view, the hit cluster in the scintillation tracker and the three-dimensional track in Baby MIND are matched. When there are multiple candidates of the clusters to be matched, the candidate with the smallest difference is selected. When the track has both the horizontal and vertical clusters to be matched, the hit–track matching is performed. The selection criteria are shown as red lines in Fig. 7.11.

7.3.2.3 Reconstruction of position and angle

After the hit–track matching, the tentative position in the scintillation tracker and the position of the track at the second layer in Baby MIND are used to reconstruct the angle. The angle in each view is reconstructed as

$$\tan\theta_{x(y)} = \frac{x(y)_{\mathrm{BM}} - x(y)_{\mathrm{ST}}}{d}, \tag{7.7}$$

where $x(y)_{\mathrm{BM}}$ and $x(y)_{\mathrm{ST}}$ are the horizontal (vertical) positions of Baby MIND and the scintillation tracker, respectively, and $d \sim 75$ cm is the distance in the z direction between the two positions.

The final reconstruction of the position in the scintillation tracker–Baby MIND matched tracks is almost the same as the reconstruction of the tentative position in the scintillation tracker. The difference is that the tracks are not necessarily in the z direction but have the reconstructed angle in Eq. (7.7) as the slope and are extrapolated from each scintillator vertex. Each of them is checked if it makes the pattern of the hit cluster as shown in Fig. 7.12. If there are the tracks satisfying the hit pattern, the average of the minimum and maximum positions of the tracks is regarded as the reconstructed position of the hit cluster; otherwise the averaged position of all scintillator bars are treated as it. The position and angle reconstructed in this process are used for the track matching between the emulsion shifter and the scintillator detectors described in Sect. 7.3.3.

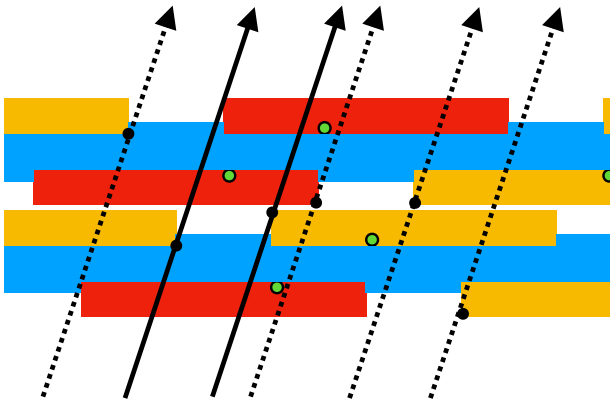

Figure 7.12: Reconstruction of the position in the scintillation tracker. The red areas represent the hit scintillator bars in one cluster. The black solid lines determine the minimum and maximum candidates of position and dotted lines are examples not satisfying the hit pattern [184].

7.3.3 Track matching between the emulsion detectors and the scintillator detectors

Each track matched between the scintillation tracker and Baby MIND has timing information of the neutrino beam bunch. Thus, the appropriate spots of the emulsion shifter can be selected using the timing information. The spot records the track candidate to be connected. The number of tracks in the emulsion shifter is approximately $3 \times 10^5/\mathrm{m}^2$ within four hours, while that induced by the neutrino beam is around $400/\mathrm{m}^2$. Therefore, in order to identify the correct candidate to be matched, the positional and angular information are used.

Inside the emulsion shifter, the track matching is performed as follows.

(1) **Spot determination**
The tracks in the fixed wall and moving walls are matched, and the four-hour timing information is added to each track in the fixed wall.

(2) **Track matching between the fixed wall and TSS**
The tracks in the fixed wall and TSS are matched using the positional and angular information. This process gives four-hour timing information to the tracks in TSS.

(3) **Track matching between the fixed wall and OSS**
The tracks in the fixed wall and OSS are matched using the positional and angular information. This process gives four-hour timing information to the tracks in OSS.

Next, the positional and angular relationships between the emulsion shifter (TSS) and the scintillation tracker are adjusted by similar process inside the emulsion shifter. Then, the χ^2 parameter is defined from the positional and angular differences in the horizontal and vertical views. By selecting the tracks with the smallest χ^2 value in the four-hour timing, the tracks are matched between the emulsion shifter and the scintillator detectors. Finally, the track

matching between OSS and ISS is performed using the positional and angular information in each SS. The tracks in ISS are already connected to the tracks in the upstream emulsion films in Sect. 7.1.3. After these processes, the tracks are matched from Baby MIND to the ECC with a muon identification and beam-timing information.

7.3.4 Performance of the track matching between the NINJA detectors

7.3.4.1 Efficiency of the scintillation tracker

The efficiency of the scintillation tracker is evaluated using the data obtained during the beam exposure. The muon tracks coming from the upstream wall of the detector hall are selected as a sample. This efficiency is defined as a ratio of the number of the matched tracks to the number of the tracks in Baby MIND. By definition, this is a product of the detection efficiency of the scintillation tracker and the hit–track matching efficiency between the scintillation tracker and Baby MIND. To ensure that the muons are coming from the upstream of the detectors, the tracks are required to have hits in the upstream WAGASCI module or Proton Module. In addition, the extrapolated position of the tracks is required to be in the inner area (400 mm × 600 mm) at the position of the scintillation tracker. The evaluated efficiency of the scintillation tracker as a function of the reconstructed angle of the three-dimensional track in Baby MIND is shown in Fig. 7.13. In the forward region ($\theta < 25^\circ$), where more than half of the muon tracks exist, the efficiency is 97–98%, while that deteriorates with a larger angle. The inefficiency is mainly due to the poor track reconstruction of the low-momentum or large-angle tracks with the small number of hits in Baby MIND.

7.3.4.2 Positional and angular resolutions after the hit–track matching

Positional and angular resolutions of the tracks matched between the scintillation tracker and Baby MIND can be evaluated using the information in the emulsion shifter. Since the positional and angular resolutions of the emulsion shifter are much better than that of the scintillation tracker, the variances of the positional and angular differences between the emulsion shifter and the scintillation tracker represent the resolutions for the matched track. Figure 7.14 shows the distributions of the positional differences. The distributions are fitted by the Gaussian functions, and the width $\sigma \sim 2.5$ mm is obtained for each one. The values are almost identical as expected since the horizontal and vertical modules of the scintillation tracker have the same structure.

Figure 7.15 shows the obtained widths of the fitted Gaussian functions for horizontal and vertical views as a function of the track angle. Here, the angle of the track in the emulsion shifter is used as the track angle. For forward-going tracks, the positional resolution of the scintillation tracker is around 2.5 mm, and it is less than 3.5 mm even in the larger angular region. The positional resolution is ideally expected to be $24\,\text{mm}/6/\sqrt{12} = 1.2$ mm when we assume the hits in each virtual segmentation is uniform. However, the value is twice worse as ~ 2.5 mm. The scintillator bars are actually not straight in the horizontal or vertical direction but slightly sagged by a few millimeters. Such a sag is not considered in the reconstruction of the position, and the positional resolution is deteriorated by it. In particular, the vertical direction is more

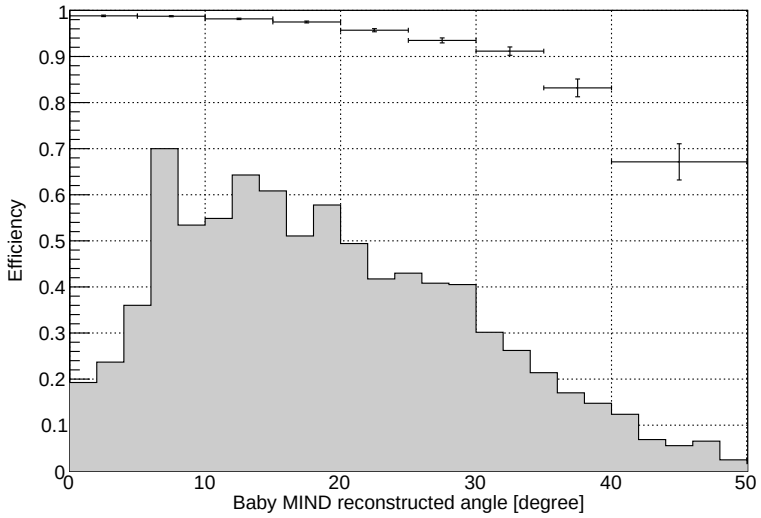

Figure 7.13: Efficiency of the scintillation tracker as a function of the reconstructed angle of the three-dimensional track in Baby MIND. The expected distribution of Baby MIND reconstructed angle of muon tracks from neutrino-water interactions in the ECCs is shown in a gray histogram [184].

affected by the gravity, and the sag will be larger. Moreover, the effect from the mis-alignment of the scintillator bars will be also larger for the bars horizontally set since the bars tend to move downward by the gravity. When the detector alignment is adjusted precisely and locally, such effects will be reduced.

The angular resolution is similarly evaluated to the positional resolution. The angular difference distributions are shown in Fig. 7.16, and they are fitted by the Gaussian functions. The width of the horizontal distribution is $\sigma \sim 40\,\mathrm{mrad}$, while that of the vertical one is $\sigma \sim 20\,\mathrm{mrad}$. It is evident that the angular resolution is different between the horizontal and vertical views since the scintillator width of Baby MIND is different between each other.

Figure 7.17 shows the obtained widths of the fitted Gaussian functions for horizontal and vertical views as a function of the track angle. The angular resolution of the muon tracks reconstructed by the scintillation tracker and Baby MIND is less than 100 mrad for a wide angular range. The vertical resolution is dominated by the multiple Coulomb scatterings between the scintillation tracker and Baby MIND, and the expectation is almost similar to the obtained value ($\sigma \simeq 20\,\mathrm{mrad}$). On the other hand, the horizontal resolution is dominated by the positional resolution of the three-dimensional reconstructed track in Baby MIND, i.e. the width of the scintillator bar. A simple calculation from the width of the scintillator bar gives $\sigma = 21\,\mathrm{cm}/\sqrt{12}/75\,\mathrm{cm} \simeq 80\,\mathrm{mrad}$, but it is twice better since the position is actually determined from the linear fitting to the hits.

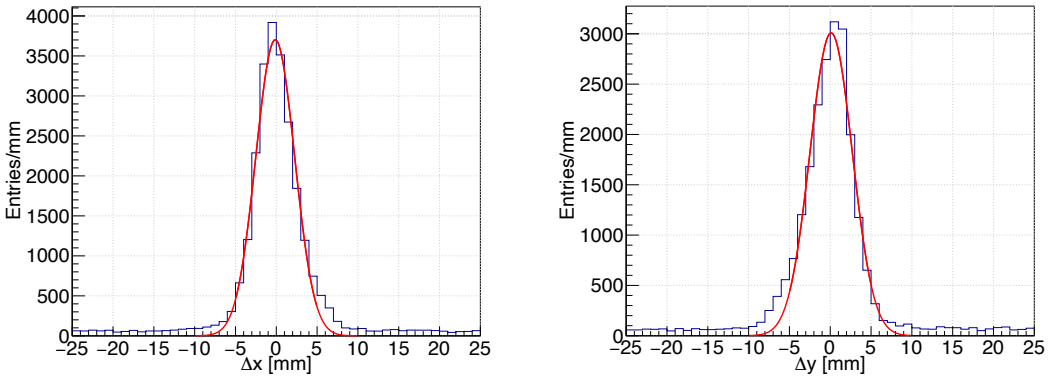

Figure 7.14: Positional difference distributions of the scintillation tracker and the emulsion shifter. The horizontal (left) and vertical (right) distributions are shown. The fitted Gaussian functions are shown as red lines [184].

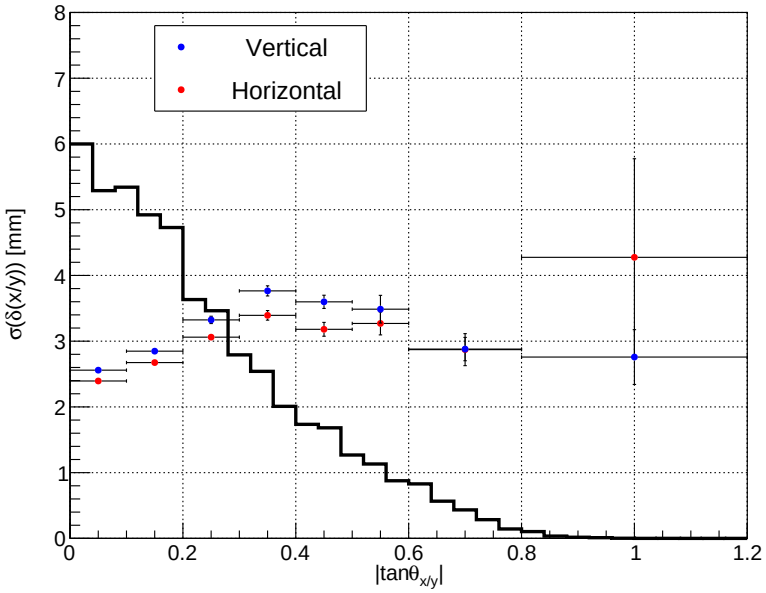

Figure 7.15: Positional resolutions of the scintillation tracker as a function of the track angle. The plot is obtained from the Gaussian fitting to each distribution, and the vertical bars represent the statistical errors. The histogram is the expected distribution of the angle of muons from the neutrino-water interactions in the ECCs [184].

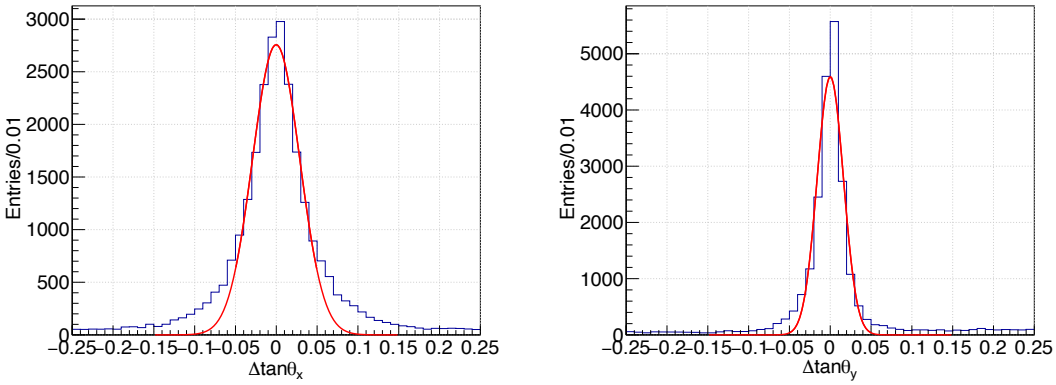

Figure 7.16: Angular difference distributions of the scintillation tracker and the emulsion shifter. The horizontal (left) and vertical (right) distributions are shown. The fitted Gaussian functions are shown as red lines [184].

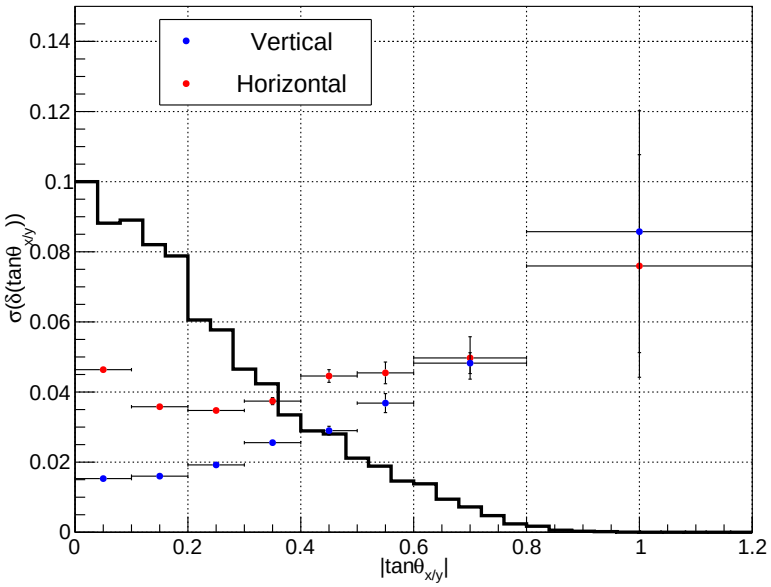

Figure 7.17: Angular resolutions of the scintillation tracker as a function of the track angle. The plot is obtained from the Gaussian fitting to each distribution, and the vertical bars represent the statistical errors. The histogram is the expected distribution of the angle of muons from the neutrino-water interactions in the ECCs [184].

7.3.4.3 Other matching efficiencies

The track matching efficiency between the emulsion shifter and the scintillator detectors is evaluated to be around 94% for a wide angular region as shown in Fig. 7.18, and that between the emulsion shifter and the ECCs is evaluated to be around 99%. Thus, the total muon matching efficiency among the NINJA detectors for forward-going muons is around $0.97 \times 0.94 \times 0.99 \simeq 90\%$.

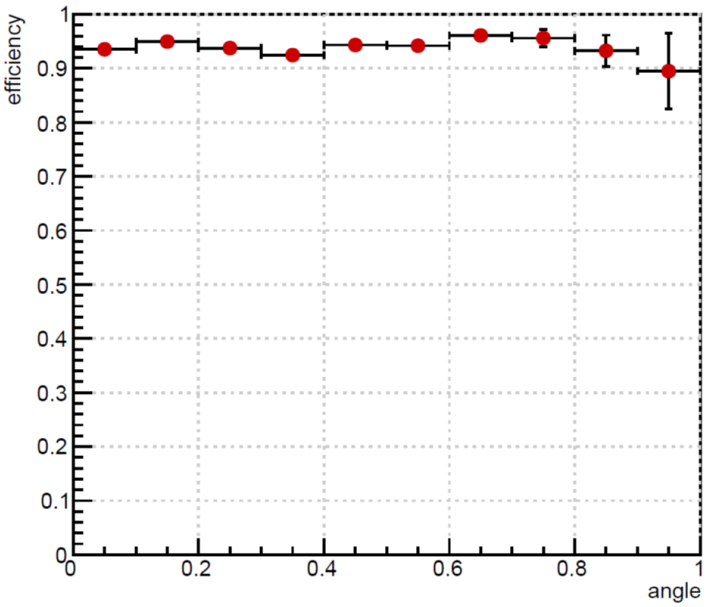

Figure 7.18: Track matching efficiency between the emulsion shifter and the scintillation tracker–BabyMIND. The horizontal axis represents $\tan\theta$ of the basetrack in the emulsion shifter.

Chapter 8

Event Selection

In this study, we use the data of one out of nine ECCs, called ECC5 hereafter, which was placed in the center of the 3×3 array. Our signal is the ν_μ CC interactions on water in ECC5. The event selection and the determination of the track multiplicity are performed as follows.

(1) **Muon track matching**
Track matching between the ECC and Baby MIND is performed using the timestamp detectors as described in Sect. 7.3. The matched track is regarded as a muon candidate.

(2) **Fiducial volume cut**
Most of the matched tracks are the muons from the neutrino interactions in the upstream wall of the detector hall. Each track is checked whether it is starting from the water target of the ECC. The Fiducial Volume (FV) of the ECC is determined as follows.

The alignment parameters are necessary for the analysis of the basetracks. Without the parameters, the basetracks cannot be correctly connected to those in the other films, i.e. the basetracks cannot be used in the linklet or chain reconstructions. In addition, if the alignment parameters are not obtained, the angular difference to those in the other films is meaningless. The angular difference is used in the momentum reconstruction using multiple Coulomb scatterings, thus the alignment parameters have to be obtained for the areas to be used in the analysis. In order to obtain the alignment parameters with a sufficient precision, statistics of the linklets are necessary. In the alignment, one film is separated into 2 mm $\times$ 2 mm local areas. When a sufficient number of basetracks in the area are connected to the adjacent film, the alignment parameters can be calculated as described in Sect. 7.1.3.1. When the alignment parameters are obtained for the local area, it is counted for the FV of the film. The most outer points of the local areas are connected, and the edge of the FV is determined. Accordingly, the FV differs for each emulsion film. Figure 8.1 shows the FV of one film in ECC5. The FV of the ECC is defined as the water volume covered by the FV of the emulsion films. The ratio of the FV of the ECC to the total volume of the water is around 80% in the NINJA physics run.

The most upstream two emulsion films in the ECC are used as veto, i.e. if chains have a basetrack in these films, they are rejected. The muon candidate chains are extrapolated to

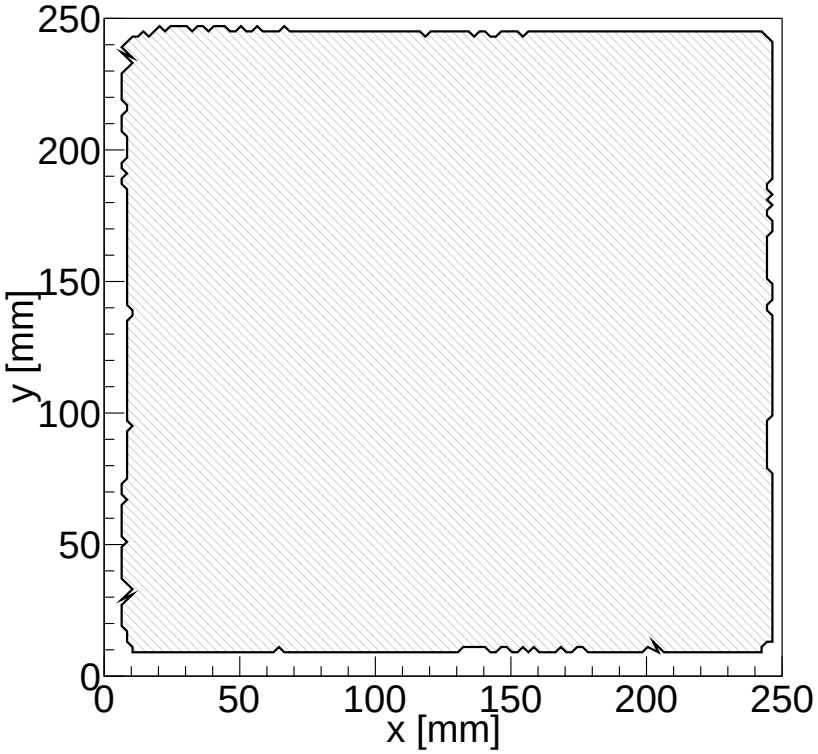

Figure 8.1: FV of one film in ECC5.

its four upstream films. When the all four extrapolated tracks are within the FV of a film, the chain remains as a signal candidate; otherwise they are rejected.

(3) **Partner track search and vertex determination**

After the muon candidate is confirmed to be starting from the ECC FV, partner tracks are searched for. First, the basetracks in the same emulsion film as where the most upstream one of the muon candidate chain exists are collected. These basetracks correspond to the candidates of the forward-going partners. For each basetrack of the forward-going partner candidate, it is checked whether the basetrack is the most upstream of a chain. If the basetrack does not constitute a chain, it is rejected from the partner candidates. In addition, if the basetrack is connected to the one in more upstream emulsion films, it is also rejected. The similar selection is applied for the backward-going partners. In this case, the candidates are selected from the one upstream emulsion film, and the basetrack is required to be the most downstream one in a chain. After the selection, the minimum distance (MD) between the films is calculated for the muon candidate basetrack and each partner candidate

Table 8.1: Summary of the event selection.

Step	MC (background)	Data
Muon track matching	-	8899
Fiducial volume cut	-	242
Partner track search and vertex determination	-	93
Momentum consistency check	92.0 (8.0)	82

basetrack. Basetracks satisfying

$$\mathrm{MD} < \sqrt{A(|dz_0|, \tan\theta_0) + A(|dz_1|, \tan\theta_1)}, \tag{8.1}$$

$$A(|dz|, \tan\theta) = \left(|dz| \times (0.04 \times \tan\theta + 0.04) + 5\,\mu\mathrm{m}\right)^2, \tag{8.2}$$

are identified as the tracks from the same vertex, and the chains are identified as the partners. Here, θ_0 and θ_1 are the angles of the muon and partner candidate basetracks with respect to the z direction, respectively, and dz_0 and dz_1 are the extrapolation lengths in the z direction from the positions of the candidates on the surface of the films, respectively. This criterion is determined by the MC simulation so that more than 99% partner detection efficiency is achieved. To minimize the number of accidentally matched tracks, the numbers in Eq. (8.2) (i.e. 0.04, 0.04, and 5 µm) are required to be as small as possible. The vertex position is then determined as follows. When there are partner candidates attaching to the muon candidate track, the averaged point of the midpoints of each line which makes the minimum distance for a pair of the muon and partner candidates is treated as the vertex point; otherwise the track is extrapolated to the middle point of the upstream water layer. When the vertex point is not reconstructed in the water layers, the candidate is rejected.

(4) **Momentum consistency check**

To exclude the events with muon candidates which are mis-matched between the emulsion and scintillator detectors, the consistency of the muon momenta reconstructed by two independent methods are compared. The detail of the momentum consistency check will be described in Chap. 9 after the momentum reconstruction methods are introduced.

The number of the selected events after each step is summarized in Table 8.1. In total, 82 events are selected in data, while the MC prediction is 92.0 events.

Chapter 9

Momentum Reconstruction and Particle Identification

The tracks matched between the ECC and Baby MIND are regarded as the muon candidates, and the starting point of the tracks inside the ECC volume is considered as the interaction vertex. The other tracks starting from the vertex, so-called "partner tracks," are considered as protons or charged pions. In this chapter, the momentum reconstruction of those tracks is firstly described, then the PID between the protons and charged pions is shown.

9.1 Overview of the momentum reconstruction and particle identification

The momentum of charged particles can be measured by several methods in the NINJA experiment. Figure 9.1 shows a flow chart of the momentum reconstruction and PID. The muon identification is performed by the track matching described in Sect. 7.3. When there are multiple tracks matched between the ECC and Baby MIND from the same vertex, the longest track is selected as a muon candidate. When the track is stopping inside the FV of Baby MIND, the momentum can be measured using the Baby MIND track range, while that escaping from or penetrating through the FV is measured using multiple Coulomb scatterings (MCS) inside the ECC. The detailed information of the momentum reconstruction using the ECC MCS is described in Sect. 9.2.2. The PID is performed to the partner tracks using the momentum measured by the ECC MCS and VPH, which is a strongly correlated value to dE/dx. After the PID process, their momentum is measured by two methods. One uses the track range in the ECC when the track is stopping inside the ECC FV which was described in Chap. 8; otherwise the momentum is measured by the ECC MCS.

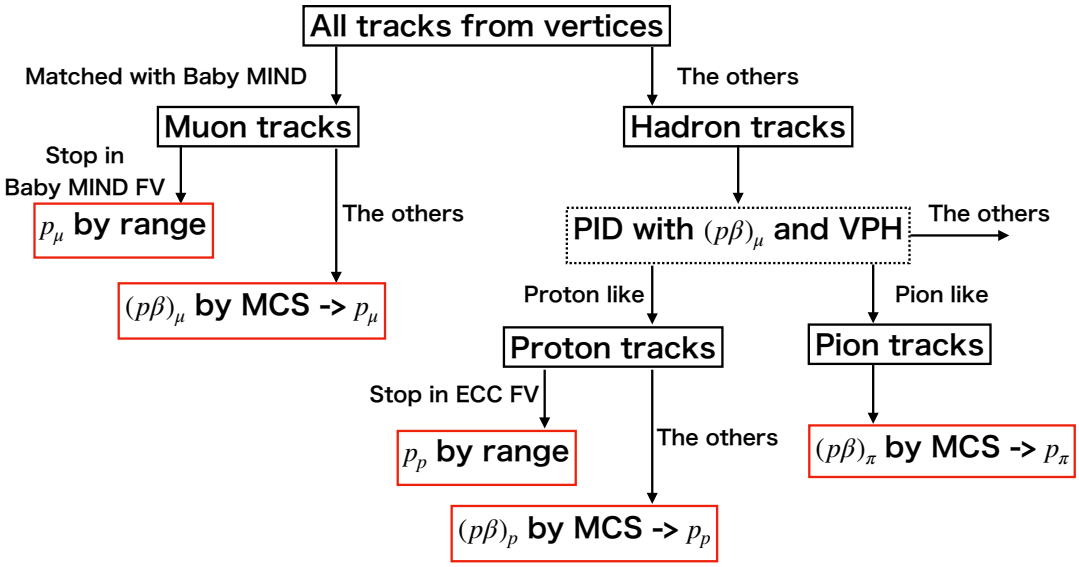

Figure 9.1: Flow chart of the momentum reconstruction and PID. The momentum of muons is measured by the Baby MIND track range and ECC MCS. Protons stopping inside the ECC volume are measured by the ECC track range, and the other protons are measured by the ECC MCS. The momentum of all charged pions is measured by the ECC MCS.

9.2 Momentum reconstruction of muon tracks

In this section, the momentum reconstruction of muon tracks in two methods is described.

9.2.1 Muon momentum reconstruction using the track range

The first method of the muon momentum reconstruction uses a track range in Baby MIND. The three-dimensional track has two-dimensional hit information in each scintillator module of Baby MIND, and the track lengths between each neighboring module are calculated by the positions of the hits. The track angles differ between each pair of the scintillator modules because of the magnetic field in Baby MIND. Using the calculated length and the numbers of scintillator and iron plates between the modules, the total track range in Baby MIND is calculated. In addition, materials in the ECC and downstream WAGASCI module are also considered although they have only a small effect. The total track range is converted into an equivalent value in iron. Finally, using a spline shown in Fig. 9.2, the momentum of the track is reconstructed. According to the total material thickness inside Baby MIND, we can measure momenta up to around 1.5 GeV/c using the track range.

Although the momentum of muons stopping inside the Baby MIND FV can be reconstructed using the track range, it is not applicable to the tracks escaping from or penetrating through it. In order to measure the momentum of such tracks, we need another reconstruction method.

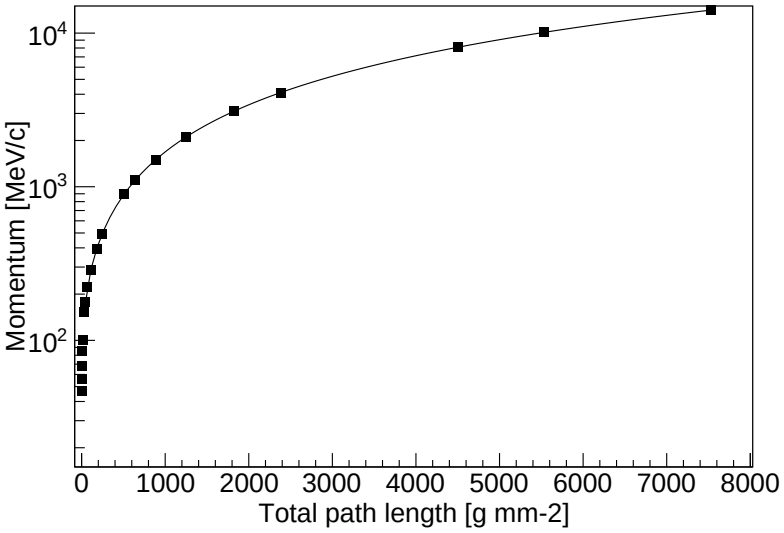

Figure 9.2: Spline used in the conversion from the total track range to the muon momentum. The plot is made from the PDG data [152].

9.2.2 Muon momentum reconstruction using the ECC MCS

In the NINJA experiment, the momentum of the charged particles can be also reconstructed using MCS inside the ECC. Since this reconstruction method only uses the measured scattering angles and path lengths of the particle in the trajectory, the particle is not required to be stopping inside the detector volume. Besides, this method does not require a magnetic field.

A charged particle traveling through a material is scattered by MCS as shown in Fig. 9.3. The scattering angle is modeled by a Gaussian distribution with its mean at zero and the width explained by so-called Highland formula [208, 209], and is strongly correlated to the momentum of the particle. The Highland formula is expressed as

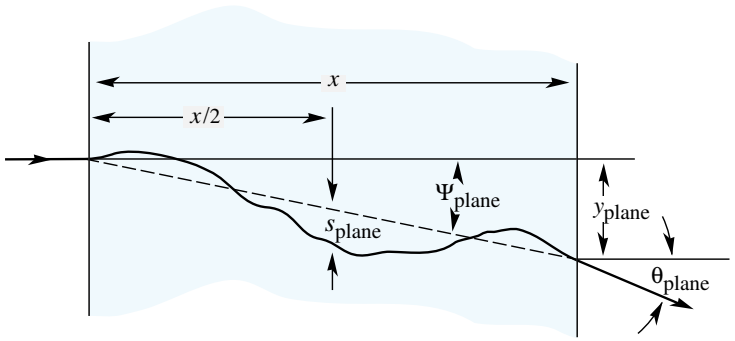

Figure 9.3: Schematic view of multiple Coulomb scatterings. The incident track is parallel to the sheet, while that after the scatterings is projected to the sheet. θ_{plane} corresponds to the scattering angles expresses as $\Delta\theta_{\text{rad}'}$ or $\Delta\theta_{\text{lat}'}$ in Eq. (9.4) or (9.5) [152].

$$\sigma_{\mathrm{HL}}(p\beta, w/X_0) = \frac{13.6\,\mathrm{MeV}/c}{p\beta}|q|\sqrt{\frac{w}{X_0}}\left[1 + 0.038\ln\left(\frac{xq^2}{X_0\beta^2}\right)\right], \tag{9.1}$$

where p is the momentum, and β is the velocity of the particle. q is the electric charge of the particle, and w/X_0 is the path length of the particle in a unit of the radiation length of the scattering medium. To measure the scattering angles, a detector with a high angular resolution is generally required because such angles are very small, e.g. a few milliradian for a $1\,\mathrm{GeV}/c$ muon penetrating 500 µm of iron. In addition to the angular resolution, the detector is also required to have a high sampling structure. The Highland formula is a relationship between the momentum and the statistical width of the scattering angles of one particle. Therefore, the detector should have the capability of measuring a large number of scattering angles for a given particle along its track. In particular for hadrons, a large number of the scattering angles are required to be measured within a short distance before they interact with materials of the detector. Since the ECC has an alternate structure of thin material layers and emulsion films, it is one of good solutions for these requirements. Making use of the advantage, the momentum reconstruction using the ECC MCS has been applied in the DONUT [210] and OPERA experiments [211].

In the NINJA physics run, we have developed a new method of momentum reconstruction of charged particles using MCS based on a maximum likelihood. In the previous analyses of the NINJA experiment [168–170], the momentum of particles inside the ECC was assumed to be constant during their travel in the detector volume. In practice, it did not largely affect the performance of the momentum reconstruction thanks to the higher neutrino energy and the smaller detector volume than the physics run. However, in our measurement, the charged particles from the neutrino interactions have a lower momentum, from a few to several hundred MeV/c. Thus, they lose a significant amount of their energy inside the larger detector volume.

In the new method, we construct a likelihood to consider the decrease of momentum due to the energy deposit [175]. The likelihood has the initial momentum as its parameter. The reconstructed momentum is obtained from the parameter value which maximizes the likelihood. The maximum likelihood-based method is firstly proposed and used in the MicroBooNE experiment [212]. They measure scattering angles of charged particles in liquid argon with the path length equivalent to the radiation length unit of liquid argon since the LArTPCs typically have a uniform material medium and a sufficient range of $\mathcal{O}$(m). On the other hand, our ECC has a complicated alternate structure of emulsion films and target materials. The tracks are only detected by the emulsion films, and the path length is determined by the detector structure. In the ECC, the method can be used even for the smaller path length because the angular resolution of the nuclear emulsion film is better than the magnitude of MCS. Thus, the ECC is capable of reconstructing the momentum even if the track range is shorter than the radiation length unit.

9.2.2.1 Definition of the scattering angles

The Highland formula is an equation for the scattering angles projected to a plane parallel to the incident track direction. Since the nuclear emulsion film is a three-dimensional tracking

device, two independent scattering angles can be measured by projecting the scattered track to two orthogonal planes.

First, a Cartesian coordinate system to measure the scattering angles is introduced. The x, y, and z directions are defined as described in Sect. 7.1.1. The scattering angles are measured on two orthogonal planes parallel to the incident track direction. The measurement error of HTS is much larger in the z direction than in the x and y directions. This is because HTS takes tomographic images with a 4-µm pitch in the z direction, while the size of one pixel is $0.45\,\mu\mathrm{m} \times 0.45\,\mu\mathrm{m}$ on the x-y plane. Thus, the two planes are selected in such a way that one of them is totally independent of the measurement error in the z direction.

Three unit vectors $\hat{\boldsymbol{t}}$, $\hat{\boldsymbol{l'}}$, and $\hat{\boldsymbol{r'}}$ are defined as follows. $\hat{\boldsymbol{t}}$ is along the incident track, and

$$\hat{\boldsymbol{l'}} = \frac{\hat{\boldsymbol{z}} \times \hat{\boldsymbol{t}}}{|\hat{\boldsymbol{z}} \times \hat{\boldsymbol{t}}|}, \tag{9.2}$$

$$\hat{\boldsymbol{r'}} = \hat{\boldsymbol{t}} \times \hat{\boldsymbol{l'}}. \tag{9.3}$$

Here, $\hat{\boldsymbol{z}}$ is the unit vector in the z direction. The vector $\hat{\boldsymbol{l'}}$ is orthogonal to the z direction and independent of the measurement error in it. By definition, these three vectors constitute another Cartesian coordinate system.

The scattering angles of the particle are projected to the planes made by the $\hat{\boldsymbol{r'}}$-$\hat{\boldsymbol{t}}$ and $\hat{\boldsymbol{l'}}$-$\hat{\boldsymbol{t}}$ vectors. HTS measures each angle of the basetrack as a vector form of the tangent: $\boldsymbol{a} = (\tan\theta_x, \tan\theta_y, 1)$. Using the track directions before and after the scattering, the scattering angles on each plane can be calculated as follows.

$$\begin{aligned}
\Delta\theta_{\mathrm{rad}'} &= \arctan\left(\frac{\boldsymbol{a}_1 \cdot \hat{\boldsymbol{r'}}}{\boldsymbol{a}_1 \cdot \hat{\boldsymbol{t}}}\right) \\
&= \arctan\left(\frac{-\tan\theta_{x0}\tan\theta_{x1} - \tan\theta_{y0}\tan\theta_{y1} + \tan^2\theta_{x0} + \tan^2\theta_{y0}}{\sqrt{\tan^2\theta_{x0} + \tan^2\theta_{y0} + (\tan^2\theta_{x0} + \tan^2\theta_{y0})^2}}\right. \\
&\qquad \left. \Big/ \frac{\tan\theta_{x0}\tan\theta_{x1} + \tan\theta_{y0}\tan\theta_{y1} + 1}{\sqrt{\tan^2\theta_{x0} + \tan^2\theta_{y0} + 1}}\right),
\end{aligned} \tag{9.4}$$

$$\begin{aligned}
\Delta\theta_{\mathrm{lat}'} &= \arctan\left(\frac{\boldsymbol{a}_1 \cdot \hat{\boldsymbol{l'}}}{\boldsymbol{a}_1 \cdot \hat{\boldsymbol{t}}}\right) \\
&= \arctan\left(\frac{-\tan\theta_{y0}\tan\theta_{x1} + \tan\theta_{x0}\tan\theta_{y1}}{\sqrt{\tan^2\theta_{x0} + \tan^2\theta_{y0}}}\right. \\
&\qquad \left. \Big/ \frac{\tan\theta_{x0}\tan\theta_{x1} + \tan\theta_{y0}\tan\theta_{y1} + 1}{\sqrt{\tan^2\theta_{x0} + \tan^2\theta_{y0} + 1}}\right).
\end{aligned} \tag{9.5}$$

Here, $\boldsymbol{a}_i = (\tan\theta_{xi}, \tan\theta_{yi}, 1), (i = 0, 1)$ are the direction vectors of the track before and after the scattering, respectively, and $\hat{\boldsymbol{t}} = \boldsymbol{a_0}/|\boldsymbol{a_0}|$. The scattering angles $\Delta\theta_{\mathrm{rad}'}$ and $\Delta\theta_{\mathrm{lat}'}$ are on the $\hat{\boldsymbol{r'}}$-$\hat{\boldsymbol{t}}$ and $\hat{\boldsymbol{l'}}$-$\hat{\boldsymbol{t}}$ planes, respectively.

Figure 9.4 shows the angular resolutions used in this method [203]. Since the $\hat{\boldsymbol{l}}'$ direction is independent of the measurement error in the z direction, the angular resolution of $\Delta\theta_{\mathrm{lat}'}$ is much better than that of $\Delta\theta_{\mathrm{rad}'}$ in all angular region. The angular resolution of $\Delta\theta_{\mathrm{rad}'}$ is degraded with a larger angle in the $\tan\theta < 1$ region, while it gets improved in the region of $\tan\theta > 1$. This is because the measurement error in the z direction worsen the resolution with the larger angle, whereas the longer baseline improves it. These two effects are comparable when $\tan\theta \simeq 1$. Except for these angular resolutions, two scattering angles can be similarly treated.

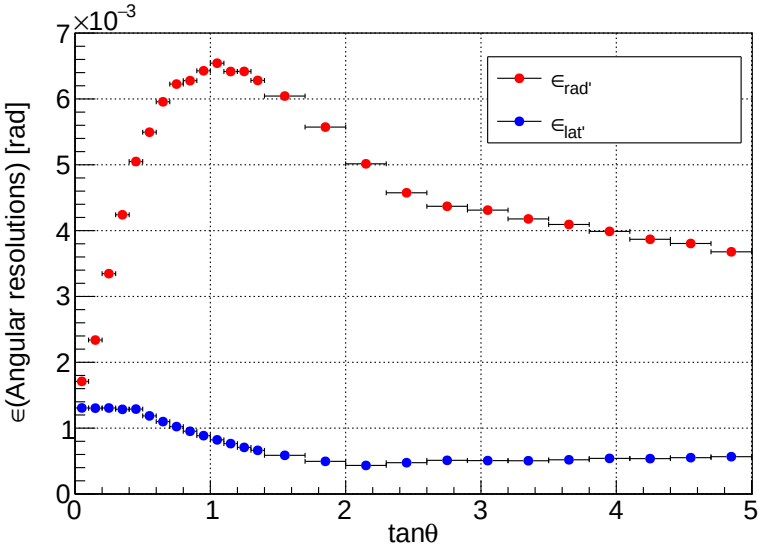

Figure 9.4: Angular resolutions for each scattering angle in the ECC MCS method. The horizontal axis represents the track angle with respect to the z direction. The red plots are the resolution of $\Delta\theta_{\mathrm{rad}'}$, and blue ones are of $\Delta\theta_{\mathrm{lat}'}$ [203].

9.2.2.2 Definition of the maximum likelihood

In the ECC, particles are mainly scattered by the 500-µm thick iron plates. In this analysis, we only consider the scatterings in one iron plate although the scattering angles in the water layer are also potentially available. The two scattering angles, $\Delta\theta_{\mathrm{rad}'}$ and $\Delta\theta_{\mathrm{lat}'}$, follow the Gaussian probability function:

$$f(\Delta\theta; p\beta, w/X_0, \tan\theta) = (2\pi\sigma(p\beta, w/X_0, \tan\theta)^2)^{-1/2} \times \exp\left[-\frac{1}{2}\left(\frac{\Delta\theta}{\sigma(p\beta, w/X_0, \tan\theta)}\right)^2\right]. \tag{9.6}$$

Here, $\tan\theta = \sqrt{\tan^2\theta_x + \tan^2\theta_y}$ is a track direction before the scattering, and w/X_0 is a path length in the material in a radiation length unit. w/X_0 is proportional to the distance of the positions of the basetracks before and after the scattering. The scattering angle, $\Delta\theta_{\mathrm{rad}'}$ or $\Delta\theta_{\mathrm{lat}'}$,

is represented as $\Delta\theta$, and $\sigma(p\beta, w/X_0, \tan\theta)$ is the width of the Gaussian function. The width $\sigma(p\beta, w/X_0, \tan\theta)$ consists of two parts. One is the angular deviation induced by MCS, and the other is from the angular resolution. The width $\sigma(p\beta, w/X_0, \tan\theta)$ can be written using the MCS part, σ_{HL}, and the angular resolution part, $\epsilon_{\mathrm{rad}'}(\tan\theta)$ or $\epsilon_{\mathrm{lat}'}(\tan\theta)$ as

$$\sigma(p\beta, w/X_0, \tan\theta) = \sqrt{(\sigma_{\mathrm{HL}}(p\beta, w/X_0))^2 + (\epsilon(\tan\theta))^2}. \tag{9.7}$$

To obtain the likelihood, the product of the probability functions written in Eq. (9.6) is considered. When the particle penetrates N iron plates, the scattering angles $\Delta\theta_i$ $(i = 0, 1, \ldots N-1)$ can be calculated across each iron plate, and the likelihood is written as follows:

$$\begin{aligned}
&L((\boldsymbol{\Delta\theta}); (\boldsymbol{p\beta}), (\boldsymbol{w/X_0}), (\boldsymbol{\tan\theta})) \\
&= (2\pi)^{-N} \times \prod_{j=0}^{N-1} (\sigma_{\mathrm{rad}'}((p\beta)_j, (w/X_0)_j, \tan\theta_j))^{-1} \times \prod_{j=0}^{N-1} (\sigma_{\mathrm{lat}'}((p\beta)_j, (w/X_0)_j, \tan\theta_j))^{-1} \\
&\times \exp\left[-\frac{1}{2} \sum_{j=0}^{N-1} \left(\left(\frac{\Delta\theta_{\mathrm{rad}',j}}{\sigma_{\mathrm{rad}'}((p\beta)_j, (w/X_0)_j, \tan\theta_j)} \right)^2 + \left(\frac{\Delta\theta_{\mathrm{lat}',j}}{\sigma_{\mathrm{lat}'}((p\beta)_j, (w/X_0)_j, \tan\theta_j)} \right)^2 \right) \right].
\end{aligned} \tag{9.8}$$

Here, $\sigma_{\mathrm{rad}'}$ and $\sigma_{\mathrm{lat}'}$ are expressed as Eq. (9.7) with $\epsilon = \epsilon_{\mathrm{rad}'}$ and $\epsilon_{\mathrm{lat}'}$, respectively. $(\boldsymbol{\Delta\theta}) = (\Delta\theta_{\mathrm{rad}',0}, \Delta\theta_{\mathrm{rad}',1}, \ldots \Delta\theta_{\mathrm{rad}',N-1}, \Delta\theta_{\mathrm{lat}',0}, \Delta\theta_{\mathrm{lat}',1}, \ldots \Delta\theta_{\mathrm{lat}',N-1})$ is the scattering angles. $(\boldsymbol{w/X_0}) = ((w/X_0)_0, (w/X_0)_1, \ldots (w/X_0)_{N-1})$ is the path lengths, and $(\boldsymbol{\tan\theta}) = (\tan\theta_0, \tan\theta_1, \ldots \tan\theta_{N-1})$ is the track directions before each scattering. Due to the energy deposit mainly in each iron plate, $p\beta$ decreases as $(\boldsymbol{p\beta}) = ((p\beta)_0, (p\beta)_1, \ldots (p\beta)_{N-1})$, where $(p\beta)_0$ is what we want to measure.

The decrease of $p\beta$ between each pair of adjacent iron plates is treated as follows. In the detector simulation described in Sect. 5.3, muon particle guns with different β ranging between 0.5 and 0.999 ($\gamma \simeq 22$) are generated in the z direction. The averaged energy deposit as a function of β is plotted and fitted by a fourth order polynomial function as shown in Fig. 9.5. Here, the energy deposit in one iron plate or one water layer is calculated from the MC-truth information. The decrease of $p\beta$ is calculated one by one assuming that the particle is a muon using Eqs. (9.9) and (9.10):

$$(p\beta)_i = \frac{p_i^2}{E_i} = \frac{E_i^2 - M^2}{E_i}, \tag{9.9}$$

$$E_{i+1} = E_i - \Delta E_i. \tag{9.10}$$

Here, M is the muon mass, and p_i and E_i are the momentum and energy of the particle at the i-th iron plate, respectively. The energy deposit ΔE_i is calculated using β, the values in Fig. 9.5 and the path length in an iron plate the particle penetrates, and that in a water layer. This process is repeated until the most downstream iron plate is reached or the kinetic energy of the

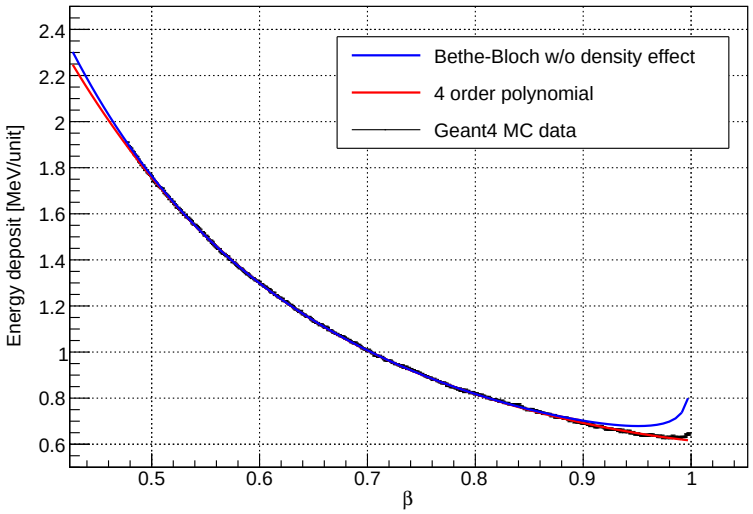

Figure 9.5: Energy deposit across one iron plate of a muon perpendicularly penetrating the emulsion films calculated by MC-truth information. The plot is fitted by the polynomial function and Bethe Bloch function without density effect as a reference. Without density effect, the Bethe Bloch function results in higher value than the expected one in the region of $\beta > 0.9$ [175].

particle becomes negative.

The likelihood is dependent only on the positions and angles measured by the emulsion films and has one parameter, $(p\beta)_0$. When the likelihood in Eq. (9.8) is maximized, the value of $(p\beta)_0$ corresponds to the reconstructed initial momentum of the particle. In this likelihood, when $\Delta\theta_i$ is more than three times larger than the RMS of them, such scattering angles are not used. This is because the Gaussian approximation is only applicable to the central 98% of the scattering angles.

Instead of maximizing the likelihood in Eq. (9.8), the negative log likelihood is minimized using the MINUIT framework [213] in ROOT:

$$\begin{aligned} -l &= -2\log(L) + N\log(2\pi) \\ &= 2\sum_{j=0}^{N-1} [\log(\sigma_{\mathrm{rad}'}((p\beta)_j, (w/X_0)_j, \tan\theta_j)) + \log(\sigma_{\mathrm{lat}'}((p\beta)_j, (w/X_0)_j, \tan\theta_j))] \\ &\quad + \sum_{j=0}^{N-1} \left[\left(\frac{\Delta\theta_{\mathrm{rad}',j}}{\sigma_{\mathrm{rad}'}((p\beta)_j, (w/X_0)_j, \tan\theta_j)} \right)^2 + \left(\frac{\Delta\theta_{\mathrm{lat}',j}}{\sigma_{\mathrm{lat}'}((p\beta)_j, (w/X_0)_j, \tan\theta_j)} \right)^2 \right]. \end{aligned} \tag{9.11}$$

Here, a constant term $-N\log(2\pi)$ is subtracted from $-2\log(L)$.

9.2.2.3 Parameter tuning

The Highland formula is phenomenologically tuned using the detector MC simulation instead of Eq. (9.1). Each experiment tunes the parameters depending on their detector structures or scattering medium [210–212] because the coefficients in the Highland formula (i.e. 13.6 and 0.038) are determined so that the formula is applicable to various materials. Each experiment actually has their own detector materials and structures, thus the tuned formula is more useful. In this method, the coefficient 13.6 MeV/c in Eq. (9.1) is replaced by a free parameter S [MeV/c] as

$$\sigma_{\mathrm{HL}}(p\beta, w/X_0) = \frac{S\,[\mathrm{MeV}/c]}{p\beta}\sqrt{\frac{w}{X_0}}\left[1 + 0.038\ln\left(\frac{w}{X_0}\right)\right]. \tag{9.12}$$

Hereafter, q in Eq. (9.1) is always set to unity since we only consider muons, protons, or charged pions. In addition, β in the logarithm function is also set to one because the muon in this simulation is relativistic. Tuning of the other coefficient (i.e. 0.038) has a smaller effect compared to that of S. Thus, only the tuning of S is considered in this method.

To consider only the Highland formula, the angular resolution is set to zero in this tuning. First, the momentum of muon particle guns is reconstructed with $S = 13.6$. The mean of the relative residual distribution is biased a few percent from zero. The bias of the reconstruction is defined as the mean of the fitted Gaussian to the relative residual distribution of $1/p\beta$. Figure 9.6 shows the relative residual distributions of $1/p\beta$ for muon particle guns of $p = 500\,\mathrm{MeV}/c$. The blue histogram in Fig. 9.6 shows the distribution before the tuning. This bias is obtained for the muon particle guns with $p = 300$–$2000\,\mathrm{MeV}/c$, and the average of the biases over the momentum is obtained as 2.7% in this region. Figure 9.7 shows the biases obtained for particle gun simulations with different momenta before and after the tuning.

To compensate the bias of $1/p\beta$, the $1/p\beta$ reconstruction should be scaled by $1/(1+\delta)$, where the bias is written as δ. The measured scattering angles are not changed, thus the parameter S should be scaled as

$$\sigma_{\mathrm{HL}} \propto \frac{13.6}{p\beta} \rightarrow \sigma_{\mathrm{HL}} \propto \frac{S}{(1+\delta)\times p\beta} \tag{9.13}$$

to adjust the reconstructed $1/p\beta$. In this study, S is tuned as $S = 1.027 \times 13.6 \simeq 14.0$, and the bias is expected to be reduced.

After S is tuned to be 14.0, the momentum reconstruction is performed again, and the distribution is changed as shown on the red histogram in Fig. 9.6. The bias is not dependent on the momentum and is now around 0.1%. These biases after the tuning for different momenta are shown on the red plots in Fig. 9.7.

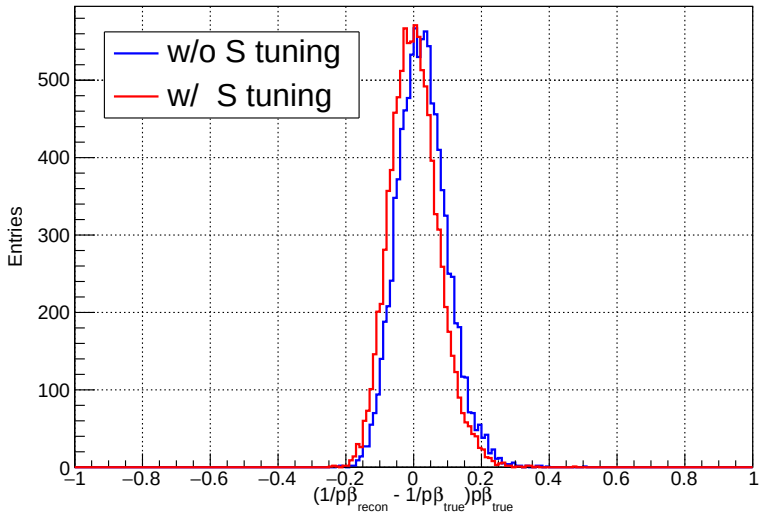

Figure 9.6: Relative residual distribution of $1/p\beta$ of $p = 500\,\mathrm{MeV}/c$ muon particle guns before and after the S parameter tuning [175].

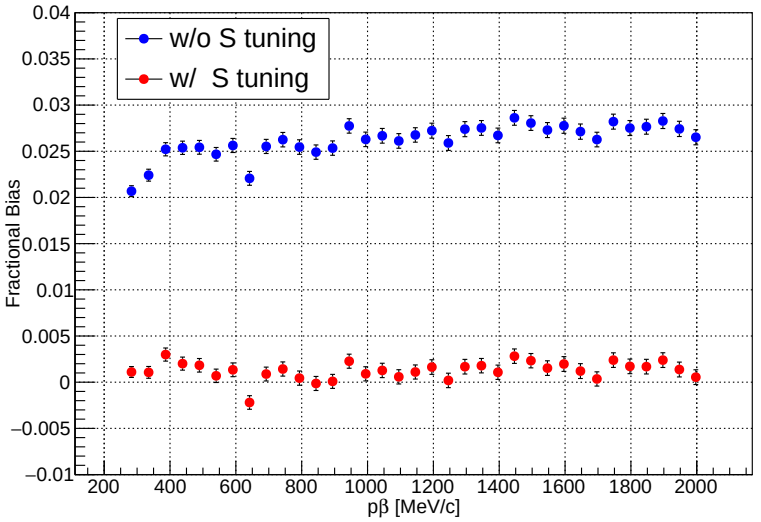

Figure 9.7: Fractional bias of the relative $1/p\beta$ as a function of $p\beta$ before (blue) and after (red) the S parameter tuning. The vertical error bars are the statistical ones in the Gaussian fitting [175].

9.2.2.4 Effect from the angular resolution

To study the effect on the reconstruction performance from the angular resolution, the MC simulation is also used. First, the muon particle gun MC simulation is generated in the most upstream water layer of the water ECC and directed downstream in the z direction. The

simulation is firstly performed using the MC-truth information to check the performance without the angular resolutions. The muon penetrates at most 69 iron plates until it escapes from the detector volume. To reconstruct the momentum in this simulation, we set the angular resolution in the likelihood to zero. Hereafter, we refer to the width of the fitted Gaussian to the relative residual distribution of $1/p\beta$ as "the momentum resolution" of this method. The results of the momentum resolution is typically 7% with 0.1% bias.

Next, the angular differences are smeared, and the reconstruction is performed with the likelihood including the angular resolution. In this case, the performance as a function of the momentum is changed from the blue to the red plots in Figs. 9.8 and 9.9. The performance is determined by the ratio of the magnitude of MCS to the angular resolution. The angular resolution is not dependent on the momentum of the particle, while the magnitude of MCS decreases for the higher momentum. Thus, MCS is hidden by the angular resolution for high-momentum particles. For high-momentum particles, the momentum information is harder to obtain from the likelihood since it is primarily determined by the angular resolution. In addition to the momentum resolution in Fig. 9.9, the bias in Fig. 9.8 also shows the momentum dependence. In the high-momentum region, a larger fractional bias is seen, i.e. the reconstructed momentum value is smaller than the true one. This is because, when the magnitude of MCS is much smaller than the angular resolution, the angular resolution mimics MCS, and the reconstructed momentum is biased to the lower value.

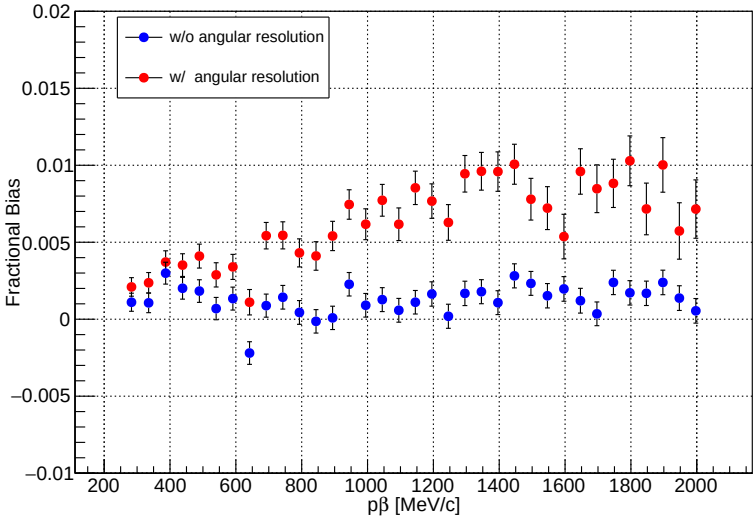

Figure 9.8: Fractional bias of the relative residual distributions of $1/p\beta$ as a function of $p\beta$. The vertical error bars are the statistical ones in the Gaussian fitting [175].

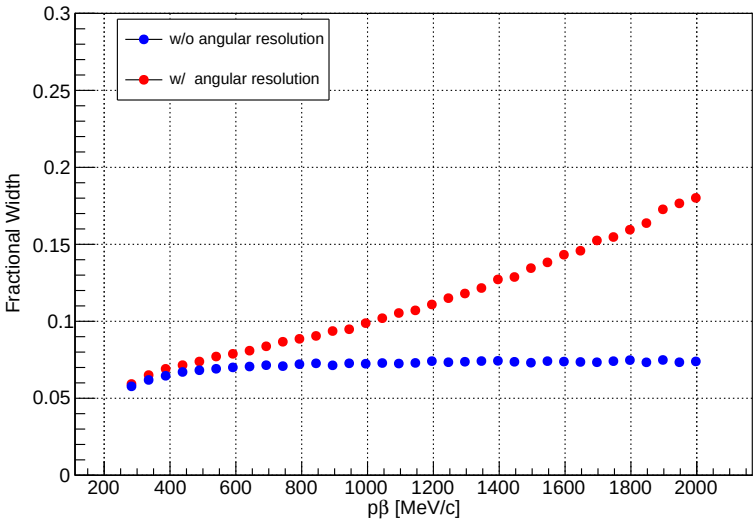

Figure 9.9: Fractional width of the relative residual distributions of $1/p\beta$ as a function of $p\beta$. The vertical errors are negligible [175].

The fractional bias and width as a function of the incident angle of the particle are similarly studied using the particle gun MC simulation. In this study, muons with $p = 500\,\mathrm{MeV}/c$ are generated with different incident angles. The performance is changed from the blue plots to the red ones in Figs. 9.10 and 9.11 for with and without the angular resolution. Here, the muon particle guns are required to penetrate the most downstream emulsion film of the ECC, i.e. muon penetrates 69 iron plates. According to the angular resolution in Fig. 9.4, the performance is expected to be the worst around $\tan\theta = 1$ and become better in the larger angular region. However, the momentum resolution improves with a larger angle for $\tan\theta > 0.6$ in reality. This can be understood by considering not only the angular resolution but also the path length. The angular resolution gets worse with the larger angle in the region of $\tan\theta < 1$, while the path length gets longer. Since the magnitude of MCS increases as the path length becomes longer, the momentum reconstruction shows the worst performance for the smaller angle around $\tan\theta = 0.6$.

Considering the effect from the angular resolution, the momentum resolution is 10–20% in a region of momentum from a few hundred MeV/c to $2\,\mathrm{GeV}/c$ and angle up to $\tan\theta = 1$. The bias is less than 1% up to $p\beta = 1.5\,\mathrm{GeV}/c$. It should be noted that this bias is largely affected by the mis-modeling of the angular resolution. When the angular resolution is mistakenly evaluated to be larger than the reality, it means σ_{HL} is evaluated to be smaller than the "truth" information. Therefore, the momentum of the particle is reconstructed to be higher. This effect is negligible in the low-momentum region where the magnitude of MCS is sufficiently larger than the angular resolution. In Sect. 9.2.3, it is shown with the data that this method is applicable up to $1\,\mathrm{GeV}/c$.

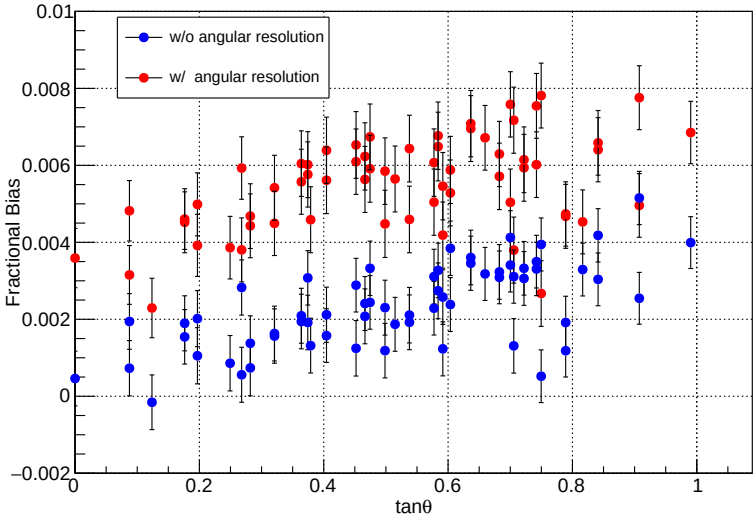

Figure 9.10: Fractional bias of the relative residual distributions of $1/p\beta$ as a function of the incident angle. The vertical error bars are the statistical ones in the Gaussian fitting [175].

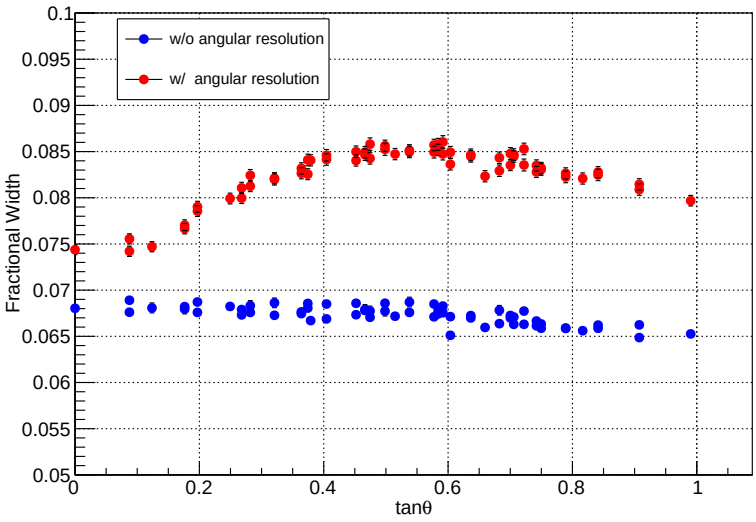

Figure 9.11: Fractional width of the relative residual distributions of $1/p\beta$ as a function of the incident angle. The vertical error bars are the statistical ones in the Gaussian fitting [175].

9.2.2.5 Improvement by the energy deposit implementation

In this new method, the implementation of the energy deposit plays an essential role to improve the performance from the previous method. To study this improvement, the results in

Sect. 9.2.2.4 are compared to the case without the energy deposit implementation. For simplicity, the reconstruction without the energy deposit implementation is studied by setting $\Delta E_i = 0$ in Eq. (9.10), i.e. $p\beta$ is assumed to be unchanged as $(p\beta)_i = (p\beta)_0$ along its trajectory. As mentioned in the previous chapters, it is the similar situation to the previous analyses in the NINJA experiment. The muon particle gun simulation from the most upstream water layer to the downstream is also used in this study. Figures 9.12 and 9.13 show the fractional bias and width of the relative residual distribution of the $1/p\beta$, respectively. When the energy deposit is not considered, the bias is not negligible. In particular, it is more than 10–20% below $p\beta = 500\,\mathrm{MeV}/c$. On the other hand, in a high-momentum region, the bias is expected to be reduced since the fraction of the energy deposit to the initial energy is small. However, the bias is still seen in the region of $p\beta > 1\,\mathrm{GeV}/c$. This bias can be considered as follows. For a $1\,\mathrm{GeV}/c$ muon in the z direction, the total energy deposit in the detector volume is expected to be $0.6\,\mathrm{MeV/unit} \times 69$ iron plates $\simeq 40\,\mathrm{MeV}$ from Fig. 9.5. When we consider the additional energy deposit by the water layers and other materials, it represents 8% of the initial energy. We can assume that the reconstructed momentum value without the energy deposit is the average of the incident and final momenta of the particle in the detector, thus the 8% energy deposit leads to a 4% fractional bias. Since the muons in this region can be considered as MIPs and the energy deposit is independent from the momentum, the bias is smaller for the higher momentum. According to Fig. 9.12, the implementation of the energy deposit in the reconstruction method significantly reduces this bias to less than 1% and improves the measurement accuracy. This reduction of the fractional bias has a large importance in the NINJA physics run. A large portion of the particles to be analyzed have $p\beta$ below $1\,\mathrm{GeV}/c$ with originally 5–25% fractional bias.

The fractional width, which corresponds to the momentum resolution, is mainly determined by the number of the measurements of the scattering angles. Thus, it is not largely changed, particularly in the high-momentum region. In the low-momentum region, on the other hand, the difference is clearer. In this region, the constraint to the initial momentum comes from not only σ but also the ΔE as a function of β. Thus, the momentum resolution also improves when the energy deposit is considered.

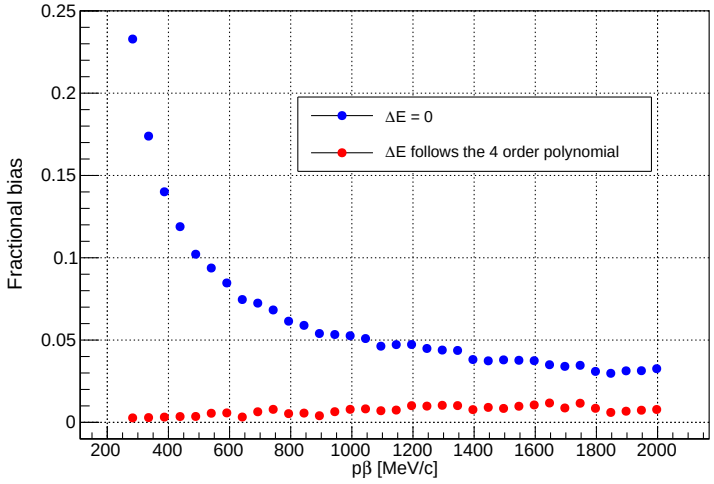

Figure 9.12: Fractional bias of the relative residual distribution of $1/p\beta$ as a function of the momentum with and without the energy deposit implementation. The vertical errors are negligible [175].

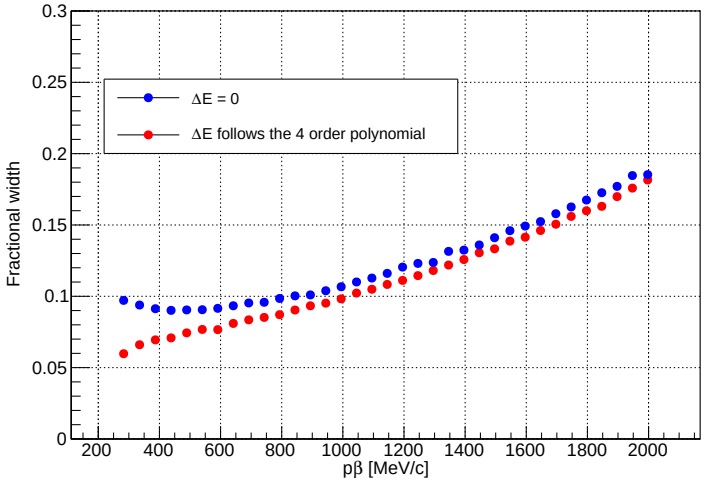

Figure 9.13: Fractional width of the relative residual distribution of $1/p\beta$ as a function of the momentum with and without the energy deposit implementation. The vertical errors are negligible [175].

9.2.3 Performances of the muon momentum reconstruction methods

The momentum reconstruction using the Baby MIND track range can measure the momentum up to 1.5 GeV/c. Figure 9.14 shows the relation between the true and reconstructed momenta of muons from the neutrino interactions using the Baby MIND track range in the MC simulation. The momentum threshold for this method is around 400 MeV/c, and the effect of the scintillator

module structure in Baby MIND is seen. The momentum resolution of the Baby MIND range method is evaluated to be $\sim 8\%$ by the T2K experiment.

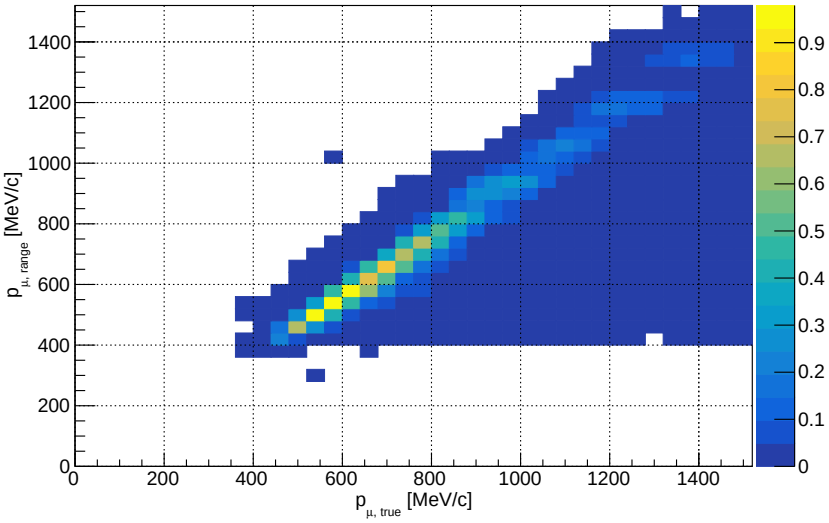

Figure 9.14: Relation between the true and reconstructed momenta of muons from neutrino interactions using the Baby MIND track range in the MC simulation.

Figure 9.15 shows the relation between the true and reconstructed momenta of muons from the neutrino interactions using the ECC MCS in the MC simulation. It starts to saturate around $1\,\mathrm{GeV}/c$ due to the angular resolution. The muon momentum below that value can be reconstructed with the 10–30% momentum resolution depending on the momentum, angle, and the number of iron plates the muon penetrates.

The two methods are compared to each other using the muon sample from the upstream wall of the detector hall. The tracks matched between the ECC and Baby MIND are obtained in Sect. 7.3.3. In addition, the sample is required to be penetrating through ECC5 from the most upstream to the most downstream films. The reconstructed momenta of each track using the two methods are shown in Figure 9.16. The two methods are consistent up to $1\,\mathrm{GeV}/c$ above which the ECC MCS method starts to saturate.

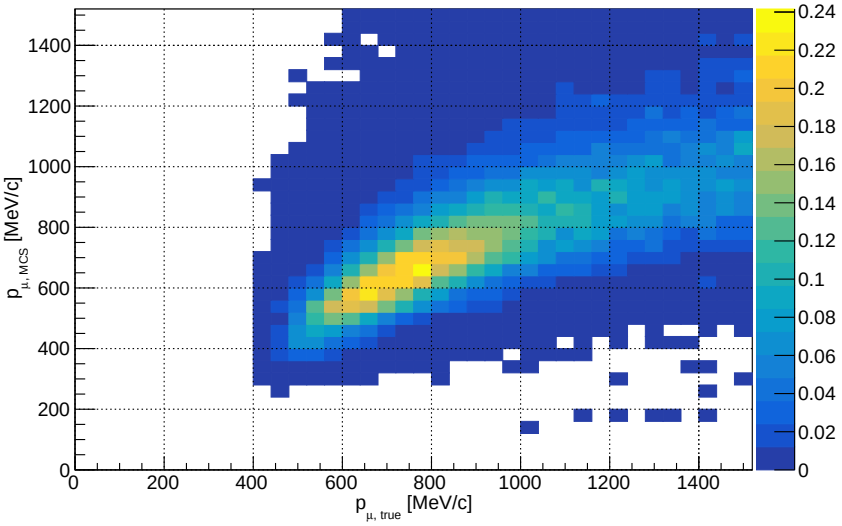

Figure 9.15: Relation between the true and reconstructed momenta of muons from neutrino interactions using the ECC MCS in the MC simulation.

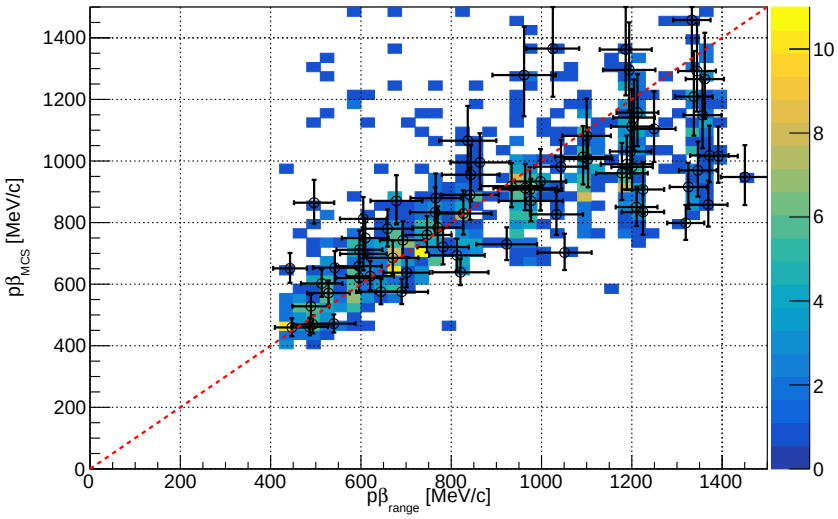

Figure 9.16: Two-dimensional correlation between the momenta reconstructed using the Baby MIND track range and ECC MCS in data. The colored histogram shows all the samples and plots are randomly selected entries (10% of the total entries) [175].

Figure 9.17 shows the residual distribution of $p\beta$ with $400\,\mathrm{MeV}/c < p\beta_{\mathrm{range}} < 900\,\mathrm{MeV}/c$. The bias and width are obtained to be 2% and 13%, respectively, from the Gaussian fitting. The agreement of the two results experimentally verifies the new method of momentum reconstruction with the ECC MCS.

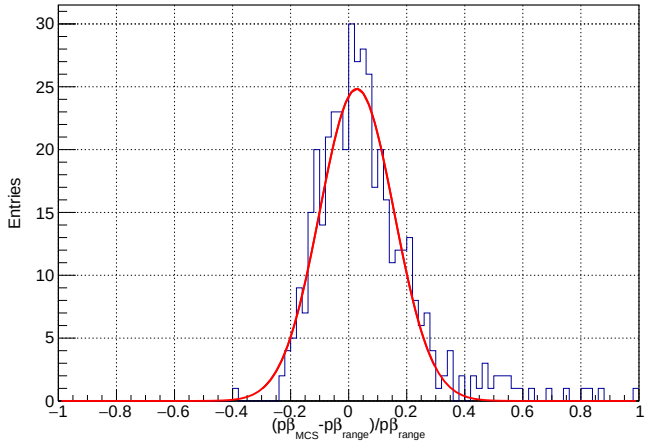

Figure 9.17: Residual distribution of $p\beta$ with $400\,\mathrm{MeV}/c < p\beta_{\mathrm{range}} < 900\,\mathrm{MeV}/c$ [175].

The momentum reconstruction using the ECC MCS is well applicable up to $p < 1\,\mathrm{GeV}/c$ according to the data. The reconstructed value is more accurate than in the previous analysis. In the NINJA physics run, the muons from the neutrino interactions are mainly distributed in this region. Owing to the momentum reconstruction using the ECC MCS, the momentum can be measured for all the muons detected in Baby MIND whether it is stopping inside the Baby MIND FV or not. Thus, combining the momentum reconstruction methods using the track range and ECC MCS gives a large phase space for the muons from the neutrino interaction.

9.2.4 Momentum consistency check

When the muon candidate track is incorrectly matched between the emulsion and scintillator detectors, the inconsistency between the reconstructed values of momentum using the Baby MIND range and ECC MCS arises. Thus, using the two reconstructed values, such mis-matched muon candidate tracks can be rejected. In addition, this check can also remove the case where a hadron is mis-identified as a muon since the Baby MIND track range tends to be shorter for the hadron tracks. The momentum reconstruction using the ECC MCS starts to saturate around $1\,\mathrm{GeV}/c$, while that using the Baby MIND track range does not saturate. Thus, only when $p_{\mathrm{range}} < 1\,\mathrm{GeV}/c$, this momentum consistency check is applied. When the muon track is not stopping inside the Baby MIND FV, the Baby MIND track range only gives the lower limit of the momentum. Thus, if $p_{\mathrm{MCS}} > p_{\mathrm{range}}$, the momentum consistency check is not applied. Otherwise, the difference of the two reconstructed momenta is checked if they satisfy

$$\frac{|p_{\mathrm{MCS}} - p_{\mathrm{range}}|}{\sqrt{\sigma^2_{\mathrm{MCS}} + \sigma^2_{\mathrm{range}}}} < 2.5, \tag{9.14}$$

where σ_{MCS} and σ_{range} are the errors of the reconstructed momenta. If the muon track does not satisfy the condition in Eq. (9.14), it is rejected. For the momentum reconstruction using the ECC MCS, the error is different between the positive and negative sides. The value of σ_{MCS} of the side nearer to the value of p_{range} is used in this check. After the momentum consistency check, 11 out of 93 candidates are rejected. Results of the momentum consistency check are shown in Fig. 9.18 for the muon stopping in and escaping from the Baby MIND FV, separately.

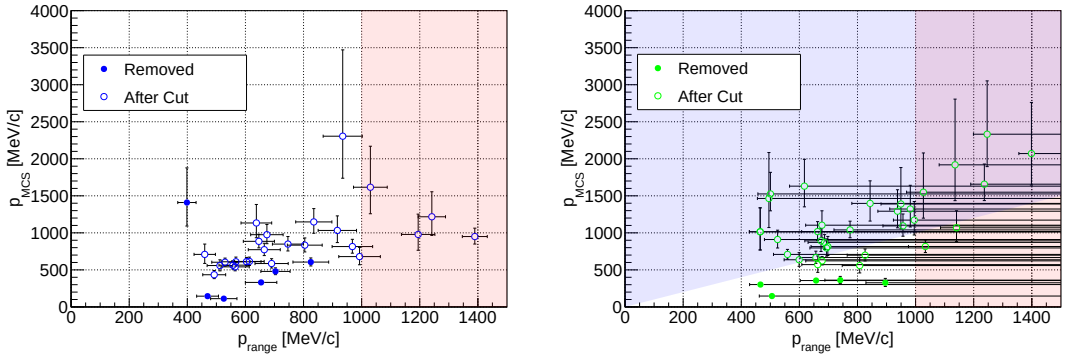

Figure 9.18: Results of the momentum consistency check for the muon stopping inside the Baby MIND FV (left) and that escaping from it (right). The check cannot be applied to events in the red shaded region due to the saturation, nor in the blue shaded region since only the lower limit is obtained from the track range.

9.3 Momentum reconstruction and particle identification of hadron tracks

Muon-like tracks are identified by the track matching between the ECC and Baby MIND. When there are multiple candidates for the muon-like tracks, the longest one in Baby MIND is regarded as a muon, and the other ones are treated as hadron tracks. This section describes the PID of the hadron tracks as well as the momentum reconstruction after that.

9.3.1 Particle identification

The PID of the hadron tracks are performed using the reconstructed momentum using the ECC MCS and VPH. MCS itself gives $p\beta$ independently from the particle as expressed in Eq. (9.1). However, in our reconstruction using the ECC MCS, the energy deposit is considered, and it is dependent on the velocity of the particle. Thus, the assumption of the muon mass in Eq. (9.9) gives a poor reconstruction of $p\beta$ for different particles, in particular protons. Fortunately, the performance of the momentum reconstruction using the ECC MCS with the assumption of the muon mass still gives a sufficient performance of the PID. For each hadron tracks, the momentum is firstly reconstructed by the same method as for muon tracks. Hereafter,

reconstructed $p\beta$ assuming the muon mass is expressed as $(p\beta)_\mu$. Figure 9.19 shows the two-dimensional distribution of VPH and $(p\beta)_\mu$ for $0.5 < \tan\theta < 0.6$. In the low-momentum region, the proton-like and pion-like tracks are clearly separated with larger and smaller values of VPH, respectively.

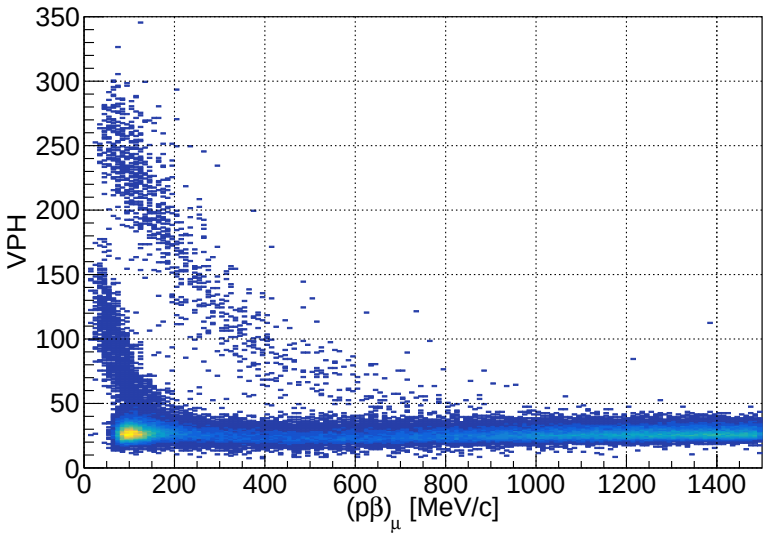

Figure 9.19: Two-dimensional distribution of VPH and $(p\beta)_\mu$ of all the accumulated tracks in the ECC with $0.5 < \tan\theta < 0.6$.

9.3.1.1 VPH correction

The value of VPH is different between each emulsion film because VPH depends on not only dE/dx but also other factors such as the AgBr density in the emulsion gel, different configurations in the development process, the parameters of HTS, and its decrease over time. The values also vary in each sensor of HTS due to the different sensitivities of the sensors. These differences are corrected by calculating the scaling factors for each emulsion gel and each sensor. In addition, the values of VPH are also different in each angle because of the hit pixel detection criteria of HTS.

First, the correction between the sensors are applied. The 72 sensors in HTS are categorized into two groups with the higher and lower sensitivities. To remove the difference between the two groups, the correlation of the mean value of VPH in each group in the same chain is checked.

Next, the correction in each emulsion gel layer is performed. The two-dimensional distributions of VPH and $(p\beta)_\mu$ are generated for angular bins: [0.0, 0.1, 0.2, 0.3, 0.4, 0.5, 0.6, 0.7, 0.9, 1.1, 1.3, 1.5, 1.9, 2.3, 2.7, 4.0] in $\tan\theta$. The chains of protons are preliminarily selected by checking the correlation between VPH and $(p\beta)_\mu$ in each angular bin. For each emulsion gel layer, the mean VPH of the chains is compared to that of the other emulsion gel layers, and the correction factor is obtained so that the two values are the same within the statistical uncertainty.

Finally, the decrease of VPH value over time, so-called "fading" is corrected. Chains in the ECC are connected to the emulsion shifter as described in Sect. 7.3.3 and have four-hour timing information. The change of the mean VPH of such chains are checked for each angular bin. The values of VPH decrease 30% in 100 days. The mean value of VPH over time is calculated, and the values in other timing are scaled to it. The likelihoods of protons and pions are obtained from all the accumulated tracks in the ECC as explained in Sect. 9.3.1.2. The accumulated tracks cannot have timing information because they are not always connected to the emulsion shifter or the scintillation tracker. Thus, this correction should be scaled to the mean value over time to reduce the systematic difference of the VPH distributions.

9.3.1.2 Proton and pion likelihoods

After the correction to VPH, likelihoods for protons and pions are obtained from all the accumulated tracks in the ECC.

First, the probability distribution function (PDF) of MIPs is obtained. The MIP chains are preliminarily obtained from the two-dimensional distribution of VPH and $(p\beta)_\mu$ in each angular bin. The VPH distribution of MIP chains is obtained for each angular bin, and they are treated as the PDF of MIPs. Figure 9.20 shows the obtained PDF of MIPs in $1.3 < \tan\theta < 1.5$. It has a longer tail in the higher VPH side because the number of hit pixels follows the Poisson statistics.

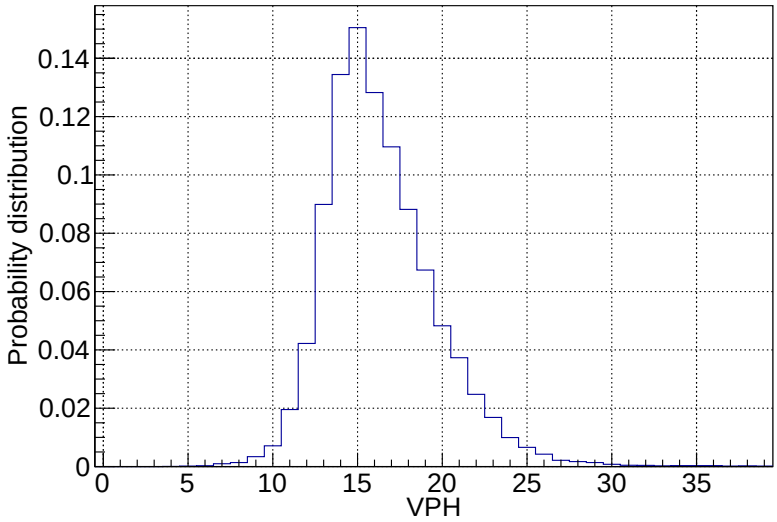

Figure 9.20: Probability distribution function of MIPs in $1.3 < \tan\theta < 1.5$.

When the momentum of protons or pions gets lower, they are no longer MIPs. The PDFs of protons and pions in the non-MIP region are obtained as follows. In each angular bin, the VPH distribution is obtained in each 100 MeV/c bin. The distribution is fitted by one, two, or three Gaussian function(s), which correspond to electron, pion (muon), and proton distributions, respectively. Since the distribution has all the accumulated tracks, there are a lot of electron

tracks from the environmental radioactivity as shown in the left-bottom of Fig. 9.19 although they are negligible in our analysis of the ν_μ CC interactions. The PDFs of electrons, pions (muons) and protons for $0.0 < \tan\theta < 0.1$ and $(p\beta)_\mu < 100\,\mathrm{MeV}/c$ are shown in Fig. 9.21. The mean and width of the pion (muon) and proton PDFs are written as $\mu_{\pi(p)}$ and $\sigma_{\pi(p)}$, respectively.

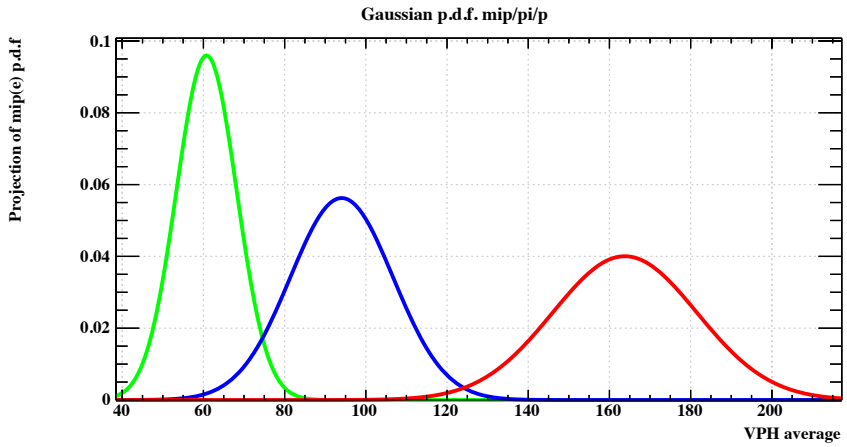

Figure 9.21: PDFs of the electron, pion (muon) and proton for $0.0 < \tan\theta < 0.1$ and $(p\beta)_\mu < 100\,\mathrm{MeV}/c$. The green, blue, and red Gaussians correspond to the electron, pion (muon) and proton PDFs, respectively.

The proton and pion likelihoods are defined as follows. The proton likelihood is expressed as

$$\mathcal{L}_p = \frac{1 + \mathrm{erf}\left(\frac{\mathrm{VPH}-\mu_p}{\sqrt{2}\sigma_p}\right)}{2}, \tag{9.15}$$

which is the right side integral of VPH of the proton PDF. On the other hand, when VPH is smaller than the threshold value, which corresponds to $(p\beta)_\mu = 200(300)\,\mathrm{MeV}/c$ for $\tan\theta > 1.1$ ($\tan\theta < 1.1$), the left side integral of VPH of the MIP PDF is the value of the pion likelihood, $\mathcal{L}_\pi$; otherwise the pion likelihood is expressed as

$$\mathcal{L}_\pi = 1 - \frac{1 + \mathrm{erf}\left(\frac{\mathrm{VPH}-\mu_\pi}{\sqrt{2}\sigma_\pi}\right)}{2}. \tag{9.16}$$

The likelihood ratio is defined as

$$\mathcal{R} = \frac{\mathcal{L}_\pi}{\mathcal{L}_p + \mathcal{L}_\pi}. \tag{9.17}$$

When $\mathcal{R}$ is larger than 0.5, the hadron is identified as a pion; otherwise it is identified as a proton. In addition to that, when $(p\beta)_\mu > 700\,\mathrm{MeV}/c$, the PID is performed only using VPH. If $(p\beta)_\mu > 700\,\mathrm{MeV}/c$ but VPH is larger than a certain value, such a particle is identified as a proton since the momentum resolution of such a low-momentum proton is not good. The value is set to VPH = 125 in this study. Otherwise, the PID cannot be performed since the PDFs are not different so much between pions and protons. In such a case, we only identify the track as

a "charged hadron" or "no-pid."

9.3.1.3 Performance of the hadron PID

Figure 9.22 shows the distribution of the likelihood ratio evaluated by the MC simulation. In each particle in the simulation, VPH is calculated by the MC-truth information of the particle and a random number following the PDFs obtained in Sect. 9.3.1.2. Then, the likelihood ratio is calculated. The evaluation is only performed for the track with $(p\beta)_\mu < 700\,\mathrm{MeV}/c$, i.e. the particle is always identified as a pion or a proton. The proton selection efficiency is evaluated to be 99% with 99% purity, while the pion selection efficiency is evaluated to be 99% with 97% purity for the tracks from the ν_μ CC interactions in the ECC. These high efficiencies and purities are highly important for the study of the ν_μ CC interactions. As mentioned in Sect. 6.1, measurement of the ν_μ CC interactions separated by the number of charged particles in the final state is one of the important goals of the NINJA experiment. The clear separation of the protons and charged pions will make the multiplicity of the charged particles as a powerful tool to study the neutrino interactions.

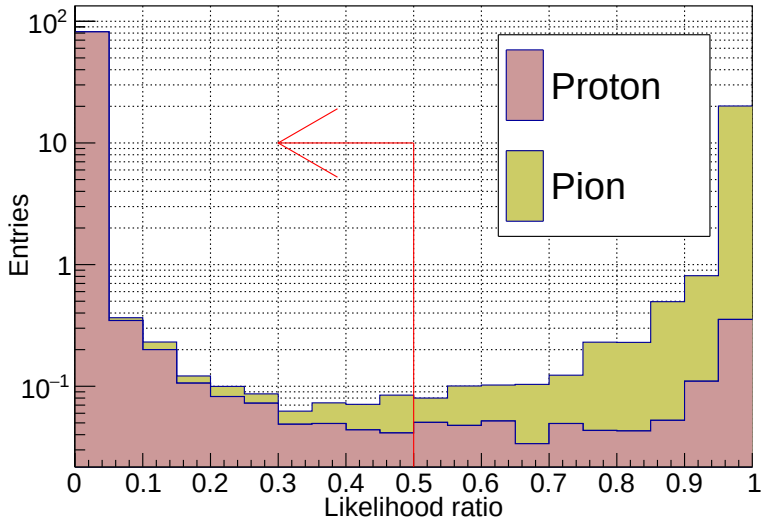

Figure 9.22: Likelihood ratio evaluated by the MC simulation. The red line represents the proton selection criterion.

9.3.2 Hadron momentum reconstruction using the ECC track range

As mentioned in Sect. 9.3.1, the momentum reconstruction needs to be applied after the PID. In addition to the ECC MCS, the track range in the ECC gives a better reconstructed value of the momentum of the proton when the particle is stopping inside the ECC FV.

After the PID, the momentum of the proton is reconstructed using the track range inside the ECC if the track is identified as a proton and satisfies "stopping" criteria below.

- The chain is stopping inside the ECC FV.
- In the MC simulation, the momentum of the most downstream basetrack is less than $200\,\mathrm{MeV}/c$, while in data, VPH of the most downstream basetrack is consistent to the low-momentum proton value (around 200–300).

For the selected tracks, the momentum of the proton is calculated using the continuous slowing down approximation (CSDA). The total track range, R, is calculated from the positional and angular information of each basetrack in the chain. In the CSDA, R can be expressed as

$$R = \int_0^E \left\langle -\frac{dE}{dx} \right\rangle^{-1} dE, \tag{9.18}$$

where E is the initial kinetic energy of the proton, and $\langle -dE/dx \rangle$ is expressed by the Bethe-Bloch formula. From the obtained R, the initial kinetic energy of the proton and thus the initial momentum of it can be reconstructed. Since we require protons to penetrate at least one tracking unit, the momentum threshold is determined to be around $200\,\mathrm{MeV}/c$.

9.3.3 Hadron momentum reconstruction using the ECC MCS

The reconstruction of hadron momentum using the ECC MCS is almost the same as the one for muons. The difference is that M in Eq. (9.9) is not the muon mass but the proton or pion mass. If M is not changed, the reconstructed values would have significant bias. Figure 9.23 shows the relative residual distributions of $1/p\beta$ for proton particle guns with $p = 500\,\mathrm{MeV}/c$. When the protons are reconstructed assuming the muon mass, there is a significant bias, and the momentum resolution is also bad, while the proton mass assumption recovers the reconstruction performance. Thus, after the PID process, the reconstruction should be re-applied although the momentum is already reconstructed assuming the muon mass.

9.3.4 Performances of the proton momentum reconstruction methods

The relation between the true and reconstructed momenta of protons from the ν_μ CC interactions using the ECC track range in the MC simulation is shown in Fig. 9.24. The momentum threshold around $p = 200\,\mathrm{MeV}/c$ can be clearly seen in the distribution, and the resolution is 1–6%.

Figure 9.25 shows the relation between the true and reconstructed momenta of protons from the ν_μ CC interactions using the ECC MCS in the MC simulation. Since the protons have lower $p\beta$ than the muons, the saturation is not clear. The PID limit, $(p\beta)_\mu < 700\,\mathrm{MeV}/c$, corresponds to $p \lesssim 1\,\mathrm{GeV}/c$ for protons, and we cannot reconstruct the meaningful values above it.

The momentum of protons are mainly reconstructed using the ECC track range with a momentum resolution. This resolution is important for the precise measurement of the proton momentum. In addition, the momentum reconstruction using the ECC MCS plays an important role to extend the measurable phase space of the protons.

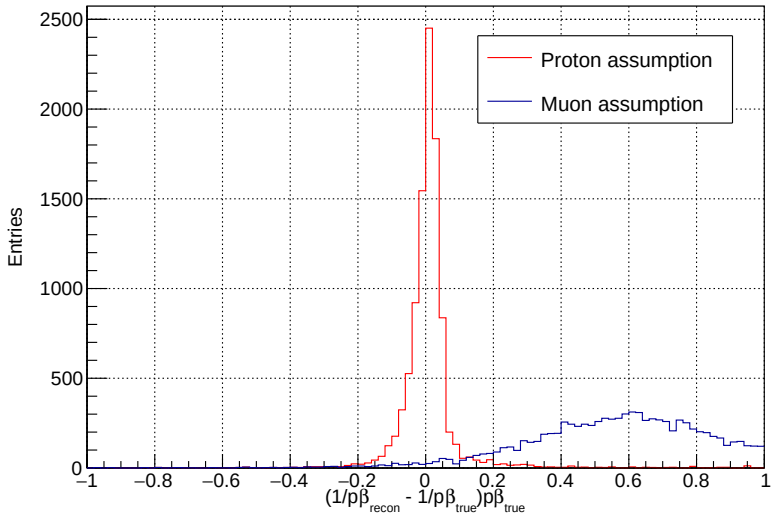

Figure 9.23: Relative residual distributions of $1/p\beta$ for proton particle guns with $p = 500\,\mathrm{MeV}/c$ assuming different particle's mass.

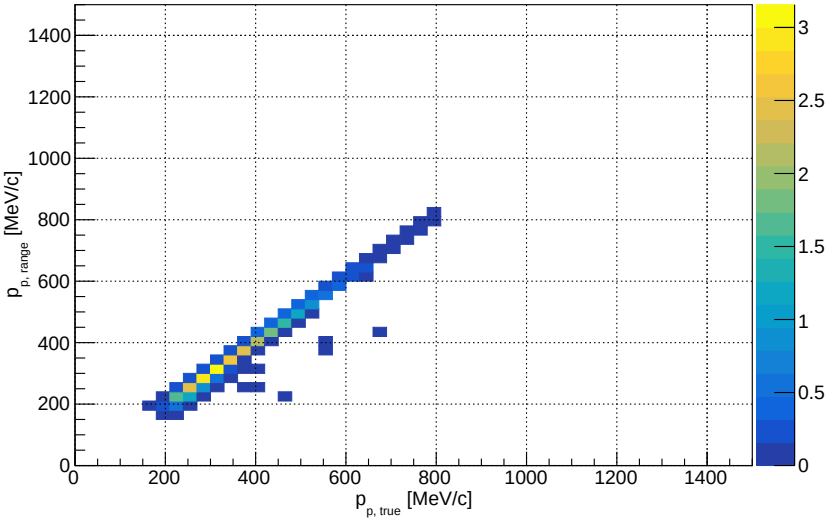

Figure 9.24: Relation between the true and reconstructed momenta of protons from neutrino interactions using the ECC track range in the MC simulation.

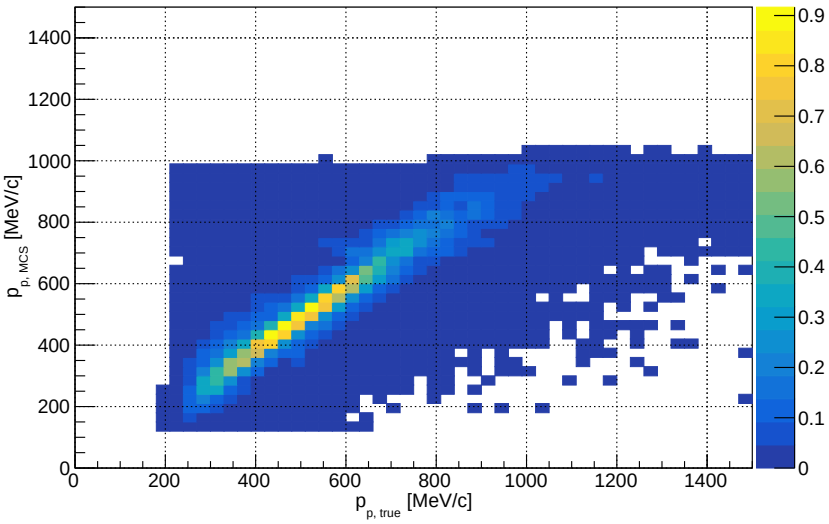

Figure 9.25: Relation between the true and reconstructed momenta of protons from neutrino interactions using the ECC MCS in the MC simulation.

Chapter 10

Results

10.1 Analysis targets

The number of selected events in this analysis is 82, while the number of predicted events is 92.0 as shown in Table 8.1. The statistical uncertainty of the inclusive cross section will be around 10%, which is the similar value to the difference between the data and MC prediction. As mentioned in the previous chapters, the inclusive cross section is not enough to get the information on the mechanism of the neutrino interaction on nucleus. We will rather focus on the direct comparison of the distributions of the reconstructed kinematics between the data and MC prediction. In addition to the preliminary results of the distributions of the reconstructed kinematics, it is also essential to evaluate the efficiencies, backgrounds, and systematic uncertainties toward the measurement of the differential cross sections. In the following sections, the efficiencies, background estimation, and systematic uncertainties are first summarized. Then, the results of the direct comparison of the reconstructed kinematics between the data and MC prediction are presented.

10.2 Efficiency

The event detection efficiency as a function of the true muon kinematics is evaluated by the MC simulation. The efficiency is shown in Fig. 10.1 two-dimensionally. This efficiency is defined as the ratio of the number of muon candidates after the all selections to that of the ν_μ CC interactions in the water target with muon detection in the most downstream film of the ECC. Figure 10.2 shows the proton identification efficiency as a function of the true proton kinematics evaluated by the MC simulation. The efficiency is defined as the ratio of the number of protons correctly identified to that of true protons with at least two basetracks. As mentioned in several times, the proton identification can be done only in the $(p\beta)_\mu < 700\,\mathrm{MeV}/c$ region, which corresponds to $p \lesssim 1\,\mathrm{GeV}/c$. When the true momentum of the proton is higher than the value, it is identified as a proton only when $(p\beta)_\mu$ is reconstructed as less than $700\,\mathrm{MeV}/c$ due to the momentum resolution. Thus, the efficiency gets worse above $p = 1\,\mathrm{GeV}/c$. On the other hand, the proton with its momentum below $200\,\mathrm{MeV}/c$ cannot be detected since we require

the particle to penetrate at least 500 µm of iron. The blank bins around 90° is the region out of our angular acceptance. The angular acceptance of HTS is up to $|\tan\theta| = 5.4$ for microtracks. When we reconstruct a basetrack from microtracks, microtracks are required to have good angular accuracy since the reconstruction is done by the connection of microtracks. We limit the angular acceptance of basetracks up to $|\tan\theta| = 4$ to show reliable measurements. In addition, the difference between $\tan\theta = 4$ and 5.4 is 3°, thus no significant change is expected with our current statistics.

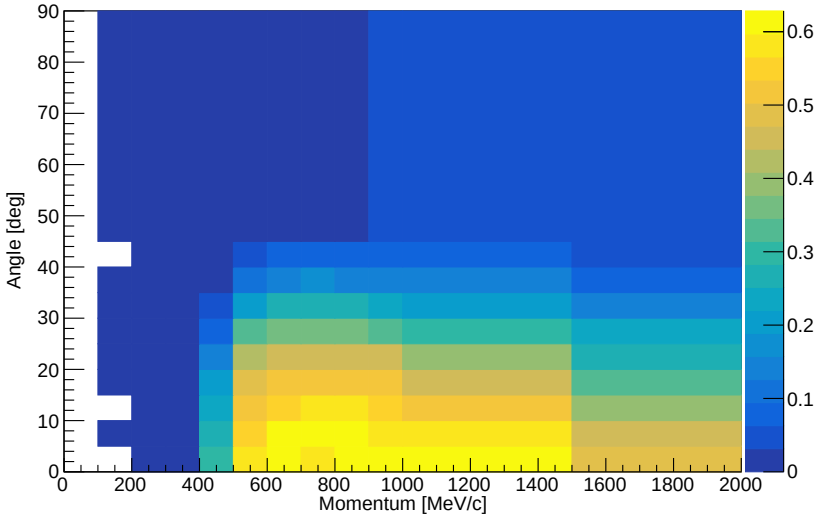

Figure 10.1: Event detection efficiency as a function of true muon kinematics evaluated by the MC simulation.

10.3 Background estimation

To estimate the amount of the background, the following sources are considered. There are beam-related background, which is induced by the neutrinos from the J-PARC beamline, and beam-unrelated background, which is mainly related to all the cosmic-muon tracks in the ECC after the film production and before the development process.

Internal beam-related background

Neutrino interactions in ECC5 other than the ν_μ-water CC interactions sometimes mimic the signal. This type of background is called the "internal beam-related background." Depending on the signal definition, this background can be treated as a signal in other analyses of the NINJA physics run. The most dominant background in this category is the $\bar{\nu}_\mu$-water interactions. Although the neutrino beam is operated in the Forward Horn Current (FHC) mode, which is dominated by a ν_μ component, the neutrino flux has a $\bar{\nu}_\mu$ component. Baby MIND is magnetized and has a capability of discrimination between μ^+ and μ^-, thus ν_μ and $\bar{\nu}_\mu$ CC interactions. However, the charge identification analysis

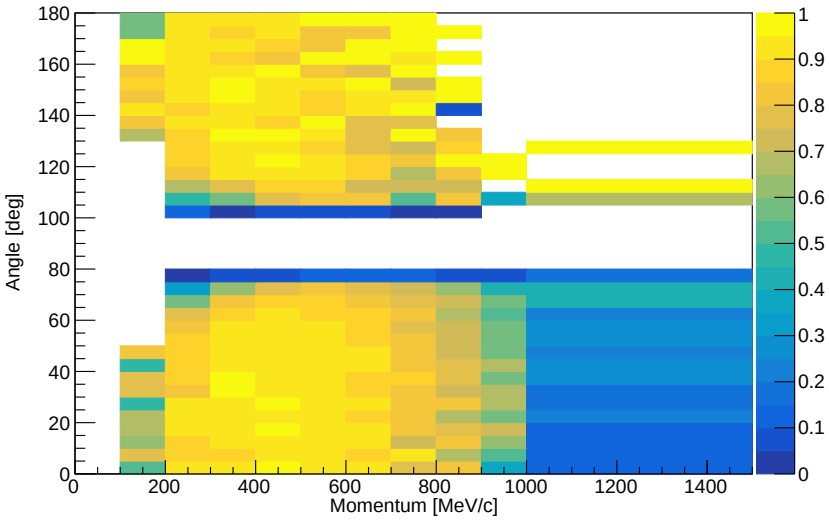

Figure 10.2: Proton identification efficiency as a function of true proton kinematics evaluated by the MC simulation.

is not implemented in this study. Therefore, the $\bar{\nu}_\mu$ CC interaction on water mimics the signal. The $\bar{\nu}_\mu$ interactions are generated in the MC simulation using the $\bar{\nu}_\mu$ flux, and the number of events is evaluated to be 4.2. The ν_μ interaction on the iron target in ECC5 can also be the background when the most upstream basetrack is not correctly identified. The neutrino interactions on iron target are generated in the MC simulation, and the number of backgrounds is evaluated to be 0.8 in total. In fact, neutrino interaction on nuclear emulsion in the upstream and downstream of each iron plate similarly contaminates the signal. The number of backgrounds is scaled by 1.2 according to the total mass. In addition, $\bar{\nu}_\mu$-iron CC interaction is also contaminated, but it is negligible.

For the NC interactions, high-momentum pions or protons are sometimes detected as a three-dimensional track in Baby MIND. These events remain after all event selections. In addition, the high-momentum hadrons from the CC interactions can be identified as a muon while the true muon is not detected as the longest three-dimensional track from the event. The total number of such events is evaluated to be 2.0 by the MC simulation.

For single-track events, the interactions on the packing envelope cannot be excluded since the vertex is automatically determined in the upstream water layer of the most upstream basetrack. We scale the signal prediction of the single-track events by 9% according to the total mass, and it is treated as the background from the neutrino interaction in the packing envelope.

External beam-related background

When a muon from outside of ECC5 is mis-identified to be starting from the inside of it due to the mis-connection or large scattering, they contaminate signal events. Such a kind of background is called the "external beam-related background." Considering the cause

of the background, this background is observed as an event with one or two tracks. The backgrounds caused by the neutrino interactions in the WAGASCI complex, the other ECCs, and the upstream wall of the detector hall are evaluated using the MC simulation and found to be negligible in this study.

Beam-unrelated background

In the ECC, there are lots of tracks accumulated after the film production and before the development. The tracks are mainly attributed to the cosmic muons. When they are mis-identified to be the ones from the neutrino interactions by chance, they become the backgrounds. For example, if the cosmic-muon tracks which look starting from the ECC are matched to a different muon tracks in the emulsion shifter by chance, they become backgrounds to the neutrino interactions. This also happens in the track matching between the emulsion shifter and the scintillation tracker. These backgrounds are called the "beam-unrelated background." In this study, each chain is checked manually, and the backgrounds are found to be negligible. They should be carefully taken into account in detail in near future.

Cosmic muons may also be mis-identified as partner tracks by chance. Fortunately, some of the tracks can be rejected from the partner candidates. The emulsion films were stored with a different arrangement before the beam exposure. Therefore, when the basetracks make chains with the different arrangement, they can be regarded as the cosmic tracks before the beam exposure. We can reject 10% of all the accumulated cosmic-muon tracks by this method. After this rejection, we assume this background is also a negligible level and decide not to consider it in this study.

Partner mis-id background

As described in Sect. 9.3.1.3, the PID is performed with 99% proton identification efficiency with 99% purity when $(p\beta)_\mu < 700\,\mathrm{MeV}/c$. When pions are mis-identified as protons, they contaminate the proton multiplicity and kinematics measurements as the "partner mis-id" background. The background will be 1% of the signal protons. In addition, for the measurement of the proton multiplicity, charged hadron tracks with $(p\beta)_\mu \geq 700\,\mathrm{MeV}/c$ are also considered as a background. When there are partner tracks identified as neither proton nor pion, the event is also considered as the "partner mis-id" background in this study.

10.4 Systematic uncertainty

The sources of the systematic uncertainties are categorized into three: the neutrino flux, the detector response, and the background estimation. In this study, we only compare the data to the MC predictions on the reconstructed distribution basis. The uncertainty of the neutrino interaction models is not treated as the systematic error of the results. Rather the results will test the neutrino interaction models and their uncertainty. Therefore, the uncertainty of the neutrino interaction models in NEUT is separately evaluated. The variation of the number of

events in each bin by the uncertainty of the models are checked. Each source of the systematic uncertainties is evaluated as follows.

Neutrino flux

Figure 10.3 shows the covariance matrix, where the neutrino flux uncertainty and correlations are described. In this analysis, 20 energy bins with their edges: [0.09, 0.1, 0.2, 0.3, 0.4, 0.5, 0.6, 0.7, 0.8, 0.9, 1.0, 1.2, 1.5, 2.0, 2.5, 3.0, 3.5, 4.0, 5.0, 7.0, 10.0 [GeV]] are used. This matrix is obtained from the uncertainties of the hadron interaction in the neutrino beamline and the J-PARC neutrino beamline configurations. The total flux uncertainty of the ν_μ component in the FHC mode beam is shown in Fig. 10.4. Thanks to the external data by the NA61/SHINE experiment, the hadron production uncertainty is reduced from $\sim 7\%$ in the previous analyses to $\sim 5\%$ in the NINJA physics run. The systematic errors from the neutrino flux is calculated using toy MC simulations. According to the covariance matrix, a change of the number of predicted events in each bin of the results is calculated. This process is repeated 10^5 times, and the distribution of the changes is fitted by a Gaussian function. The width of the fitted Gaussian is regarded as the size of the systematic error.

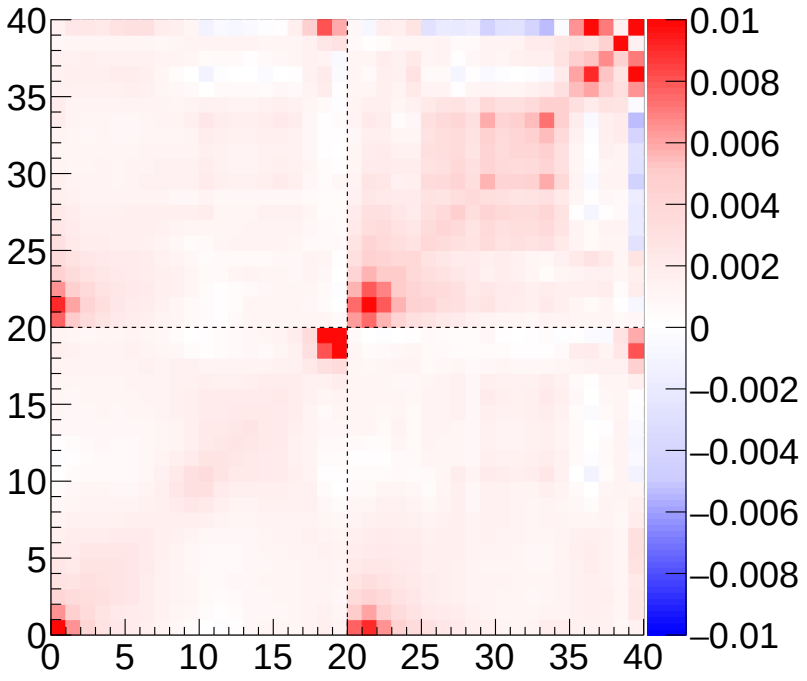

Figure 10.3: Covariance matrix of the flux uncertainties. Bin-id 0–19 and 20–39 correspond to the ν_μ and $\bar{\nu}_\mu$ components, respectively.

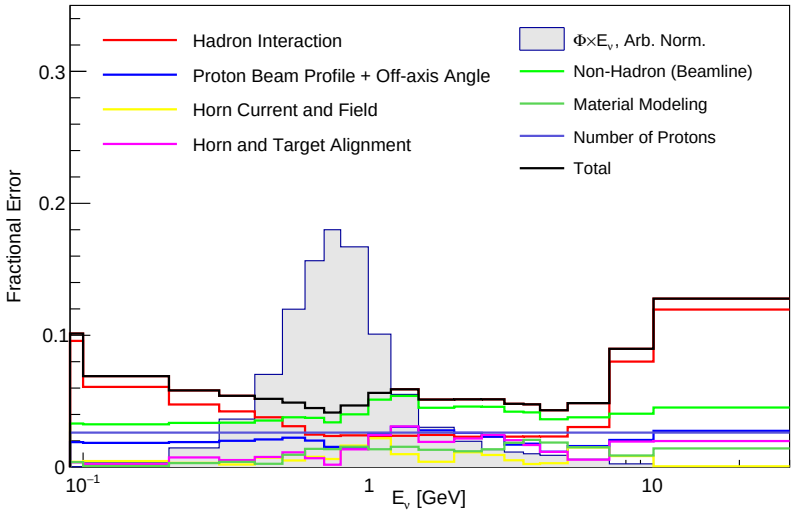

Figure 10.4: Total flux uncertainty of the ν_μ component in the FHC mode beam at the location of the NINJA detectors. The gray histogram corresponds to the flux in an arbitrary normalization.

Detector response

Systematic errors from the detector response are evaluated using the MC simulation and the data obtained during the beam exposure. In the detector simulation, parameters such as the strength of the magnetic field in Baby MIND, the scintillator optical features, and the alignment of the scintillator bars and the detectors are varied, and their effects to the final kinematics distributions are checked. The angular resolution and detection efficiency of the basetracks and the PDFs used in the PID are also varied within their statistical uncertainties. The systematic error from the hadron secondary interaction is evaluated by changing the Geant4 physics list to QGSP BIC (binary cascade) and QGSP INCLXX (Liège intranuclear cascade).

The dominant sources of the systematic uncertainty from the detector response are the MPPC dark noise in the scintillation tracker and the angular resolution of the basetracks. First, the systematic uncertainty from the MPPC dark noise is evaluated as follows. The rate of the dark noise is calculated using the off-beam data taken before the beam exposure. The obtained value is 0.55%, and it is conservatively varied ±100% in the MC simulation. In particular in the low-momentum region of muons, the variance of the number of entries in each bin is around 10%. In the track matching between the scintillation tracker and Baby MIND, if the dark noise makes a one-hit cluster in the scintillation tracker, it is equivalently treated as the other clusters with multiple hits induced by a charged particle. Thus, the three-dimensional track in Baby MIND is sometimes wrongly connected to the one-hit cluster, and the number of events is affected by the dark noise rate. A few ideas to reduce this error are discussed in Sect. 11.1.1.

Next, the systematic error from the angular resolution of the basetracks is evaluated as follows. The angular resolution is evaluated by the statistics of the basetracks accumulated during the beam exposure. The angular resolution used in the smearing of the basetracks in the MC simulation is varied with the statistical error of the obtained resolution. The variance of the angular resolution is considered to affect the reconstructed distributions in several ways. The reconstructed angles of each particle are slightly changed due to the smearing of the most upstream basetrack. The reconstruction of the linklets or chains are performed by the angular differences between two basetracks, and it is also affected. The dominant effect from the angular resolution is the saturation of the momenta reconstructed by the ECC MCS. The momentum reconstruction using the ECC MCS is saturated when the magnitude of MCS and the angular resolution get comparable. The variance of the angular resolution changes the saturation, and in particular in the high-momentum region of the muons, the number of entries in each bin is varied around 7%. Ideas to reduce the saturation are discussed in Sect. 11.1.2.

Background estimation

The uncertainty of the background estimation is separately evaluated from the signal. Since the most of the background is the internal beam-related background, the number of backgrounds is also affected by the neutrino flux, detector response, and interactions. The relative uncertainty of 5% from the neutrino flux, 10% from the detector response, and 10% from the neutrino interactions are assigned as the systematic error from the background estimation, i.e. 15% in total for each bin. Since the background contamination is around 20% at most (in the single multiplicity bin), the systematic error from the background estimation is less than a few %.

Neutrino interaction

In the neutrino interaction and FSI models in NEUT, there are various uncertainties. The uncertainties from these sources are evaluated by varying the parameters in NEUT. Table 10.1 summarizes the nominal values of the parameters in NEUT and their 1σ uncertainties. The distributions of muon kinematics are mainly deviated by the M_A^{QE} and $C_5^A(0)$ parameters, while those of protons are by the M_A^{QE} and pion FSI ones. The total uncertainty from the neutrino interaction models is 10–30% depending on the bins.

The systematic errors for each reconstructed bin are summarized in Figs. 10.5, 10.6, and 10.7. In some bins, the quadrature sum of the errors from the neutrino flux, detector response, and background estimation is comparable or smaller than that from the neutrino interaction models in NEUT. After enough statistics are accumulated, the NINJA experiment has a capability of testing the neutrino interaction models.

Table 10.1: Nominal values of the parameters in NEUT and their 1σ uncertainties.

Parameter	Nominal value	1σ uncertainty
M_A^{QE}	$1.03\,\mathrm{GeV}/c^2$	$0.196\,\mathrm{GeV}/c^2$
Reweight CCQE ($0.25 < Q^2 < 0.5$)	1	0.11
Reweight CCQE ($0.5 < Q^2 < 1$)	1	0.18
Reweight CCQE ($Q^2 > 1$)	1	0.4
SF Optical Potential Correction	0	0.19
2p2h normalization	1	0.2
2p2h shape (delta-like/NN-like for nn)	0	0.2
2p2h shape (delta-like/NN-like for np)	0	0.2
2p2h shape (nn or np)	0	0.33
Resonant SPP E_{B}	25 MeV	5 MeV
Isospin 1/2 non-resonant background	1.3	0.15
$C_5^A(0)$	1.01	0.15
M_A^{RES}	$0.95\,\mathrm{GeV}/c^2$	$0.15\,\mathrm{GeV}/c^2$
DIS/Multi pion normalization	1	0.1
Pion FSI absorption	1.404	0.432
Pion FSI single charge exchange (high E)	1.8	0.288
Pion FSI single charge exchange (low E)	0.697	0.305
Pion FSI hadron production	1.002	1.101
Pion FSI QE scattering (high E)	1.824	0.859
Pion FSI QE scattering (low E)	1.069	0.313
FSI nucleon fate	0	0.3

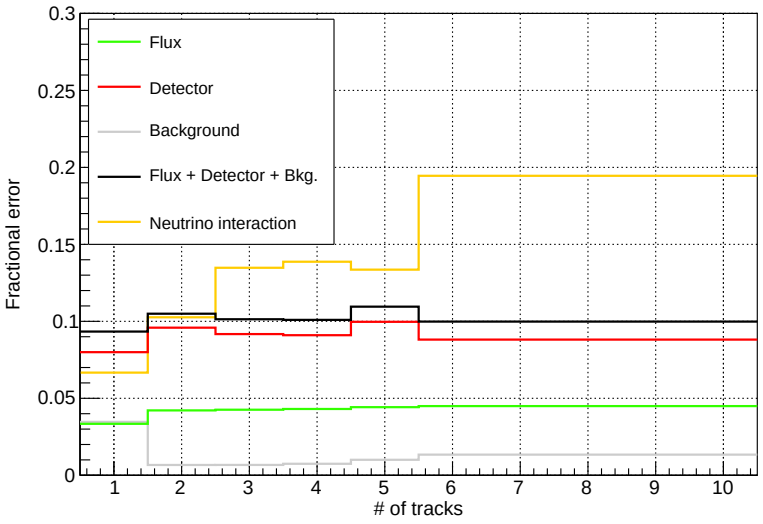

Figure 10.5: Summary of the fractional errors of charged particle multiplicity. The breakdown of the uncertainty of the neutrino flux, the detector response, and the background estimation are shown, and the uncertainty of the neutrino interaction model is compared to them.

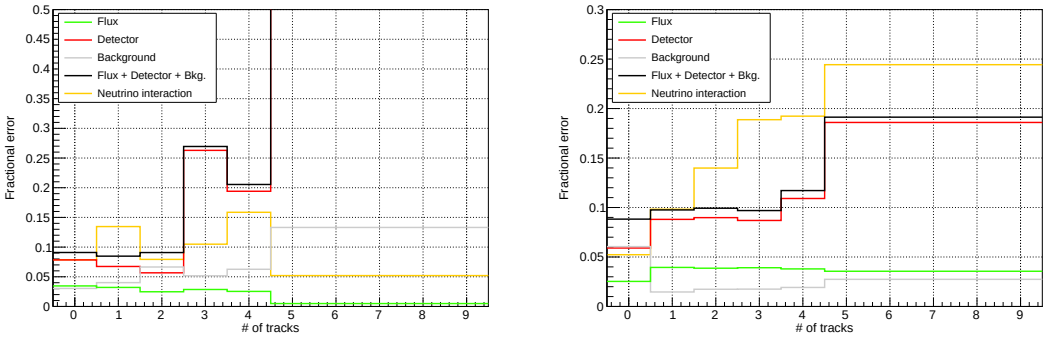

Figure 10.6: Summary of the fractional errors of pion (left) and proton (right) multiplicities. The breakdown of the uncertainty of the neutrino flux, the detector response, and the background estimation are shown, and the uncertainty of the neutrino interaction model is compared to them.

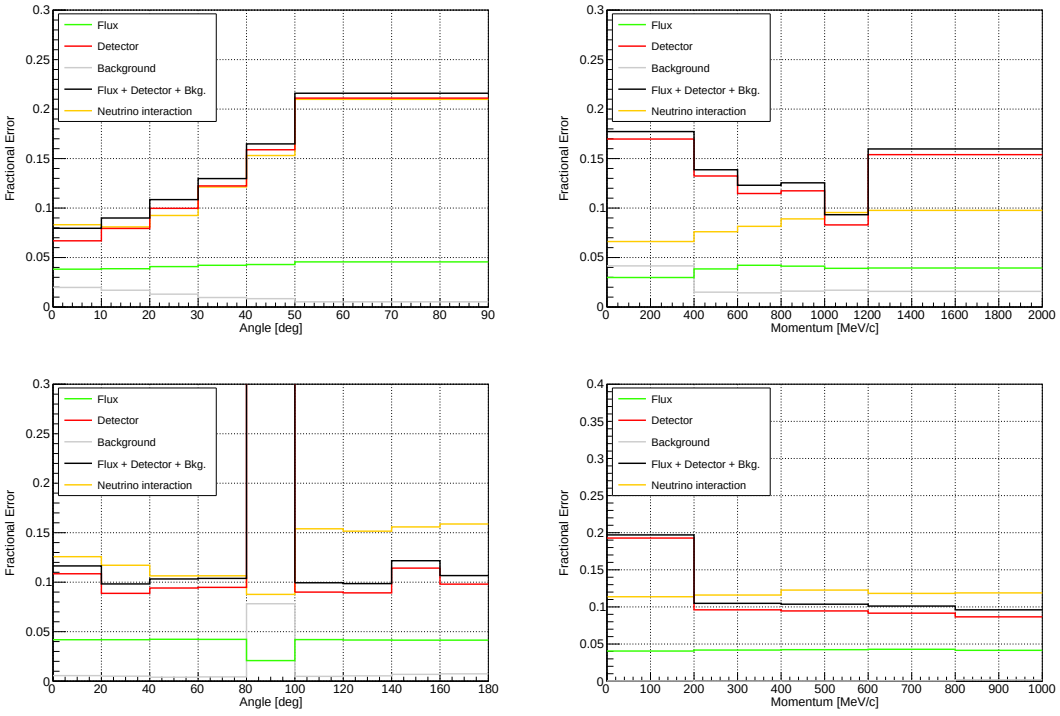

Figure 10.7: Summary of the fractional errors of the muon and proton kinematics. The errors on the muon angle (top left) and momentum (top right), and that on the proton angle (top left) and momentum (top right) are shown. The breakdown of the uncertainty of the neutrino flux, the detector response, and the background estimation are shown, and the uncertainty of the neutrino interaction model is compared to them.

10.5 Measurement results

This section describes the results of the multiplicity and kinematics measurements of the ν_μ CC interactions on water in ECC5. The results are the direct comparisons of the distributions between the data and MC prediction. This comparison is more suitable to get insights into the difference of the data and MC simulation and to demonstrate the performance of the kinematics measurements.

Figure 10.8 shows the distribution of the total multiplicity of the charged particles. The total multiplicity is one of powerful variables to study the neutrino interactions. Since the ECC has high detection efficiency for charged particles in a large phase space, the number of detected particles much directly reflects the number of emitted particles. Thus, this distribution is important for the detailed study of the neutrino interaction modes. In this measurement, the most dominant mode of the neutrino interactions is the charged-current quasi-elastic scattering (CCQE: $\nu_\mu + n \rightarrow \mu^- + p$), which is expected to be detected as the two-track events. It is also important to study some of the charged-current resonant pion productions (CCRES) and 2p2h interactions, where three charged particles are emitted from the primary processes; $\nu_\mu + p \rightarrow \mu^- + p + \pi^+$ and $\nu_\mu + n + p \rightarrow \mu^- + p + p$, respectively. According to the MC prediction, the information of CCQE is expected to be obtained mainly from the two-track events, while that of CCRES can be seen in the two- and three-track events. The 2p2h interactions are also mainly distributed as the two- and three-track events. The number of selected events with one or two tracks are smaller in the data compared to the MC prediction, while the events with larger multiplicity are consistent between them.

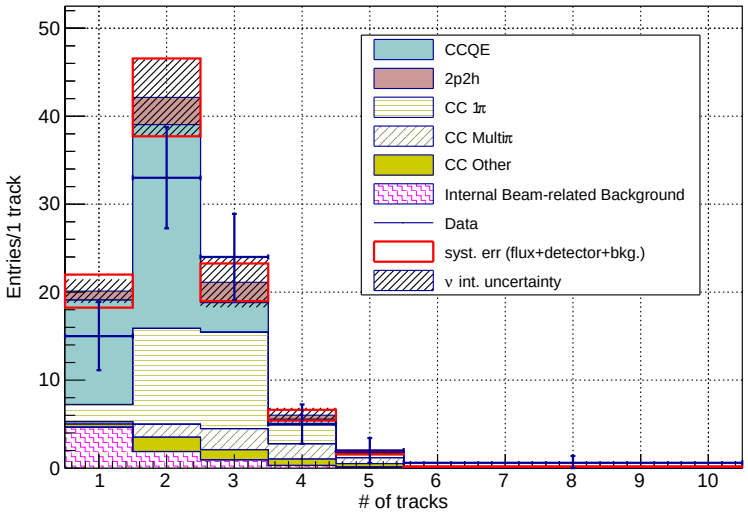

Figure 10.8: Distribution of the total multiplicity of the charged particles.

The distributions of the angle and momentum of the muon tracks are shown in Fig. 10.9. As introduced in Eq. (3.1), the muon kinematics is essential inputs to reconstruct the incoming neutrino energy. Thus, the detailed study of these distributions is important. In addition, the

data is expected to be more consistent with the MC prediction than the other distributions since they are shown to be reliable in other experiments so far. Thus, the consistency between the data and MC prediction demonstrates our performance of the neutrino interaction measurements. Within the error, the angular distribution seems consistent between the data and MC prediction. However, the MC prediction has a tendency of smaller number of events in the forward-angular region. The momentum distribution has, on the other hand, a large discrepancy between the data and MC prediction. The cause of the discrepancy is discussed in Sect. 11.1.

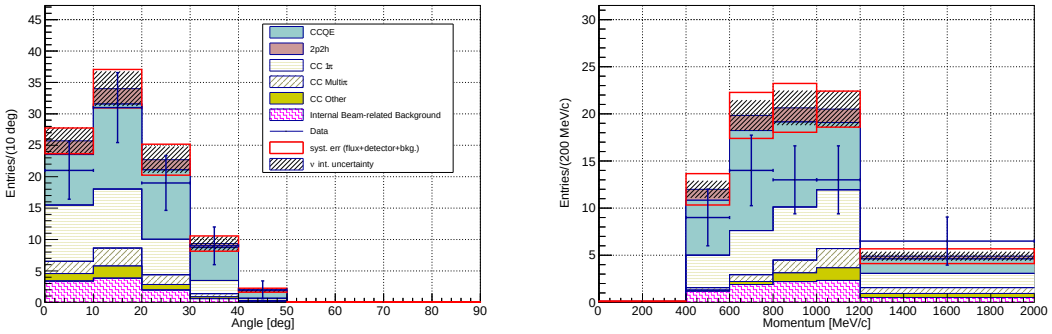

Figure 10.9: Distributions of the muon angle (left) and momentum (right).

The muon momentum can be reconstructed using two methods. The muons stopping inside the Baby MIND fiducial volume are measured with the track range, while the other muons are by the ECC MCS. Figure 10.10 shows the muon momentum distributions separated by the momentum reconstruction methods. Owing to the momentum reconstruction using the ECC MCS, high-momentum muons can be reconstructed. Even in the range of $p_\mu < 1\,\mathrm{GeV}/c$, where the momentum reconstruction using the track range is the major method, the reconstruction using the ECC MCS contributes to increase the statistics of the muons. The distributions also indicate that the discrepancy seen in the muon momentum distribution is due to the momentum reconstruction using the ECC MCS.

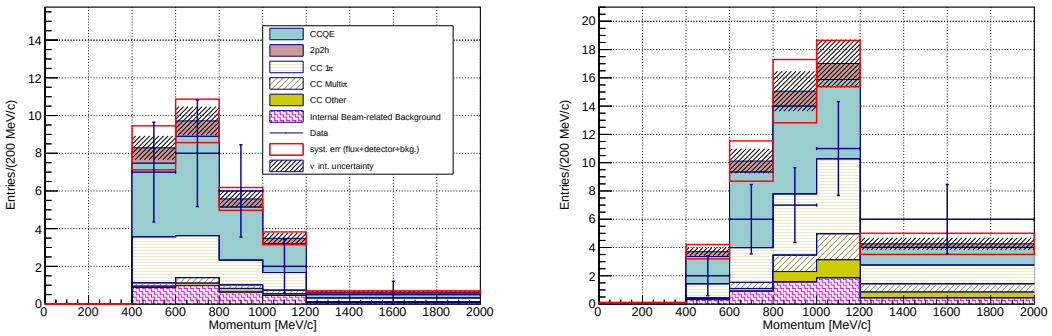

Figure 10.10: Distributions of the muon momenta measured by the track range (left) and ECC MCS (right).

The result of the PID for hadron tracks is shown in Fig. 10.11. The horizontal and vertical axes represent $(p\beta)_\mu$ and the average of VPH for all basetracks constituting the chain, respectively. In particular in the low-momentum region, a clear separation of charged pions and protons can be seen.

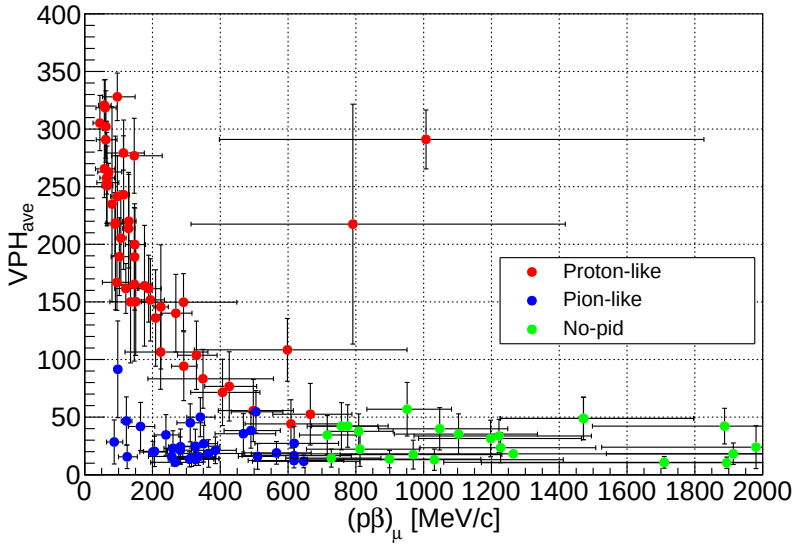

Figure 10.11: Result of the PID for hadrons.

After the PID for the hadron tracks, the numbers of charged pions and protons are obtained. The distribution of the number of charged pions are shown in Fig. 10.12. As seen in the no-pion bin in the MC prediction, the multiplicity after the PID is even stronger tool to discriminate the neutrino interaction modes. This is due to the clear separation of the pions and protons in the PID and the wide coverage of the hadron phase space. Requiring events to have no pion will significantly reject the CCRES and other events, which is highly useful in the study of the CCQE and 2p2h interactions. On the contrary, the events with one pion is concentrated by the CCRES interactions. The number of charged pions is larger in the data compared to the MC prediction.

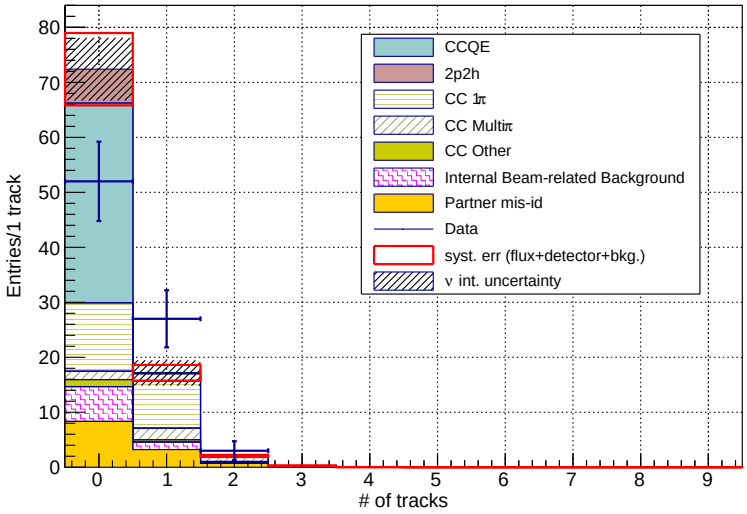

Figure 10.12: Distribution of the multiplicity of charged pions.

Figure 10.13 shows the distribution of the number of protons. This measurement also benefits from the high detection efficiency and PID performance of the ECC. Since CCQE is the dominant interaction mode in this study, the MC prediction expects that the number of events with one proton is the largest. The MC prediction shows that the 2p2h interaction is mainly seen in the one- or two-proton events. In particular, the ratio of the 2p2h interactions to the total two-proton events is relatively high although the statistics are limited. The number of protons is smaller in the data compared to the MC prediction, contrarily to the pion multiplicity.

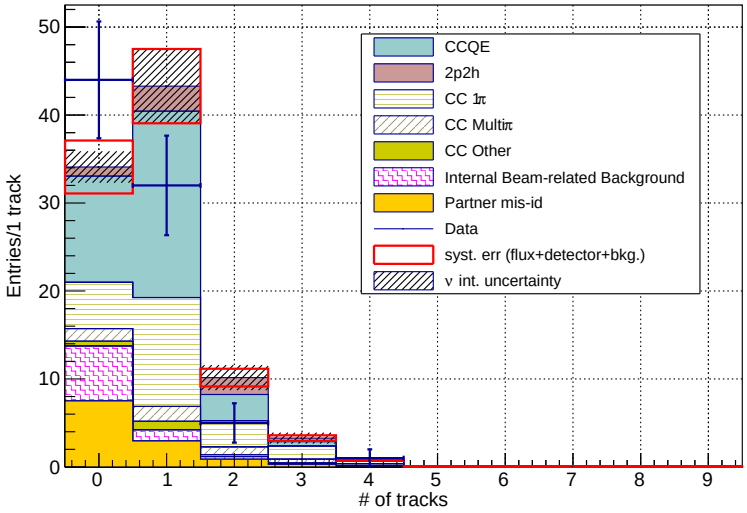

Figure 10.13: Distribution of the multiplicity of protons.

Figure 10.12 indicates that the distributions of protons in CC events without charged pions (CC0π) are more useful in the study of the CCQE and 2p2h interactions since the contribution from CCRES will be highly suppressed. The 2p2h interactions will be more enriched in CC events with two protons and no pions (CC0π2p). The number of protons in CC0π events is shown in Fig. 10.14. The contribution from the other interactions than CCQE and 2p2h is highly rejected. In the two-proton bin, more than 23% of the events come from the 2p2h interactions according to the MC prediction. In addition, the partner mis-id backgrounds are negligible in this distribution owing to the PID. The number of CC0π2p events is 8.2 in the MC prediction, while we observe 4 events in total.

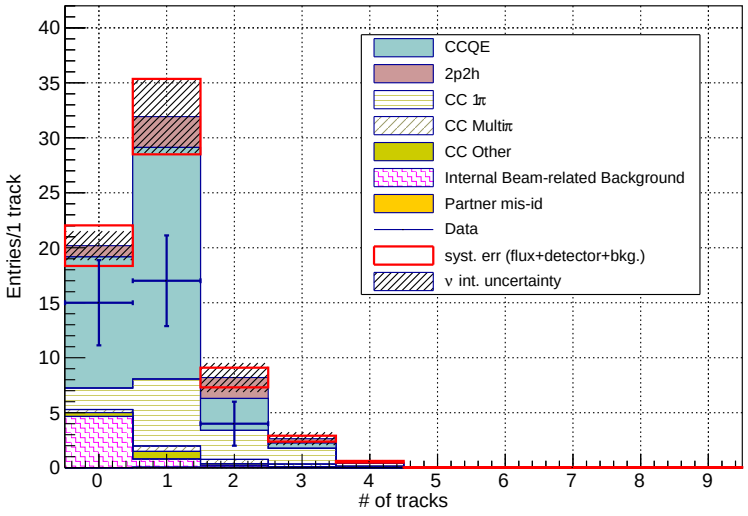

Figure 10.14: Distribution of the multiplicity of protons for CC0π events.

The distributions of the angle and momentum of protons are shown in Fig. 10.15. The proton kinematics is one of the most important observables to understand the neutrino interactions. In particular, the information of the low-momentum protons are essential items to study the nuclear effects. The low-momentum protons mainly come from the CCQE and 2p2h interactions, followed by CCRES as shown in the MC prediction of the proton momentum distribution. In this study, we observe 24 protons in the region of $200\,\mathrm{MeV}/c < p < 400\,\mathrm{MeV}/c$. These protons cannot be directly detected in the other scintillator tracking detectors with the water target, e.g. T2K ND280. As shown in Fig. 10.13, the total number of protons is smaller in the data than the MC prediction. In the data, the total number of protons is 46, while the MC prediction has 77.6 protons. The discrepancy is clearer in the forward-angular region. On the other hand, the momentum distribution does not show the tendency,k but the number of events is smaller in all bins. Although further improvements in the analysis are necessary, we have successfully detected protons with a low momentum threshold of $200\,\mathrm{MeV}/c$ and large angular acceptance of $|\tan\theta| < 4.0$.

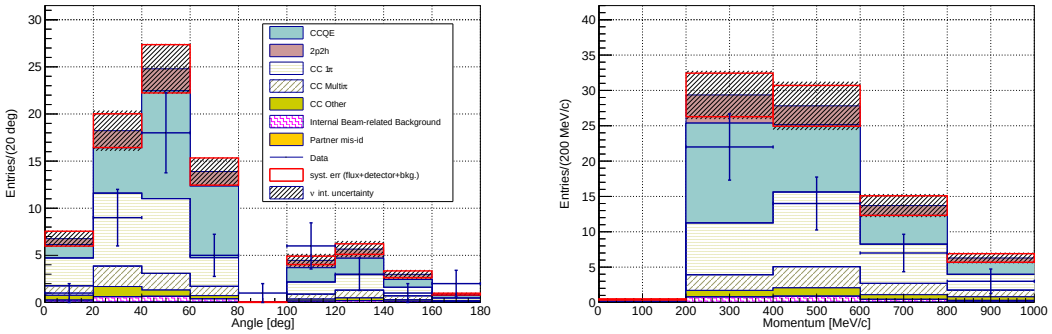

Figure 10.15: Distributions of the proton angle (left) and momentum (right).

Finally, the distributions of the proton kinematics for CC0π events are shown in Fig. 10.16. As already mentioned for the proton multiplicity, these distributions will be more important inputs to study the CCQE and 2p2h interactions. The events are more concentrated by the CCQE and 2p2h interactions as shown in the MC prediction. Comparing Figs. 10.15 and 10.16, the contamination from events with multiple pions are highly reduced after the CC0π selection. The number of protons detected in the data are almost half of the MC prediction, and the tendency of the more deficit in the overall angular region is seen in CC0π events.

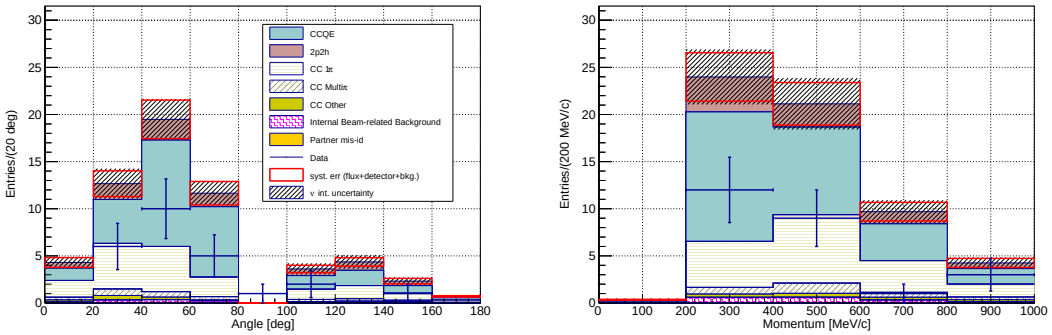

Figure 10.16: Distributions of the proton angle (left) and momentum (right) for CC0π events.

The results shown in this section experimentally demonstrate our performance of the kinematics measurements of charged particles from the neutrino-water interactions. Compared to the previous analyses in the NINJA experiment, the measurements are well improved due to the wider angular acceptance of the film scanning system, the newly introduced detectors, the improved momentum reconstruction, and well understood behavior of VPH and the PID methods. In particular, the PID for hadron tracks and the momentum measurement are well demonstrated, where the momentum reconstruction using the ECC MCS plays an essential role. The improved performance enables us to use the multiplicity of charged particles as a powerful tool in the study of the neutrino interactions, and measurement of low-momentum protons in CC0π events on water target is successfully demonstrated. In addition, the results suggest the necessity of

further improvements of the analysis methods which are discussed in the next chapter.

As for CC0π2p events, which are the most important sample to study the 2p2h interactions, we find 4 events in total. This is the first detection of CC0π2p events on a water target with the 200 MeV/c proton momentum threshold. This threshold value is one of the lowest one among the current neutrino interaction measurements. An example of the event display of a CC0π2p event detected in this study is shown in Fig. 10.17. The low-momentum proton from the neutrino-water interaction is clearly detected in a green track. The momentum of this proton is measured to be 280 MeV/c which cannot be detected in the other measurements of the ν_μ interactions on water.

Using the methods presented in this thesis, the measurement with full statistics in the physics run will be performed in near future. Since we use one out of nine ECCs in this study, the statistics will be roughly nine times larger. The number of protons in the $200\,\mathrm{MeV}/c < p < 400\,\mathrm{MeV}/c$ bin is 24, and the statistical uncertainty is around 20%. These protons from the neutrino-water interactions are difficult to be detected by the other experiments. When the total statistics get nine times larger, the statistical uncertainty will be 7%. We hope the systematic uncertainty in this bin is already reliable and the total uncertainty will be 12%, which is comparable to the systematic uncertainty from the current neutrino interaction modeling. Using the efficiencies, background estimations, and systematic uncertainties, the measurement of the differential cross sections will be performed with larger statistics. The cross section results will be crucial inputs for further understanding of the neutrino-nucleus interactions.

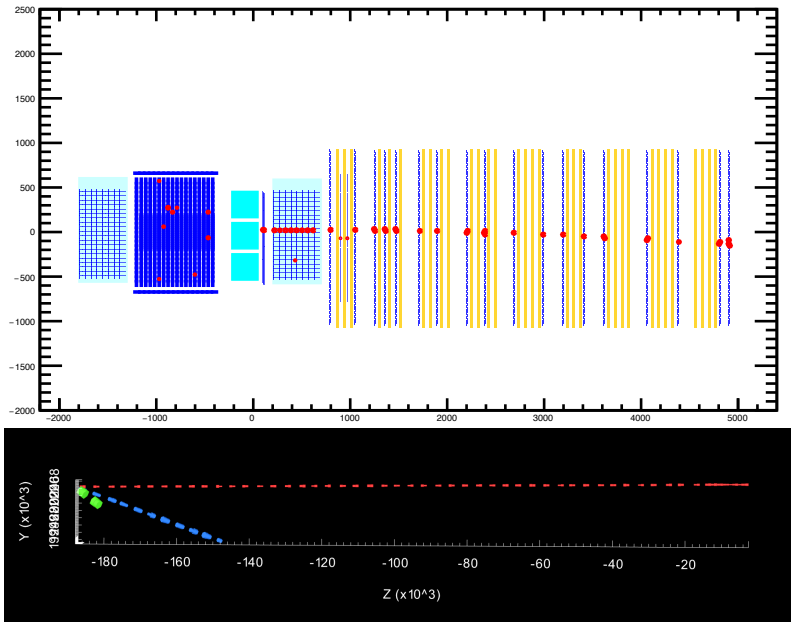

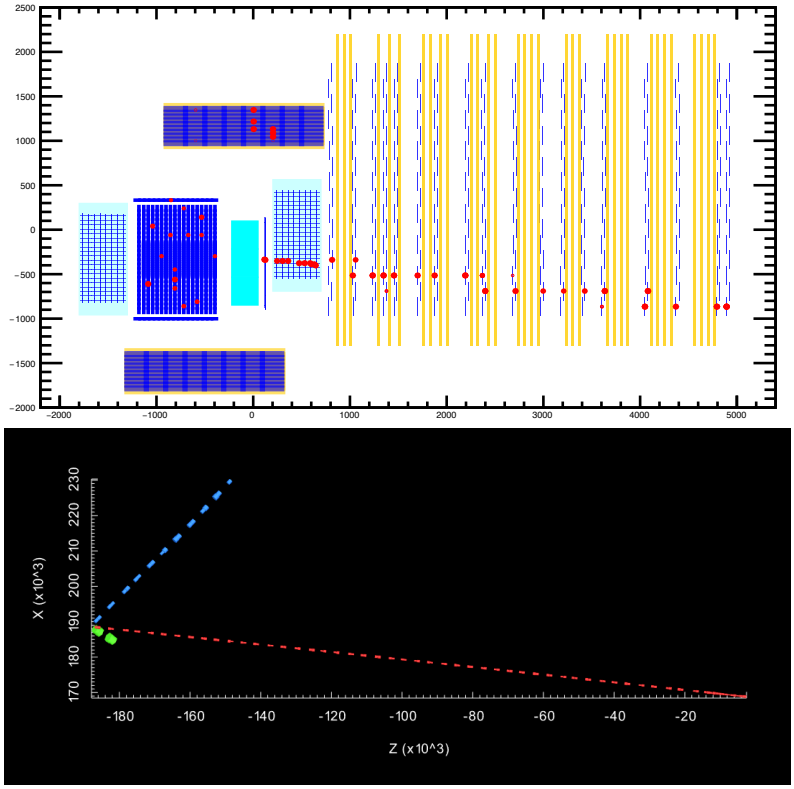

Figure 10.17: Example of the event display of a CC0π2p event. The side (top) and top (bottom) views are shown with the overall (white) and ECC detailed pictures (black).

Chapter 11

Discussions and Future Prospects

The first results of the measurement of ν_μ CC interactions on water in the NINJA physics run are presented in the previous chapters. Although the results demonstrate the performance of the kinematics measurements of charged particles from the neutrino interactions, they also suggest room for several improvements. First in this chapter, the further necessary studies of our detectors as well as the interpretation of the results are introduced. Then, the possible improvements of the analysis techniques are discussed, and finally, the future impact of the NINJA experiment on the long-baseline neutrino oscillation experiments is briefly mentioned.

11.1 Discussions on the measurement results

In addition to the demonstration of the performance of the kinematics measurements, the results shown in the previous section suggest that we need further studies on our detectors. In this section, considerations on the presented results are shown.

11.1.1 Consideration on the muon track matching

The ν_μ CC inclusive cross section is relatively well understood by the other experiments, and the distributions of the muon kinematics are expected to be consistent between the data and MC prediction. Although it is within the statistical error, the number of total selected events is 10% smaller in the data. This difference might be understood through the detailed check of the rejected events. As shown in Sect. 9.2.4, 11 events are rejected in the momentum consistency check. The information of the hits in the surrounding WAGASCI modules are checked for each rejected event. For 10 out of 11 events, the events are consistent with the one where a muon comes from the upstream of the NINJA detectors. This means that the muon track connection between the scintillator detectors and the emulsion detectors are still has room for improvement. The muon from the neutrino interaction inside the ECC happens to be incorrectly connected to another muon from the upstream of the NINJA detectors. In this case, the event detection inefficiency arises unexpectedly. The mis-matching of the tracks between the emulsion shifter and the scintillation tracker is still not fully considered in the MC simulation, but they need to be implemented. A few ideas to improve the track matching are discribed below.

Multiple connection

Although the emulsion shifter and scintillation tracker show good performance of the track matching, the scintillation tracker has a weakness in the reconstruction of the multi-track events. Since the positional and angular resolutions of Baby MIND are not sufficient, there are sometimes mis-matching between the hit cluster in the scintillation tracker and the Baby MIND track. In particular, when the multiple charged particles from the neutrino interaction make several hit clusters in the scintillation tracker, it causes inefficiency or muon mis-identification. It can also happen when the dark noise of the MPPC makes a one-hit cluster. If we accept multiple connections in the track matching and then select the best matching, the inefficiency could be compensated. In that case, the selection of the best matching needs to be also established, which would be done using the positional and angular differences.

Treatment of "multi-hit" clusters

When multiple particles from the neutrino interaction vertex come to the scintillation tracker in a narrow angle, they make one hit cluster in the scintillation tracker with a number of hits. In the current reconstruction method, one candidate of position is reconstructed for one cluster, even if it is actually induced by two or more particles. Thus, the track matching will be difficult in such a case. In the analysis described in this thesis, the muon candidate is identified in the downstream detector, and the vertex is determined by extrapolating and connecting the track from the downstream to upstream. This method is almost free from the beam-unrelated background since the DAQ system of the downstream scintillator detectors is triggered by the beam timing signal. On the other hand, owing to the high-speed film scanning system, the tracks in all the areas of the emulsion films are recognized and reconstructed in the NINJA experiment. Thus, using only the basetrack information, we can also reconstruct the neutrino interaction events although there are large portion of the cosmic background expected. The track matching efficiency could be recovered by extrapolating the tracks from the emulsion shifter to the scintillation tracker. Since the emulsion shifter can clearly separate the tracks which are merged in the scintillation tracker, the positions on the scintillation tracker can be reconstructed for each track using the information in the emulsion shifter. If there are more than one tracks expected on the scintillation tracker, corresponding event candidates can be searched for from the four-hour time window.

11.1.2 Consideration on the momentum reconstruction

The distribution of the muon momentum measured by the ECC MCS has a discrepancy between the data and MC prediction. This discrepancy comes from the mis-modeling of the angular resolution of the emulsion films. The mis-modeling of the angular resolution does not affect the momentum reconstruction of low-momentum particles since the scattering is fairly larger than the resolutions, while it matters in the high-momentum ones. In addition, due to the relatively poor momentum resolution in the high-momentum region, it also affects the low-momentum distribution. The evaluation of the angular resolution in Fig. 9.4 is not so easy. Although the

sample was carefully selected to include the minimum effect of low-momentum particles, it may still include the scatterings by 140 µm of the nuclear emulsion, which corresponds to 0.8 mrad of scatterings for a 1 GeV/c muon. When the angular resolutions are mis-evaluated to be larger than the reality, σ_{HL} is calculated to be smaller according to Eq. (9.7), thus the momentum is reconstructed to be higher than the true value. When we use the twice better value of $\epsilon_{\mathrm{lat}'}$ in the muon momentum reconstruction using the ECC MCS, the distribution is changed as shown in Fig. 11.1. The distribution of the data with the twice better angular resolution agrees better with the MC prediction. Although the change of the angular resolution should be also implemented in the MC simulation, it suggests that we need to consider a more appropriate method to evaluate the angular resolution and implement the systematic uncertainties after that.

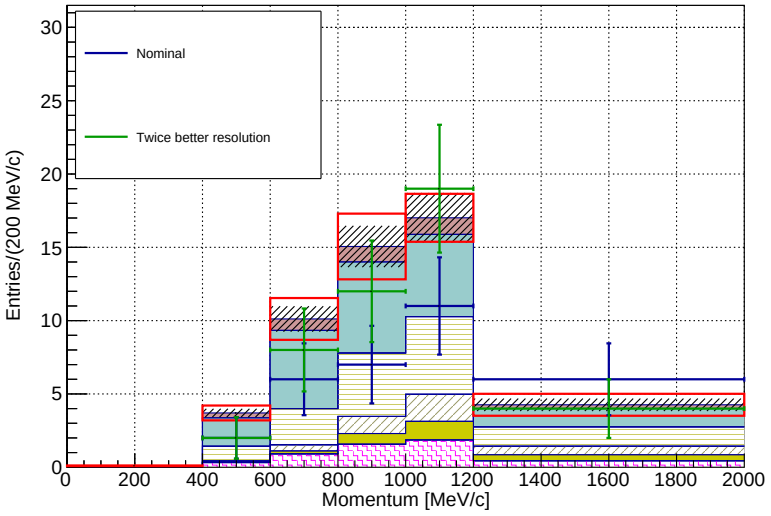

Figure 11.1: Effect of the mis-modeling of the angular resolutions.

11.1.3 Consideration on the proton distributions

As for the proton distributions, the number of protons is smaller than expected. Even though the event detection efficiency is not fully understood, this discrepancy would not be explained only by the efficiency. Thus, this discrepancy could be due to some physics, i.e. the current models in NEUT overestimates the number of forward-going protons. The variation of the number of protons in each bin evaluated in Sect. 10.4 is shown in Figs. 11.2 and 11.3. The dominant contribution is from the M_A^{QE} and $C_5^A(0)$ parameters, which is around 6–10%. The constraints to these parameters are well studied in the T2K experiment, and it is very unlikely that their values are largely different. It would be more likely that our results imply a necessity of the modification of the form factors and the neutrino interaction models. The protons detected in this study cannot be directly detected by the other experiments, and there are little data so far. The uncertainty of the proton kinematics could not be covered by the current models and

parameterizations in the T2K experiment, which would lead to the wrong reconstruction of the neutrino energy.

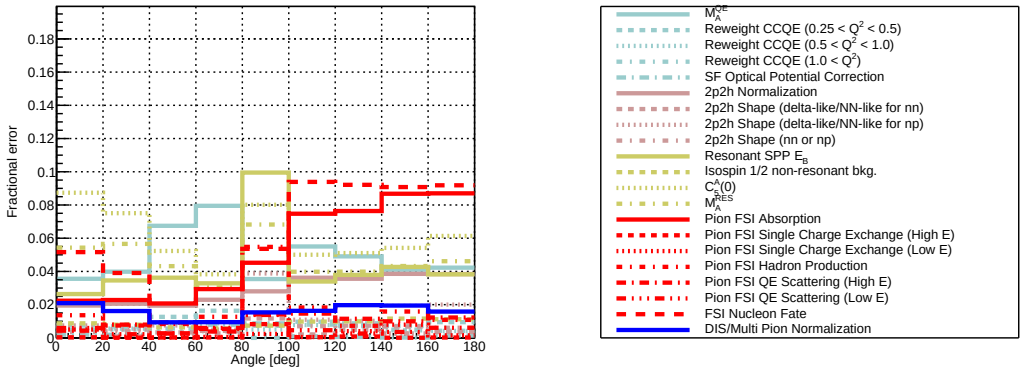

Figure 11.2: Breakdown of the uncertainty in proton angular bins from the neutrino interaction modelings.

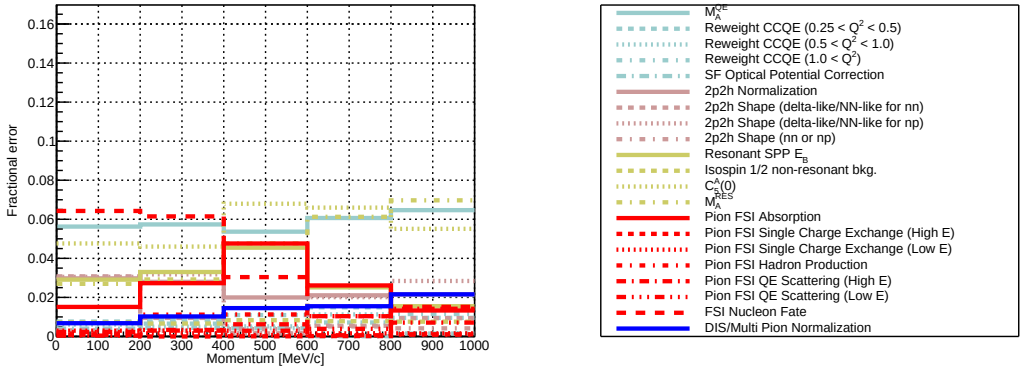

Figure 11.3: Breakdown of the uncertainty in proton momentum bins from the neutrino interaction modelings.

11.2 Improvements in the momentum reconstruction and PID

In this thesis, methods for the momentum reconstruction and PID are established. To achieve even better performances of the analysis, several ideas to improve the momentum reconstruction and PID are described below.

Momentum reconstruction using the ECC MCS in water layers

The momentum reconstruction using the ECC MCS studied in this thesis has room for improvement in addition to the evaluation of the angular resolution. The momentum resolution of the method is mainly determined by the number of measurements of the

scattering angles. In particular, low-momentum protons stop inside the detector volume, which reduces the number of the measurements. The number of the measurements can be increased by considering MCS in the water layers in addition to the iron plates in the likelihood. The magnitude of MCS in a 2.3 mm water layer is typically about half of that in the 500 µm iron plate, but it still has an impact on low-momentum particles which scatter largely enough compared to the angular resolution. Without considering the angular resolution, the momentum resolution is evaluated to be 5% using scatterings in both water and iron, while that is 7% with scatterings in only iron.

Reconstruction of higher momentum particles using the ECC MCS

In the high-momentum region, the saturation of the reconstructed momentum value is the main problem. Since the magnitude of MCS is smaller than the angular resolution for high-momentum particles, it is biased to the lower momentum value. In the previous analyses of the NINJA experiment [168, 170], "coordinate method" is applied, which uses the positional differences of the tracks instead of the angular differences. Since the RMS of the positional differences is proportional to $(w/X_0)^{3/2}$ and the positional resolution is proportional to w/X_0, the method can be applied in the high-momentum region with pairs of the emulsion films skipping several films. In the previous analyses, the method can be applied for muons up to 5 GeV/c. Another idea of improvement in the high-momentum region is similar to but slightly different from the coordinate method. The scattering angle calculated from a pair of the emulsion films skipping more than one iron plate should show a larger magnitude of MCS since the particle is more scattered by the materials. The angular resolution, in principle, does not change by the number of skipped iron plates. In this case, the number of the measurements decreases, i.e. the momentum resolution will get worse, while the saturation will be reduced. For example, the magnitude of MCS across three iron plates is typically comparable to the angular resolution when $p\beta = 1.9\,\mathrm{GeV}/c$. In this idea, the likelihood defined in Eq. (9.8) does not change, thus extension will be easier than the coordinate method in our current analysis.

Finally, using a combination of the scattering angles (and positional differences if possible) between a pair of films over N ($N = 1, 2, 3, \dots$) iron plates would give much more precise information. It should be noted that the scattering angles over the different number of iron plates are correlated between each other, and they should be treated simultaneously in the likelihood considering the correlation.

New variable to measure the energy deposit

VPH is a useful variable and has been used in analyses of the nuclear emulsion films for a long time. However, the definition of VPH is somewhat complicated, and thus it is not easy to construct models to convert from dE/dx to VPH. In the new method of the track reconstruction in emulsion gel, we select hit pixels along the track projected to the x-y plane. The number of hit pixels is almost proportional to the projected path length $\sqrt{1 + \tan^2\theta_x + \tan^2\theta_y}$ and dE/dx. Thus, it will be simpler to convert the obtained information into the particle's dE/dx using the number of hit pixels. While VPH is

difficult to calculate from the true dE/dx, the number of hit pixels could be easier to be modeled and implemented in the MC simulation. A better understanding of the systematic uncertainties in the PID would be achieved with a more comprehensive simulation.

Simultaneous PID and momentum reconstruction

In the current analysis of the NINJA experiment, we firstly reconstruct the momentum of hadrons using the ECC MCS assuming the particle has a mass of muon, and then the PID is applied. However, the momentum reconstruction using the ECC MCS should have a capability of PID. In the low-momentum region, the energy deposit of the particle is clearly reflected to the likelihood as shown in Fig. 9.12. The energy deposit in a unit of length is a function of β, whereas MCS is a function of $p\beta$. Thus, the different values of the particle mass result in the different values of the likelihood. The best value of the particle mass may be selected from the smallest negative log likelihood value. Using the value of the likelihoods assuming each particle's mass, it could be possible to constrain the type of the charged particle.

Another idea is to implement VPH (or the number of hit pixels) in the likelihood. If we can get the response function of VPH from dE/dx, the function can be also considered in the likelihood as a penalty term:

$$L' = L \times \prod_{j=0}^{N-1} \exp\left[-(g_j(\Delta E_j) - \mathrm{VPH}_j)^2\right], \tag{11.1}$$

where $g_j(\Delta E)$ is a penalty term constructed from the response function, and VPH_j is the averaged VPH of the j-th tracking unit. Here, the strength of the penalty should be modified in practice. Since the response function should be different between each particle as shown in Fig. 9.19, this likelihood could constrain the particle type using both MCS and VPH simultaneously. If this idea is realized, the re-application of the momentum reconstruction using the ECC MCS will be no longer necessary.

In addition to MCS and VPH, the track range inside the ECC volume could also improve the simultaneous analysis of the momentum reconstruction and PID. When the particle is stopping inside the detector, $\sum_j \Delta E_j$ should be similar to the initial kinetic energy of the particle, E. Thus, we can include the range information in the likelihood as

$$L'' = L' \times \exp\left[-\left(E - E_0\right)^2\right]. \tag{11.2}$$

Here, E is reconstructed using the continuous slowing down approximation (CSDA) and ΔE_j in the momentum reconstruction using the ECC MCS, while E_0 is calculated from $(p\beta)_0$. This likelihood also considers the consistency between the momentum reconstruction using the track range and ECC MCS. The momentum reconstruction using the track range could be automatically applied by selecting the smallest negative log likelihood value.

11.3 Future prospects

In the previous chapter, the distributions of the muon and proton kinematics are shown. Using the methods described in this thesis, the NINJA experiment can contribute to other various subjects about the neutrino interactions. The future prospects of the study of ν_μ CC interactions in the NINJA experiment are described in this section.

11.3.1 Measurement of CC$0\pi Np$ events

As discussed in Sect. 3.3.2, the measurement of CC$0\pi Np$ events is important to understand the neutrino interaction models. The low momentum threshold for protons in the NINJA experiment will highly help the further understandings of the nuclear effects in various ways. A few possible measurements are described below.

Single transverse variables in CC0π1p events

Measurements of the single transverse variables (STVs) for CC$0\pi 1p$ events are already performed in the T2K and MIVERνA experiments. The STV is considered to represent the nuclear effect including the Fermi motion, nucleon-nucleon correlations, and FSI. For example, the results from the MINERνA experiment in Fig. 3.14 show that the different FSI leads to the different distribution of $\delta\alpha_T$ in Eq. (3.16). According to the results in Chap. 10, CC$0\pi 1p$ events detected by the NINJA experiment are more enriched by the CCQE interactions than those detected by the other experiments, owing to the wide coverage of the proton phase space. Thus, the STV measured by the NINJA experiment will contribute to separate such nuclear effects from the CCRES and 2p2h interactions. Figure 11.4 shows the distribution of $\delta\alpha_T$ measured in this study. In particular in the region of $\cos\delta\alpha_T < 0$, the distribution is enriched by the CCQE interactions. The $\cos\delta\alpha_T < 0$ region is considered to be dominated by the decelerated protons, and such a nuclear effect could be tested for the CCQE interactions with small backgrounds.

Proton opening angle in CC0π2p events

The results from the LArTPC experiments show the proton kinematics of CC$0\pi 2p$ events, but the interpretation to the physics is still not clear. The NINJA experiment can also measure the proton kinematics for the neutrino-water interactions. The CC$0\pi 2p$ events measured by the NINJA experiment will be a 2p2h enriched sample, and they will be important inputs for the study of the 2p2h interactions on water target. The distribution of the opening angle of two protons in CC$0\pi 2p$ events in the lab frame (written as γ) is shown in Fig. 11.5. A considerable amount of the events are the 2p2h interactions, and each interaction mode has a different distribution. For instance, the 2p2h interaction tends to have more events in the $\cos\gamma < 0$ region.

11.3.2 Measurement of low-momentum pions

The information of pions from the neutrino interaction which can be detected in Super-Kamiokande will be important in the T2K experiment since the T2K experiment nowadays starts to use sam-

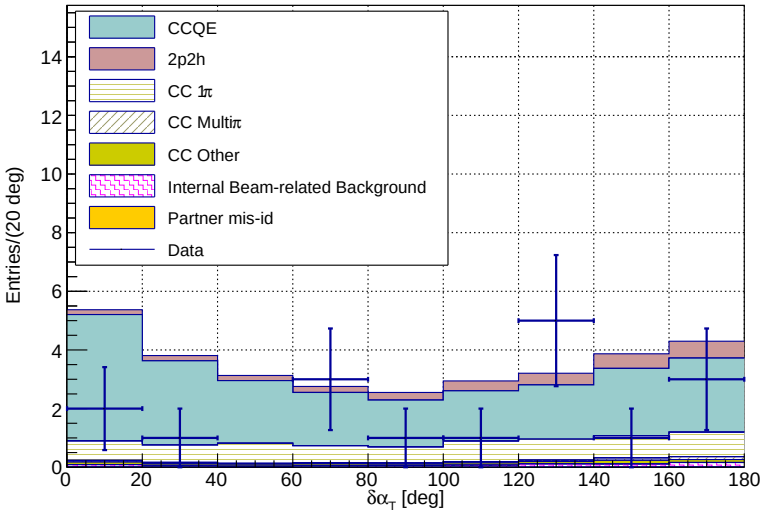

Figure 11.4: Distribution of $\delta\alpha_T$ for CC0π1p events.

ples with charged pions in their final state in the oscillation analysis. When the pions from the ν_μ CC interaction are not detected, it mimics the CCQE interaction. Recently, the NINJA experiment has shown that the number of low-momentum pions emitted backwardly from the neutrino interaction on iron is larger than the prediction of NEUT as shown in Fig. 4.5. Further understanding of the pion production with low momentum threshold is anticipated. As shown in Fig. 10.11, low-momentum pions can be clearly separated from protons in the current analysis method of the NINJA experiment. The pion measurement results with high PID efficiency will be important inputs to the construction of the neutrino interaction and FSI models.

11.3.3 J-PARC E71b

The next physics run of the NINJA experiment, or J-PARC E71b, is planned in autumn of 2023. It is planned to install four times larger target in the same location. The detectors will be exposed to the neutrino beam corresponding to 5.0×10^{20} POT. The four times larger statistics will allow us to measure single- or double-differential cross section of the neutrino interaction on water for the first time in the NINJA experiment. According to the systematic uncertainties evaluated in this thesis, the results from the NINJA experiment with higher statistics will have a capability of testing and constraining the neutrino interaction models. Using the higher statistics, the NINJA experiment can obtain the double-differential measurement in the next physics run. The events are analyzed in more detail, and the results shall give a large impact on the understanding of the nuclear effects and neutrino interactions.

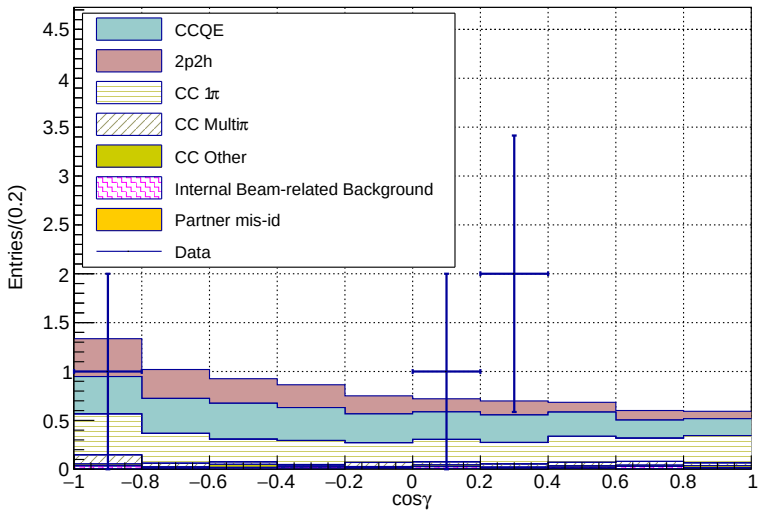

Figure 11.5: Distribution of the opening angle of two protons in CC0π2p events in the lab frame.

11.4 Impact on long-baseline neutrino oscillation experiments

In this study, we have shown that the NINJA experiment can measure hadron kinematics which have so far not been measured. In the current and future long-baseline neutrino oscillation experiments, it is important to understand the neutrino interactions for the discovery of the CP violation in the lepton sector and the precise measurement of the parameters in the PMNS matrix. In the T2K experiment, the flux and neutrino interaction models are constrained by the data measured by ND280. The most straightforward use of the data measured by the NINJA experiment is to combine them to the ND280 ones and constrain the parameters simultaneously. A previous study shows that some parameters of the neutrino interaction models are more constrained by the inclusion of the NINJA data to the neutrino oscillation analysis [174]. However, the total error in the measurements of the oscillation parameters does not change so much. It can be said even for the situation with the larger statistics, i.e. results from nine ECCs or J-PARC E71b. This is because the set of the models and their parameters used in the T2K experiment is selected so that the analysis is robust to the hadron kinematics. The measurements of the oscillation parameters are not so sensitive to the low-momentum hadron kinematics where the NINJA experiment plays an important role.

Even if the measurements from the NINJA experiment is not effectively contribute to reduce the current systematic error of the oscillation parameters, it does not mean that the results from the NINJA experiment are meaningless. As shown in Table 2.3, the systematic error from the neutrino interaction models after the ND280 constraint is a few % level nowadays. This uncertainty is based on the current-best knowledge on the neutrino interaction and FSI models. These models are constructed using various inputs such as the cross-section measurements from the T2K ND280 and MINERνA experiments, the results from the bubble chamber experiments,

the electron scattering experiments, and theoretical considerations. However, there are still not well-known parts due to the lack of the sufficient experimental results as described in Chap. 3. If the set of the models and their parameters is not perfect and some uncertainties are not covered by them, the results from the neutrino oscillation experiments would be biased. In the T2K experiment, such effects are checked by a set of "fake" data [33]. The fake data are produced by changing the neutrino interaction models in the MC simulation. The fake data are fitted with the nominal models in the same way as the real data, and the biases of the obtained value of the oscillation parameters are checked.

These checks using the fake data may still not be perfect, in particular for the low-momentum hadrons which cannot be directly detected by ND280. The NINJA experiment can provide the data which cannot be directly covered by the other detectors. Thus, even with small statistics, the data will be important input to understand the neutrino interaction models. For example, the kinematics of protons shown in Fig. 10.15 is not consistent to the prediction from the current-best neutrino interaction models. After the further considerations on the detector systematics, the results would suggest a new set of fake data or even modifications of the neutrino interaction models used in the measurement of the neutrino oscillation parameters. Whether the systematic error of the oscillation parameters would change or not, the evaluation of the systematic errors will be more reliable owing to the measurements of low-momentum hadrons by the NINJA experiment.

Chapter 12

Conclusion

The discovery of the CP violation is one of the main goals in the current and future long-baseline neutrino oscillation experiments. To achieve this goal, the neutrino interaction models have to be well understood. The T2K experiment is a long-baseline neutrino oscillation experiment to measure the neutrino oscillation parameters. So far, the T2K experiment has measured the neutrino oscillation parameters with one of the best precisions in the world and indicated the CP violation in the lepton sector. One of the largest sources of systematic error in the T2K experiment is the uncertainty of the neutrino-nucleus interaction models. This uncertainty comes from the nuclear models which describe hadrons moving and interacting inside the nuclear medium. To understand such a "nuclear-effect," it is important to measure the hadrons emitted from the neutrino interactions. In addition to the reduction of the systematic uncertainties, a better understanding of the neutrino interaction itself is important. The current systematic uncertainty in the T2K experiment is based on the existing neutrino interaction models and experimental data. However, low-momentum hadrons from the neutrino interactions are hard to detect, and there are insufficient data. Thus, the models cannot be tested and validated for the low-momentum hadrons. To further understand the neutrino-nucleus interactions, it is important to measure the hadrons with a wide coverage of the phase space.

The NINJA experiment aims to measure neutrino-nucleus interactions using nuclear emulsion detectors. The nuclear emulsion has wide angular acceptance and a high three-dimensional spatial resolution, which enables us to measure low-momentum charged particles. The momentum threshold for protons is down to $200\,\mathrm{MeV}/c$ in the NINJA experiment, while that of the T2K near detector is $600\,\mathrm{MeV}/c$. It will give new data of low-momentum protons which cannot be directly measured by the other experiments. In this thesis, studies of neutrino-nucleus interactions with improvement of event reconstructions in the NINJA physics run are reported. The detector configurations, track reconstruction methods, momentum reconstruction, and particle identification are much improved from the previous analyses in the NINJA experiment.

We carried out the first physics run of the NINJA experiment, J-PARC E71a, from November 2019 to February 2020. In the physics run, a 75 kg water target detector was installed in the T2K near detector hall, and it was exposed to the neutrino beam corresponding to 4.7×10^{20} protons on target. The measurement of neutrino-water interactions is especially important for the T2K

experiment since the T2K far detector, Super-Kamiokande, is a water Cherenkov detector. The emulsion detectors have high positional and angular resolutions, which are suitable for the detailed study of the hadrons. However, they do not provide any timing information. Therefore, two kinds of the timestamp detectors, the emulsion shifter and the scintillation tracker, are newly introduced in the physics run. They connect muon tracks between the emulsion detector and the downstream muon range detector, Baby MIND. The data acquisition system of Baby MIND and the scintillation tracker is synchronized to the beam trigger signal, thus the connected muon tracks have precise timing information. The scintillation tracker has a new unique arrangement of the plastic scintillator bars with deliberate gaps between each other. This design is for the extension of the detector size to cover an area of $1\,\mathrm{m} \times 1\,\mathrm{m}$ without increasing the number of readout channels. The gap virtually constrains the position of the charged particle, and, by recognizing the hit pattern, a positional resolution of a few mm is achieved while the number of readout channels is as small as 248. The achieved positional resolution enables us to connect the tracks from Baby MIND to the emulsion shifter. Then, the emulsion shifter connects the tracks with the nuclear emulsion detectors.

The momentum reconstruction method is also developed and improved for the physics run. The momentum reconstruction based on the maximum likelihood using multiple Coulomb scatterings in the nuclear emulsion detector is newly developed to consider the energy deposit inside the detector volume. In addition, the treatment of the scattering angles used in the method is also updated. This method highly reduces the bias observed in the low-momentum region from 25% to 1%, and the momentum reconstruction becomes more precise. According to the MC simulation, the momentum resolution is 10% for $500\,\mathrm{MeV}/c$ muons passing through 69 iron plates in the ECC perpendicularly. In addition, the particle identification method is developed. Thanks to several data-driven corrections, the performance of the proton identification is evaluated to be 99% efficiency with 99% purity. After the particle identification, the momentum of protons is measured with the ECC track range or multiple Coulomb scatterings.

Using the developed methods, measurements of the track multiplicity and kinematics of charged particles from ν_μ charged-current interactions on a water target are performed. In this measurement, we analyze the data corresponding to around $8\,\mathrm{kg}$ of the water target, and 82 candidates are observed in total. The results show that the number of charged particles from the neutrino interactions is a powerful tool to discriminate the neutrino interaction modes, in particular, after the particle identification. The wide coverage of the phase space is also achieved in the results, which is essential for the further understandings of the neutrino interactions. The results also indicate that the improvements mentioned above play important roles in the measurements. The momentum reconstruction using multiple Coulomb scatterings extends the measurable momentum of the muons and hadrons, and it also contributes to the accurate particle identification. Although the statistical uncertainty is large and the further understanding of the systematic uncertainty from the detector response is necessary, the number of protons is much smaller than the MC prediction. This deficit may indicate that the current neutrino interaction models overestimate the number of emitted protons.

Four CC0π2p events are detected in this study. This is the first detection of CC0π2p events on the water target with the $200\,\mathrm{MeV}/c$ proton momentum threshold. In those events, protons

with lower momentum than 300 MeV/c are detected. The sample is one of the most important inputs to study the 2p2h interactions, and this is a significant improvement in the study of the neutrino-water interactions.

The results shown in this study experimentally demonstrate our performance of the kinematics measurements of charged particles from the neutrino-water interactions. The methods developed and improved in this study will contribute to the better understandings of the neutrino interactions with nine times larger statistics in near future. The expected results will help to reduce the systematic error in the long-baseline neutrino oscillation experiments and to construct the reliable neutrino interaction models for them. The precise measurement of the neutrino oscillation parameters with the more reliable neutrino interaction models will lead to the observation of the CP violation in the lepton sector.

List of Tables

List of Figures

List of Abbreviations

1p1h one-particle-one-hole

2p2h two-particle-two-hole

ADC Analogue to Digital Converter

APD Avalanche Photo-Diodes

ArgoNeuT Argon Neutrino Teststand

Baby MIND prototype Magnetized Iron Neutrino Detector

BIC BInary Cascade

BooNE Booster Neutrino Experiment

CCQE Charged-Current Quasi-Elastic

CCRES Charged-Current RESonant pion production

CC Charged-Current

CKM Cabibbo–Kobayashi–Maskawa

CP Charge conjugation and Parity

CSDA Continuous Slowing Down Approximation

DAQ Data AcQuisition

DIS Deep Inelastic Scattering

DONUT Direct Observation of the NU Tau

DUNE Deep Underground Neutrino Experiment

EASIROC Extended Analogue Si-pm Integrated ReadOut Chip

ECAL Electromagnetic CALorimeter

ECC Emulsion Cloud Chamber

EMT Electron Multiplier Tube

ES Electron Scattering

FGD Fine Grained Detector

FHC Forward Horn Current

FLUKA FLUktuierende KAskade

FSI Final State Interaction

FV Fiducial Volume

GALLEX GALLium EXperiment

Geant Geometry and tracking

GENIE Generates Events for Neutrino Interaction Experiments

GFRP Glass Fiber Reinforced Plastic

GiBUU Giessen Boltzman–Uehling–Uhlenbeck

GNO Gallium Neutrino Observatory

GRAINE Gamma-Ray Astro-Imager with Nuclear Emulsion

HA-TPC High Angle TPC

HTS Hyper Track Selector

ICARUS Imaging Cosmic And Rare Underground Signals

ID Inner Detector

IH Inverted Hierarchy

INCLXX the Liège IntraNuclear Cascade

INGRID Interactive Neutrino GRID

IO Inverted Ordering

ISS Inside Special Sheet

J-PARC Japan Proton Accelerator Research Complex

K2K KEK to Kamioka

KamLAND Kamioka Liquid scintillator Anti-Neutrino Detector

LArTPC Liquid Argon Time Projection Chamber

LEP Large Electron–Positron collider

LFG Local Fermi Gas

LINAC LINear ACcelerator

LSND Liquid Scintillator Neutrino Detector

MCS Multiple Coulomb Scatterings

MC Monte Carlo

MD Minimum Distance

MEC Meson Exchange Current

MicroMEGAS Micro MEsh GAseous Structure

MINERνA Main Injector Neutrino ExpeRiment to study ν-A interactions

MINOS Main Injector Neutrino Oscillation Search

MIP Minimum Ionizing Particle

MPPC Multi-Pixel Photon Counter

MRD Muon Range Detector

MR Main Ring

MSW Mikheyev–Smirnov–Wolfenstein

MUMON MUon MONitor

NC Neutral-Current

NH Normal Hierarchy

NINJA Neutrino Interaction research with Nuclear Emulsion and J-PARC Accelerator

NN Nucleon-Nucleon correlation

NOνA NuMI Off-axis ν_e Appearance

NOMAD Neutrino Oscillation MAgnetic Detector

NO Normal Ordering

OA Off-axis Angle

OD Outer Detector

OPERA Oscillation Project with Emulsion-tRacking Apparatus

OSS Outside Special Sheet

P0D Pi-zero Detector

PCAC Partially Conserved Axial Current

PDF Probability Distribution Function

PID Particle IDentification

PMNS Pontecorvo–Maki–Nakagawa–Sakata

PMT PhotoMultiplier Tube

PN PhotoNuclear effect

POT Protons On Target

QCD Quantum ChromoDynamics

QGSP BERT Quark Gluon String Precompound and the BERTini cascade model

RCS Rapid Cycling Synchrotron

RENO Reactor Experiment for Neutrino Oscillation

RFG Relativistic Fermi Gas

RHC Reverse Horn Current

RPA Random Phase Approximation

SAGE Soviet–American Gallium Experiment

SBN Short Baseline Neutrino

SFGD Super Fine Grained Detector

SF Spectral Function

SHINE SPS Heavy Ion and Neutrino Experiment

SI Secondary Interaction

SK Super-Kamiokande

SLC SLAC Linear Collider

SMRD Side Muon Range Detector

SM Standard Model

SNO Sudbury Neutrino Observatory

SS Special Sheet

STV Single Transverse Variable

SuSA Super Scaling Approach

T2K Tokai to Kamioka

TDC Time to Digital Converter

TKI Transverse Kinematic Imbalance

TOF Time Of Flight counter

TPC Time Projection Chamber

TSS Tracker Special Sheet

UA1 Underground Area 1

VPH Volume Pulse Height

WAGASCI WAter Grid And SCIntillator

WLS WaveLength Shifting

WMRD Wall Muon Range Detector

Xsec cross section

Bibliography

[1] W. Pauli, Phys. Today **31N9**, 27 (1978).

[2] F. Reines, C. L. Cowan, F. B. Harrison, A. D. McGuire, and H. W. Kruse, Phys. Rev. **117**, 159 (1960).

[3] G. Danby, J. M. Gaillard, K. A. Goulianos, L. M. Lederman, N. B. Mistry, M. Schwartz, and J. Steinberger, Phys. Rev. Lett. **9**, 36 (1962).

[4] K. Kodama *et al.* (DONUT Collaboration), Phys. Lett. B **504**, 218 (2001), arXiv:hep-ex/0012035 .

[5] D. DeCamp *et al.* (ALEPH Collaboration), Phys. Lett. B **231**, 519 (1989).

[6] S. Schael *et al.* (ALEPH, DELPHI, L3, OPAL, and SLD Collaborations, LEP Electroweak Working Group, and SLD Electroweak and Heavy Flavour Groups), Phys. Rept. **427**, 257 (2006), arXiv:hep-ex/0509008 .

[7] B. Pontecorvo, Zh. Eksp. Teor. Fiz. **34**, 247 (1957).

[8] Z. Maki, M. Nakagawa, and S. Sakata, Prog. Theor. Phys. **28**, 870 (1962).

[9] E. Majorana, Nuovo Cim. **14**, 171 (1937).

[10] L. Wolfenstein, Phys. Rev. D **17**, 2369 (1978).

[11] S. P. Mikheyxev and A. Yu. Smirnov, Nuovo Cim. C **9**, 17 (1986).

[12] R. Davis, D. S. Harmer, and K. C. Hoffman, Phys. Rev. Lett. **20**, 1205 (1968).

[13] K. S. Hirata *et al.* (Kamiokande-II Collaboration), Phys. Rev. Lett. **63**, 16 (1989).

[14] W. Hampbel *et al.* (GALLEX Collaboration), Phys. Lett. B **447**, 127 (1999).

[15] M. Altmann *et al.* (GNO Collaboration), Phys. Lett. B **490**, 16 (2000), arXiv:hep-ex/0006034 .

[16] J. N. Abdurashitov *et al.* (SAGE Collaboration), J. Exp. Theor. Phys. **95**, 181 (2002), arXiv:astro-ph/0204245 .

[17] K. S. Hirata *et al.* (Kamiokande-II Collaboration), Phys. Lett. B **205**, 416 (1988).

[18] Y. Fukuda *et al.* (Super-Kamiokande Collaboration), Phys. Rev. Lett. **81**, 1562 (1998), arXiv:hep-ex/9807003 .

[19] Q. R. Ahmad *et al.* (SNO Collaboration), Phys. Rev. Lett. **87**, 071301 (2001), arXiv:nucl-ex/0106015 .

[20] S. Fukuda *et al.* (Super-Kamiokande Collaboration), Phys. Rev. Lett. **86**, 5651 (2001), arXiv:hep-ex/0103032 .

[21] T. Araki, *et al.* (KamLAND Collaboration), Phys. Rev. Lett. **94**, 081801 (2005), arXiv:hep-ex/0406035 .

[22] K. Abe *et al.* (Super-Kamiokande Collaboration), Phys. Rev. D **94**, 052010 (2016), arXiv:1606.07538 [hep-ex] .

[23] B. Aharmim *et al.* (SNO Collaboration), Phys. Rev. C **88**, 025501 (2013), arXiv:1109.0763 [nucl-ex] .

[24] G. Bellini *et al.* (Borexino Collaboration), Phys. Rev. D **89**, 112007 (2014), arXiv:1308.0443 [hep-ex] .

[25] S. Abe *et al.* (KamLAND Collaboration), Phys. Rev. Lett. **100**, 221803 (2008), arXiv:0801.4589 [hep-ex] .

[26] M. Apollonio *et al.* (CHOOZ Collaboration), Phys. Lett. B **466**, 415 (1999), arXiv:hep-ex/9907037 .

[27] K. Abe *et al.* (T2K Collaboration), Phys. Rev. Lett. **107**, 041801 (2011), arXiv:1106.2822 [hep-ex] .

[28] D. Adey *et al.* (Daya Bay Collaboration), Phys. Rev. Lett. **121**, 241805 (2018), arXiv:1809.02261 [hep-ex] .

[29] H. de Kerret *et al.* (Double Chooz Collaboration), Nature Phys. **16**, 558 (2020), arXiv:1901.09445 [hep-ex] .

[30] G. Bak *et al.* (RENO Collaboration), Phys. Rev. Lett. **121**, 201801 (2018), arXiv:1806.00248 [hep-ex] .

[31] M. H. Ahn *et al.* (K2K Collaboration), Phys. Rev. D **74**, 072003 (2006), arXiv:hep-ex/0606032 .

[32] P. Adamson *et al.* (MINOS+ Collaboration), Phys. Rev. Lett. **125**, 131802 (2020), arXiv:2006.15208 [hep-ex] .

[33] K. Abe *et al.* (T2K Collaboration), Phys. Rev. D **103**, 112008 (2021), arXiv:2101.03779 [hep-ex] .

[34] M. A. Acero *et al.* (NOνA Collaboration), Phys. Rev. D **106**, 032004 (2022), arXiv:2108.08219 [hep-ex] .

[35] N. Agafonova *et al.* (OPERA Collaboration), Phys. Rev. D **100**, 051301 (2019), arXiv:1904.05686 [hep-ex] .

[36] M. Jiang *et al.* (Super-Kamiokande Collaboration), Prog. Theor. Exp. Phys. **2019**, 053F01 (2019), arXiv:1901.03230 [hep-ex] .

[37] M. G. Aartsen *et al.* (IceCube Collaboration), Phys. Rev. D **99**, 032007 (2019), arXiv:1901.05366 [hep-ex] .

[38] C. Bronner (on behalf of the T2K Collaboration), Recent results and future prospects from T2K (2022), The XXX International Conference of Neutrino Physics and Astrophysics (Neutrino 2022).

[39] I. Esteban, M. C. Gonzalez-Garcia, M. Maltoni, T. Schwetz, and A. Zhou, J. High Energy Phys. **2020** (09), 178, arXiv:2007.14792 [hep-ph] .

[40] NuFIT 5.1 (2021), www.nu-fit.org.

[41] N. Cabbibo, Phys. Rev. Lett. **10**, 531 (1963).

[42] M. Kobayashi and T. Maskawa, Prog. Theor. Phys. **49**, 652 (1973).

[43] A. D. Sakharov, Pisma Zh. Eksp. Teor. Fiz. **5**, 32 (1967).

[44] J. H. Christenson, J. W. Cronin, V. L. Fitch, and R. Turlay, Phys. Rev. Lett. **13**, 138 (1964).

[45] B. Aubert *et al.* (BaBar Collaboration), Phys. Rev. Lett. **87**, 091801 (2001), arXiv:hep-ex/0107013 .

[46] K. Abe *et al.* (Belle Collaboration), Phys. Rev. Lett. **87**, 091802 (2001), arXiv:hep-ex/0107061 .

[47] K. Abe *et al.* (Hyper-Kamiokande Proto-Collaboration), arXiv:1805.04163 [physics.ins-det] (2018).

[48] R. Acciarri *et al.* (DUNE Collaboration), arXiv:1512.06148 [physics.ins-det] (2015).

[49] L. Aliaga *et al.* (MINERνA Collaboration), Nucl. Instrum. Methods Phys. Res. A **743**, 130 (2014), arXiv:1305.5199 [physics.ins-det] .

[50] R. Acciarri *et al.* (MicroBooNE Collaboration), J. Instrum. **2017** (12), P02017, arXiv:1612.05824 [physics.ins-det] .

[51] K. Abe *et al.* (T2K Collaboration), Nucl. Instrum. Methods Phys. Res. A **659**, 106 (2011), arXiv:1106.1238 [physics.ins-det] .

[52] S. Igarashi *et al.*, Prog. Theor. Exp. Phys. **2021**, 033G01 (2021).

[53] K. Matsuoka, A. Ichikawa, H. Kubo, T. Maruyama, A. Murakami, T. Nakaya, and M. Yokoyama, Nucl. Instrum. Methods Phys. Res. A **623**, 385 (2010).

[54] K. Matsuoka *et al.*, Nucl. Instrum. Methods Phys. Res. A **624**, 591 (2010), arXiv:1008.4077 [physics.ins-det] .

[55] S. Bahdra *et al.*, Nucl. Instrum. Methods Phys. Res. A **703**, 45 (2013), arXiv:1201.1922 [physics.ins-det] .

[56] A. K. Ichikawa, Nucl. Instrum. Methods Phys. Res. A **690**, 27 (2012).

[57] K. Abe *et al.*, Nucl. Instrum. Methods Phys. Res. A **694**, 211 (2012), arXiv:1111.3119 [physics.ins-det] .

[58] Y. Ashida, M. Friend, A. Ichikawa, T. Ishida, H. Kubo, K. G. Nakamura, K. Sakashita, and W. Uno, Prog. Theor. Exp. Phys. **2018**, 103H01 (2018), arXiv:1805.07712 [physics.ins-det] .

[59] M. Yokoyama *et al.*, Nucl. Instrum. Methods Phys. Res. A **622**, 567 (2010), arXiv:1007.2712 [physics.ins-det] .

[60] M. Barranco-Luque *et al.* (UA1 Collaboration), Nucl. Instrum. Methods **176**, 175 (1980).

[61] S. Assylbekov *et al.*, Nucl. Instrum. Methods Phys. Res. A **686**, 48 (2012), arXiv:1111.5030 [physics.ins-det] .

[62] P. A. Amaudruz *et al.* (T2K ND280 FGD Collaboration), Nucl. Instrum. Methods Phys. Res. A **696**, 1 (2012), arXiv:1204.3666 [physics.ins-det] .

[63] N. Abgrall *et al.* (T2K ND280 TPC Collaboration), Nucl. Instrum. Methods Phys. Res. A **637**, 25 (2011), arXiv:1012.0865 [physics.ins-det] .

[64] I. Giomataris, R. De Oliveira, S. Andriamonje, S. Aune, G. Charpak, P. Colas, A. Giganon, Ph. Rebourgeard, and P. Salin, Nucl. Instrum. Methods Phys. Res. A **560**, 405 (2006), arXiv:physics/0501003 .

[65] D. Allan *et al.* (T2K UK Collaboration), J. Instrum. **2013** (8), P10019, arXiv:1308.3445 [physics.ins-det] .

[66] S. Aoki *et al.*, Nucl. Instrum. Methods Phys. Res. A **698**, 135 (2013), arXiv:1206.3553 [physics.ins-det] .

[67] K. Abe *et al.* (T2K Collaboration), arXiv:1901.03750 [physics.ins-det] (2019).

[68] D. Attié *et al.*, Nucl. Instrum. Methods Phys. Res. A **1025**, 166109 (2022), arXiv:2106.12634 [physics.ins-det] .

[69] A. Korzenev *et al.*, J. Instrum. **2022** (17), P01016, arXiv:2109.03078 [physics.ins-det] .

[70] K. Abe *et al.* (T2K Collaboration), Phys. Rev. D **97**, 032002 (2018), arXiv:1704.07467 [hep-ex] .

[71] K. Abe *et al.* (T2K Collaboration), Phys. Rev. Lett. **117**, 192501 (2016), arXiv:1604.04406 [hep-ex] .

[72] K. Abe *et al.* (T2K Collaboration), Phys. Rev. D **95**, 012010 (2017), arXiv:1605.07964 [hep-ex] .

[73] K. Abe *et al.* (T2K Collaboration), Phys. Rev. D **96**, 052001 (2017), arXiv:1706.04257 [hep-ex] .

[74] K. Abe *et al.* (T2K Collaboration), Phys. Rev. D **97**, 012001 (2018), arXiv:1708.06771 [hep-ex] .

[75] K. Abe *et al.* (T2K Collaboration), Phys. Rev. D **98**, 012004 (2018), arXiv:1801.05148 [hep-ex] .

[76] K. Abe *et al.* (T2K Collaboration), Phys. Rev. D **98**, 032003 (2018), arXiv:1802.05078 [hep-ex] .

[77] K. Abe *et al.* (T2K Collaboration), J. Phys. G **46**, 08LT01 (2019), arXiv:1902.03848 [hep-ex] .

[78] K. Abe *et al.* (T2K Collaboration), Phys. Rev. D **101**, 012007 (2020), arXiv:1909.03936 [hep-ex] .

[79] K. Abe *et al.* (T2K Collaboration), Phys. Rev. D **101**, 112001 (2020), arXiv:2002.09323 [hep-ex] .

[80] K. Abe *et al.* (T2K Collaboration), J. High Energy Phys. **2020** (10), 114, arXiv:2002.11986 [hep-ex] .

[81] K. Abe *et al.* (T2K Collaboration), Phys. Rev. D **101**, 112004 (2020), arXiv:2004.05434 [hep-ex] .

[82] K. Abe *et al.* (T2K Collaboration), Phys. Rev. D **103**, 112009 (2021), arXiv:2102.03346 [hep-ex] .

[83] K. Abe *et al.* (T2K Collaboration), Phys. Rev. D **90**, 052010 (2014), arXiv:1407.4256 [hep-ex] .

[84] K. Abe *et al.* (T2K Collaboration), Phys. Rev. D **91**, 112002 (2015), arXiv:1503.07452 [hep-ex] .

[85] S. Yamamoto *et al.*, IEEE Trans. Nucl. Sci. **52**, 2992 (2005).

[86] A. A. Aguilar-Arevalo *et al.* (SciBooNE Collaboration), arXiv:hep-ex/0601022 (2006).

[87] K. Abe *et al.* (T2K Collaboration), Prog. Theor. Exp. Phys. **2019**, 093C02 (2019), arXiv:1904.09611 [hep-ex] .

[88] K. Abe *et al.* (T2K Collaboration), Prog. Theor. Exp. Phys. **2021**, 043C01 (2021), arXiv:2004.13989 [hep-ex] .

[89] Y. Fukuda *et al.* (Super-Kamiokande Collaboration), Nucl. Instrum. Methods Phys. Res. A **501**, 418 (2003).

[90] K. Abe *et al.* (Super-Kamiokande Collaboration), Nucl. Instrum. Methods Phys. Res. A **1027**, 166248 (2022), arXiv:2109.00360 [physics.ins-det] .

[91] L. Wan (on behalf of the Super-Kamiokande Collaboration), New Results with Atmospheric Neutrinos at Super-Kamiokande (2022), The XXX International Conference of Neutrino Physics and Astrophysics (Neutrino 2022).

[92] T. Stuttard (on behalf of the IceCube Collaboration), Particle physics with atmospheric neutrinos at IceCube/DeepCore (2022), The XXX International Conference of Neutrino Physics and Astrophysics (Neutrino 2022).

[93] K. Abe *et al.* (T2K Collaboration and J-PARC Neutrino Facility Group), arXiv:1908.05141 [physics.ins-det] (2019).

[94] Y. Hayato and L. Pickering, Eur. Phys. J. Spec. Top. **230**, 4469 (2021), arXiv:2106.15809 [hep-ph] .

[95] C. Andreopoulos *et al.*, Nucl. Instrum. Methods Phys. Res. A **614**, 87 (2010), arXiv:0905.2517 [hep-ph] .

[96] T. Golan, C. Juszczak, and J. T. Spbczyk, Phys. Rev. C **86**, 015505 (2012), arXiv:1202.4197 [nucl-th] .

[97] D. Casper, Nucl. Phys. B Proc. Suppl. **112**, 161 (2002), arXiv:hep-ph/0208030 .

[98] O. Buss, T. Gaitanos, K. Gallmeister, H. van Gees, M. Kaskulov, O. Lalakulich, A. B. Larionov, T. Leitner, J. Weil, and U. Mosel, Phys. Rept. **512**, 1 (2012), arXiv:1106.1344 [hep-ph] .

[99] C. H. Llewellyn Smith, Phys. Rept. **3**, 261 (1972).

[100] R. G. Sachs, Phys. Rev. **126**, 2256 (1962).

[101] M. Gourdin, Phys. Rept. **11**, 29 (1974).

[102] R. Bradford, A. Bodek, H. S. Budd, and J. Arrington, Nucl. Phys. B Proc. Suppl. **159**, 127 (2006), arXiv:hep-ex/0602017 .

[103] J. Liu *et al.* (UCNA Collaboration), Phys. Rev. Lett. **105**, 181803 (2010), arXiv:1007.3790 [nucl-ex] .

[104] D. Mund, B. Naerkisch, M. Deissenroth, J. Krempel, M. Schumann, H. Abele, A. Petoukhov, and T. Soldner, Phys. Rev. Lett. **110**, 172502 (2013), arXiv:1204.0013 [hep-ex] .

[105] V. Bernard, L. Elouadrhiri, and U. Meißner, J. Phys. G **28**, R1 (2002), arXiv:hep-ph/0107088 .

[106] S. L. Adler, Phys. Rev. **135**, B963 (1964).

[107] D. Rein and L. M. Sehgal, Annals Phys. **133**, 79 (1981).

[108] C. Berger and L. M. Sehgal, Phys. Rev. D **76**, 113004 (2007), arXiv:0709.4378 [hep-ph] .

[109] K. M. Graczyk, J. Żmuda, and J. T. Sobczyk, Phys. Rev. D **90**, 093001 (2014), arXiv:1407.5445 [hep-ph] .

[110] M. Kabirnezhad, Phys. Rev. D **97**, 013002 (2018), arXiv:1711.02403 [hep-ph] .

[111] L. Tiator, D. Drechsel, S. Kamalov, M. M. Giannini, E. Santopinto, and A. Vassallo, Eur. Phys. J. A **19**, 55 (2004), arXiv:nucl-th/0310041 .

[112] D. Rein and L. M. Sehgal, Nucl. Phys. B **223**, 29 (1983).

[113] D. Rein and L. M. Sehgal, Phys. Lett. B **657**, 207 (2007), arXiv:hep-ph/0606185 .

[114] M. Hasegawa *et al.* (K2K Collaboration), Phys. Rev. Lett. **95**, 252301 (2005), arXiv:hep-ex/0506008 .

[115] K. Hiraide *et al.* (SciBooNE Collaboration), Phys. Rev. D **78**, 112004 (2008), arXiv:0811.0369 [hep-ex] .

[116] A. Higuera *et al.* (MINERνA Collaboration), Phys. Rev. Lett. **113**, 261802 (2014), arXiv:1409.3835 [hep-ex] .

[117] C. Berger and L. M. Sehgal, Phys. Rev. D **79**, 053003 (2009), arXiv:0812.2653 [hep-ph] .

[118] M. Glück, E. Reya, and A. Vogt, Eur. Phys. J. C **5**, 461 (1998), arXiv:hep-ph/9806404 .

[119] A. Bodek and U. K. Yang, AIP Conf. Proc. **670**, 110 (2003), arXiv:hep-ex/0301036 .

[120] T. Sjostrand, Comput. Phys. Commun. **82**, 74 (1994).

[121] R. A. Smith and E. J. Moniz, Nucl. Phys. B **43**, 605 (1972), [Erratum: Nucl. Phys. B 101, 547 (1975)].

[122] J. Nieves, E. Oset, and C. Garcia-Recio, Nucl. Phys. A **554**, 509 (1993).

[123] J. Nieves, I. Ruiz Simo, and M. J. Vincente Vacas, Phys. Rev. C **83**, 045501 (2011), arXiv:1102.2777 [hep-ph] .

[124] B. Boutguille, J. Nieves, and F. Sánchez, J. High Energy Phys. **2021** (04), 004, arXiv:2012.12653 [hep-ph] .

[125] M. Valverde, J. E. Amaro, and J. Nieves, Phys. Lett. B **638**, 325 (2006), arXiv:hep-ph/0604042 .

[126] O. Benhar, A. Fabrocini, S. Fantoni, and I. Sick, Nucl. Phys. A **579**, 493 (1994).

[127] O. Benhar and A. Fabrocini, Phys. Rev. C **62**, 034304 (2000), arXiv:nucl-th/9909014 .

[128] E. G. Moniz, I. Sick, R. R. Whitney, J. R. Ficenec, R. D. Kephart, and W. P. Trower, Phys. Rev. Lett. **26**, 445 (1971).

[129] V. L. Martinez-Consentino, S. I. Ruiz, J. E. Amaro, and E. R. Arriola, Phys. Rev. C **96**, 064612 (2017), arXiv:1710.04988 [nucl-th] .

[130] R. D. Woods and D. S. Saxon, Phys. Rev. **95**, 577 (1954).

[131] R. Gran *et al.* (K2K Collaboration), Phys. Rev. D **74**, 052002 (2006), arXiv:hep-ex/0603034 .

[132] A. A. Aguilar-Arevalo *et al.* (MiniBooNE Collaboration), Phys. Rev. D **81**, 092005 (2010), arXiv:1002.2680 [hep-ex] .

[133] L. B. Auerbach *et al.* (LSND Collaboration), Phys. Rev. C **66**, 015501 (2002), arXiv:nucl-ex/0203011 .

[134] V. Lyubushkin *et al.* (NOMAD Collaboration), Eur. Phys. J. C **63**, 355 (2009), arXiv:0812.4543 [hep-ex] .

[135] K. S. Egiyan *et al.* (CLAS Collaboration), Phys. Rev. C **68**, 014313 (2003), arXiv:nucl-ex/0301008 .

[136] K. S. Egiyan *et al.* (CLAS Collaboration), Phys. Rev. Lett. **96**, 082501 (2006), arXiv:nucl-ex/0508026 .

[137] R. Shneor *et al.* (Jefferson Lab Hall A Collaboration), Phys. Rev. Lett. **99**, 072501 (2007), arXiv:nucl-ex/0703023 .

[138] A. Bodek, H. S. Budd, and M. E. Christy, Eur. Phys. J. C **71**, 1726 (2011), arXiv:1106.0340 [hep-ph] .

[139] M. Martini, M. Eficson, G. Chanfray, and J. Marteau, Phys. Rev. C **80**, 065501 (2009), arXiv:0910.2622 [nucl-th] .

[140] G. D. Megias, J. E. Amaro, M. B. Barbaro, J. A. Caballero. T. W. Donnelly, and I. Ruiz Simo, Phys. Rev. D **94**, 093004 (2016), arXiv:1607.08565 [nucl-th] .

[141] J. Nieves, I. Ruiz Simo, and M. J. Vincente Vacas, Phys. Lett. B **707**, 72 (2012), arXiv:1106.5374 [hep-ph] .

[142] L. Alvarez-Ruso *et al.* (NuSTEC Collaboration), Prog. Part. Nucl. Phys. **100**, 1 (2018), arXiv:1706.03621 [hep-ph] .

[143] L. L. Salcedo, E. Oset, M. J. Vincente-Vacas, and C. Garcia-Recio, Nucl. Phys. A **484**, 557 (1988).

[144] G. Rowe, M. Salomon, and R. H. Landau, Phys. Rev. C **18**, 584 (1978).

[145] R. Seki and K. Masutani, Phys. Rev. C **27**, 2799 (1983).

[146] H. W. Bertini, Phys. Rev. C **6**, 631 (1972).

[147] A. Ankowski, O. Benhar, and M. Sakuda, Phys. Rev. D **91**, 033005 (2015), arXiv:1404.5687 [nucl-th] .

[148] F. J. Hasert *et al.* (Gargamelle Neutrino Collaboration), Phys. Lett. B **46**, 138 (1973).

[149] S. J. Barish *et al.*, Phys. Rev. D **16**, 3103 (1977).

[150] N. J. Baker, A. M. Cnops, P. L. Connolly, S. A. Kahn, H. G. Kirk, M. J. Murtagh, R. B. Palmer, N. P. Samios, and M. Tanaka, Phys. Rev. D **23**, 2499 (1981).

[151] T. Kitagaki *et al.*, Phys. Rev. D **28**, 436 (1983).

[152] P. A. Zyla *et al.* (Particle Data Group), Prog. Theor. Exp. Phys. **2020**, 083C01 (2020).

[153] C. Rubbia, The Liquid Argon Time Projection Chamber: A New Concept for Neutrino Detectors (1977).

[154] S. Amerio *et al.* (ICARUS Collaboration), Nucl. Instrum. Methods Phys. Res. A **527**, 329 (2004).

[155] C. Anderson *et al.*, J. Instrum. **2012** (7), P10019, arXiv:1205.6747 [physics.ins-det] .

[156] M. Antonello *et al.* (MicroBooNE, LAr1-ND, and ICARUS-WA104 Collaborations), arXiv:1503.01520 [physics.ins-det] (2015).

[157] R. Acciarri *et al.* (ArgoNeuT Collaboration), Phys. Rev. D **90**, 012008 (2014), arXiv:1405.4261 [nucl-ex] .

[158] P. Abratenko *et al.* (MicroBooNE Collaboration), arXiv:2211.03734 [hep-ex] (2022).

[159] X. Lu, L. Pickering, S. Dolan, G. Barr, D. Coplowe, Y. Uchida, D. Wark, M. O. Wascko, A. Weber, and T. Yuan, Phys. Rev. C **94**, 015503 (2016), arXiv:1512.05748 [nucl-th] .

[160] X. Lu and J. T. Sobczyk, Phys. Rev. C **99**, 055504 (2019), arXiv:1901.06411 [hep-ph] .

[161] X. G. Lu *et al.* (MINERνA Collaboration), Phys. Rev. Lett. **121**, 022504 (2018), arXiv:1805.05486 [hep-ex] .

[162] T. Cai *et al.* (MINERνA Collaboration), Phys. Rev. D **101**, 092001 (2020), arXiv:1910.08658 [hep-ex] .

[163] D. Coplowe *et al.* (MINERνA Collaboration), Phys. Rev. D **102**, 072007 (2020), arXiv:2002.05812 [hep-ex] .

[164] C. M. G. Lattes, H. Muirhead, G. P. S. Occhialini, and C. F. Powell, Nature **159**, 694 (1947).

[165] K. Niu, E. Mikumo, and Y. Maeda, Prog. Theor. Phys. **46**, 1644 (1971).

[166] N. Agafonova *et al.* (OPERA Collaboration), Phys. Rev. Lett. **115**, 121802 (2015), arXiv:1507.01417 [hep-ex] .

[167] K. Yamada *et al.*, Prog. Theor. Exp. Phys. **2017**, 063H02 (2017), arXiv:1703.03737 [physics.ins-det] .

[168] H. Oshima *et al.* (NINJA Collaboration), Prog. Theor. Exp. Phys. **2021**, 033C01 (2021), arXiv:2012.05221 [hep-ex] .

[169] H. Oshima *et al.* (NINJA Collaboration), Phys. Rev. D **106**, 032016 (2022), arXiv:2203.08367 [hep-ex] .

[170] A. Hiramoto *et al.* (NINJA Collaboration), Phys. Rev. D **102**, 072006 (2020), arXiv:2008.03895 [hep-ex] .

[171] T. Fukuda *et al.*, Prog. Theor. Exp. Phys. **2017**, 063C02 (2017), arXiv:1703.03659 [hep-ex] .

[172] P. Adamson *et al.* (MINOS Collaboration), Phys. Rev. D **81**, 072002 (2010), arXiv:0910.2201 [hep-ex] .

[173] K. Abe *et al.* (T2K Collaboration), Phys. Rev. D **93**, 072002 (2016), arXiv:1509.06940 [hep-ex] .

[174] A. Hiramoto, Ph.D. thesis, Kyoto University (2021).

[175] T. Odagawa *et al.*, Prog. Theor. Exp. Phys. **2022**, 113H01 (2022), arXiv:2207.06640 [physics.ins-det] .

[176] K. Kodama *et al.*, Adv. Space Res. **37**, 2120 (2006).

[177] S. Takahashi *et al.*, Nucl. Instrum. Methods Phys. Res. A **620**, 192 (2010).

[178] H. Rokujo *et al.*, Nucl. Instrum. Methods Phys. Res. A **701**, 127 (2013).

[179] S. Takahashi *et al.*, Prog. Theor. Exp. Phys. **2015**, 043H01 (2015).

[180] S. Takahashi *et al.*, Prog. Theor. Exp. Phys. **2016**, 073F01 (2016).

[181] S. Takahashi, S. Aoki *et al.* (GRAINE Collaboration), Adv. Space Res. **62**, 2945 (2018).

[182] H. Rokujo *et al.*, Prog. Theor. Exp. Phys. **2018**, 063H01 (2018).

[183] Y. Nakamura *et al.*, Porg. Theor. Exp. Phys. **2021**, 123H02 (2021).

[184] T. Odagawa *et al.*, Nucl. Instrum. Methods Phys. Res. A **1034**, 166775 (2022), arXiv:2201.06828 [physics.ins-det] .

[185] Kuraray Co., Ltd, Plastic Scintillating Fibers (2014), kuraray.co.jp.

[186] K. Yoshida, Master's thesis, Kyoto University (2015), in Japanese.

[187] I. Nakamura, N. Ishijima, K. Hanagaki, K. Yoshimura, Y. Nakai, and K. Ueno, Nucl. Instrum. Methods Phys. Res. A **787**, 376 (2015), New Developments in Photodetection NDIP14.

[188] K. Abe *et al.* (T2K Collaboration), Phys. Rev. D **87**, 012001 (2013), [Addendum: Phys. Rev. D 87, 019902 (2013)], arXiv:1211.0469 [hep-ex] .

[189] S. Agostinelli *et al.* (GEANT4 Collaboration), Nucl. Instrum. Methods Phys. Res. A **506**, 250 (2003).

[190] J. Allison *et al.*, IEEE Trans. Nucl. Sci. **53**, 270 (2006).

[191] J. Allison *et al.*, Nucl. Instrum. Methods Phys. Res. A **835**, 186 (2016).

[192] R.Brun, F. Bruyand, F. Carminati, S. Giani, M. Maire, A. McPherson, G. Patrik, and L. Urban, GEANT Detector Description and Simulation Tool (1994).

[193] A. Ferrarim P. R. Sala, A. Fasso, and J. Ranft, FLUKA: A multi-particle transport code (Program version 2005) (2005).

[194] T. T. Böhlen *et al.*, Nucl. Data Sheets **120**, 211 (2014).

[195] N. Abgrall *et al.* (NA61/SHINE Collaboration), Phys. Rev. C **84**, 034604 (2011), arXiv:1102.0983 [hep-ex] .

[196] N. Abgrall *et al.* (NA61/SHINE Collaboration), Phys. Rev. C **85**, 035210 (2012), arXiv:1112.0150 [hep-ex] .

[197] N. Abgrall *et al.* (NA61/SHINE Collaboration), Eur. Phys. J. C **76**, 84 (2016), arXiv:1510.02703 [hep-ex] .

[198] N. Abgrall *et al.* (NA61/SHINE Collaboration), Eur. Phys. J. C **76**, 617 (2016), arXiv:1603.06774 [hep-ex] .

[199] J. B. Birks, Proc. Phys. Soc. A **64**, 874 (1951).

[200] G. D'Agostini, Improved iterative Bayesian unfolding (2010), Alliance Workshop on Unfolding and Data Correction, arXiv:1010.0632 [physics.data-an] .

[201] R. H. Barlow and C. Beeston, Comput. Phys. Commun. **77**, 219 (1993).

[202] M. Yoshimoto, T. Nakano, R. Komatani, and H. Kawahara, Prog. Theor. Exp. Phys. **2017**, 103H01 (2017), arXiv:1704.06814 [physics.ins-det] .

[203] Y. Suzuki *et al.*, Prog. Theor. Exp. Phys. **2022**, 063H01 (2022), arXiv:2112.02887 [physics.ins-det] .

[204] K. Hamada *et al.*, J. Instrum. **2012** (7), P07001.

[205] Y. Suzuki, Ph.D. thesis, Nagoya University (2022), in Japanese.

[206] H. Maesaka, Ph.D. thesis, Kyoto University (2005).

[207] T. Kikawa, Ph.D. thesis, Kyoto University (2014).

[208] V. L. Highland, Nucl. Instrum. Methods **129**, 497 (1975).

[209] G. R. Lynch and O. I. Dahl, Nucl. Instrum. Methods Phys. Res. B **58**, 6 (1991).

[210] K. Kodama *et al.*, Nucl. Instrum. Methods Phys. Res. A **574**, 192 (2007).

[211] N. Agafonova *et al.* (OPERA Collaboration), New J. Phys. **14**, 013026 (2012), arXiv:1106.6211 [physics.ins-det] .

[212] P. Abratenko *et al.* (MicroBooNE Collaboration), J. Instrum. **2017** (12), P10010, arXiv:1703.06187 [physics.ins-det] .

[213] F. James and M. Roos, Comput. Phys. Commun. **10**, 343 (1975).